DISS. ETH NO. 28812

SHAPE DESIGN OF 3D-CONCRETE-PRINTED MASONRY STRUCTURES

A thesis submitted to attain the degree of

DOCTOR OF SCIENCES
(Dr. sc. ETH Zurich)

presented by

SHAJAY BHOOSHAN
MPhil in Digital Architectonics, University of Bath, United Kingdom

born on *18.06.1979*

accepted on the recommendation of

Prof. Dr. Philippe Block (doctoral thesis supervisor)
Dr. Tom Van Mele (co-examiner)
Dr. Patrik Schumacher (co-examiner)

2023

ABSTRACT

The research aims to contribute to the 'digitalisation' of concrete – digital design of 3D concrete-printed (3DCP) structures and robotic manufacture of the concrete parts – and thus pave the way for its sustainable use. The motivation to achieve such a Sustainable Digital Concrete (SDC) stems from three insights:

- The importance of a common language of geometry to empower a collaborative approach between Architecture, Engineering and Construction (AEC) to fully realise the promise of 3DCP - the time and resource efficient, aesthetically appealing realisation of high-performance shapes and structures.

- The relevance of historic, unreinforced masonry design methods and their contemporary computational extensions to interactive shape design, and design-to-manufacturing tools for 3DCP that in turn, support the mainstream adoption of the advances in 3DCP. There is a current lack of such tools, despite the rapid evolution of hardware and material technologies of 3DCP.

- The effectiveness of unreinforced masonry design and construction with 3DCP 'stone' to achieve circular construction goals to *reduce, reuse and recycle* material, and *repair* of structures.

Specifically, the research investigates an Interactive Design Environment (IDE) and the underlying Computational Framework (CF) to adapt equilibrium modelling techniques from rigid-block masonry to aid the interactive shape and print-path design for unreinforced, 3DCP masonry structures. It focuses on enabling the synthesis of geometries that are structurally and materially feasible vis-a-vis 3DCP. The masonry analogy is also extended to a second scale of the concrete printed in layers, by utilising the masonry design techniques of stereotomy – a practice aligning material layout with expected compressive force flows.

These insights, and observations about the necessity of design exploration of novel technologies such as 3DCP, yields the principal contributions of the research: A computational framework that allows for geometric reasoning about shape, exploration of associated design space, and proof-of-concept physical realisation s including a full-scale, 16m-span 3DCP masonry footbridge, which demonstrates the concepts and technologies described in this dissertation.

Keywords: design space, design explorer, robotic 3D printing in concrete, computational geometry, CAGD, architectural geometry, stereotomy, function representation, implicit modelling, shape design, 3D Concrete Printing

ABSTRACT

Ziel der Forschungsarbeit ist es, einen Beitrag zur "Digitalisierung" des Betons zu leisten - digitales Design von 3D-Beton-Druckstrukturen (3D Concrete-Printing, 3DCP) und robotergestützte Herstellung von Betonbauteilen - und damit den Weg für eine nachhaltige Nutzung von Beton zu ebnen. Die Motivation, einen solchen nachhaltigen digitalen Beton (Sustainable Digital Concrete, SDC) zu erreichen, ergibt sich aus drei Erkenntnissen:

- Die Bedeutung einer einheitlichen Geometriesprache für die Zusammenarbeit zwischen Architektur, Ingenieurwesen und Bauwesen (AEC), um das Versprechen von 3DCP, die zeit- und ressourceneffiziente, ästhetisch ansprechende Realisierung von hochleistungsfähigen Formen und Strukturen, voll zu erfüllen.

- Die Relevanz historischer, unbewehrter Mauerwerksentwurfsmethoden und ihrer zeitgenössischen computergestützten Erweiterungen für den interaktiven Formenentwurf und Design-to-Manufacturing Tools für 3DCP, die wiederum die allgemeine Akzeptanz von Fortschritten bei 3DCP fördern. Trotz der schnellen Entwicklung der Hardware- und Materialtechnologien für 3DCP gibt es derzeit einen Mangel an solchen Tools.

- Wirksamkeit von unbewehrtem Mauerwerk und Bauen mit 3D-Beton-gedruckten 'Steinen' zur Erreichung der Ziele der Kreislaufwirtschaft wie Reduzierung, Wiederverwendung und Recycling von Materialien und Reparatur von Bauwerken.

Konkret werden eine interaktive Entwurfsumgebung (Interactive Design Environment, IDE) und das zugrundeliegende Computational Framework (CF) untersucht, um die Methoden der Gleichgewichtsmodellierung von Mauerwerk aus starren Blöcken für den interaktiven Entwurf von Formen und Druckpfaden für unbewehrte 3DCP-Mauerwerkskonstruktionen zu nutzen. Der Schwerpunkt liegt auf der Synthese von Geometrien, die strukturell und materiell für 3DCP geeignet sind. Die Analogie zu Mauerwerk wird auch auf eine zweite Skala von schichtweise gedrucktem Beton angewendet, indem Stereotomietechniken für den Entwurf von Mauerwerk verwendet werden - eine Praxis, bei der die Anordnung der Materialien an die erwarteten Druckkräfte angepasst wird.

Aus diesen Erkenntnissen und der Notwendigkeit, neue Technologien wie 3DCP zu erforschen, ergeben sich die Schwerpunkte dieser Forschungsarbeit: Ein computergestütztes Framework, das geometrische Schlussfolgerungen über die Form erlaubt, die Untersuchung des zugehörigen Entwurfsraums und die Demonstration der konkreten Umsetzung, einschließlich einer 3D-Beton-gedruckten Fußgängerbrücke mit einer Spannweite von 16 m in Originalgröße, die die in dieser Dissertation beschriebenen Konzepte und Technologien demonstriert.

Schlagworte: Entwurfsraum, Entwurfsexplorer, robotergestützter 3D-Druck in Beton, computergestützte Geometrie, CAGD, architektonische Geometrie, Stereotomie, Funktionsdarstellung, implizite Modellierung, Formgebung

ACKNOWLEDGEMENTS

I would like to express my sincere gratitude and thanks to the following people without whom this research and dissertation would not have been possible.

- Dr. Prof Philippe Block, who has been a mentor, friend, a reservoir of energy, enthusiasm, and conviction for all things related to geometry, masonry design, digital fabrication, the finer details of contemporary design and gastronomic culture, apart from being exceedingly generous with his time, knowledge, and insights. His own seminal PhD and subsequent career is motivational - to have had a close quarter view of his progress has been rewarding, educational and exciting in equal measure. Extra thanks for leaving no stone unturned to make Striatus happen.
- Dr. Tom Van Mele, who has been exceptionally patient and lucid in clarifying the intricacies of matrix algebra, rigors of computer programming, and the subtleties of geometrical algorithms, apart from providing company in many a (wine fueled!) stimulating conversation. The accelerated growth and maturation of his intellectual and technical baby - the COMPAS framework - in the same span of time as my PhD has been very beneficial to assimilate and articulate all manner of computational best practices. Extra thanks for near-singular efforts in the realisation of Striatus.
- Dr. Patrik Schumacher, who has supported my entire career at Zaha Hadid Architects thus far, providing both inspiration and the enterprising playbook to align design-research and technological advancements with a critically reflexive framing of their architectural merit, and impact. His conviction to fearlessly speak his mind has been most encouraging, whilst his historically and intellectually searing perspectives have been instrumental in my efforts to foreground contributions of design-research, as also to balance research with practice.
- Late Dr. Matthias Rippmann for his influential, inspirational research, dissertation and career that was cruelly cut short. His work paved the way for much that is covered in my PhD, both in the conceptual framing and technical implementation. He also saved me from a ton of writing-up by being able to summarily refer to his dissertation and papers!
- Johannes Megens of incremental3D, for matching the conviction and ambitions of the research for a first-principles-based design-to-fabrication pipeline by miraculously scaling a tentative idea into a world-class 3DCP start-up. His designerly attention and craft is evident in the fine quality of the 3DCP prototypes and the masonry blocks of Striatus, featured in the PhD research. A man and a robot can do much!
- Colleagues at the Block Research Group (BRG) for sharing the long journey with me. Special thanks to Alessandro Dell'Endice, who started his PhD after, and completed it before mine (!), being a fellow contributing PhD to the Striatus demonstrator. Much gratitude and thanks also to Noelle Paulson for administrative support, helping understand the peculiarities of the Swiss culture and bureaucracy, and proof-reading many of the promotional materials related to Striatus.
- Colleagues at the Computation and Design research group at Zaha Hadid Architects (ZHACODE). Particularly Jianfei Chu, and Vishu Bhooshan who generously poured their talents and technical expertise to make Striatus successful. Special thanks to Vishu, for many insights, robust technical implementations of the ideas developed in the PhD and general support in the capacity of being my brother!
- Colleagues and students at the Design Research Laboratory of the Architectural Association in London, that saw the early architectural promise of 3DCP, explored the design space of architectural solutions and made many a clay-printed prototype that provided me with motivation to pursue the topic of this dissertation.

- My parents of course, for persevering through their PhDs in their time. My father, also for being the earliest introduction to masonry, sun-dried bricks, vaults, domes and the Auroville Institute In India.

Last but most emphatically not the least, my wife Alicia Nahmad Vazquez and son Elai Nahmad Bhooshan, for being the most avid, unconditional supporters of my endeavours, and understanding about the frequent separation. Their exacting aesthetic standards has had immeasurable impact on the research and the demonstrator project of Striatus. Alicia's wonder woman energy and superpowers to juggle her own research, career, start-up and frequently being a solo-mother was an ever-present, encouraging beacon even as they supremely dwarfed my efforts.

It has been a real. It has been worth it.

CONTRIBUTIONS FROM COLLABORATIVE WORK

Some aspects of the research presented in this dissertation were a collaborative effort that included the author, particularly in the physically realised demonstrator project of Striatus, related development of illustrative diagrams and research papers. This has been highlighted in Chapter 11.

Contents

PART I - CONTEXT AND FRAMING 19
1 MOTIVATIONS 20
1.1 3D Concrete Printing and lack of design tools 21
1.2 Congeniality of Architectural Geometry and Tectonism 22
1.3 Funicular structures and 3D Concrete Printing 24
1.4 Appropriate design paradigm to realise the benefits of 3DCP 24
1.5 Masonry paradigm, sustainability and 3DCP 25
1.6 Shape exploration for 3DCP and integrated design-to-production 25
1.7 Contributions 27
1.7.1 Sustainable digital concrete and unreinforced masonry 28
1.7.2 Shape exploration and integrated design-to-production 28
1.7.3 3DCP specific shape representation 29
1.7.4 Print-path synthesis and post-processing 29
1.7.5 Physical prototypes and proof of concept 29
1.7.6 Literature review and software implementation 30
1.8 Limitations of scope 30
1.8.1 Print-viability via buckling simulation 30
1.8.2 Type of 3DCP and specifications of ‘ink’ 30
1.8.3 Print-path specifications 30
1.8.4 Structural design and verification 31
1.8.5 Software implementation 31
2 GEOMETRIC APPROACH AND SUSTAINABLE DIGITAL CONCRETE 32
2.1 Applying a geometric approach to the structural aspects of 3DCP 33
2.2 Design Explorers 34
2.3 Industry assimilation and Design Explorers 35
2.3.1 Integration with existing Design Pipelines 35
2.3.2 Novel design outcomes for Novel technology 36
2.4 A Design Explorer for Robotic 3D Concrete Printing 36
2.4.1 Shape design methods for masonry structures 36
2.4.2 Masonry and stereotomy 38
2.4.3 Geometry and economic construction 40
2.4.4 Statics and fabrication-oriented Design Explorers 41
2.5 Forward and inverse approaches to shape design for robotic 3DCP 42
2.6 Sustainable Digital Concrete 43

3 RELEVANT PRIOR WORK AND CONCEPTS 44
3.1 Geometry processing 44
3.2 Simulation of 3DCP concrete 44
3.3 Equilibrium and fabrication-aware computational design 45
3.4 Masonry and 3DCP 46
3.4.1 Equilibrium modelling and limit analysis 46
3.4.2 Shape design for Pitch brick masonry 48
3.5 Implicit shape modelling 48
3.5.1 Implicit shape representation 49
3.5.2 Skeleton based implicit modelling 49
3.5.3 Medical imaging and layered printing 50
3.6 Function representation 50
3.6.1 Optimal Mass transport 51
3.6.2 Spatially coherent scalar-field interpolation using mass transport 52
3.7 Print-path synthesis for 3DCP 53
3.8 3D-Concrete-Printed bridge structures 53
PART II - COMPUTATIONAL FRAMEWORK 55
4 A COMPUTATONAL FRAMEWORK 56
4.1 Serial thread 57
4.2 Data structures 59
4.3 Shape design 60
4.3.1 User-specified host mesh and it derivates 61
4.3.2 Creation of masonry blocks 62
4.3.3 Planarization of the interfaces 62
4.4 Print-path synthesis 63
4.4.1 Function Representation - Primitive field functions & operations 64
4.4.2 Booleans 64
4.4.3 Trim with plane 65
4.4.4 Linear interpolation 65
4.5 Print viability and guiding heuristic 65
4.5.1 Extending the print viability heuristic 66
4.6 Handling spatial skeletons 67
4.7 Interactive and informed design procedure 68
5 PRINT PLANE AND PRINT-PATH INTERPOLATION 71
5.1 Benefits 71
5.2 Morph and slerp 72
5.3 Morph: Shape Interpolation 72
5.4 Slerp: Plane Interpolation 75

5.4.1 Motion paths and Frenet-Serret frames 75
5.4.2 Spherical Linear Interpolation 75
5.4.3 Affine transformation and spatial coherence 76
5.5 Parameter choice 76
5.6 Design-to-production 76
5.6.1 Complex topologies 77
6 SOFTWARE IMPLEMENTATION 79
6.1 Form finding of global shape 79
6.2 Stereotomy 80
6.2.1 Data export 80
6.3 Print-path generation 81
6.4 Expert users 82
PART III - PROTOTYPES AND DEMONSTRATORS 83
7 PHYSICAL PROTOTYPES 84
7.1 Generalizing from early prototypes 84
7.1.1 Inclined-plane printing 84
7.2 Simple, tubular topologies 84
7.3 Bifurcating tube topology 86
7.4 Intersecting, multi-tube topology 89
7.4.1 Geometry processing 90
7.4.2 Robotic 3D printing 91
7.4.3 Path planning 91
7.4.4 Results 92
8 STRIATUS – A FULL SCALE, TECHNOLOGY DEMONSTRATOR 93
8.1 Design-to-production toolchain 94
8.2 Structural principles and constraints 95
8.3 File format and data structure 97
8.4 Implementation 98
8.5 Serial thread of DTP 99
8.5.1 Shape design 99
8.6 Stereotomy 100
8.6.1 Block interface planarization 101
8.7 Print-path synthesis 102
8.7.1 Plane interpolation 102
8.7.2 Cross section interpolation 103
8.8 Post processing 104
8.9 Structural thread of DTP toolchain 104
8.9.1 Best-fit TNA 104

8.9.2 DEM analysis 105
8.9.3 FEM analysis 106
8.10 Material and prototyping thread of DTP toolchain 106
8.11 Printing, construction, and assembly 107
9 PRINT-PATH DESIGN FOR INCLINED-PLANE 3D CONCRETE PRINTING 110
9.1 Path synthesis-to-manufacture workflow 110
9.2 Print-path synthesis to production 111
9.3 Print-path generation 111
9.3.1 Print plane interpolation 111
9.3.2 Print profile generation 112
9.4 Post Processing 113
9.5 Contiguous Print-paths 114
9.6 Machine Code Generation 115
9.6.1 Raft generation 115
9.6.2 Assigning robot speed 116
9.7 Material Tests and Prototyping 117
9.8 Generalization 117
PART IV - CONCLUSIONS 119
10 DISCUSSION 120
10.1 Summaries 121
10.2 Outlook 121
10.2.1 Computational Framework 121
10.2.2 Function representation and print-path synthesis 123
10.2.3 Striatus, technology demonstrator 123
10.3 Conclusions 124
10.3.1 Benefits of the masonry paradigm & incline-plane 3D Concrete Printing 124
10.3.2 Integrated computational design, robotic 3DCP and construction 125
10.3.3 New language for concrete 125
11 STRIATUS PROJECT CREDITS 126
11.1 Full credits 126
11.1.1 Design 126
11.1.2 Structural engineering 126
11.1.3 Fabrication design 126
11.1.4 3D concrete printing 126
11.1.5 Concrete material development 126
11.1.6 Assembly & Construction 126
11.1.7 Logistics 126
11.1.8 Additional partners 126

11.1.9 Documentation 127
12 Appendix I 128
12.1 Rigid-Block Equilibrium 128
12.1.1 Equilibrium formulation 128
12.2 Soft-Rigid Body Equilibrium (sRBE) 129
12.3 Implementation 130
12.3.1 Contact interfaces and collisions 130
REFERENCES 131

List of figures

Figure 1 – History of 3D printing. (Left) Patent for constructing topographic models by stacking contours (Blanther, 1892). (Right) Process of producing 3D sculpture from multiple views of the same object or person (Sobieszek, 1980). 20

Figure 2 – desktop 3D printing. (Column 1 and 2) Patent for automated production of 3D figure (Swainson, 1977). (Column 3) 3D Systems® patent for stereo lithography (Hull, 1986). (Column 4) Early description of completely digital process: 3D geometry generation, slicing support generations etc. (Beaman et al., 1997). 20

Figure 3 – Pioneers in large format 3D Concrete Printing (3DCP): (Left column) D-Shape® printing process (Dini, 2009). (Middle column) Freeform technology from Loughborough University (Lim et al., 2012). (Right column) Contour Crafting® technology (Khoshnevis, 2004). 21

Figure 4 – Growth of 3D Concrete Printing since 2010 (Ma et al., 2022). (Left top) cumulative number of projects, (Left bottom) cumulative number of 3DCP projects by type, (Middle top) Cumulative number of published patents, (Middle bottom) cumulative number of published articles, (Right) Global distribution of project location and number. 22

Figure 5 – Design to production tool chain and physical demonstrator. 23

Figure 6 – Material properties of 3D printed concrete. (Left) Dominant material properties of printed concrete. (Right) Intention to discretise the print layers into micro-blocks, to enable geometric reasoning about equilibrium and print feasibility 24

Figure 7 – Equilibrium design space. (Left column) Various compression-only geometries form found using Thrust Network Analysis (Block et al., 2014); (Middle column) Various tensile geometries form found using the Force Density Method (Schek, 1974). (Right column) Early results from proposed IDE and CF. 26

Figure 8 – Integrated design to production toolchain unrolled into threads. (a,b,c) serial thread, (i, ii, iii) parallel structural threads, (iv) material testing and prototyping thread, (v) foundation design thread, and (vi) scaffold design thread. 26

Figure 9 – Photographs of a force-aligned, inclined-plane 3DCP of components of funicular structures 27

Figure 10 – Proposed Interactive Design Explorer (IDE) for concrete printing 29

Figure 11 – Print path synthesis, including infill generation, for inclined-plane printing and large-batch production. 29

Figure 12 – Details of development plan of Contour Crafting® (CC) technology. The focus of robotic and material technologies is particularly notable (Khoshnevis, 2004). 32

Figure 13 – Prior design explorers for 3DCP. (Left column) Designer handbook and other aspects of funicular shell design considered relevant by Contour Crafting® 3D printing company (Khoshnevis et al., 2006a). (Middle Column) Parametric design exploration of feasible designs, online customization interface, structural analysis and realised result by tutors and students of Xi'an Jiaotong-Liverpool University (Chien et al., 2016). (Right column) Design tools developed by Foster and Partners and Loughborough University to slice existing geometries and explore toolpaths of the 3d Printer and resultant geometries (De Kestelier and Buswell, 2009). 33

Figure 14 – Structural properties of hardened and freshly printed concrete. (Left Column) Compressive and flexural strength of hardened concrete (Le et al., 2012b). (Middle Top) use of FEA to simulate fresh concrete flow in Contour Crafting® process (Kwon, 2002). (Middle Bottom) relation of Bond strength between layers and the time gap between printing them (Kwon, 2002). (Right top) collapse of freshly printed concrete due to material failure (Le et al., 2012a). (Right bottom) collapse of freshly printed concrete due to geometric complexity of layers. 34

Figure 15 – Computer Aided Geomtric Design (CAGD) in the automboile industry. (Left and Middle columns) Digital reconstruction process of Master-mould using Unisurf CAD system, in use at Renault Car Company around 1970: mark-up on clay master, 3d scanning, numerical input of points, creation of curve networks (Bezier, 1971). (Right column) similar system in use at British Aircraft Company (Sabin, 1971). 35

Figure 16 – Graphical methods of finding equilibrium shapes. (Left) 2D geometrical construction of the so-called Elastic curve of a simple beam with a single, point load (Wolfe, 1921). (Right) 3D construction of funicular geometry with Thrust Network Analysis (Block and Ochsendorf, 2007). 37

Figure 17. Various computational means of authoring self-supporting geometries in 3D. Left top – *Design of Self-supporting Surfaces:* Interactive editing and visualising destruction sequence (Vouga et al., 2012). Left Bottom - *Computing self-supporting surfaces by regular triangulation* (Liu et al., 2013). Right Top and Bottom- *Form finding with Polyhedral Meshes* (Tang et al., 2012). 37

Figure 18 – Design of concrete structures using graphical methods by engineer Robert Malliart. (Left) Salginatobel Bridge, Switzerland (Fivet and Zastavni, 2012). (Right) Chiasso Shed, Switzerland (Zastavni, 2008). 38

Figure 19 – Computational limit analysis of masonry structures. (Left) Limit analysis based on the so-called 'equilibrium' formulation (Livesley, 1992). (Right) Limit analysis based on the so-called 'collapse' formulation (Gilbert and Melbourne, 1994). 39

Figure 20 – Interactive structural design. (Left Column and Middle Top) Interactive guidance regarding structural stability of stone masonry and suggestions to improve stability (Whiting, 2012). (Middle bottom and Right column) Complete design tool-set for generating self-supporting masonry structures, tessellating them into blocks, and prototyping with desktop 3D printing (Panozzo et al., 2013). 39

Figure 21 – Force-flow aligned tessellation of funicular geometries and built results (Rippmann, 2016)..... 40

Figure 22 – Statics and fabrication-oriented Design Explorers. (Left top) Graphical analysis manual available in the late 19th century (Huerta, 2006). (Left Bottom) Use of those methods by Antonio Gaudi in the design of Church of *Colonia Guell* and *Sagrada familia* (Huerta, 2006). (Right) 19th century manuals for construction detailing in timber and stone, and drawing instruments, to realise complex geometries (Witt, 2010b)..... 41

Figure 23 – Shape agnostic, inverse design paradigm. A user-provided mesh (a), typically modelled agnostic to printing constraints, is 'sliced' to derive print-paths (b) by intersecting horizontal cutting planes with the input mesh. The dashed red circle highlights the problematic parts for printing due to a lack of spatial coherence causing infeasible, unsupported overhangs between subsequent layers (c)..... 42

Figure 24 – Use of and problems related to Finite Element Analysis (FEA) of Concrete Printing. (Column 1) Modifying the macroscopic properties of material in ABAQUS simulation software to predict behaviour of hardened sulfur-concrete (Khoshnevis et al., 2017). (Column 2) Use of FEA to predict fresh concrete (Tanigawa and Mori, 1989). (Column 3) Lagrangian, Eulerian and hybrid models of describing material (Donea et al., 2004). (Column 4) Problems of handling large deformations in Lagrangian description, and comparison to hybrid description (Donea et al., 2004). 45

Figure 25 – Equilibrium design space. (Left) various compression-only geometries form-found using TNA (Block et al., 2014). (Right) various compression-only geometries form-found using the Force Density Method (Schek, 1974). 46

Figure 26 – Interactive Equilibrium Modelling (Lachauer, 2015). (Left column) Human computer interaction in the search for a satisfactory result within the space of equilibrium shapes. (Middle Column) Authoring of various constraints to the modelling process, Right column – Interactive manipulation of the constraints and the resultant equilibrium shapes. 47

Figure 27 – Graph representation to generate print-paths for wall-like components. (a) Zero-contour of a signed distance field computed in relation to the edges of a graph. (b) evolving the zero-cotnour over time to represent the 2.5D object. (c) printing related artefacts created when using this approach..... 50

Figure 28 – 'Slicing' and print-paths. Processing of BRep mesh representation (a) to generate horizontal print-paths (b) and field-aligned print-paths (c). The print-paths are post-processed to generate machine code (d). (e) Shows the strong visual presence of the task graphs in the physically realised shapes. 51

Figure 29 – Advantages of implicit modelling. (a,b) two scalar fields. (c) Boolean difference operation of (b) on (a). (d) The natural extension of specifying interior task graphs as contours of a scalar field. (e) Natural handling of topological change of many closed curves at the bottom layer to a singular closed curve on the top layer. 51

Figure 30 – Fluid-dynamics-based, Eulerian optimal transport. (a) The fluid-dynamics formulation of Optimal Transport (Papadakis et al., 2014) and corresponding C++ code (Bonneel, 2013) was used to produce this interpolation sequence of morphing top-left image to bottom right image. (b) corresponding zero contours with start (red), end profile(blue) and interpolated zero-contours(grey). (c) Resulting 3D shape obtained by stacking the consecutive zero contours..... 52

Figure 31 – Interactive Design Explorer (IDE) for concrete printing 56

Figure 32 – BRep based, shape agnostic 'slicing'. Processing of mesh representation (left) to generate horizontal or field-aligned print-paths (middle) and subsequent attaching of a micro-block model to evaluate their print viability (right)..... 57

Figure 33 – Skeletal graphs and print paths. (a) A user-specified skeleton graphs (red) and related distance field. (b) Extracted Level curve. (c) 2.5D evolution of level curve (blue) and resulting print-paths. 58

Figure 34 – Computational framework, to compute and store graph, enclosing solid, interface planes, and print-paths..... 58

Figure 35 – Using an MME for shape design. (a) It is often easier for a designer to create the initial state of skeletal graph (FG initial state) on a host mesh (HM initial state). HM is then form-found along with the graph. (b,c,d) a MME provides graph and mesh processing and the so-called subdivision algorithms, which help in the various geometry processing tasks involved in the Stereotomy and print-path synthesis stages of design..... 60

Figure 36 – Interactive, informed design 61

Figure 37– Mesh walking and stereotomy. (a) The form-found mesh can be discretised or a stereotomy assigned to the mesh (staggered red patches or segments in this case) by using so-called mesh walking and breadth-first or depth first graph search algorithms. (b) planes that represent interface between masonry blocks can similarly be extracted. (c) A spine is constructed by connecting the centres of the extracted planes with edges. (d) downstream steps of print-path synthesis. See Figure 38 for more..... 62

Figure 38 – Print-path synthesis. (a) Processing the funicular spine generated in the previously (b), to synthesise print profiles for each masonry block created by the stereotomy step. 63

Figure 39 –Signed distance fields (SDF). (a) SDF in relation to the nodes a skeletal graph. (b) SDF in relation to the edges of a skeletal graph. 64

Figure 40 – Boolean operations. (a) and (b) Primitive fields. (c) Difference, (d) Intersection and (e) Union operations on (a) and (b). (f) Consequence of trim operation on the scalar field. (g) (h) trim operations applied successively..... 64

Figure 41 – Linear blend operation. (a,b) Two signed distance fields (SDF). (c-g) Blend sequence of the zero contour as SDF (a) blends to SDF (b). The effect of a faster blend rate on the shape of the geometry described by the stack of zero-contours is shown in (i). 65

Figure 42 – Guiding heuristic. Typical check for spatial coherence between two consecutive print layers; (b) zoom-in of (a) and an example of two consecutive layers exhibiting partial lack of spatial coherence between them (dashed red circles). Layer 1(blue) is to be printed on top of layer 0 (black) and thus needs sufficient overlap interface (red) to be adequately supported. When curves are not fully coherent, layer 1 can become partially or entirely unsupported (inset); (c) zoom-in of (a) and an example of two consecutive layers exhibiting good spatial coherence between themselves and thus adequate overlap (red line in inset) and overhang within bounds. 66

Figure 43 – Evaluating stability of the task graph. (a) A skeletal graph (red) and a micro-block model attached to the resulting print-path. (b) Contact interface and forces when two rigid-bodies are in resting contact. (c) Similar forces when two soft-rigid bodies are in contact See Appendix I for more. 67

Figure 44 – Spatial funicular skeleton and its stereotomy. (a) Initial state of graph on host low-poly. (b) Form-found graph. (c) n-sided tubes around the edges of the graph. (d) Convex hulls computed around the nodes of the graph. (e) Combined mesh of (c) and (d). (e) Indicative print-paths computed on combined mesh. 67

Figure 45 – Extending CF and MME to spatial funicular graphs. (a) Graph to tubular mesh. (b) Splitting the tube into left and right parts and using the bisector plane as the interface plane for blocks. (c) Subdivision meshes. (d) Using (c) and (b) to interpolate print-paths. . 67

Figure 46 – Design of globally funicular shapes and their discretization, using Thrust Network Analysis and a mesh modelling environment. The results are from a 5-day workshop (“digitalFutures ,” 2017). 69

Figure 47 – Graph-to-print-paths workflow to recreate the funicular ramp example from Figure 46 . The study was explored and executed by professional designers at Zaha Hadid Architects in a few hours, after only summary instructions and the tools were provided (Chapter 6). 69

Figure 48 – Graph-to-Print-paths workflow to recreate the funicular shell example from Figure 46 . The study was explored and executed by professional designers at Zaha Hadid Architects in a few hours, after only summary instructions and the tools were provided (Chapter 6). 70

Figure 49 Graph-to-print-paths workflow for a funicular floor slab, explored and executed by professional designers at Zaha Hadid Architects within a few hours after only summary instructions and the tools were provided (Chapter 6). 70

Figure 50 – Radial Basis Function (RBF) based, Lagragian optimal transport. (a,d) Source and target RBF-based scalar-field. (b,c) Intermediate, interpolated RBF and scalar-field state. The Displacement Interpolation algorithm and corresponding C++ code was adapted to produce this interpolation sequence (Bonneel, 2018) (Bonneel et al., 2011b; “Network Simplex,” 2009). (e) Resultant 3D shape achieved by stacking the consecutive zero contours. 73

Figure 51 – Planar Inputs. (a,b) Starting and End scalar-fields and corresponding zero-contours (red) produced by respective Radial Basis Functions (RBFs) (dashed). (c) User-provided start and end print planes (red) and optionally a curve connecting them. (d) In-plane Euclidean paths between centres of all pairs of RBFs of starting and end scalar-fields. Alternatively, segmented paths may be generated from a graph connecting the centres (Figure 53). 73

Figure 52 – Morph & Slerp. (a,b) Morph operation: blending two topological circles in the starting scalar-field to one circle in the end. (c,d) Slerp operation. (a) Displacement interpolation between start and end scalar-fields. (b) Zero-contours extracted in-plane and in-place, from various intermediate states of the evolving scalar-field shown in (a). (c) Moving frames (black) extracted from a curve connecting the start and end planes (red). (d) Resulting 3D shape achieved by transforming each in-plane curve in (b) unto respective planes in (c). 73

Figure 53 – Displacement trajectories. (a) User-provided graph connecting centres of source RBF (black circles) and sink RBF (black dots). (b) A family of segmented curve handles generated by walking between source (black circles) and target mass points (pink dashed circles) marked on graph in (a) and computing the so-called Dijkstra paths. (c) Smoothed version of the family of curves shown in (b). It can be noted that the zero-contours of the shape (blue) evolve along the control curves in both (b) and (c). (d,e) Resulting 3D shapes corresponding to (b) and (c) respectively, with the smooth family (c) producing more gentle curvature and inclination in the print layers, hence more amenable to printing with wet concrete. Thus, control handles like (c) is recommended. 74

Figure 54 – Plane interpolation. (a) Intermediate profile curves (blue) obtained by interpolating between start (red) and end (black) profiles using the Morph operation (Section 3.1). (b-left) Frenet-Serret moving frames extracted from a curve (red) and (b-right) spherical linear interpolation of frames between start and end frames (red). (c) Resulting 3D shapes obtained by transforming (a) unto each family of planes (b-left and b-right) and subsequently thickening the curves. 75

Figure 55 – Affine Transformation. (a) Zero-contours of interpolated scalar-field (blue) obtained from the Morph operation (Section 5.3). The smooth gradation of bounding boxes of each consecutive zero contour (black squares) is a consequence of the spatial coherence of the zero-contours. (b) Each of the zero-contours of (a) individually scaled to fit a unit square. (c) Interpolated planes using the Slerp operation (Section 5.4); (d) Resulting 3D shape obtained by affine transformation of each (a) unto (c). (e) Resulting 3D shape obtained by affine transformation of each (b) unto (c). This shows the use-case of scaling all zero-contours to fit within a unit square and generating tubular shapes. 76

Figure 56 – Stand-alone applications. (left) Proof-of-concept, stand-alone computer application to synthesise shapes for robotic 3D printing using the proposed method. (right) application for downstream processing of geometry for manufacturing used (courtesy of Incremental 3D GmbH). 77

Figure 57 – Branching topology and inclined print-paths example. The proposed shape description only requires (a) graph with the location of start and end mass-points (pink and black dashed circles respectively), start and end planes (b) to automatically produce spatially coherent, gradually inclined print-paths of a topologically complex shape (e). (c,d) Intermediate zero-contours created from inputs (a,b). It would require considerable expertise in both BRep based shape modelling and 'slicing' to produce (e) using currently ubiquitous methods. (f) 3D shape obtained by thickening the (blue) curves in (e)..... 77

Figure 58 – Lagrangian Optimal mass transport example. (L-R) Top-down, top and bottom-up offline rendered views of an example geometry produced using the Morph & Slerp shape description. The displacement interpolation scheme used in this paper makes it easy to create spatially coherent blends between cross sectional curves with different topology such as in this example – four circles of the bottom profile are morphed into two touching circles on the top cross section. The bulbous curves are a feature of the RBF-based formulation. 78

Figure 59 – Eulerian Optimal mass transport examples. (a-d) Offline rendered images of example geometries with spatially-coherent blends between pairs of profiles curves, produced with relative ease using the Morph & Slerp shape description; These examples highlight the possibility of having smooth curve profiles if we use the fluid-dynamics-based formulation of optimal transport instead of the bulbous curves that are a feature of the RBF-based formulation used in Figure 58. The M&S shape description can admit either of the two formulations of optimal transport..... 78

Figure 60 – Using Rhino Vault for form finding. (a) Coarse mesh (left) and Catmull Clark subdivision mesh (right). (b) Two important form finding steps - Horizontal equilibrium (left) and vertical equilibrium (right). 79

Figure 61 – Using a Mesh modelling environment (MME). Autodesk Maya (shown here) used to derive user specifications needed for stereotomy (left and middle) (Sections 4.3.2 and 6.2) from a form found mesh (right) (Sections 4.3 and 6.1)..... 80

Figure 62 – Slicing example from COMPAS_Slicer object (Van Mele, 2020). (Left) Set of slicing planes and the corresponding sliced contours on the mesh. (Right) Various constituent parts of a synthesized print-path that are useful to generate corresponding machine instructions or so-called G-Code. 81

Figure 63 – Stereotomy of the form found surface mesh and print-paths visualised on the masonry blocks. 81

Figure 64 – Early tests of physically realising print-paths generated using the Interactive Design Explorer. (Left and Middle) Results from the 2.5D extrusion. (Right) Inclined-plane printing. Photographs from Johannes Megens (c). 84

Figure 65 – Tests of using signed distance fields to generate print-paths and machine instructions to deposit clay. (Left and Middle): Outward radiating task graph because of a radial distance function. (Right) 3D printing of one of the layers in clay..... 85

Figure 66 – Prototype for the Integrated Design Environment (IDE). (Left) Synthesis of print-paths, and their post-processing for printed related parameters (right). 85

Figure 67 – Post-processing of print paths by 3D concrete Printing (3DCP) manufacturer ("Incremental3d," 2017). (Left) Processing of an outcome produced by proposed IDE by the manufacturer. (Right) Prototype demonstrating the application of the proposed method. 86

Figure 68 – Using the IDE to synthesize tubular topology objects. 2.5D wall-like structural components, produced user specified input graphs (Red). 86

Figure 69 – Bifurcating tubular topology shape design results. Results produced by first-time user, architectural students during a 5-day design-to-production workshop ("digitalFutures," 2018)..... 87

Figure 70 – Bifurcating tubular topology shape design results. Results produced by first-time user, architectural students during a 5-day design-to-production workshop ("digitalFutures," 2018)..... 88

Figure 71 – Bifurcating tubular topology shape design results. Results produced by first-time user, architectural students during a 5-day design-to-production workshop ("digitalFutures," 2018)..... 89

Figure 72 – Typical geometric processing of spatial graphs for 3D printing. (a-c) Generating convex hulls around nodes and bars of a graph, (c) contouring the combined mesh. (e) Alignment and interface problems with task graphs. 90

Figure 73 – A procedure of translate and trim to synthesise task graphs for each node segment. (b) Task graphs of one of the four parts meeting at node show in (a). (c) Stages of evolution of the print layers of print-path shown in (b). 90

Figure 74 – FRep based processing of spatial graphs. (a) Secondary composite primitives formed by Boolean operations on primary primitives (b,c). (b,c) Primary primitive scalar fields generated as Signed Distance Fields (SDFs) in relation to the vertices and edges of the spatial graph..... 91

Figure 75 – Printing sequence of a compound, spatial print-path. Computer generated images showing (a - c) printing sequence of the constituent parts of a node and (b) result highlighting the groove feature that adds internal support to the print. 91

Figure 76 – Visual inspection of print trajectories, for potential collision of print head with the already printed parts and/or the ground92

Figure 77 – Materially bonded, compound 3DCP objects. Photographs showing various types of nodes that vary in valence and angles between incident edges..... 92

Figure 78 – Force-aligned, inclined-plane 3DCP of a node in a funicular skeleton. 92

Figure 79 – Schematic drawings of Striatus. (a) plan, (b) elevation A, (c) section BB, and (d) section CC 93

Figure 80 – Photograph of Striatus, Venice 2021(naaro (c)). 93

Figure 81 – DTP Tool chain unrolled into threads. (a,b,c) serial thread, (i, ii, iii) parallel structural threads, (iv) material testing and prototyping thread, (v) foundation design thread & (vi) scaffold design thread 94

Figure 82 – Masonry logic at two scales. (a) Arched balustrade and deck voussoirs, (b) start and end plane of a print block - P_s, P_e 95

Figure 83 – Structural principles. (a) Stable, bifurcating deck arches. (b) Inward leaning balustrade arches. (c) Balustrade arches prevented from falling over by stable deck (d) Outward thrust resultants of masonry structure. (e) Tension ties to counter outward thrust resultants. (f) The final geometry. 96

Figure 84 – Block interface planes. (a) Block interface planes represented as a non-manifold mesh. (b) Detail inset showing interface planes for one block - with adjacent blocks & internal left - right interface 97

Figure 85 – Stereotomy. (a) Key plan highlighting mesh patches of block b22 & b41. (b) Medial Spine. (c) List for left & right faces of the block (F_l,F_r). (c) Interpolated left & right print plane normals (PN_l,PN_r). (d) Block interface planes - start (P_{sl}, P_{sr}), end (P_{el}, P_{er}), sides (P_{side}) & internal ($P_{internal}$). (e) Print contours left & right from start to end planes (C_{sl}, C_{sr},C_{el}, C_{er}) 98

Figure 86 – Half-edge data structure. (a) JSON attributes & schema stored on a half edge mesh. (b) List storing per face f_i one of its half-edge index *he*, (c) List storing per vertex v_i, one of its outgoing half-edge index *he*. (d) List storing per half-edge he_i indices for next half-edge (next), previous half-edge (prev), associated face *f* & associate start vertex index *v*. (e) Attribute list storing face normal $\boldsymbol{nf}_i$ per face f_i. (f) Attribute list storing vertex position $\boldsymbol{vpos}_i$, vertex normal $\boldsymbol{nv}_i$ per vertex v_i. 99

Figure 87 –Shape design. (a) 2D spine graph. (b) Coarse mesh. (c) Subdivision mesh. (d) Form found mesh. (e) Manipulated coarse mesh. (f) Subdivision mesh using the Catmull-Clark subdivision algorithm. (g) Guide mesh with balustrade for transmission via JSON format exchange file. 99

Figure 88 – Mesh two-colouring and stereotomy. (a) Spine edges for deck and balustrade. (b) Spine walk stride for deck. (c) Spine walk stride for balustrade. (d) Face coloured mesh. (e) Thickened mesh 100

Figure 89 –Mesh walking. (a) Mesh walks on spine and block face collections using the half edge data structure. (b) Boundary representation of the solid voussoirs. 101

Figure 90 – JSON attributes & schema added in the stereotomy step. (a) block attribute stored as face colour, (b) thickness attribute storing corresponding vertex position of top $\boldsymbol{v}_{itop}$ and bottom $\boldsymbol{v}_{ibottom}$ per vertex v_i, (c) interface plane attribute storing plane origin $\mathbf{o}_i$ and normal $\mathbf{pn}_i$ per half-edge he_i 101

Figure 91 – Block interface planarization. (a) Block interface planes before and (b) after the perturbation procedure for planarization 102

Figure 92 – Details of planarization of Block interface faces. (a) Computing of the projection-based perturbation force $\boldsymbol{F}_i$ per vertex v_i of the interface planes -$Plane_{input}$, N_{input} - to make them planar using the best-fit target planes - $Plane_{target}$, N_{target}. (b) Showing the iterative steps ($Plane_{iterations}$) of the solver for 6 interface planes. 102

Figure 93 – Interpolation schemes to compute new planes between the start and end planes. (a) Linear interpolation scheme highlighting some print height is below the minimum printing height. (b) Optimised weighted non-linear interpolation scheme to ensure all print heights lie in the specified printing height domain. 103

Figure 94 – Print plane interpolation. (a) Left Planes interpolated between start & end planes - P_{sl}, P_{el}. (b) Right planes interpolated between start & end planes - P_{sr}, P_{er}. (c) Example left plane profile generation. (d) Corresponding right plane profile generation. (e) Combined left and right profiles. 103

Figure 95 – SDFs for deck blocks. (a) Base cross-sectional profile, polygonal SDF. (b) Offset polygonal SDF. (c) Offset polygonal SDF. (d) Infill SDF. (e) Trim SDF. (f) Resultant SDF 104

Figure 96 – Post processing of pirnt-paths. Re-sampling of cross section profiles of the previous step (Figure 95) to make it amenable to robotic print constraints such as spacing and maximum number of points. (a) Key map showing the number of re-sampling points per block sequence. (b) Various re-sampling strategies tested on the contours: un-resampled print profile (top), distance-based resampling (middle) and adaptive feature-based resampling (bottom). (c,d) 3DCP result from un-resampled and adaptive feature-based resampling respectively. 105

Figure 97 – Iterative solver for best-fit thrust network analysis (TNA), showing the form and force diagram. (a) Iteration 1. (b) Final iteration 105

Figure 98 – Discrete element modelling. (a) Resultant force vectors at interface planes. (b) 3Dec Analysis. (c) example of a point-load test. 106

Figure 99 – Finite element modelling and analysis. 106

Figure 100 – Material testing and prototyping. (a,b) establishing Minimum and maximum for layer-height and print wdiths respectively. (c,d) Close-up views of the cross-sectional infill on a inclined-plane-printed block. 107

Figure 101 – Translation of material and prototyping tests to geometric constraints. (a) Initial sketches for a stereotomy strategy based on print constraints. (b) Print recommendations for block orientation, layer height and width, and material calculation with various infill patterns. 107

Figure 102 – data visualisations of (a) individual block metrics showing variation of print layer heights through the blocks, the print bounds, angle deviation between start and end plane, total number of points etc & (b) metrics for all 53 blocks. 108

Figure 103 – Printing, construction, and assembly. (a) 3D printing of block. (b) Preparation for transportation. (c,d,e) Transportation and storage on site. (f) Erection of scaffold. (g) Placement of deck blocks. (h) Placement of key stone balustrade block. 109

Figure 104 – Print-path synthesis-to-manufacturing. (a) Print-path generation using function representation (FRep). (b) Post processing of print-paths. (c) Evaluation of printability & generation of machine code. (d) Robotic 3d Concrete Printing (3DCP) of blocks. (e) Assembly process. (f) Finished bridge. 110

Figure 105 – Print-path synthesis. (a) Workflow diagram for print-path synthesis to production. (b) Global shape with stereotomy. (c,d) left & right planes interpolated between start (P_{sl}, P_{sr}) & end planes (P_{el}, P_{er}). (e,f) Base cross section profile. 111

Figure 106 – Print profile generation. (a,g) The resultant SDF (f_{result}) representing the compound cross-sectional print-path. f_{result} is constituted as the Boolean of five individual SDFs (b-f). 112

Figure 107 – SDFs for balustrade blocks. (a) Base profile polygonal SDF f_0. (b) Offset polygonal SDF f_1. (c) Offset polygonal SDF f_2. (d) Infill SDF f_3. (e) Trim SDF f_4. (f) Resultant SDF f_5. 113

Figure 108 – Printing paths sampling. (a) Print-path synthesis from SDFs. (b) Uniform resampling. (c) Adaptive feature-based resampling. (d,e) Result of the printing for un-resampled and adaptive feature-based resampling print-paths, respectively. 114

Figure 109 – Adaptive resampling. (a) Adaptive sampling of cross section profiles based on feature points. The feature point is computed as the nearest intersection of vector $\boldsymbol{y}_i$ with the cross-section profile, where $\boldsymbol{y}$ is the cross product of input guide vector $\boldsymbol{x}_i$ and the plane normal $\boldsymbol{z}$. The cross-section profiles are split at these feature point to maintain alignment with the planes below and the individual segments are sampled using adaptive distances - low sampling distance for segments on the outside and higher sampling distance for the internal parts of the block. (b) Procedure to connect the left and right cross section profiles to create one continuous print-path 114

Figure 110 – Generation of continuous printing path. (a) Left and right contours. (b) Connected layer. (c) Spiralling path. (d) Sequence for the connection of the left and right paths. 115

Figure 111 – JSON attributes & schema added in the print-path synthesis step. (a) List storing per vertex of the print contour, the position $\boldsymbol{v}_i$, print normal $\boldsymbol{n}_i$, print height h_i. print height is computed as distance between $\boldsymbol{v}_i$ and the intersection point $\boldsymbol{pt}_i$ of ray $\boldsymbol{n}_i$ with the previous print plane. (b) Specified print width $w_{i.}$ 115

Figure 112 – Block reorientation for printing. (a) Horizontally aligned unstable axis of base layer (right), to correct reorientation axis and to minimise raft (magenta). (b) Rotation around unstable axis: alignment along centre of gravity axis avoids slipping between block and raft as well as providing a stable print position. 116

Figure 113 – Kinematic simulation with colour indication of print speeds. (a) via mesh color and (b) via so-called Robot Targets. (c) Per print point layer, dimensions *lw* and *lh* are transformed into speed settings for each robot target, along with common kinematic parameters. 116

Figure 114 – Material tests and prototyping. (a) Path and infill tests. (b) Defining material and processing parameters for consistency. (c,d) Learnings had been reintroduced for the final design, most relevant being the seam details for the deck blocks. 117

Figure 115 – Photo of the finished project on site, Giardini della Marinaressa, Venice, Italy. (c) Photographs by Naaro 117

Figure 116 – Striatus, an arched unreinforced masonry footbridge. (c) Photograph by Naaro 120

Figure 117 – Reinterpreting the so-called 5-over-1 housing typology with 3DCP podium. Early sketches for a 3DCP podium to support stacked modular timber houses, considered after nominal instructions regarding a workflow for 3DCP informed design was suggested (Chapter 6). Courtesy Zaha Hadid Architects, London. 122

Figure 118 – Benefits of MME compatibility. The design procedures being compatible with a MME lends well to the quick production of virtual reality, mixed reality experiences and other game-technology based promotional assets. Courtesy Zaha Hadid Architects, London. 122

Figure 119 Contact interface and forces when two rigid-bodies are in resting contact 128

Figure 120 Soft-rigid body equilibrium forces (right) and (Left) time-dependent evolution of the bearing capacity of the material. Graph from (Wangler et al., 2016). 129

Figure 121 Application of method to test print feasibility. In the current implementation, areas where a non-trivial contact (blue) interface exists, the sRBE method is executed to evaluate feasibility. If such contact is not found, the infeasibility is indicated by pink arrows. The skeletal graph (red) is manipulated based on this visual feedback. 130

PART I - CONTEXT AND FRAMING

1 MOTIVATIONS

Solid Freeform Fabrication (SFF), now popularly known by the name of one of the many early variants –3D Printing, has both deep historic roots and rapid contemporary progress (Cima et al., 1992; Hull, 1986). It can historically be traced back to 19th-century to the making of topographic models and the practice of photo sculpture (Blanther, 1892; "Photosculpture," 2016; Sobieszek, 1980) (Figure 1). However, the modern definition of SFF, which includes the generation of 3D geometry on a computer and its physical realisation via layer-by-layer deposition of material by a computer-controlled machine, is more recent (Swainson, 1977) (Figure 2). With the founding of pioneering commercial companies – 3D systems in 1986 and Stratasys in 1988, the technology has seen rapid progress.

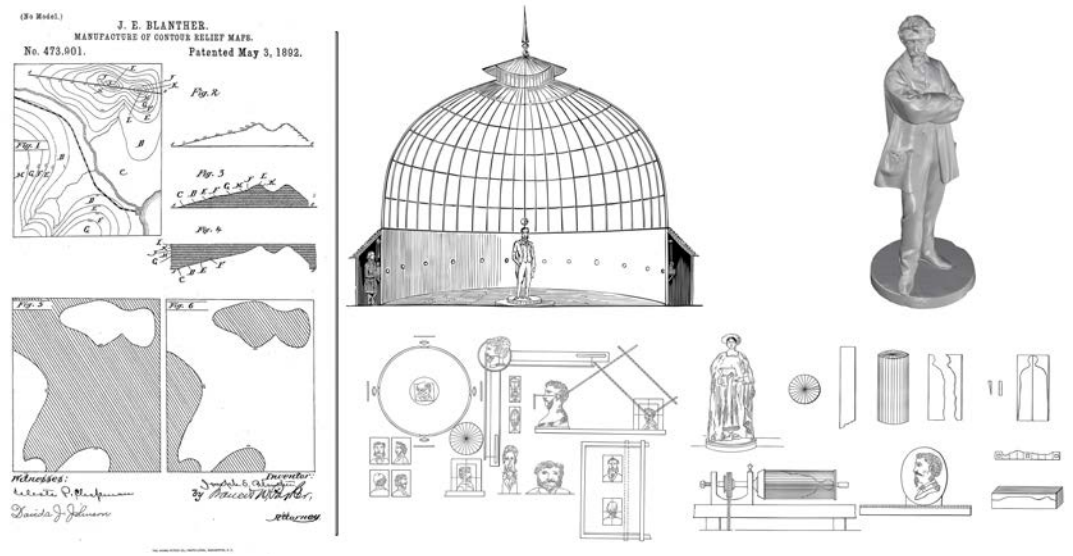

Figure 1 – History of 3D printing. (Left) Patent for constructing topographic models by stacking contours (Blanther, 1892). (Right) Process of producing 3D sculpture from multiple views of the same object or person (Sobieszek, 1980).

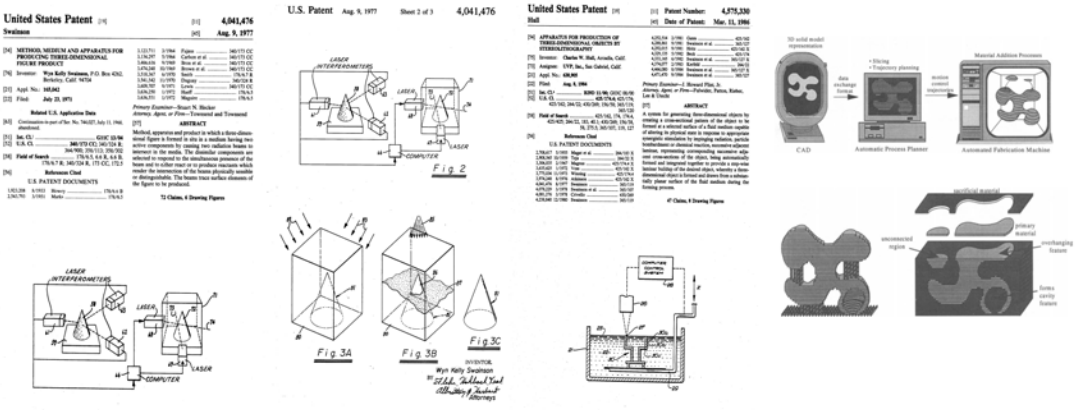

Figure 2 – desktop 3D printing. (Column 1 and 2) Patent for automated production of 3D figure (Swainson, 1977). (Column 3) 3D Systems® patent for stereo lithography (Hull, 1986). (Column 4) Early description of completely digital process: 3D geometry generation, slicing support generations etc. (Beaman et al., 1997).

The development of similar technology for use at architectural scale – Construction Scale Additive Manufacturing (CSAM) – is widely credited to have started with the efforts of Pegna (1997), and is following a similar trajectory. Since 2015, there has been accelerated development motivated by commercial collaborations between by large building contractors and companies such as Skanska partnering with Loughborough University and Foster and Partners for concrete printing (Loughborough University, 2014), Laing O'Rourke developing their freeFormFab™ wax-based technology (Gardiner and Janssen, 2014), the large Hadrian brick-laying robot (FastBrickRobotics, 2015), Acciona in Spain debuting their printing efforts (Acciona, 2016), and the controversial yet impressive attempts by a company named Winsun (Yingchuang, 2015). There have been several new entrants in this arena since 2015.

Principal techniques and materials in CSAM that have had sustained research and commercial efforts in the last two decades include Robotic 3D welding of metal (Dickens et al., 1992; Hu et al., 2002; MX3D, 2015; Warton et al., 2014), Extrusion of plastic (DUSArchitects, 2014; Kooij, 2016), clay (Giannakopoulos and Markopoulou, 2015), and glass (Klein et al., 2015), robotic laying of bricks (Andres et al., 1994; Dörfler et al., 2016; Pivac and Wood, 2012) and the pressurised deposition or selective hardening of concrete (Buswell et al., 2007; Dini, 2009; Khoshnevis, 2004) (Figure 3) . There are other notable efforts in CSAM, which do not share this discrete, layered-end-result similarity with SFF, but which instead produce more materially isotropic results. These include sand sintering (Dillenburger and Hansmeyer, 2013; Tang et al., 2003), dynamic slip-form casting of concrete (Gramazio et al., 2015; Lloret et al., 2015), printing of plastic and metal cages for concrete casting (Hack and Lauer, 2014) etc.

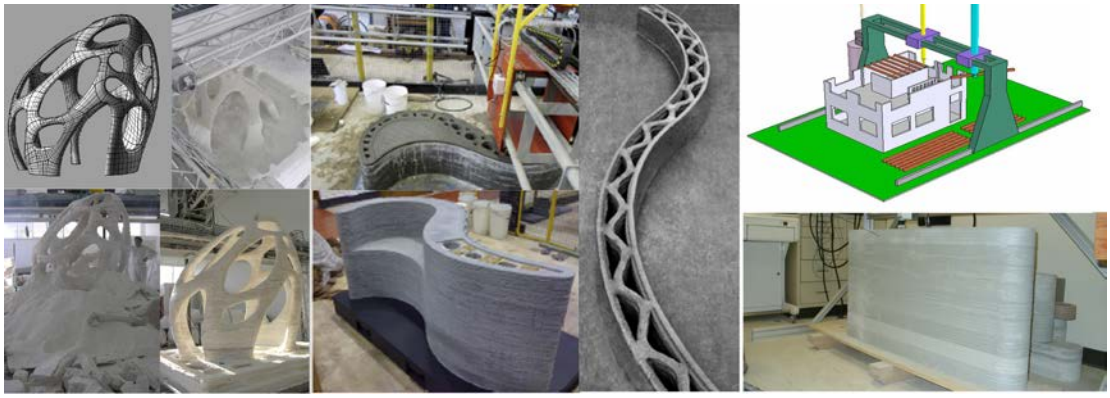

Figure 3 – Pioneers in large format 3D Concrete Printing (3DCP): (Left column) D-Shape® printing process (Dini, 2009). (Middle column) Freeform technology from Loughborough University (Lim et al., 2012). (Right column) Contour Crafting® technology (Khoshnevis, 2004).

1.1 3D Concrete Printing and lack of design tools

The synthesis of shapes that are guaranteed to be physically produced by robotic 3D Concrete Printing (3DCP), needs research attention. This is necessitated by the rapid development of the hardware, commercial availability of and interest in concrete printing. Furthermore, the need is amplified by the lack of easy-to-implement-and-use shape-design tools.

Building on the work of early pioneers (Figure 3), robotic concrete printing technology matured rapidly with the advent of several new competitors midway through the last decade (CyBe-

Construction, 2016; Emerging-Objects, 2016; Giannakopoulos and Markopoulou, 2015; "Incremental3d," 2017; "Vertico," 2017; XtreeE, 2016). The computational shape-design framework investigated in this research is motivated by the maturation of 3DCP technology (Ma et al., 2022) (Figure 4). Furthermore, the underlying research is based on a novel insight regarding the applicability of design and analysis methods used in unreinforced masonry to large-scale, layered 3D printing with low-tensile-capacity materials such as concrete.

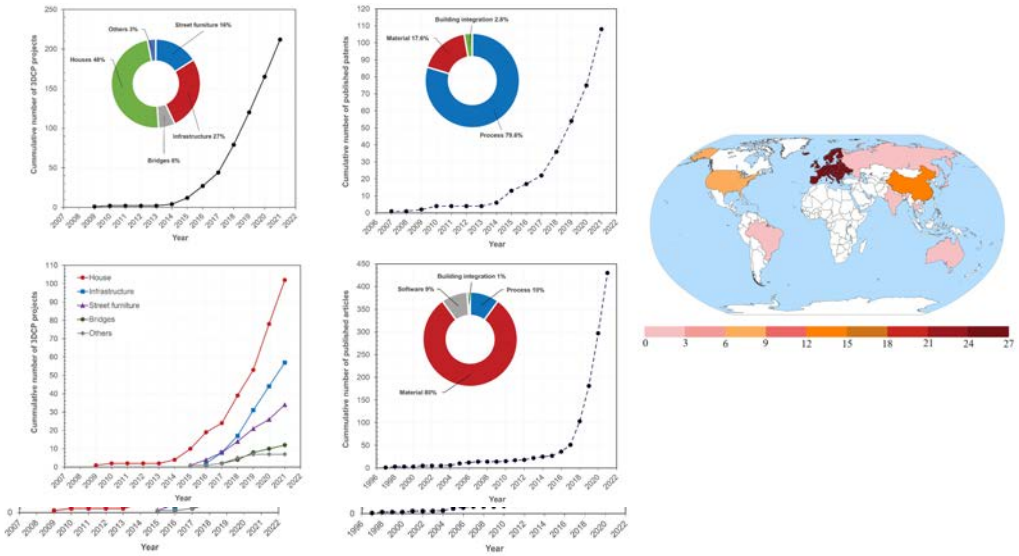

Figure 4 – Growth of 3D Concrete Printing since 2010 (Ma et al., 2022). (Left top) cumulative number of projects, (Left bottom) cumulative number of 3DCP projects by type, (Middle top) Cumulative number of published patents, (Middle bottom) cumulative number of published articles, (Right) Global distribution of project location and number.

Khoshnevis et al (2006a) of Contour-Crafting®, pioneers in large-scale 3D printing of concrete, deliberate two shape-design related working points for the further development of the technology: (1) expressiveness of geometric modelling for designers and (2) constructive guidance about the feasibility constraints imposed by the fabrication process. Similar design and data related issues were also outlined and nominally addressed, by the other pioneering effort at Loughborough University (Buswell et al., 2008). Together, they provide the context of the proposed work and opportunity to address the very design-related goals that have been hitherto side-lined.

1.2 Congeniality of Architectural Geometry and Tectonism

The contemporary paradigm in Computer Aided Design (CAD) and specifically Computer Aided Geometric Design (CAGD), privileges intuitive, real-time, and edit-and-observe interaction between the human designer and the computational model. The research in this dissertation in deeply motivated by this paradigm of shape design and exploration. It is influenced by the so-called Architectural Geometry (AG) – a field of research that incorporates the structural, fabrication and constructional constraints into the shape-modelling process. It should be noted that this paradigm does not aim to digitally simulate the structural behaviour nor the fabrication or construction processes. In fact, it explicitly avoids detailed physical simulations because they are incompatible with interactive manipulation of shape; instead, the underlying mathematical models are modified to encode the critical structural and constructional parameters as constraints within the geometry synthesis process (Bouaziz et al., 2012; Jiang et al., 2015; Pottmann, 2010).

A related topic in the architectural design discourse is the practise of Tectonism – the stylistic heightening of structural and fabrication related parameters, such that they visually and texturally emphasise the often deliberately concealed, structural and constructional logic (Schumacher, 2017). The importance of investment into these stylist resources for the architectural design discipline and profession has also been made (Schumacher, 2018). Furthermore, the congeniality and compatibility of such a design practice, with geometry-based structural design, masonry and shell structures has been articulated from both the architectural and structural design sides (Block, 2016; Schumacher, 2014a). Lastly, both AG technologies, and geometry-based, didactic structural design methodologies are relevant to the rapid, iterative, and evolutionary practise common in contemporary design – this has been expanded and illustrated in the case-study article by Bhooshan(2017) and the corresponding special issue (Oxman, 2017).

In this context of both research adaptation and practical application of the AG paradigm to statics and construction informed design and physical realisation of 3DCP structures (Figure 5), two recent doctoral dissertations are important precedent works: *Funicular Shell Design: Geometric Approaches to Form Finding and Fabrication of Discrete Funicular Structures* (Rippmann, 2016) and *Interactive Equilibrium Modelling - A new approach to the computer-aided exploration of structures in architecture* (Lachauer, 2015). Together, they thoroughly argue and articulate the labour and falsework costs of otherwise structurally and materially efficient shell structures, the subsequent importance of geometric methods of structural design, and the integration of structural and fabrication-aware computational methods in the early-design phase to alleviate the same. The insight that this research aims to investigate is that there is a strong compatibility between the unreinforced masonry paradigm of structures described therein and layered 3D Concrete Printing (3DCP). The compatibility extends to geometric methods of equilibrium modelling. It can be noted, however, that recent efforts to include structural analyses within the design of 3DCP structures have tended to prefer other methods – methods rooted in shape-agnostic, general purpose numerical methods, such as Finite-Element Modelling (FEM) (Chien et al., 2016; Kwon, 2002; Wolfs and Salet, 2015).

Figure 5 – Design to production tool chain and physical demonstrator.

1.3 Funicular structures and 3D Concrete Printing

The dominant structural properties of printed concrete are high density (~2200 Kg/m^3), high compressive strength (~100MPa), relative weak flexural strength (10% of compressive strength), and a unique orthotropic behaviour induced by the layered printing process, yielding a weak tensile bond between layers (~0.5-3MPa) (Le et al., 2012b; Perrot et al., 2016; Wangler et al., 2016) (Figure 6 - left). These properties make it ill-suited for the use of ubiquitous FEM methods, but well suited for the adaptation of the design methods of unreinforced masonry structures. These include the historic methods of graphics statics (Culmann, 1875), their application to the design of concrete structures (Fivet and Zastavni, 2012; Zastavni, 2008), and their recent computational extensions (Block and Ochsendorf, 2007; De Goes et al., 2013; Liu et al., 2013; Mozaffari et al., 2020; Tang et al., 2012; Van Mele et al., 2014; Vouga et al., 2012). In addition, the structural aspects of the practice of stereotomy, which align material layout orthogonal to the expected dominant force flow through the structure, are particularly relevant (Rippmann, 2016; Sakarovitch, 2003). The layered filaments of 3DCP, especially when they can be aligned along orthonormal directions of a surface, would require similar careful consideration (Gosselin et al., 2016). The premise of the proposed research is that the material printed in layers can be viewed as micro-scale bricks that are initially soft and harden into rigid filaments (rows of blocks) over time – a kind of micro-stereotomy (Figure 6 - right).

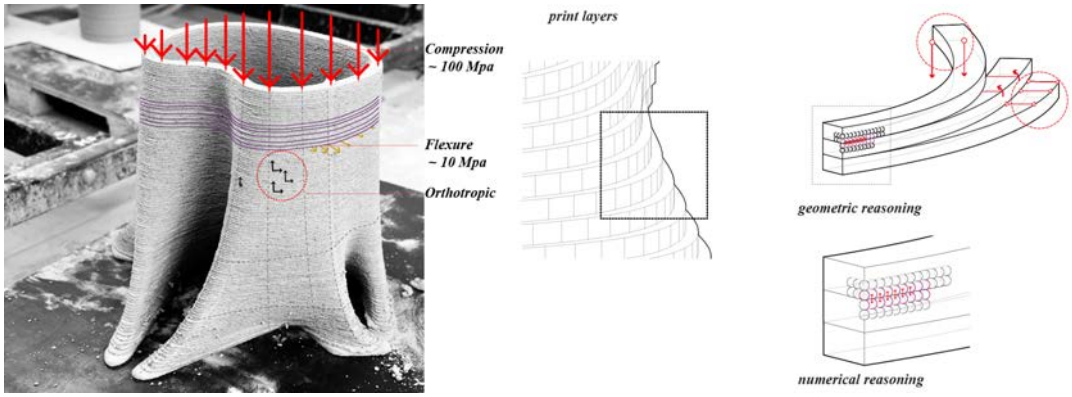

Figure 6 – Material properties of 3D printed concrete. (Left) Dominant material properties of printed concrete. (Right) Intention to discretise the print layers into micro-blocks, to enable geometric reasoning about equilibrium and print feasibility

1.4 Appropriate design paradigm to realise the benefits of 3DCP

The positive aspects of concrete as a construction material include its low cost, ready availability, fire resistance, thermal mass, compressive strength, longevity etc. 3DCP is generally anticipated to ameliorate the negative aspects of concrete including labour intensiveness, adverse effects of worker health and safety, excessive wastage due to the casting process, and significant carbon emissions (Bos et al., 2016; Buswell et al., 2008; Khoshnevis et al., 2006a). It is widely recognised that, unlike desktop printing, which admits a wide range of arbitrary shapes, only specific types of geometries that adhere to the constraints imposed by large-format 3DCP and incorporate the layer-by-layer deposition of linear filaments in the creation of the shapes, can be printed. Furthermore, the careful design of such shapes is critical to fully deliver the benefits of 3DCP (Bos et al., 2016; Wangler et al., 2016).

On the other hand, the unreinforced masonry design paradigm and techniques can specifically meet these requirements and is highly compatible with the compression-dominant, orthotropic material properties of layered 3DCP (S. Bhooshan et al., 2018a, 2018b; Khoshnevis, 2004; Motamedi et al., 2019). Alignment of the printed layers orthogonal to expected compressive force flows engages the compressive strength of 3DCP whilst eliminating the need for tensile reinforcement (Bhooshan et al., 2020). In other words, we could consider the 3DCP blocks as synthetic stone, which could be dry assembled to create fully unreinforced masonry structures. Furthermore, the wider benefits of structural geometry and the masonry paradigm to improve recyclability, repair, and reuse of material due to dry-assembly and clean separation of tensile and compressive materials has also been recently highlighted (Block et al., 2020).

1.5 Masonry paradigm, sustainability and 3DCP

The research presented in this document aims to articulate and provide guidance to adopt an unreinforced masonry paradigm for the design of 3DCP structures. The explicit motivation for such an approach is that unreinforced masonry structures made from 3DCP blocks presents a design-congenial pathway to sustainable use of concrete. It helps achieve the so-called *Reduce, Repair, Recycle and Reuse* objectives of sustainable and circular building construction with concrete:

- Reduce the amount of concrete used by allowing precise placement of concrete only and exactly where needed along the compressive flow of forces,
- Reduce the amount of steel needed by reducing tensile and flexural strength requirements through a compression-appropriate design,
- Reduce the amount of wasteful, sacrificial formwork typically needed for concrete structures,
- Repair structures more easily as the reversible, dry assembly of masonry blocks, and the separation of concrete and steel allow for straightforward maintenance strategies,
- Reuse components easily, due to the dry-assembled construction and thus non-destructive disassembly that masonry structures allow, and
- Recycle material with low energy consumption due to both separation of materials and easy disassembly.

1.6 Shape exploration for 3DCP and integrated design-to-production

The motivation of the research is to address the lacunae in interactive, designer-friendly shape design tools that provide practical and didactic understanding of the physical viability of shapes for 3DCP (S. Bhooshan et al., 2018b). This approach and the tools stemming from it, may further find compatible extensions to address the similar lack of shape design tools for other layered construction techniques such as corbelling and pitched-brick vaulting in masonry. Furthermore, to achieve the specific geometries that deliver the benefits of 3DCP, both the development of intuitive, shape exploration friendly tools (Figure 7) and integrated design-to-production (DTP) solutions are needed (Figure 8).

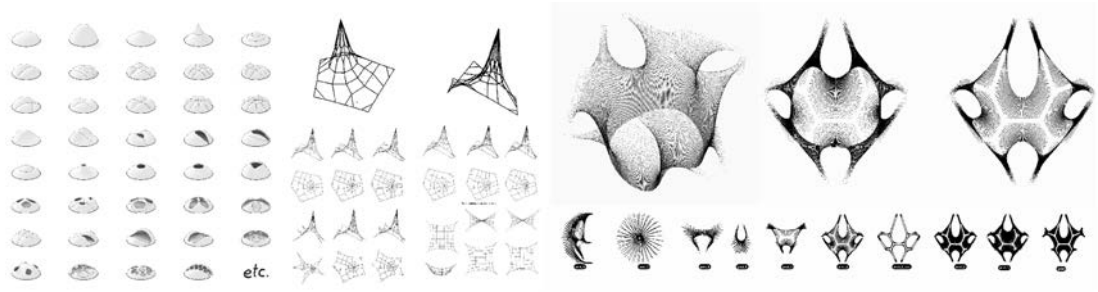

Figure 7 – Equilibrium design space. (Left column) Various compression-only geometries form found using Thrust Network Analysis (Block et al., 2014); (Middle column) Various tensile geometries form found using the Force Density Method (Schek, 1974). (Right column) Early results from proposed IDE and CF.

The relevance of the so-called AG paradigm to the development to interactive shape design has been previously articulated (Section 1.2). An important point of note when applying the AG paradigm to the design of 3DCP structures is that the physical realisation of the shapes created using an interactive design process requires careful further steps of geometry processing. Furthermore, the design development process downstream from the early geometric explorations is typically collaborative, non-linear and requires the use of several tools within a custom-developed toolbox. As such, this dissertation distinguishes several design-exploration tools from those in an integrated DTP toolbox.

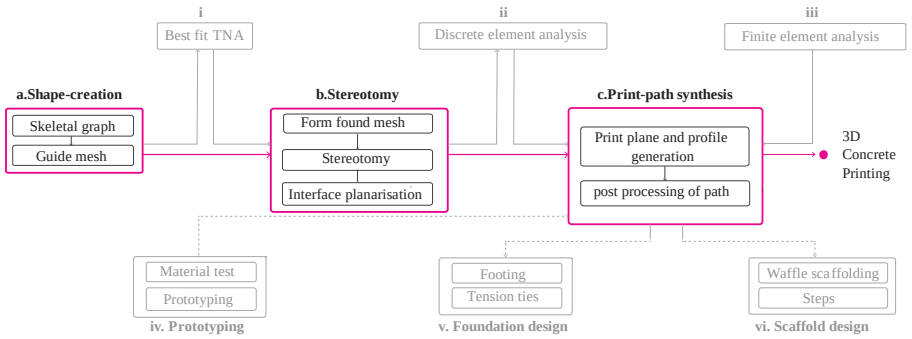

Figure 8 – Integrated design to production toolchain unrolled into threads. (a,b,c) serial thread, (i, ii, iii) parallel structural threads, (iv) material testing and prototyping thread, (v) foundation design thread, and (vi) scaffold design thread.

As mentioned previously (Section 1.4-1.5), both early pioneers and recent researchers have emphasised the relevance of the masonry-based design paradigm to address the critical, but often ignored need for a 3DCP-specific, integrated DTP toolkit. Shape-design and analysis methods used in masonry design along with recent advances in computational masonry and associated geometry processing methods can be combined to create such a toolkit. However, whilst potential features of a CAGD pipeline are discussed, attention is usually devoted to material and process aspects of 3DCP. Furthermore, these descriptions are typically restricted to simple geometries with practical implementation details absent. This is particularly so for non-parallel, inclined-plane printing (Bos et al., 2016; De Kestelier and Buswell, 2009; Gosselin et al., 2016; Lim et al., 2016).

Thus, the research presented in this document is motivated to articulate and develop such a integrate design- to-production toolkit that could provide

(i) expressive geometric modelling for designers whilst also being didactic regarding structural and process parameters,

(ii) a rich variety of 3DCP-compatible shapes,

(iii) constructive guidance about the feasibility constraints imposed by the 3DCP process, and

(iv) methods to align inclined layers of material filaments orthogonal to compressive forces (Figure 9).

These goals are also aligned with the contemporary design approach of Tectonism and parametric architectural design described previously (Section 1.2). These features of a shape-design framework and corresponding tools allow designers greater degrees of freedom in the shape-manipulation process to address spatial use-scenarios and other contextual concerns of architectural design whilst also helping "secure both greater efficiency as well as greater morphological rigour" (Bhooshan, 2016a; Schumacher, 2017). The importance of a design-friendly framework and tools to the practical, mass-scale adoption of new fabrication technologies is further articulated in Section 2.3.

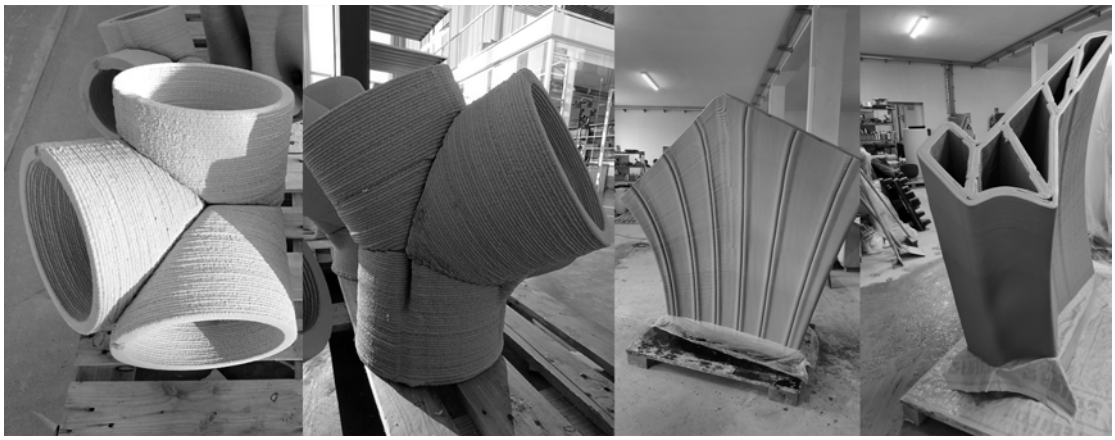

Figure 9 – Photographs of a force-aligned, inclined-plane 3DCP of components of funicular structures

1.7 Contributions

In summary, the motivations of the research are two-fold: addressing the often ignored, design related aspects of 3DCP and a novel insight of extending methods of design and analysis of unreinforced masonry to 3DCP. In particular, the contributions of the research stem from the explicit motivation to operate within the designer and shape exploration friendly AG paradigm, recognise the specific requirements of adapting AG to 3DCP structures, and explore-exploit the deep compatibility between unreinforced masonry structures and 3DCP. The intention to integrate both interactive statics and fabrication aware shape exploration and DTP toolbox to fully realise the benefits of 3DCP, yield the technical contributions of the research.

The research develops a strong foundation for exploring the design aspects of large-scale 3DCP, a unified representation of design and fabrication related parameters and thus the development of a novel architectural language of concrete extrusion – a new Tectonism. The research aims to enable, as an alternative to traditional cast concrete construction, a new language of concrete that expresses and optimises the interrelated properties of masonry structures, 3DCP and contemporary design.

Together, the research aims to contribute to the 'digitalising' of concrete – digital design of 3DCP structures and robotic fabrication of the concrete parts – and thus paving the way for its sustainable use (Bos et al., 2020). The research intends to distinguish itself from other attempts at 'digital concrete' by addressing the emerging consensus that 3DCP structures achieve shape efficiency – less material, faster construction, less labour, but at the cost of higher carbon footprints of the ink needed for 3DCP and lowered durability of 3DCP structures compared to standard concrete structures (Flatt and Wangler, 2022). Thus, in addition to the primary contributions of the research towards shape efficiency, this work provides, through the combination of unreinforced masonry paradigm and 3DCP, a positive outlook towards minimizing carbon footprints of the concrete used in 3DCP and durability concerns of current 3DCP structures. The combination leads to reduced material use along with lower stresses and thus requiring lower strength concrete, which typically has lower carbon footprint and higher carbon reabsorption rates (See Chapter 8).

Lastly, the research expects to contribute to widespread understanding and adoption of architectural design-to-production workflows in 3DCP. In particular, the research is motivated by so-called white box technologies that are didactic and easy to implement using open-source computer code due to the clarity of the underlying geometric reasoning and the simplicity of the corresponding algorithms.

Therefore, the specific contributions of the research are:

1.7.1 Sustainable digital concrete and unreinforced masonry

Articulating the deep congeniality between sustainable digital concrete, unreinforced masonry, and 3DCP. The dissertation articulates the relevance of unreinforced masonry design to both achieve a sustainable use of concrete and realise the benefits of 3D concrete printing (3DCP) (Chapter 2). Furthermore, a practical pathway to design and construct bridge structures that reduce the amount concrete and steel used in addition to being repair, reuse and recycling friendly, is detailed.

1.7.2 Shape exploration and integrated design-to-production

An Interactive Design Explorer (IDE) for the shape-design and a computational framework (CF) for integrated design-to-production of 3DCP structures (Chapter 4,5). The design-to-production (DTP) toolchain, which was critical for the collaborative, multi-author, and integrated computational design, robotic 3DCP and construction of the arched bridge demonstrator, is also described. The DTP toolchain allowed for parallel investigations in design, structural engineering, material development and physical prototyping. These investigations fed into a thread of processes to produce a structurally informed, printing-feasible, and expressive design (Chapter 8, 9).

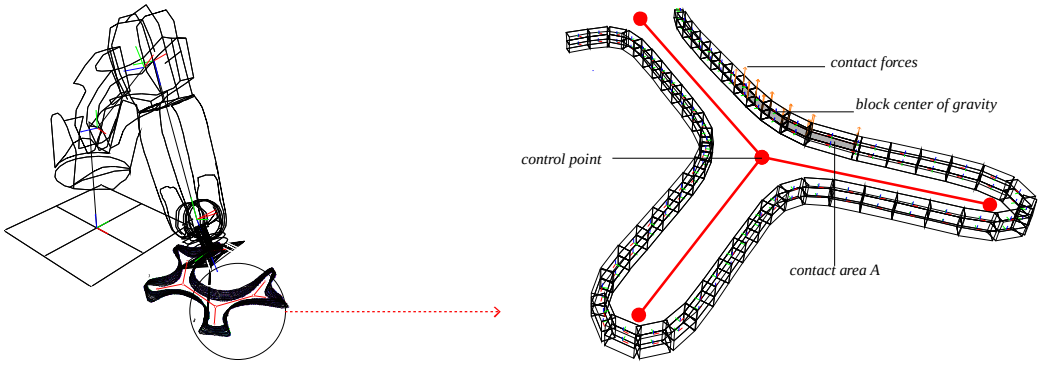

Figure 10 – Proposed Interactive Design Explorer (IDE) for concrete printing

1.7.3 3DCP specific shape representation

Specifications of a proposed shape representation tailored to enable expressive design, novel results and easing 3DCP-related post-production (Figure 10). The dissertation focuses on parametric shape description and providing geometry and heuristics-based guidance with respect to printability, i.e., that the printed layers will not collapse during printing (Section 4.5 and Chapter 5).

1.7.4 Print-path synthesis and post-processing

The dissertation developed a field-tested computational toolkit for print-path synthesis and robotic 3D concrete printing (Chapter 5 and 9). A schema based on Function Representation (FRep) for inclined-plane print-path generation, and its full implementation for practical and large-batch production is also described. The research also implements specific extensions to generate the infill print-paths typically needed in 3D concrete printing (Figure 11).

Figure 11 – Print path synthesis, including infill generation, for inclined-plane printing and large-batch production.

1.7.5 Physical prototypes and proof of concept

Physical prototypes and a proof-of-concept, unreinforced masonry structure realised using the IDE and CF (Chapter 7,8, and 9). Prototypes were produced using the IDE and the proof-of-concept structure outlines the expansion of the CF to include structural evaluation, material, and printing validation.

1.7.6 Literature review and software implementation

The minor contributions of the dissertation include a comprehensive review of the state-of-the-art at the unusual intersection of architectural design, structural form finding, computational geometry, masonry, shape-design and design-to-production fields including seminal precedents (Chapter 3). An easy-to-recreate software implementation of both the IDE and DTP pipeline is also outlined (Chapter 6).

1.8 Limitations of scope

The dissertation limits its scope to computational design aspects of 3DCP. Consequently, the following assumptions and exclusions are made, including certain aspects of the 3DCP technology, structural design, engineering etc.

1.8.1 Print-viability via buckling simulation

3D printing in concrete has two important material and process aspects to be considered: i) the stability of the printed layers during printing, and ii) failure of the material upon non-axial loading after the print is hardened. The former is a primary concern for the synthesis of print-paths and the latter a matter of concern for the global form and its discretisation. Currently, there are no available tools for the former that compute the buckling stability of the print layers, except for recent work (Concre3DLab Ghent, 2019; Wu, 2020). We use the corbelled-masonry analogy (S. Bhooshan et al., 2018b) and provide a simple, geometric heuristic as guidance. In the spirit of geometric reasoning that guides all the research (Section 1.2, 2.1), a ‘soft’ adaption of the Rigid-Body-Equilibrium formulation (Frick et al., 2015) was considered and explored. This was, however, not pursued further and has been outlined for future work (see Section 4.5.1).

1.8.2 Type of 3DCP and specifications of ‘ink’

The research is specific to the prefabrication paradigm offered by industrial robotic-arm-based, 6-degree-of-freedom (6-DOF) printing machines. Further, we assume the use of so-called two-component (2K) concrete formulations and printing setups to print along continuously varied inclinations and thicknesses. In other words, on-site printing robots – both gantry and rail based – that typically use a single component (1K) concrete mix are not considered. Similarly, details regarding material mix and printing processes receive only a cursory description.

1.8.3 Print-path specifications

The dissertation limits itself to the synthesis of the print-paths and their post-processing insofar as it is relevant to the visual and structural attributes of the printed objects and blocks. Thus, aspects like the detailed, robot-specific instructions (so-called GCode generation) receive only high-level description.

1.8.4 Structural design and verification

Rigorous computational structural design, verification and approval reports were needed for the realisation of the proof-of-concept, arched, unreinforced masonry footbridge (Chapter 8). The detailed descriptions of those aspects are beyond the focus and scope of this dissertation. However, a broad overview of the computational design and analysis of unreinforced masonry structures adapted to 3D-concrete-printed masonry bridge design is provided. This includes global form finding and Discrete Element Modelling for evaluation of structural mechanics and stability. Furthermore, the Python-based open-source platform of COMPAS already implements all the masonry-related, structural design algorithms as used and outlined in this dissertation and prior work (van Mele et al., 2017)(Chapter 3).

1.8.5 Software implementation

The software implemented as part of the research uses a combination of custom C++ applications and COMPAS. However, all the data structures and algorithms described can be fully implemented using only COMPAS (Chapter 6).

2 GEOMETRIC APPROACH AND SUSTAINABLE DIGITAL CONCRETE

One of the early, research-initiating documents of Contour-Crafting®, a pioneering effort for large-scale 3D Concrete Printing(3DCP), outlines the Information Technology (IT) that they thought to be mission critical (Khoshnevis et al., 2006a). The IT framework they envisioned, should provide:

- geometric modelling expressiveness for designers,
- constructive guidance about the feasibility constraints imposed by the fabrication process and suggestions to improve feasibility, and

  generation of a fabrication plan, detailing the manufacturing sequence steps needed to construct the design artifact.

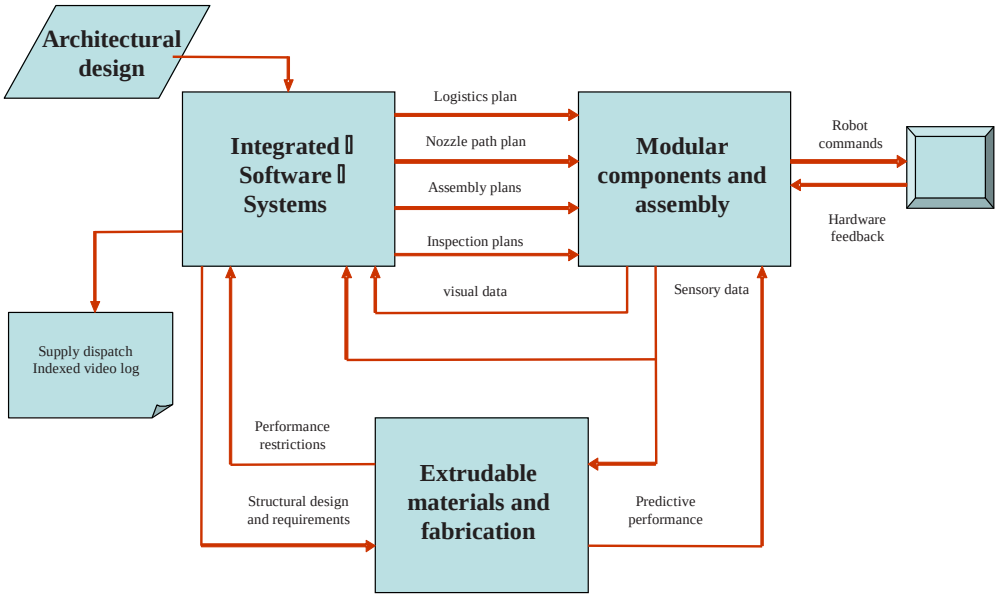

Figure 12 – Details of development plan of Contour Crafting® (CC) technology. The focus of robotic and material technologies is particularly notable (Khoshnevis, 2004).

However, their primary efforts were concentrated towards robotic and materialisation aspects (Figure 12). In such an expedient focus, aspects of architectural design appear to have been considered outside their remit. Similar design and data related issues were also outlined and nominally addressed by the other pioneering effort at Loughborough University (Buswell et al., 2008) (Figure 13). However, the maturation of the concrete printing technology in the last decade and Construction-Scale Additive Manufacturing (CSAM) technologies in general, along with the advent of several new competitors, indicates the necessity and opportunity to address the very design-related goals that have been hitherto side-lined. On the other hand, the importance of geometric methods of structural design, and the integration of structural and construction-aware computational methods in early-design phase to alleviate the same has been previously articulated (Section 1.2).

Broadly then, the research presented in this dissertation, builds on the synergies between funicular structures, geometric design methods and the materialisation technology of 3D Concrete Printing

(3DCP). This entails exploring and exploiting the mutually beneficial relation between both funicular shell and spatial structures and printing with compressive materials such as concrete. In other words, the thesis aims to address the points of the IT framework of Khoshnevis et al., (2006), and its expansion into:

- the applicability of historic techniques of masonry design and construction, to layered printing (Figure 13),
- notions of a designer handbook (Figure 13),
- abstraction of numerical (structural) analysis of feasibility into geometric reasoning, (Khoshnevis et al., 2006a)
- minimisation of sacrificial support, and
- data structures amenable to interactive design exploration.

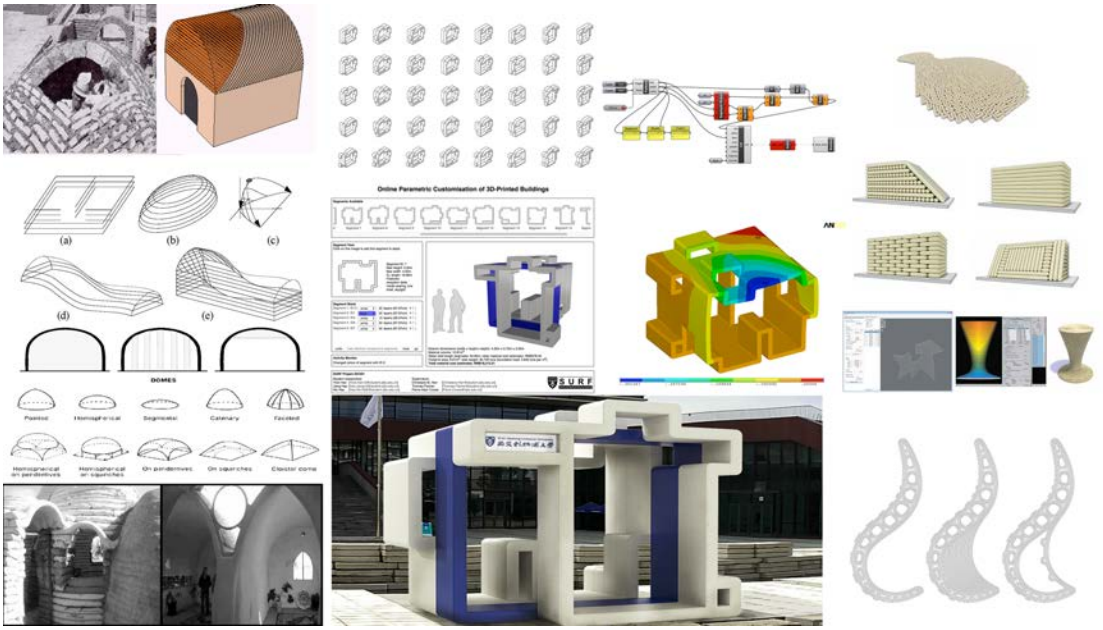

Figure 13 – Prior design explorers for 3DCP. (Left column) Designer handbook and other aspects of funicular shell design considered relevant by Contour Crafting® 3D printing company (Khoshnevis et al., 2006a). (Middle Column) Parametric design exploration of feasible designs, online customization interface, structural analysis and realised result by tutors and students of Xi'an Jiaotong-Liverpool University (Chien et al., 2016). (Right column) Design tools developed by Foster and Partners and Loughborough University to slice existing geometries and explore toolpaths of the 3d Printer and resultant geometries (De Kestelier and Buswell, 2009).

2.1 Applying a geometric approach to the structural aspects of 3DCP

Two critical structural aspects of 3DCP relate to the structural stability of (complex) geometries made of concrete printed parts and the feasibility of printing the parts.

Structural evaluation of (printed) concrete – a phase-changing material - implies predicting the response of its hardened state to external forces. 3D-printed concrete is a special variant of cast concrete whose structural behaviour is relatively well-understood. On the other hand, fresh concrete is often considered a so-called Bingham plastic – a type of non-Newtonian fluid, which will resist flow or deformation up to a stress threshold i.e., when applied stress is below this stress threshold, it behaves like an elastic solid (Mechtcherine et al., 2014). This implies that not all geometries are

feasible, i.e., certain configurations of print layers are susceptible to collapse during printing (Figure 14). Thus, the feasibility of printing a given shape is critically dependent on the curvature of the geometry to be printed and the configuration of the layers into which it is sliced (Khoshnevis et al., 2006a), and a paradoxical material parameter - the rheological parameters of concrete have to be balanced such that it is flows well enough to be extruded and bond with new layers, whilst being solid enough to withstand the pressure of the new (Le et al., 2012a).

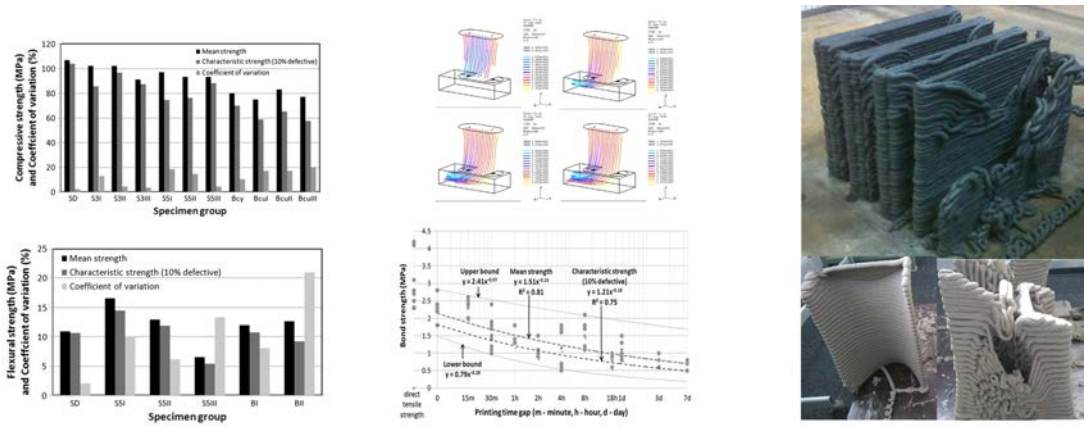

Figure 14 – Structural properties of hardened and freshly printed concrete. (Left Column) Compressive and flexural strength of hardened concrete (Le et al., 2012b). (Middle Top) use of FEA to simulate fresh concrete flow in Contour Crafting® process (Kwon, 2002). (Middle Bottom) relation of Bond strength between layers and the time gap between printing them (Kwon, 2002). (Right top) collapse of freshly printed concrete due to material failure (Le et al., 2012a). (Right bottom) collapse of freshly printed concrete due to geometric complexity of layers.

This section summarizes the conceptual facets to digitally representing these critical aspects and the design-friendly and didactic benefits of choosing a geometric approach.

2.2 Design Explorers

Digital environments – termed *Design Explorers* by Kilian (2006) - that enable an exploration of digital fabrication technologies are a key ingredient in the development of novel design methods and outcomes. Further, an essential aspect of such environments is the abstraction of complex physical phenomena and machine parameters associated with manufacturing method, into geometric properties and constraints. Famous examples include the automobile, aircraft, and shipbuilding industry motivating the development and use of Bezier curves and surfaces, physical splines, developable surfaces etc (Bezier, 1971; De Casteljau, 1986; Pérez and Suárez, 2007; Pottmann and Wallner, 1999; Sabin, 1971) (Figure 15). Additionally, these environments might also choose to similarly encode structural aspects (Bächer et al., 2014; Panozzo et al., 2013; Prévost et al., 2013; Rippmann et al., 2012; Schek, 1974). Others address assembly aspects of digitally fabricated parts (Deuss et al., 2014; Schwartzburg and Pauly, 2013; Song et al., 2012).

The essential focus of the thesis, then, is the development of such an *explorer* to exploit the potentials of Construction Scale Additive Manufacturing (CSAM) stemming from digital generation of geometry, robotic material realisation, and assembly.

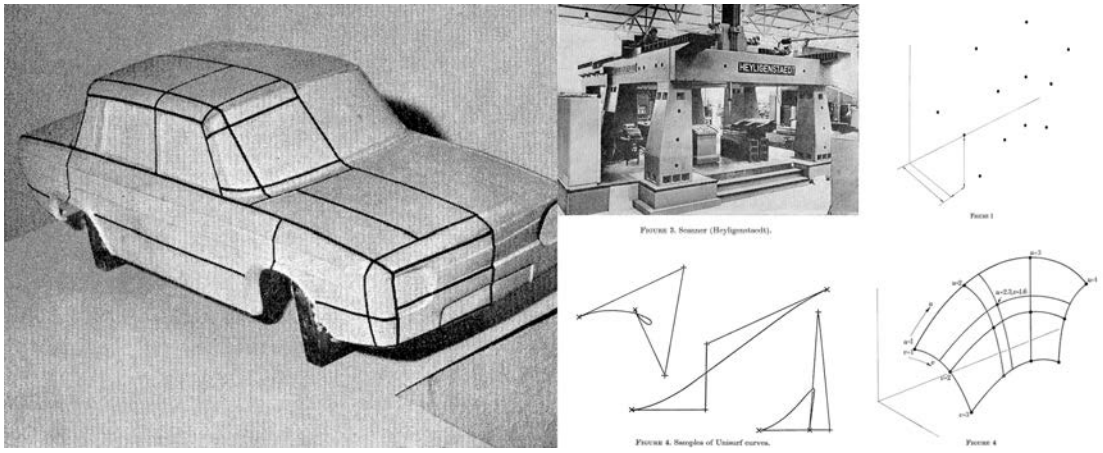

Figure 15 – Computer Aided Geomtric Design (CAGD) in the automboile industry. (Left and Middle columns) Digital reconstruction process of Master-mould using Unisurf CAD system, in use at Renault Car Company around 1970: mark-up on clay master, 3d scanning, numerical input of points, creation of curve networks (Bezier, 1971). (Right column) similar system in use at British Aircraft Company (Sabin, 1971).

2.3 Industry assimilation and Design Explorers

In CSAM, the aspect of design explorers has not received much attention either, barring a few recent efforts e.g., (Chien et al., 2016; De Kestelier and Buswell, 2009)(Figure 13). CSAM technologies like their predecessors in Solid Freeform Fabrication (SFF), face two main hurdles in their assimilation within the construction industry and thus to their ubiquitous use: integration with existing design to production pipelines, and the need for novel design to exploit new technology (Buswell et al., 2008; Klahn et al., 2015; Salonitis and Al Zarban, 2015).

2.3.1 Integration with existing Design Pipelines

There are several avenues of efforts that the SFF industry has made in tackling the first aspect. On the production side of the pipeline, commercial manufacturers of 3D printers bundle proprietary software to process geometric input data and automatically generate relevant machine code (G-Code) to drive their hardware (E.g., CatalystEX™ from Stratasys®, PreForm™ from FormLabs®, 3D Print™ software suite from 3D Systems® etc.). This eases the burden for the end-user. Efforts and protocols in converting geometric Computer Aided Design (CAD) data, into a format suited for G-Code production have been in development for several years (Rock and Wozny, 1992, 1991; Wozny, 1992). Further upstream, proprietary third-party software is available to help clean-up CAD geometry and correctly prepare formatted data for subsequent use with aforementioned G-code generating software (E.g., Materialise Magics™, Autodesk ® NetFabb™ etc.). Similarly, at the point of creation of geometry, there have been several recent efforts to ease data acquisition from the physical world (E.g., Autodesk® Remake™, Agisoft® Photoscan Pro™), and to interactively create geometry (Autodesk® Monolith™, 1234 Sculpt™). The recent incorporation of the ability to print directly from ADOBE® Photoshop™ and Acrobat™ software with Stratasys® printers and to be able to request price quotes from within the software(Stratasys, 2016), are efforts in a similar vein. Lastly, there have also been recent developments in enabling end-users to optimise the generation of support structures to print overhanging geometry, optimise print orientation (E.g., Autodesk® Mesh Mixer™, Ultimaker® Cura™) etc. With CSAM however, there are hardly any examples, apart from (De Kestelier & Buswell 2009)for concrete printing, and FastBricks® add-on

for Solidworks® (Paull, 2015), and Rob Technologies® BrickDesign™ plug-in for Mcneel Rhinoceros®, for bricklaying.

2.3.2 Novel design outcomes for Novel technology

This thesis is particularly interested in the latter aspect – development of novel design methods and outcomes that fully exploit the benefits that SFF and CSAM similarly afford. Significant amongst these is the feasibility of physical realisation of hitherto unfeasible, complex geometries. Such geometries can embed significant performance gains such as material reduction by optimisation of the geometry, reduction of assembly complexity by the integrated design of many parts (Klahn et al., 2015; Lim et al., 2012), etc. Another key benefit is the direct manufacture of digital geometry, allowing for automation and optimisation in process planning and lower tolerances in production (Hopkinson and Dicknes, 2003; Khoshnevis et al., 2006a).

2.4 A Design Explorer for Robotic 3D Concrete Printing

The objective of the research described in this dissertation is to develop an Interactive Design Explorer (IDE) that enables the digital creation of geometries that exploit the novel potentials of robotic 3D Concrete Printing (3DCP), whilst providing guidance on

- structural stability of the global shape,
- a force-flow-informed decomposition of the global shape into printable parts (a so-called stereotomy), and
- economical (robotic) manufacture and assembly of the blocks.

In alignment with the insight of 3DCP blocks as synthetic stone, the rich architectural construction history of unreinforced masonry-based Design Explorers is highly relevant for each of these three critical objectives.

2.4.1 Shape design methods for masonry structures

Recent efforts in investigating the history of Graphic Statics (Culmann, 1875) and its extension to 3D modelling of static equilibrium (Block, 2009; Block and Ochsendorf, 2007) (Figure 16), have contributed to several modelling methods to design free-form, self-supporting geometries (De Goes et al., 2013; Liu et al., 2013; Tang et al., 2012; Vouga et al., 2012) (Figure 17). Further, master builders such as Robert Maillart, an innovative engineer of the early 20th century, applied pre-computer methods of Graphic Statics to the design of structures, constructed using the then, relatively unknown material of concrete (Fivet and Zastavni, 2012; Zastavni, 2008) (Figure 18). This is a particularly telling example of the compatibility of methods of funicular design and materialisation in concrete. These aspects are expanded in Chapter 0.

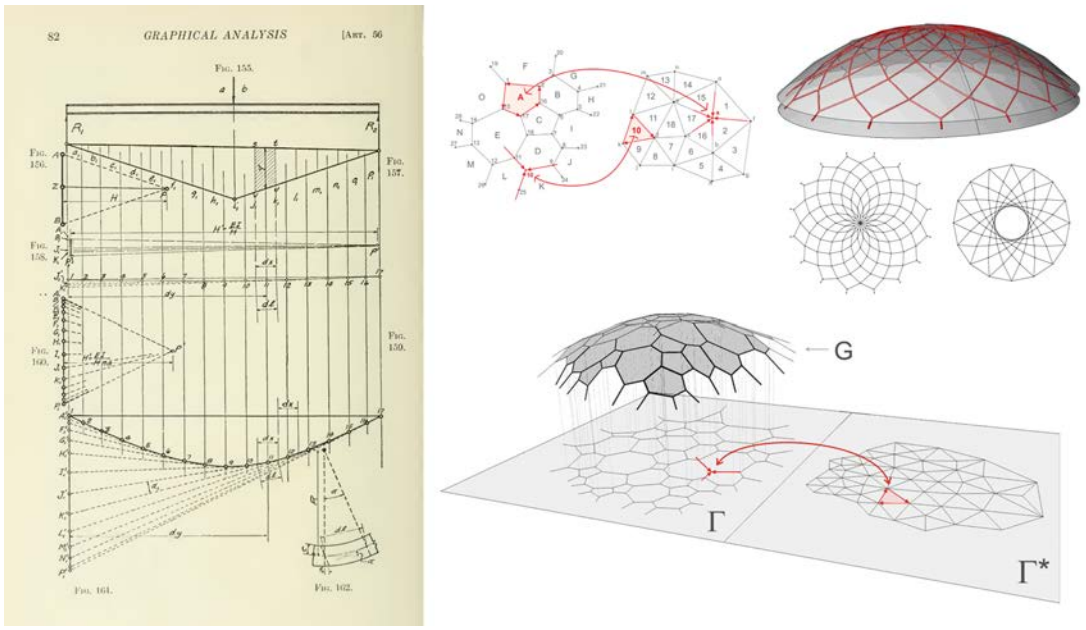

Figure 16 – Graphical methods of finding equilibrium shapes. (Left) 2D geometrical construction of the so-called Elastic curve of a simple beam with a single, point load (Wolfe, 1921). (Right) 3D construction of funicular geometry with Thrust Network Analysis (Block and Ochsendorf, 2007).

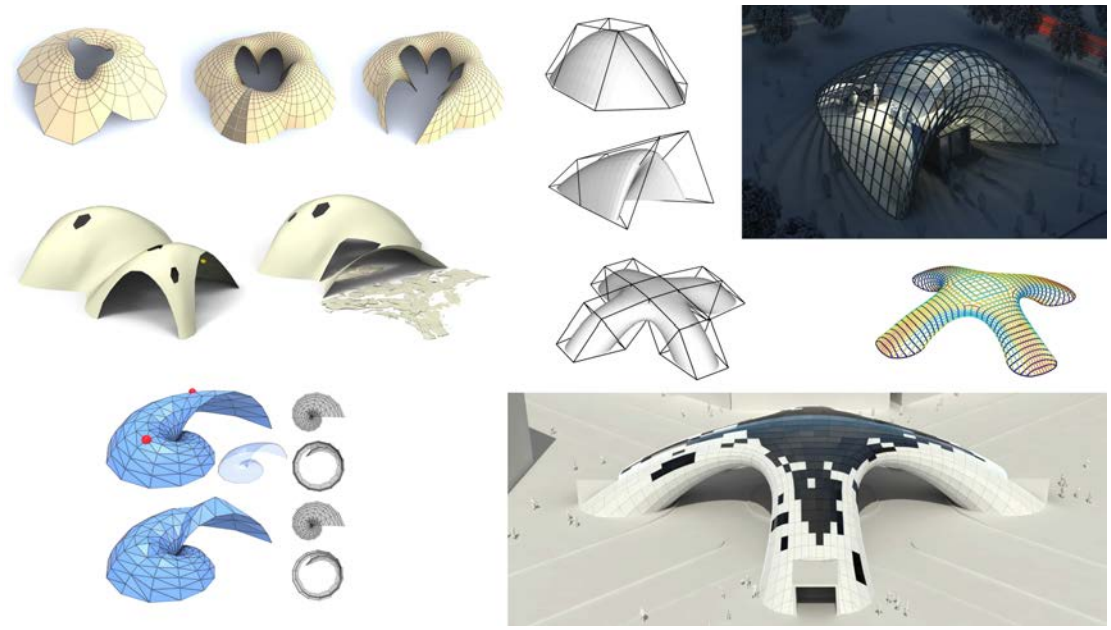

Figure 17. Various computational means of authoring self-supporting geometries in 3D. Left top – *Design of Self-supporting Surfaces:* Interactive editing and visualising destruction sequence (Vouga et al., 2012). Left Bottom - *Computing self-supporting surfaces by regular triangulation* (Liu et al., 2013). Right Top and Bottom- *Form finding with Polyhedral Meshes* (Tang et al., 2012).

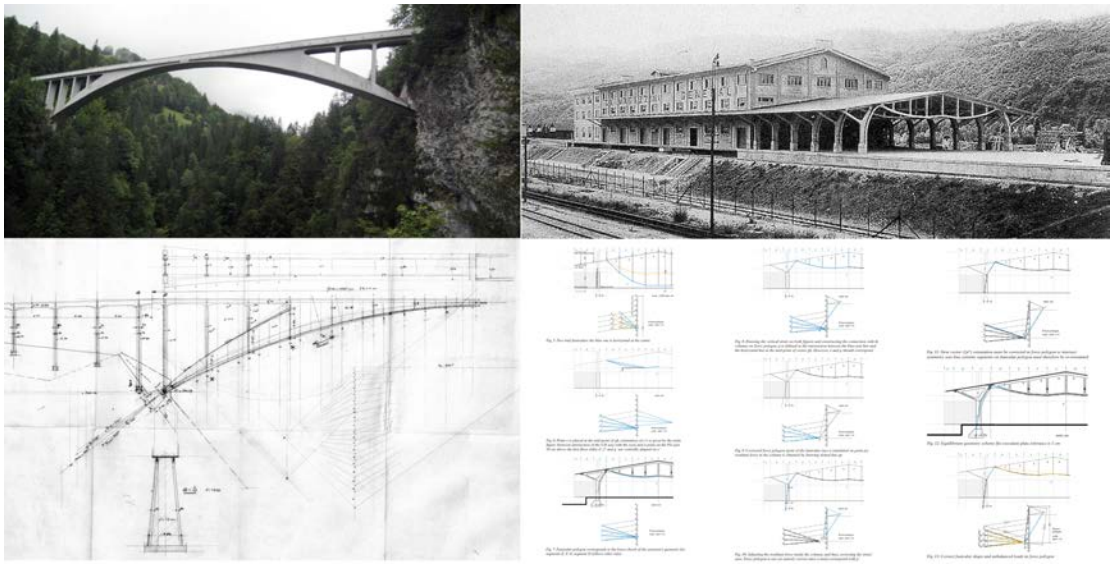

Figure 18 – Design of concrete structures using graphical methods by engineer Robert Malliart. (Left) Salginatobel Bridge, Switzerland (Fivet and Zastavni, 2012). (Right) Chiasso Shed, Switzerland (Zastavni, 2008).

2.4.2 Masonry and stereotomy

Masonry construction relies on frictional contact forces between blocks and axial compressive strength to counter the effects of gravity. This then makes the alignment of the blocks in relation to force flows within a masonry structure, a crucial aspect of design. The need for analytical and design methods for such a practise of stereotomy have contributed to the historic development of Plastic Theory of Structures (Heyman, 1966). Further, the computational development of the theory, especially Limit Analysis and collapse mechanisms by Charnes et al. (1959) and (Livesley, 1978)(Figure 19), and their application (Panozzo et al., 2013; Whiting et al., 2012a; Whiting, 2012) (Figure 20) have led to visually telling results(Rippmann et al., 2016; Rippmann and Block, 2013)(Figure 21). The layered filaments of concrete printing, especially when they can be aligned along orthonormal directions of a surface(Gosselin et al., 2016), would require similar careful consideration. Thus, the rich history of stereotomy and its methods are particularly relevant to the proposed research. These aspects are expanded in Section 3.4.

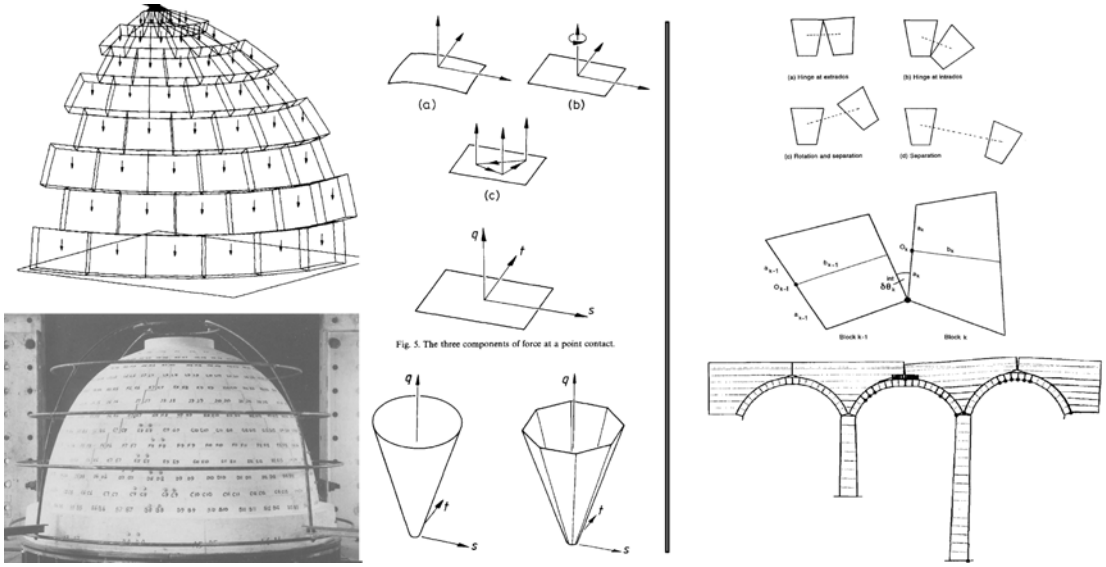

Figure 19 – Computational limit analysis of masonry structures. (Left) Limit analysis based on the so-called 'equilibrium' formulation (Livesley, 1992). (Right) Limit analysis based on the so-called 'collapse' formulation (Gilbert and Melbourne, 1994).

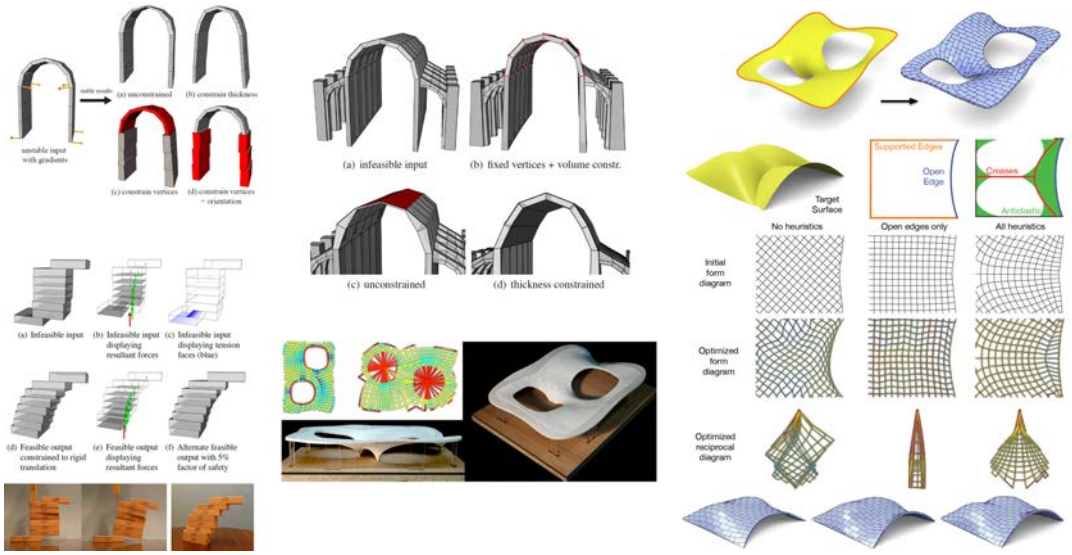

Figure 20 – Interactive structural design. (Left Column and Middle Top) Interactive guidance regarding structural stability of stone masonry and suggestions to improve stability (Whiting, 2012). (Middle bottom and Right column) Complete design tool-set for generating self-supporting masonry structures, tessellating them into blocks, and prototyping with desktop 3D printing (Panozzo et al., 2013).

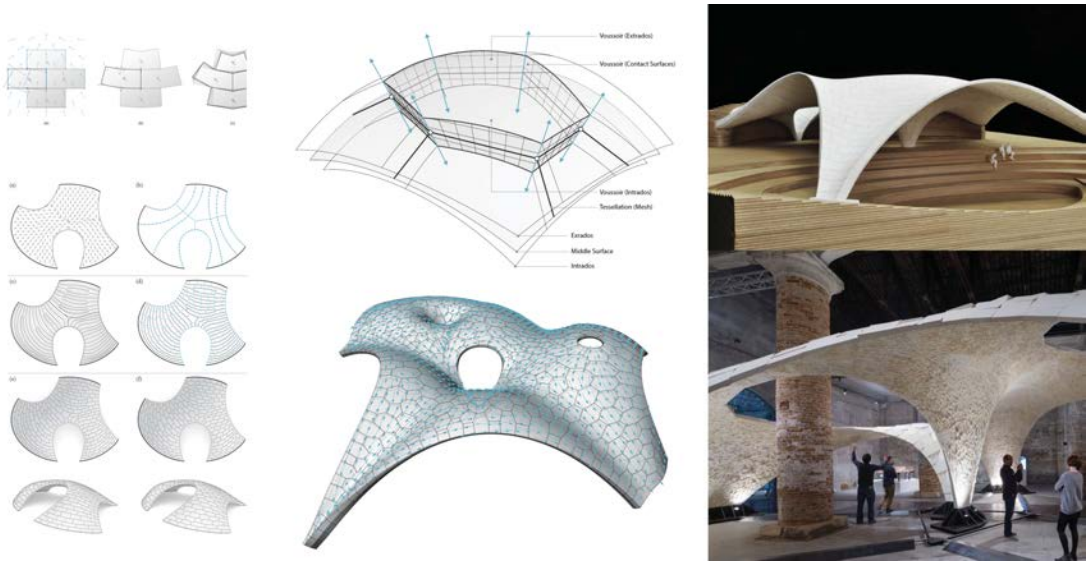

Figure 21 – Force-flow aligned tessellation of funicular geometries and built results (Rippmann, 2016).

2.4.3 Geometry and economic construction

Earliest practise of a deliberate focus on economical use of material via a geometric understanding of structure and effective channelling of (axial) forces can be attributed to the Gothic period (Heyman, 1966; Tessmann, 2008). The earliest mathematical treatment of economic (timber-framed) structures is widely credited to engineer AG Michell (Michell, 1904). Michell used geometric principles involved in the static equilibrium of funicular frames (Maxwell, 1870; Rankine, 1864) in establishing his solution for the layout of materially economic timber trusses. Recently, William Baker and his colleagues at SOM have shown the compatibility of these very methods of Graphic Staticswith FEM-based methods of material reduction – so-called Topology Optimisation (Baker et al., 2013; Beghini et al., 2014). Lastly, the seminal work of architect Frei Otto and the multi-disciplinary research efforts of the Institute of Lightweight Structures (IL, now ILEK) in Stuttgart from the mid-20th century form an important background to the work to be explored in this thesis. The efforts at ILEK contributed hugely to a comprehensive exploration of geometry-based strategies of lightweight, economical design(Bletzinger and Ramm, 2001; Schlaich and Schlaich, 2000), alongside the development of compatible numerical methods of analyses, appropriate construction methods and materials.

Funicular shell structures explicitly avoid bending stresses, which is a fundamental tenet of lightweight construction (Bletzinger and Ramm, 2001). They are thus aligned well with materially economical design (Whiting et al., 2012a). However, their construction is typically labour and time intensive, countering some of the economic benefits. Thus, aspects of the printing including preparatory processes such as decomposition of global shape into smaller parts, orientation of parts on the print bed, minimisation of sacrificial support, and print-path optimisation can provide additional economy of material and time.

It must be noted that these aspects of economical printing can all be captured as geometric attributes and addressed by using geometrical processing and optimisation techniques (see section 4.5). Furthermore, they have evolved significantly for desktop 3D-printing technologies and have

not received much attention in robotic 3DCP. Importantly, methods of stereotomy are relevant to address these topics for robotic 3DCP technology as well (see Chapter 8 and 9).

2.4.4 Statics and fabrication-oriented Design Explorers

Despite the strong compatibility of unreinforced masonry paradigm with 3DCP, including the geometric methods of equilibrium modelling, stereotomy and limit analysis described above, recent efforts to include structural analyses as part of the design of 3DCP structures have tended to prefer other methods, i.e., those rooted in elastic theory and associated numerical methods, particularly Finite-Element-Modelling (Chien et al., 2016; Kwon, 2002; Wolfs and Salet, 2015). Further, the ascendancy of elastic theory and its methods have previously been noted to have contributed to a historic separation of architectural and engineering professions (Picon, 1988; Saint, 2007; Tessmann, 2008). All authors note that such a separation caused design exploration to become linear and fragmented as opposed to collaborative, circular and integrated. On the other hand, the use of geometric methods in architectural design, has a rich history – particularly in the late 19th century (Evans, 2000; Witt, 2010)(Figure 22). Witt indicates the usefulness of such methods in the abstraction of mathematical knowledge into drawing instruments for specific types of complex geometry, manuals of construction for their physical realisation in stone and timber, etc. This led to a profusion of innovation and widespread assimilation of the material and construction technology within the building economy – geometric *design explorers* of the period, not only embedded the structural stability of the design but also guaranteed its construction feasibility, thus contributing to its assimilation.

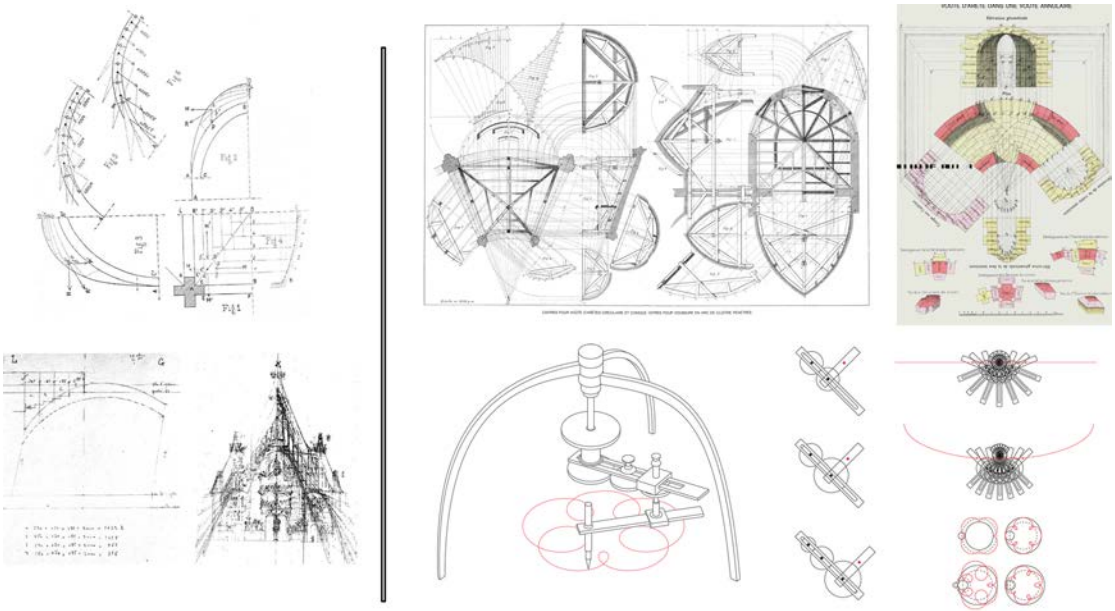

Figure 22 – Statics and fabrication-oriented Design Explorers. (Left top) Graphical analysis manual available in the late 19th century (Huerta, 2006). (Left Bottom) Use of those methods by Antonio Gaudi in the design of Church of *Colonia Guell* and *Sagrada familia* (Huerta, 2006). (Right) 19th century manuals for construction detailing in timber and stone, and drawing instruments, to realise complex geometries (Witt, 2010b).

2.5 Forward and inverse approaches to shape design for robotic 3DCP

Robotic 3D printing of shapes in concrete proceeds by depositing layer-by-layer of wet concrete that hardens over time, yielding the physical artefact. This is analogous to formwork-free masonry construction. The research initiating paper of this dissertation (S. Bhooshan et al., 2018b) articulates this analogy particularly in terms of methods of geometry creation, equilibrium analyses and construction sequencing (in stable sections). Furthermore, the work also established the need to explore more suitable shape design methods given the rapid evolution of concrete-printing hardware and material technologies. Lastly, it also addressed the benefits and the computational handling of explicitly representing and enabling designer manipulation of the printing trajectories along which the robot deposits material, the so-called print-paths.

This 'forward design' paradigm is novel in its use for fabrication-process-aware shape representation. It contrasts with the currently ubiquitous 'inverse design' method of 'slicing' process-agnostic 3D shapes, usually represented using Boundary Representation (BRep) schemes, into 2D print layers (Figure 23 a,b). Furthermore, the slicing is typically done by intersecting the input shape with parallel cutting planes. The inverse paradigm can additionally include optimisation routines to modify the input shape to meet several optimality criteria including guarantees to be printable. This is occasionally used in shape design for desktop-scale, plastic printing(Cacace et al., 2017). The inverse paradigm, as applied to concrete printing, requires significant domain expertise in both shape creation and concrete printing, apart from routinely leading to difficult-to-solve problems such as the lack of spatial coherence - each consecutive layer onto which material is deposited changes abruptly such that it has insufficient overlap with the preceding layer (Figure 23). Lack of spatial coherence is also a proxy for other problems such as extreme inclination and cantilever of the layers in cross section (Figure 23 b,c).

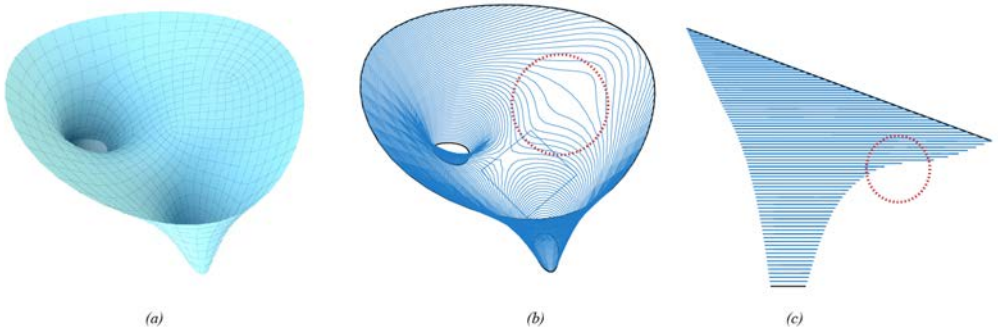

Figure 23 – Shape agnostic, inverse design paradigm. A user-provided mesh (a), typically modelled agnostic to printing constraints, is 'sliced' to derive print-paths (b) by intersecting horizontal cutting planes with the input mesh. The dashed red circle highlights the problematic parts for printing due to a lack of spatial coherence causing infeasible, unsupported overhangs between subsequent layers (c).

In contrast, the work in this dissertation follows a process-aware, forward-design paradigm. It focusses on synthesising print layers with spatial coherence, based on user-provided boundary conditions of start and end print-paths and print planes (Chapter 0,0). Importantly, the proposed shape design method significantly reduces domain expertise needed to create topologically complex, nearly-print-ready shapes. It also provides visual feedback regarding constraints of concrete printing

due to the explicit representation of the print-paths and the implementation of a guidance heuristic. Lastly, it is easy to implement and extend. The outputs of the proposed method of shape design, though not automatically guaranteed to be printable, serve as a good starting point to guide towards printable outcomes due to in-built spatial coherence of the generated print-paths.

2.6 Sustainable Digital Concrete

In summary, digital concrete refers to the broad range of efforts in developing both technologies of digital design of concrete structures and digital manufacture of the concrete parts, with related promises of economical and efficient construction, improved geometrical freedom etc(Bos et al., 2020). The research and dissertation presented here extends the domain of digital concrete by specifically investigating the deep compatibility between design of unreinforced masonry structures and 3D Concrete Printing.

The central insight presented here is that the combination of the unreinforced masonry design paradigm with robotic 3DCP, together with the associated geometrical approach to shape and structural design, modern geometry processing techniques and the resulting design explorers can yield a practise of Sustainable Digital Concrete (SDC) – the sustainable use of concrete enabled by integrated computational masonry, construction, and assembly of 3DCP structures. In other words, sustainable use of concrete implies considering concrete as synthetically produced stone and using appropriate methods of masonry design, construction, and assembly.

Specifically, such a formulation of SDC presents an operative pathway to a Reduce, *Reuse*, *Repair*, *Recycle* approach to sustainable and circular construction (Section 1.5). Furthermore, SDC is also instrumental to the critically necessary, but often ignored, 3DCP-specific, design-to-production (DTP) toolkit that is developed in this research. Thus, SDC specifically implies a (custom) toolchain and the constituent, standalone applets that enable

- the use of the unreinforced masonry paradigm for the computational design of 3DCP structures, which contrasts with both the paradigm and methods of design currently being used in practice and seen in recent examples of 3DCP structures;
- the integration of user-guided, expressive shape design, structural engineering, and robotic concrete printing;
- synthesis of force-aligned, continuously varying, inclined-plane print-paths and the generation of robot instructions; and,
- so-called Integrated Inverse Manufacturing or Design for Disassembly (DfD) whereby the processes and energy requirements of disassembly and recycling of materials is already considering at the time of design.

3 RELEVANT PRIOR WORK AND CONCEPTS

The research presented in this dissertation operates at the intersection of structure and fabrication-aware geometry processing, computational masonry, and 3D Concrete Printing (3DCP) technologies (Section 1.2 and 1.3). Consequently, shape design and manipulation friendly data representation schema, that combine so-called explicit and implicit representations, are areas of significance. Recent developments in geometry processing have shown the usefulness of mesh-based, explicit geometry representations in modelling of global shapes that meet structural and fabrication criteria (Section 1.2). On the other hand, the generation of spatially coherent, print-paths are a topic of importance. Thus, in the research herein, implicit schemes are used to represent and design the cross-sectional profiles and print-paths of objects. Consequently, topics of so-called Function Representation. scalar-field interpolation and optimal transport are related areas of relevance.

3.1 Geometry processing

Computer Aided Geometric Design (CAGD) can support the creation of wide range of arbitrarily complex geometries, and its processing for Computer Aided Manufacturing (CAM). Recent developments in the field of AG, with its explicit aim of "incorporation of essential aspects of function, fabrication and statics into the shape modelling process" (Jiang et al., 2015), extend this CAGD paradigm to architectural design – the so-called Architectural Geometry (AG) (Section 1.2). Importantly, most of the design explorers and the physical demonstrator projects utilise this representational paradigm (Section 2.4, 3.1). In other words, the appropriate choice of a representational paradigm that addresses both the aspects of exploration-friendly shape design, along with critical structural and fabrication constraints, is an important decision for a design explorer.

The design-to-production (DTP) toolkit described in this research uses a mesh-based geometry-processing paradigm that is widely used in AG (Adriaenssens et al., 2014; Botsch et al., 2010; Pottmann, 2007). The research also adopts the use of JavaScript Object Notation (JSON) and half-edge mesh data structures that are common to this paradigm, to transmit and process 3D model information(Json.org, 1999). Lastly, commonly used algorithm to planarise the faces of a mesh is also adapted (Akbarzadeh et al., 2015; Bhooshan, 2016b; Poranne et al., 2013).

3.2 Simulation of 3DCP concrete

Two critical structural aspects of 3DCP relate to the stability of (complex) geometries made of concrete printed parts and the feasibility of printing the parts (Section 2.1); The so-called Finite Element Method (FEM) is usually used for the structural forecasting of hardened concrete, and the extended FEM method (Figure 24), called Material Point Methods (MPM) and Discrete Element Methods (DEM) are preferred for materials similar to the fresh state of concrete i.e., non-Newtonian fluids.

Several state-of-the-art methods were considered for each: FEM (Kwon, 2002; Tanigawa and Mori, 1989), MPM (Stomakhin et al., 2013; Sulsky et al., 1995), and DEM (Cundall and Strack, 1979; Harada, 2007; Shyshko and Mechtcherine, 2008). See Appendix I for further description of the FEM, MPM and DEM methods in 3DCP.

However, in alignment with the geometric approach that informs the research herein, these numerical methods that simulate the deformation of a given geometry under user-specified structural boundary conditions, were eschewed in favour of more geometric and didactic methods (Chapter 2) – methods that operate in the CAGD paradigm and therefore, use geometry-based approaches to synthesise shapes that achieve static equilibrium under the structural load and boundary conditions.

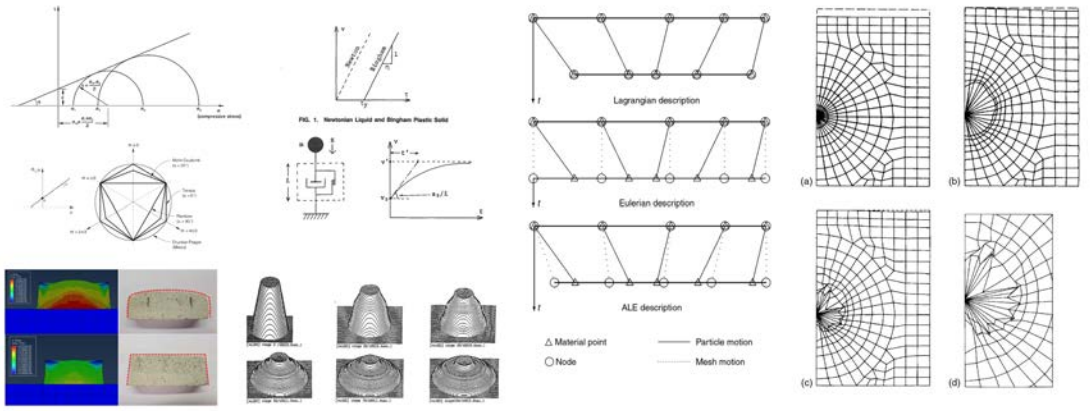

Figure 24 – Use of and problems related to Finite Element Analysis (FEA) of Concrete Printing. (Column 1) Modifying the macroscopic properties of material in ABAQUS simulation software to predict behaviour of hardened sulfur-concrete (Khoshnevis et al., 2017). (Column 2) Use of FEA to predict fresh concrete (Tanigawa and Mori, 1989). (Column 3) Lagrangian, Eulerian and hybrid models of describing material (Donea et al., 2004). (Column 4) Problems of handling large deformations in Lagrangian description, and comparison to hybrid description (Donea et al., 2004).

3.3 Equilibrium and fabrication-aware computational design

As previously mentioned, domains of computational masonry design and process-aware geometry processing are highly relevant fields to the research herein (Chapter 2). In this context, the Armadillo stone vault project and associated toolchain are an important precedent (Rippmann, 2016). The project convincingly demonstrated an expressive, computational DTP pipeline for unreinforced stone masonry. Since, simply put, 3DCP blocks can be considered as synthetic stone, the research herein incorporates several of the structural geometry principles and algorithms from this project. In addition, for the research demonstrator bridge structure (Chapter 8), the construction and assembly sequence of 3DCP blocks adapts the one used in Armadillo. The demonstrator bridge also borrows the constrained form finding of compression-only surfaces as described in Lachauer and Block, (2014a), and Discrete Element Modelling (DEM) of masonry structures for the structural heuristic, verification, and analysis steps (Dell'Endice et al., 2021; Rippmann and Block, 2013).

Prior work related to so-called mesh-based geometry processing for equilibrium-aware shape-design are important precedents. The design workflow and computational benefits of using a combination of an easy-to-specify low-poly mesh along with its sub-divided counterpart is detailed in Bhooshan and el Sayed (2011).V. Bhooshan et al., (2018) describe the benefits of a mesh-based paradigm for intuitive design manipulation, computational handling of robotic fabrication constraints, etc. The structural relevance of the skeletal topology of meshes, automated procedures to generate them from structural boundary conditions, and their structurally informed manipulation is described in Oval et al., (2018). The so-called skeleton package of COMPAS demonstrates the automatic generation of compression-only, 3D mesh-surfaces from simple 2D graph description of a medial axis of the shape

(Van Mele, 2020a). The research herein adapts principles and data structures described in these references.

3.4 Masonry and 3DCP

As mentioned previously, the central thesis of this research is the analogy of 3DCP structures to masonry design and construction. The masonry analogy is particularly important because the currently ubiquitous parallel-slicing paradigm in 3D printing shares its features and limitations with brick corbelling whereby each layer of material partially overhangs the previous, to produce shapes (Section 2.5). The research herein, however, aims to extend the analogy to pitched-brick masonry which employs evolving non-parallel courses, and thus increase the range of viable shapes. Thus, in the context of shape design, the following are the important precedent research.

3.4.1 Equilibrium modelling and limit analysis

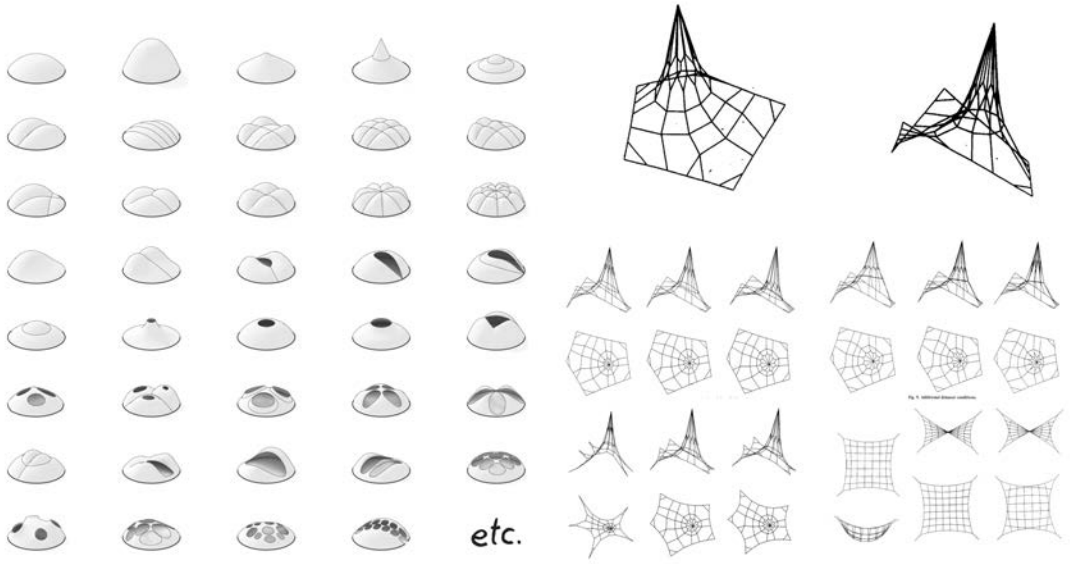

Figure 25 – Equilibrium design space. (Left) various compression-only geometries form-found using TNA (Block et al., 2014). (Right) various compression-only geometries form-found using the Force Density Method (Schek, 1974).

Equilibrium modelling is a structurally relevant, and extended case of physically based modelling. These methods attempt to find one or more geometries that satisfies equilibrium conditions, under constraints of a prescribed stress-state of the surface, user-defined boundary conditions and external forces. Specifically, they aim to completely remove or minimise the bending stress of shell surfaces, whilst being in static equilibrium. In other words, they synthesise surfaces that explicitly avoid bending and thus are well-aligned with fundamental tenet of light-weight structures (Figure 25). Procedures to find such surfaces are well-known as *form finding.*

Physical form finding proceeds by subjecting materials that cannot resist any bending forces such as chains, cloth, and soap-films, to external loads and boundary conditions. Computational methods replicate such explicit avoidance of bending, by making suitable assumptions in the so-called

equilibrium and compatibility equations (Saravanan, 2013). The Force Density Method for example, produces surfaces that resist external loads by pure tensional internal stress, whilst the Thrust Network Analysis (TNA) produces a compression-only solution (Figure 25) (Block and Ochsendorf, 2007; Schek, 1974). TNA ensures horizontal equilibrium by employing methods of Graphic Statics and vertical equilibrium by modifying the Force Density Method(Block et al., 2014). Both methods allow the user to control the stress distribution in the *found* surface, apart from boundary constraints of fixity. A recent effort from Lachauer and Block (2014), extends the force density method to make it amenable to interactive modelling and constraint authoring of both pure tension and compression surfaces (Figure 26). The relevance of these methods to find compression-only surfaces, and thus to 3DCP has been previously introduced (Section 1.3 and 1.8.2).

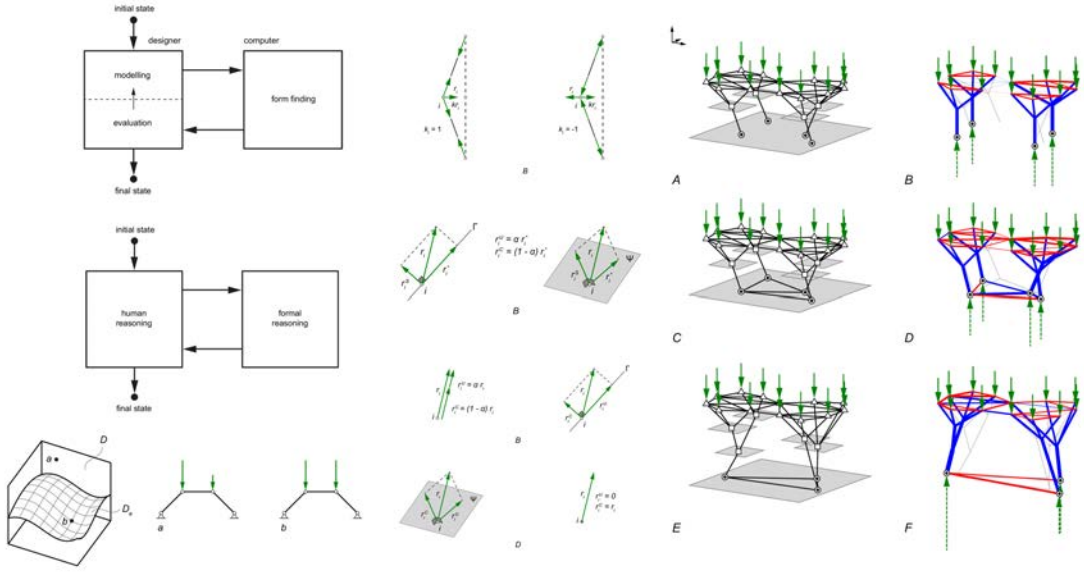

Figure 26 – Interactive Equilibrium Modelling (Lachauer, 2015). (Left column) Human computer interaction in the search for a satisfactory result within the space of equilibrium shapes. (Middle Column) Authoring of various constraints to the modelling process, Right column – Interactive manipulation of the constraints and the resultant equilibrium shapes.

It is important to note a particular feature of these methods - the material of the surfaces is not accounted for in the *form finding* and is a separate independent process once the geometry is established. Thus, its structural behaviour once realised as an assembly of discrete blocks, needs to assessed using other methods. In this regard, two classes of methods that encode rigid-body mechanics – Rigid-body dynamics (RBD) and Rigid-Block Equilibrium (RBE) – are important precedents. RBD are used to simulate the rigid linear and rotational motion of (masonry) solids under imposed loads, subject to boundary fixities (Baraff, 1997; Hahn, 1988; Hart et al., 1988). It can be noted that RBD methods are used primarily in the computer graphics industry and privilege real-time simulation over physical exactness. Dell'Endice et al., (2021) describe the use of Discrete Element Modelling to simulate the evolution of the motion of rigid blocks from the structurally design perspective; RBE is used to compute the arrangement of blocks that are guaranteed to be in static equilibrium for the given load and boundary conditions(Heyman, 1966; Livesley, 1992, 1978; Whiting et al., 2012b). Recent efforts have extended these efforts to include tensile capacities and frictional interface forces and more importantly, make them amenable to structurally informed, interactive design (Frick et al., 2015; Whiting, 2012) (Section 2.4.2 & Figure 20).

RBE methods make certain assumptions about materials. Historically, for example, pure compressive structures were materialised in stone masonry and thus leading to assumptions that masonry has zero tensile strength and effectively infinite compressive strength, sliding failure of adjacent masonry units cannot occur etc.(Gilbert and Melbourne, 1994; Heyman, 1966). Subsequently, rigorous analysis of limits and collapse mechanisms were established. Modified formulations of RBE can be used to determine the limits on the thickness of the form-found surface – the so-called Safe theorem, by determining the maximum self-weight and live loads a thickened, discretised form found surface can bear(DeJong, 2009; Gilbert and Melbourne, 1994; Livesley, 1978)

In relation to 3DCP structures, the upper bounds on the thickness of the surface, can provide additional degrees of freedom to compensate for printing constraints that might force the surface to deviate from its pure compressive states. The frictional forces and interface design aspects, on the other hand, might prove useful in developing strategies to decompose a *found* surface into smaller assembly-parts that need to fit the dimensional limits of the printer – i.e., in the so-called process of stereotomy (Section 2.4.2). It is important to note that whilst these aspects of structural modelling of the discretised blocks of the form-found surface have been considered and used in the physically realised 3DCP bridge demonstrator (Chapter 8), they fall outside the scope of this dissertation (Section 1.8.4)

3.4.2 Shape design for Pitch brick masonry

Wendland (2007) studied the design of historic masonry structures, particularly the so-called pitched-brick vaults that did not use supportive formwork during the laying of the bricks. Specifically, he showed that they are compound structures made up of simpler primitives of geometry, which in turn consist of bricks laid along self-supporting arched courses. Both the laying of bricks and lack of supportive formwork is strikingly like 3D printing along print-paths. Thus, a primitive of shape design for 3D printing could similarly be composed of i) two cross-sectional curves with their respective planes of orientation and ii) interpolated, in-between curve shapes and their respective interpolated planes. Thus, the work by Wendland is an important precedent to the Morph & Slerp formulation introduced in this research (See Chapter 5).

3.5 Implicit shape modelling

An Implicit representation scheme represents the shape of an object by defining what is inside or outside and object, rather than the shape itself. Shape modelling using Implicit representations, has widespread use in various domains including design and animation of articulated characters (Ji et al., 2010a), modelling of biological shapes (Sherstyuk, 1999a), computer-aided-design (Rossignac, 1985), physically based animation (Desbrun and Gascuel, 1995), rendering of fonts (Green, 2007) etc.

The dissertation of Keeter (2013) discusses the use of implicit modelling for desktop 3DP, whilst the popular easy-CAD tools of MeshMixer and Monolith implement it (Michalatos and Payne, 2016; Schmidt and Singh, 2010). More recently, Ntopology has developed industrial-grade software for additive, manufacturing based on implicit modelling schema(Ntopology, 2021). However, at the time of this dissertation, the use of implicit modelling has not yet been adapted to synthesise shapes

for 3DCP, apart from our previous work and its application by our collaborators (S. Bhooshan et al., 2018b). It can be noted that recently, authors from the field of desktop and object-scale additive manufacturing have also been noting the lack of 'design' (approaches) for Additive manufacturing (DfAM) (Scott, 2021; Tang and Zhao, 2016).

All forms of implicit representation share the following advantages (Opalach and Maddock, 1995): (1) efficient to check for whether a given point is inside or outside the object, (2) efficient boolean operations, (3) easy-to-make topological changes, (4) efficient blending between objects, etc. Thus, it is a natural representation scheme to be adapted for shape design for robotic and layered 3D printing of concrete, as well as its fabrication-related processing.

3.5.1 Implicit shape representation

An Implicit representation scheme represents the shape of an object by providing a function that can evaluate if a given point in space is inside or outside. More specifically, the shape of an object is represented by defining a scalar field (also called potential field or field function) that assigns positive values to points in the field that are outside the represented object and negative values for those inside. Thus, the surface of the object is implied as the boundary between the inside and outside of the object so represented. Technically, the surface of the object is the zero iso-surface of the scalar field. They contrast to Explicit shape representation schema like so-called Non-Uniform Rational Basis Splines (NURBS) and meshes, which define the boundary surface of the shape and often do not describe anything inside. See the seminal book by Bloomenthal and Bajaj (1997), for more.

3.5.2 Skeleton based implicit modelling

Skeleton-based implicit modelling is relevant precedent work that allows shape representation in relation to, and its manipulation via a skeletal, centre-line graph of vertices and edges (Bloomenthal and Shoemake, 1991; Sherstyuk, 1999a). Here, the scalar fields are defined in relation to the distance from a given skeletal graph, with distances on the inside of the object being negative and those outside positive. Thus, sometimes a related terminology of signed distance fields (SDF) is used in this context (Hubert and Cani, 2012).

The Computational Framework developed in the research herein, uses a skeletal graph to manipulate the scalar field and thus the resulting print-paths (Chapter 4 and 5). This bears similarity to the so-called skeleton-mesh co-representation (SMC) used in popular digital sculpting software such as Autodesk MudBox™ and Pixelogic ZBrush™ (Bærentzen et al., 2014; Ji et al., 2010b).

3.5.3 Medical imaging and layered printing

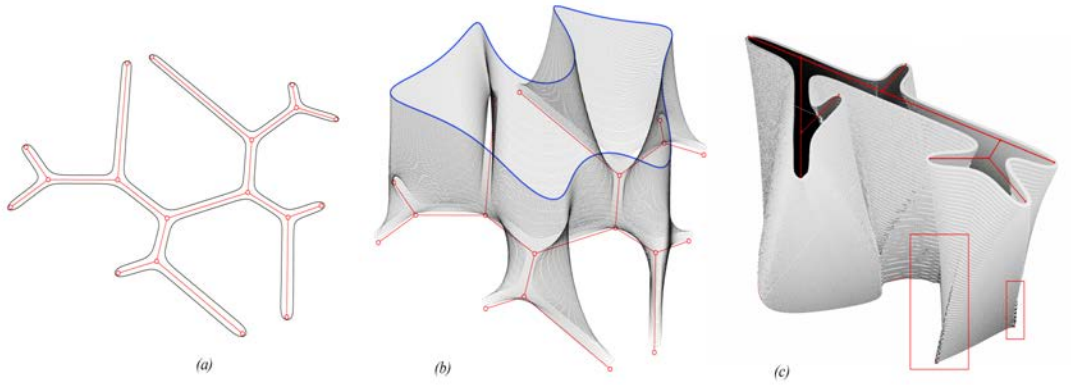

Figure 27 – Graph representation to generate print-paths for wall-like components. (a) Zero-contour of a signed distance field computed in relation to the edges of a graph. (b) evolving the zero-cotnour over time to represent the 2.5D object. (c) printing related artefacts created when using this approach.

The layered process of 3D printing, like brick masonry, can be considered as advancing or propagating ground-upwards, one layer at a time. In this context, precedent work from the field of medical imaging becomes relevant. Front propagation or advancing front can be modelled as a parametrically represented contour curve that evolves in time due to synthetically modelled forces exerted by an underlying scalar field (so-called 'snake' or active contour)(Kass et al., 1988a). It can also be modelled as the zero iso-contour of a scalar field where the field itself evolves through time (Sethian, 1998). Both methods are used in medical imaging to recover shapes from a stack of 2D images. This approach of a propagating front has also been recently used to minimise the amount of support structures required for overhanging parts in 3D printing and architecturally, to recreate the columns of Sagrada Familia (Cacace et al., 2017; Monreal, 2012).

The research presented herein has articulated and utilised the active contour formulation to model and realise shapes in 3D-printed concrete (Figure 27 (c, d)). However, such parameterised boundary representations encounter difficulties when the curve expands or shrinks along its normal field resulting in sharp corners and cusps develop or pieces of the boundary intersect (Cohen, 1991). This can be seen in some of the results (Figure 27 (e)). Importantly, such a view of a propagating or evolving front that represents consecutive print-layers is particularly instructive in understanding the stability of the layers whilst printing (Section 4.5), apart from foregrounding the layers themselves as opposed to the geometry from which they are derived (Section 2.5).

3.6 Function representation

Various models of implicit representations are unified into the so-called Function Representation (FRep) (Pasko and Adzhiev, 2002). In the context of the research herein, FRep refers to the combined use of implicit functions (primarily planes), signed distance functions in relation to points and skeletal graphs (section 3.5.1 & 3.5.2) – put simply, FRep can be thought as an image whose pixels are an amalgamation of various signed distances functions.

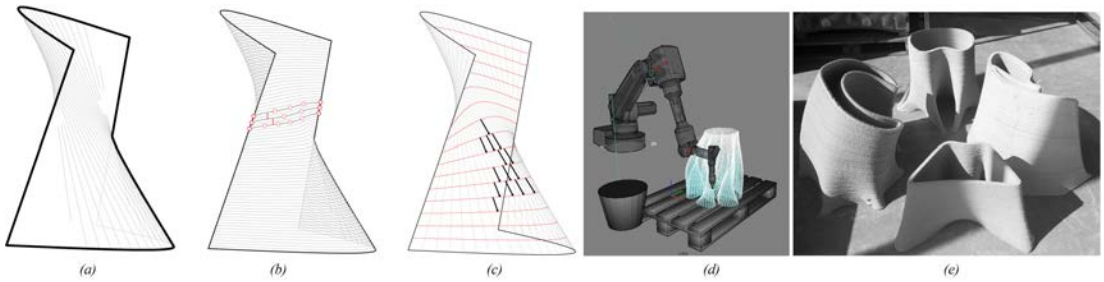

Figure 28 – 'Slicing' and print-paths. Processing of BRep mesh representation (a) to generate horizontal print-paths (b) and field-aligned print-paths (c). The print-paths are post-processed to generate machine code (d). (e) Shows the strong visual presence of the task graphs in the physically realised shapes.

The trajectories that the print head of the 3D printer must traverse - the so-called task graphs or print-paths– are usually generated by processing (BRep) surfaces (section 3.5.3) (Figure 28 (a-c)). Given the shape design focus of the research, it would be important to question this choice. Thus, in addition to design-related considerations mentioned previously (Chapter 2), the following ought to be addressed: 1) explicit representation and visualisation of the task graphs given their importance in fabrication process and strong visual presence in the physical outcome. 2) Nominal post-processing to prepare design-geometries for downstream fabrication processes thus reinforcing the what-you-see-is-what-you-get aspects (WYSIWYG) (Figure 28 (c) and (d)), and 3) edit and manipulation friendly representation.

To specifically address these aspects, an alternative shape representation schema based on FRep was pursued. FRep inherits all the advantages of implicit modelling (Section 3.5) (Figure 29).

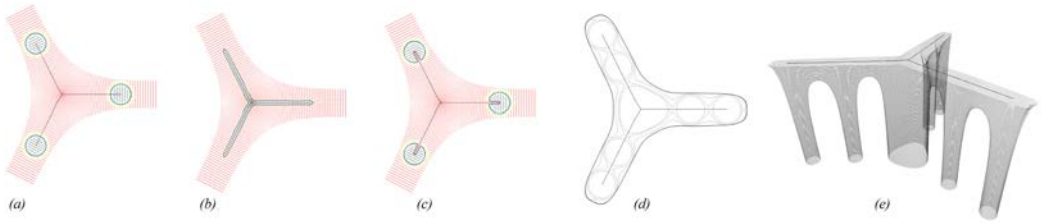

Figure 29 – Advantages of implicit modelling. (a,b) two scalar fields. (c) Boolean difference operation of (b) on (a). (d) The natural extension of specifying interior task graphs as contours of a scalar field. (e) Natural handling of topological change of many closed curves at the bottom layer to a singular closed curve on the top layer.

Thus, the research herein developed, a Function Representation (FRep) based schema, extended it for inclined-plane print-path generation including for practical, large-batch production and further implemented specific extensions to generate the infill print-paths typically needed in 3D concrete printing (Chapter 8 and 9).

3.6.1 Optimal Mass transport

Optimal Mass Transport has its historic roots in a problem formulated and addressed by Gaspard Monge – the famous Earthmovers problem of minimizing the amount of work needed to move earth from its sources to sinks, where they are needed. In image processing, optimal transport is the geodesic between two images. Papadakis (2015) provides a comprehensive treatment of the topic.

Optimal Transport has found many uses in recent times, particularly in image processing(Papadakis et al., 2014), geometry processing(Solomon et al., 2015) and machine learning (Peyré and Cuturi, 2019). Its use in 3D printing and the design of printable shapes has not been explored. Both the displacement and geodesic perspectives are relevant to the tasks of the research herein – moving/evolving a source FRep to a target FRep in a spatially coherent fashion.

3.6.2 Spatially coherent scalar-field interpolation using mass transport

Mass Transport is optimal if it preserves total mass to be transported from one location to another and minimizes total work needed to do so. In the context of shape design using FRep, however, the optimality is not strictly necessary and instead another property is useful: the spatial coherence between subsequent temporal states of the transport. Therefore, Optimal Transport is often called Displacement Interpolation. There are two main methods to compute Displacement Interpolation: i) a Eulerian formulation that is based on mass-preserving computational fluid dynamics(Papadakis et al., 2014) (Figure 30) and ii) a discrete Lagrangian formulation that moves mass-carrying points from source to target locations.

Bonneel et al., (2011) show the earliest use of the Lagrangian Mass Transport to compute the interpolation between two given bidirectional reflectance distribution function (BRDF) maps – a common intermediate image object needed in rendering pipelines to create computationally generated images. In that context, they note the advantages of using the Lagrangian model including computational speed and parameter control. The research presented in this dissertation particularly adapts the ideas and some of the code from this important precedent work (Bonneel, 2018, 2013; Bonneel et al., 2011a).

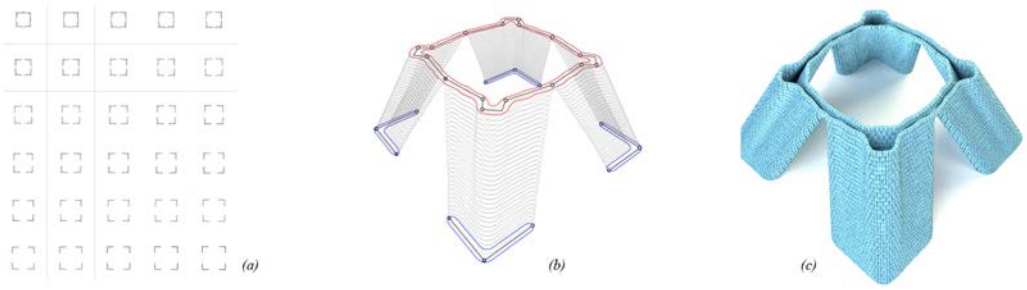

Figure 30 – Fluid-dynamics-based, Eulerian optimal transport. (a) The fluid-dynamics formulation of Optimal Transport (Papadakis et al., 2014) and corresponding C++ code (Bonneel, 2013) was used to produce this interpolation sequence of morphing top-left image to bottom right image. (b) corresponding zero contours with start (red), end profile(blue) and interpolated zero-contours(grey). (c) Resulting 3D shape obtained by stacking the consecutive zero contours.

These concepts of Function Representation, mass transport and scalar-field interpolation has been used to develop spatially coherent print-paths (Chapter 5 and 8); In Chapter 4, the advantages of using the zero contours of an evolving scalar-field representation scheme to represent the print-paths and thus implicitly the 3D shape, are described. Furthermore, it also highlights the limitations of linear, cross-fading interpolation of scalar-fields, such as abrupt transitions and lack of spatial coherence between consecutive print layers. Chapter 5 then extends this by adding shape design aspects that are simultaneously designer-friendly and improve printability of the designed shapes. It focusses on developing appropriate scalar-field interpolation schemes, adapting ideas from the field of Optimal Mass Transport.

3.7 Print-path synthesis for 3DCP

The layered deposition process of 3DCP implies that the synthesis of print-paths has a significant bearing on the physical outcome(Breseghello et al., 2021; Gosselin et al., 2016). The topic of process-appropriate print-path synthesis is beginning to receive research interest, particularly to enable support-free, in-place 3DCP of large compression shells(Motamedi et al., 2019); overcome the limitations of horizontal print-paths, including the so-called staircase effect using non-planar, spatial curved print-paths(Lim et al., 2016); achieve surface textures in the printed artefact by visualizing and manipulating the printing paths and/or the associated robotic instructions(Anton et al., 2019; Breseghello et al., 2021; Westerlind and Hernández, 2020); synthesise print-critical infill patterns (Zhao et al., 2016)and alleviate production issues such as jittery motion of the robotic arm caused by excessive number of points in the print-path, non-smooth transition between consecutive layers, feature-agnostic sampling etc.(Anton et al., 2021; SlicerXL, 2021)

The research herein shares interests with all the above. The research develops a Function Representation (FRep) based schema for inclined-plane print-path generation, its full implementation and extension for practical and large-batch production. In addition, specific extensions to visualize the toolpaths at design-time, achieve expressive textures in the printed blocks, generate the infill print-paths and post- processing routines to alleviate print-time issues, were developed (Chapter 9). The practical application of these methods was demonstrated by integration into the design-to-production toolkit that used to design, print, and assemble 3DCP blocks into masonry structure called Striatus arched-bridge (Chapter 8 and 9).

3.8 3D-Concrete-Printed bridge structures

A notable precedent project is the very first 3DCP pedestrian bridge, installed in 2016, that used a micro-fibre reinforced cement and a particle bed fusion printer to generate bridge segments that were assembled onto a steel frame (IAAC, 2016; IAAC and Acciona, 2017; Wangler et al., 2019). The fusion 3DCP method used in this bridge is unlike all the other precedents and the demonstrator bridge of the research herein (Chapter 9). Although this technology was one of the pioneering efforts, it is recognised to have drawbacks in terms of being a dusty, labour-intensive process (Lowke et al., 2018).

There are three other relevant, precedent, 3DCP bridges have been physically realised since 2018: a bicycle bridge in Gemert, Netherlands (Salet et al., 2018), a pedestrian bridge in Shanghai, China (Xu et al., 2020) and a bicycle bridge in Nijmegen, Netherlands (Kley et al., 2018). All three bridges are linear and composed of prefabricated, 3DCP blocks. It can be noted that none of the bridges use the unreinforced masonry paradigm in their structural design or for the alignment of the printed filaments orthogonal to expected compressive force flow. Consequently, none of the bridges

- are dry assembled, making disassembly, reuse, or repair difficult.
- fully engage the 3DCP material structurally. The Nijmegen Bridge, in fact, uses the 3DCP blocks as stay-in-place formwork into which steel reinforcement is placed and regular structural concrete is cast. The 3DCP deck blocks of the Shanghai bridge rest on structural steel arches. It was understood from the authors that the original intention was to use the steel arches only as temporary supports; however, regulatory restrictions forced them to

retain the steel structure (Weigou X, personal communication, October 10, 2020). The Gemert bridge is heavily post-tensioned. Both the bridges in Gemert and Shanghai use predominantly hollow 3DCP blocks without any additional concrete casting.

- use unreinforced concrete mix for their 3DCP. The bridges in the Netherlands use a proprietary tensile filament embedding technique to reinforce the parts as the concrete filaments are printed. The bridge in Shanghai uses a fibre-reinforced concrete mix.

- fully align the 3DCP filament layers to expected force flow. The bridge in Shanghai comes closest to doing so, with the layers in the simple-arched deck blocks being non-parallel and aligned to a single-radius, circular arch. The bridges in the Netherlands use parallel, horizontal extrusion printing, which make them misaligned with structural force flow; hence, the need for heavy post-tensioning or use of the 3DCP elements as moulds only.

- has a fully integrated, computational DTP pipeline. The bridges in Gemert and Shanghai are simple, single-span geometries with repetitive cross-sectional shapes. The focus of the exercise seems to have been to demonstrate the viability of the technology and to validate material and process parameters. The Nijmegen bridge, on the other hand, appears to use a parametric workflow to generate the print-paths using a designer-specified, process-agnostic, mesh geometry. To the best of our knowledge, the shape-design of the bridge uses the of the so-called subdivision modelling technique (Summum engineering, 2019).

Our research demonstrator bridge (Chapter 8) differs from the precedent bridges in all the aspects described above. It is dry-assembled, fully engages the 3DCP material structurally by discretising the structure, based on a proper unreinforced-masonry stereotomy, and aligning the printed blocks and print layers orthogonal to compressive force flows. The bridge, by directly using the hollow blocks as printed, without casting additional structural concrete in them, also fully utilises the ability of 3DCP to save material by precisely placing material only where needed. In addition, a fully unreinforced concrete mix, without fibres or filament embedding was used. Furthermore, the bridge design has complex geometry with multiple spans. Lastly, expressive design is an integral part of the demonstrator whilst also being process and structure aware. A fully integrated DTP toolchain was developed to achieve these intentional differences.

PART II - COMPUTATIONAL FRAMEWORK

4 A COMPUTATONAL FRAMEWORK

A novel insight of extending methods for design and analysis of unreinforced masonry to large-format 3D Concrete Printing (3DCP) informs the proposed Computational Framework (CF). In turn, the CF aims to address previously earmarked, but hitherto side-lined, design-related aspects of 3DCP (Khoshnevis et al., 2006a) (Chapter 2):

- abstraction of numerical analysis of feasibility of structures into geometric reasoning,
- development of an atlas of feasible and novel geometries,
- evaluating the applicability of historic techniques of masonry construction to layered printing,
- development of data structures amenable to interactive design exploration, and
- unifying the equilibrium modelling of unreinforced masonry, 3DCP structures and their design-to-production (DTP) workflow to physically realise the constituent masonry blocks.

To realise the objectives mentioned above, a computational framework along with the data structures and algorithms, needs to be carefully designed. The computational framework in turn enables both the exploration of viable 3DCP shapes and the DTP workflow to physically produce the shapes via robotic 3DCP. Together, the CF and DTP aid informed design exploration of 3DCP structures.

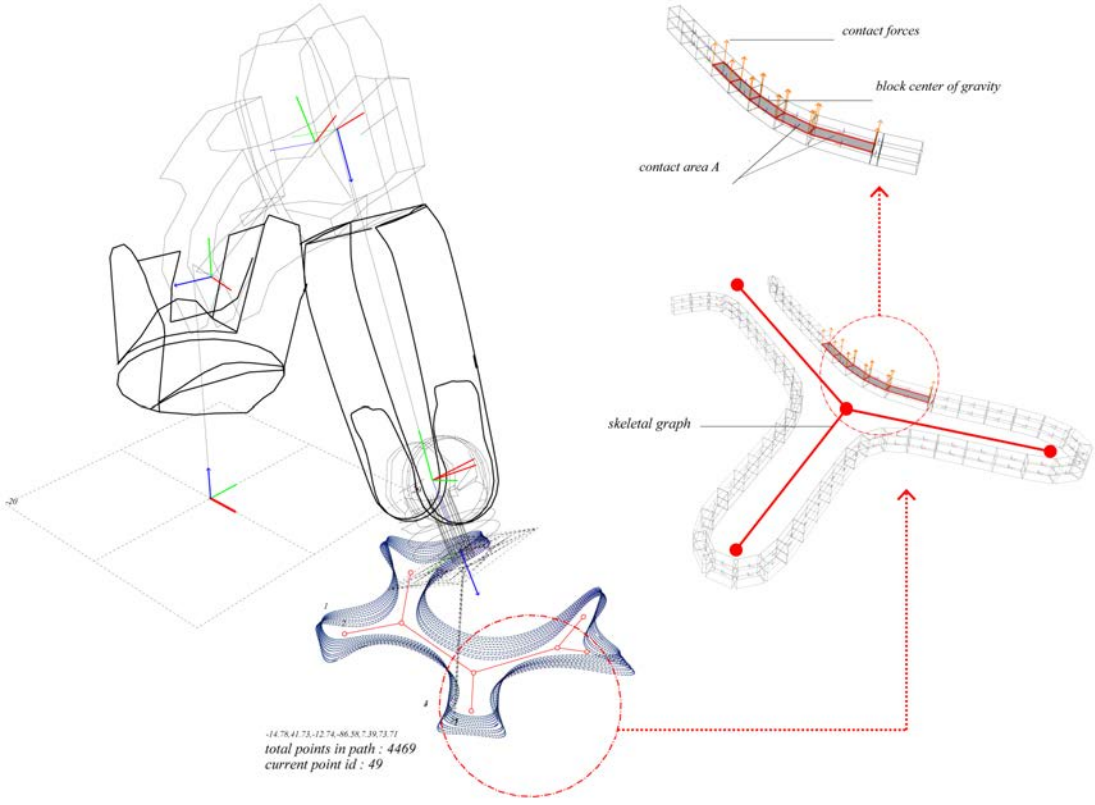

Figure 31 – Interactive Design Explorer (IDE) for concrete printing

4.1 Serial thread

It may be worthwhile to remember the forward approach to design of 3DCP structures that motivates the research herein, whereby structures are designed with awareness of the 3DCP processes and consequently of the strong visual presence of the print layers in the physical structure (Section 2.5). This contrasts with the general-purpose, post-process ‘slicing’ paradigm that is ubiquitous in the desktop-printing domain but infeasible with 3DCP (Bos et al., 2016; Wangler et al., 2019). Thus, even though the so-called task graphs or print-paths could be produced by processing explicit mesh representations (Figure 32 left and middle), the proposed CF utilises implicit distance field representations of geometry to foreground the print-paths during the design process. Specifically, task graphs are created from level curves of user-defined scalar functions (Figure 33). Thus, the CF helps design appropriate scalar functions, whose zero-contours represent print-paths. These print-paths represent 3DCP blocks of masonry. The blocks of masonry must subsequently be arranged along a globally compressive shape, such as arches, domes, vaults and other “free-form”, masonry forms that are now feasible (Block, 2009).

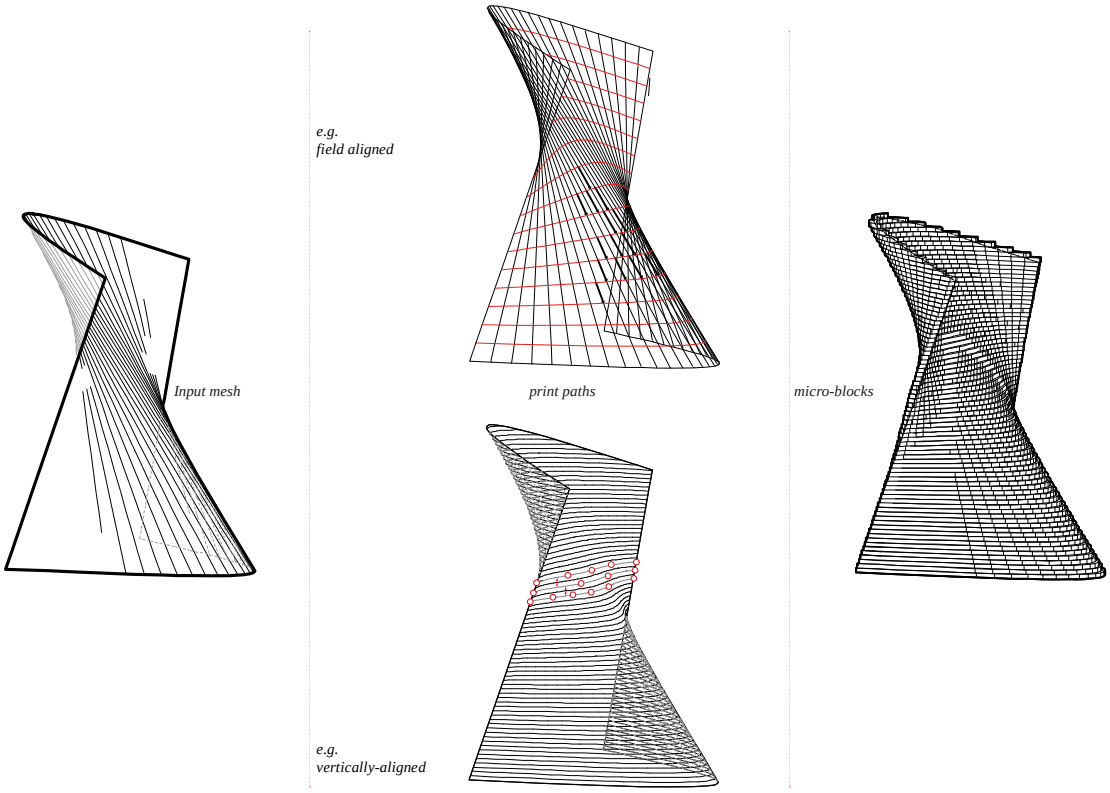

Figure 32 – BRep based, shape agnostic ‘slicing’. Processing of mesh representation (left) to generate horizontal or field-aligned print-paths (middle) and subsequent attaching of a micro-block model to evaluate their print viability (right).

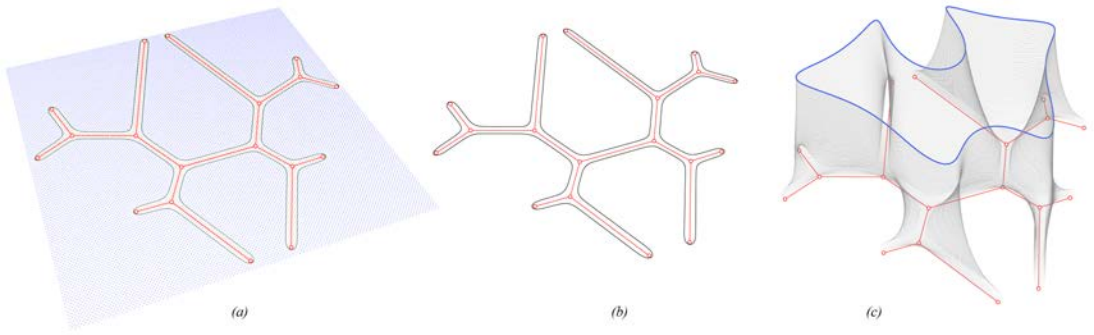

Figure 33 – Skeletal graphs and print paths. (a) A user-specified skeleton graphs (red) and related distance field. (b) Extracted Level curve. (c) 2.5D evolution of level curve (blue) and resulting print-paths.

Thus, in reverse order, starting from an awareness of 3DCP processes, the design procedure consists of three major process steps (Figure 34):

- **Shape design**: Interactive shape design of a funicular spatial surface or skeleton via form finding (Figure 34a).
- **Stereotomy**: Decomposition of the funicular skeleton or surface into segments, and synthesis of enclosing block geometries, including inter-block, (preferably) planar interfaces (Figure 34b).
- **Print-path synthesis**: Generation of the print-paths per block based on expected force flow and block interface planes as defined by the stereotomy (Figure 34c). These print-paths would be suitable for robotic printing with down-stream post-processing and calibration by a 3DCP supplier (Section 4.5, and Chapters 5, 8 & 9).

It must be noted that, whilst the structure and fabrication aware design procedure can be considered in a linear, serial fashion as presented above, detailed structural design, verification, robotic printing and coordinated physical assembly is critically necessary for the physical realisation of the 3DCP structures that are exploratively designed (Section 1.6). These critical, additional parallel steps, though demonstrated for a physically realised bridge structure, are not part of the scope of this research (Chapter 8, Section 1.8).

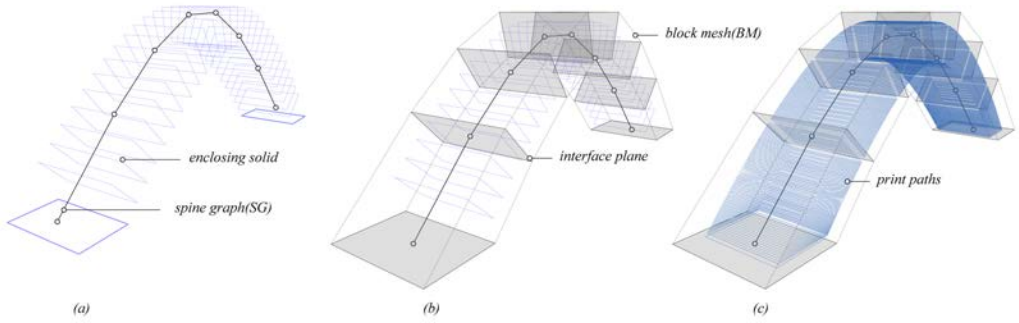

Figure 34 – Computational framework, to compute and store graph, enclosing solid, interface planes, and print-paths.

4.2 Data structures

In considering a shape representation that is appropriate for both design and fabrication processing of funicular shapes for 3DCP, we may highlight the following: (1) an ideal shape representation includes both the centre-lines of (compressive) structural action and the layers of printing; (2) the shape representation is flexible regarding the topological complexity of the spatial or surface networks; and (3) the shape representation is amenable for fabrication-related processing addressing the particular constraints of 3DCP such as heuristics related to maximum overhang, (preferably) planar assembly interfaces, etc.

A combination of graph, mesh, plane, and so-called Function Representation (FRep) data structures are used to address the first two aspects above (see Chapter 3 for terminology and references). For the third aspect, each print-path is discretised into micro-blocks (Figure 32 right). Subsequently, geometric reasoning and heuristic computations are applied to provide guidance to the designer (Section 4.5). Thus, the CF consists of the following data structure and algorithms (Figure 35):

1. Shape design
    a. a graph, to represent the funicular form (*funicular graph FG*);
    b. a mesh, optionally provided to host or assist in modelling the graph (*host mesh - HM*) (Figure 35a); and,
    c. a form finding algorithm, such as Thrust Network Analysis, to perturb the *FG (or HM)* into a state of static equilibrium (Figure 35a).
2. Stereotomy
    a. a graph and/or mesh-walking algorithm to decompose the *FG or HM* into masonry blocks, by processing the vertices, edges and faces of the *FS/HM* (Figure 35b).
    b. a polytopal or non-manifold mesh, to store the masonry blocks processed above (*block mesh - BM*). A subset of the faces of the polytopal mesh represent the connected set of interface planes between all masonry blocks (Figure 35b);
    c. a planarization algorithm, to planarise non-planar mesh faces of the polytopal mesh described above; and
    d. plane-pairs, to represent the start and end plane of each 3DCP block.
    To aid down-stream print-path synthesis, each plane in the pair is stored as the corresponding mesh face in planarized BM (Figure 35c).
    e. a so-called sub-division mesh (*host mesh subD HMSubD*) (Figure 35d), derived from the coarse host mesh, will additionally be beneficial for various geometry processing tasks (Section 4.3.1, 4.3.2).
3. Print-path synthesis
    a. so-called Function Representation (FRep) image, to represent the cross-sections and interior infill corresponding to the start and end planes. Typically, the FRep image is a composite of several so-called signed distance fields (SDFs), each fulfilling a specific function such as boundary definition, supporting infill etc. At shape design stage, the Frep image typically only contains the boundary SDF that defines the profile curves of the block (Figure 35c). See section 4.4 for description of FRep operations, Chapter 5 and Section 5.3 for application details.

b. an interpolation algorithm to interpolate both the start-end planes and cross-sectional profiles curves. See Chapter 5 for details.

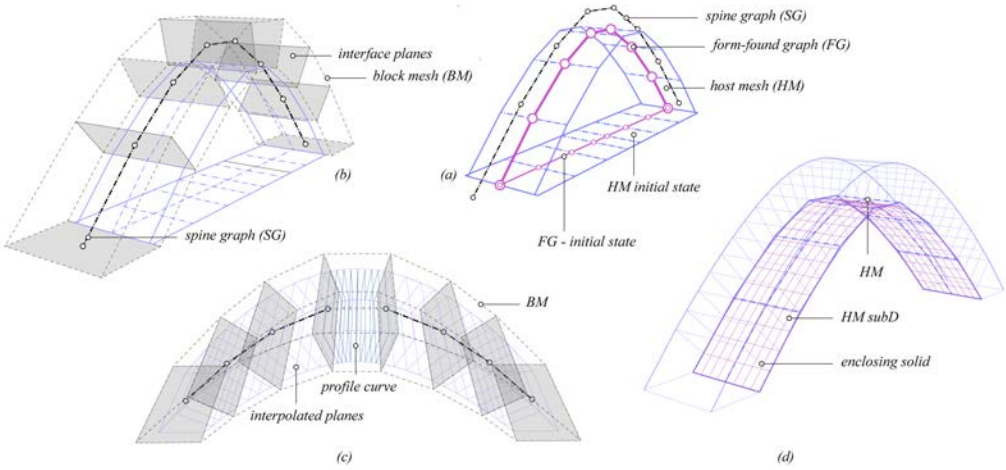

Figure 35 – Using an MME for shape design. (a) It is often easier for a designer to create the initial state of skeletal graph (FG initial state) on a host mesh (HM initial state). HM is then form-found along with the graph. (b,c,d) a MME provides graph and mesh processing and the so-called subdivision algorithms, which help in the various geometry processing tasks involved in the Stereotomy and print-path synthesis stages of design.

4.3 Shape design

The dissertation of Matthias Rippmann (2016b) provides a rich atlas of compression-dominant global shapes that can be explored using Thrust Network Analysis (TNA). Early in the doctoral research presented here, the importance of so-called Mesh Modelling Environments (MME) to expand the didactic and fabrication related value of a geometric approach to form finding and construction described by Matthias, was recognized (V. Bhooshan et al., 2018). In other words, MMEs are a crucial component of a design explorer for 3DCP (Section 2.4).

Summarising the technical features resulting from the insight here, MMEs are digital environments that incorporate a suite of tools that enable the creation and manipulation of discrete representations of geometry or meshes. Such a tool-suite includes but are not restricted to:

(i) a mesh data structure, usually a half edge or winged-edge mesh;

(ii) Conway operators (Hart, 1998) such as chamfer of vertices, bevel of edges, extrusion of faces etc.;

(iii) storage structures for attributes on vertices, edges and faces of a mesh, along with algorithms to ‘fair’ the data stored;

(iv) a brush-based toolset to interactively ‘paint’ attributes into the storage structures above;

(v) a dependency graph structure, along with persistent of data across the graph, to allow data-flow programming; and,

(vi) a constraint solver such as a projection guided solver (Bouaziz et al., 2012), for example, to perturb meshes to become planar.

4.3.1 User-specified host mesh and it derivates

Thus, shape design of 3DCP unreinforced masonry structures implies creating or generating a graph to represent the desired connectivity of the network in its initial state and, subsequently, form finding the graph to become funicular or in other words, perturbing the graph into a state of force equilibrium for specified boundary conditions of applied loads and fixities. Several algorithms, including Particle-Spring methods (PSM), Thrust Network Analysis (TNA) and Force Density Method (FDM) may be used for form finding (Adriaenssens et al., 2014). The funicular skeletal graph, along with the topology and resolution of the mesh it is hosted on, is the primary means of influencing the stereotomy and thus the alignment of the interpolated print-paths (Figure 36). The shape and force-flow agnostic prints paths that are typically used (Figure 36a), can be contrasted with the unreinforced masonry informed print-paths (Figure 36d - blue).

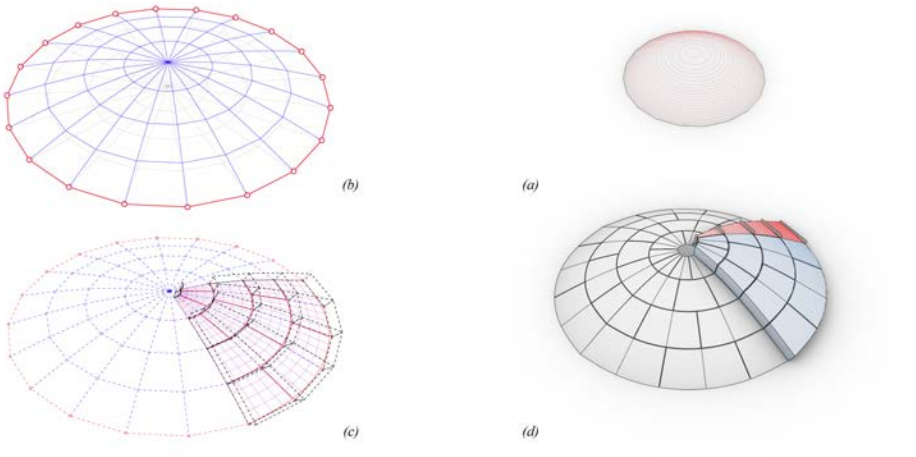

Figure 36 – Interactive, informed design

The first step of the shape design process - manually modelling properly connected graphs - is non-trivial. Using a host mesh enables the use of the designer-friendly features of the MME to aid the user-guided, semi-procedural creation of the initial (typically flat) state of the graphs (Figure 36b - grey). The host mesh (along with the graph) can be perturbed into a state of equilibrium or form-found (Figure 36b - blue). The mesh data structure and the MME are also useful for stereotomy and print-path synthesis (Figure 36 c,d and Figure 37). They described in detail in the next sections (Sections 4.3.2, 4.3.3, 4.4).

Briefly, stereotomy is the practise of aligning masonry blocks in relation to the compressive force flows within a masonry structure. Historically, it meant cutting of stone blocks such that the interfaces would be perpendicular to the compressive load paths. Computationally speaking, it involves the creation of so-called polytopal or volume meshes that encase the funicular skeleton (Figure 36d). Each volumetric cell in such a mesh represents a masonry block (Figure 36c).

4.3.2 Creation of masonry blocks

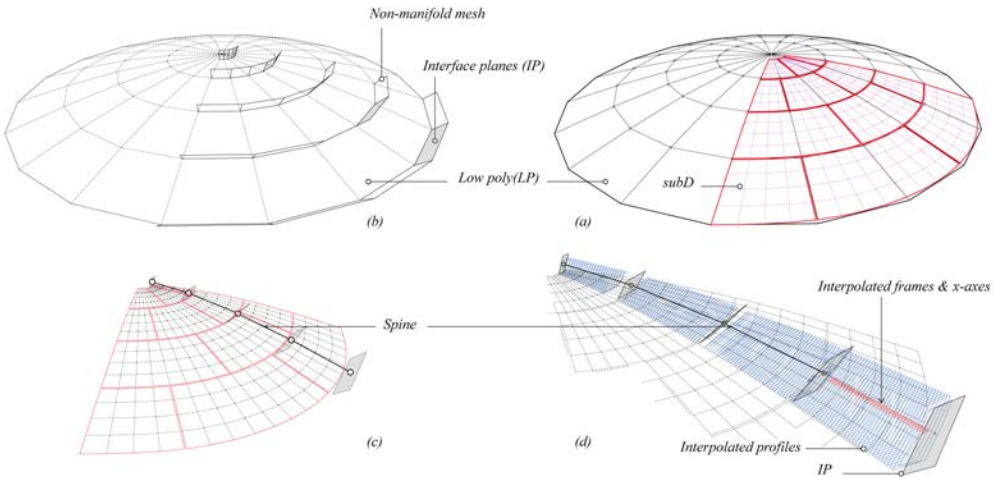

Figure 37– Mesh walking and stereotomy. (a) The form-found mesh can be discretised or a stereotomy assigned to the mesh (staggered red patches or segments in this case) by using so-called mesh walking and breadth-first or depth first graph search algorithms. (b) planes that represent interface between masonry blocks can similarly be extracted. (c) A spine is constructed by connecting the centres of the extracted planes with edges. (d) downstream steps of print-path synthesis. See Figure 38 for more.

An MME also aids the stereotomy of the funicular skeleton or surface networks, particularly, the algorithms that can process the graph and mesh data structures. For instance, if the funicular graph is hosted on a surface mesh, the volumetric mesh can be produced by utilising the quadratic relation between so-called sub-division meshes and coarse, low poly meshes (Figure 37a). MMEs utilise this relation to provide face and edge selection routines that propagate a user-specified selection pattern across the entire mesh. The staggered block pattern (Figure 37a) is thus produced by combining the two: specifying the selection pattern in the low-poly mesh and propagating that to the subdivision mesh. Similarly, an MME can aid in the extraction of the interfaces between blocks (Figure 37b). A Spine is constructed by connecting the centres of the extracted planes. Lastly, an MME can also help in the synthesis of prints-paths (Figure 37d). The print-paths (Figure 37d - blue) alert the designer to the likely location and pattern of the print layers once the blocks are physically realised.

4.3.3 Planarization of the interfaces

The primary mesh faces are the ones most orthogonal to the load path, i.e., the funicular Spine (Figure 37c and Figure 38b). These interfaces transfer the compressive axial forces from one masonry block to the next, until the load reaches the ‘ground’ or fixed boundary faces. The primary interfaces on each block also represent the start and end plane for the 3DCP process. Furthermore, the primary and secondary interfaces represent planes of frictional contact forces between blocks, which add to the stability of the discrete masonry structure. Taken together, it is beneficial for the mesh faces (representing interfaces) between blocks to be planar, and for the primary mesh faces to be as orthogonal to the funicular load path as possible. It can be noted that these interface planes form an interconnected set or a so-called non-manifold mesh. The faces of the non-manifold mesh are planarized using an iterative algorithm (Poranne et al., 2013).

4.4 Print-path synthesis

The goal of this step is to produce spatially coherent print-paths that represent the 3DCP block, i.e., print-paths whereby consecutive print layers vary smoothly, without discontinuities and with sufficient overlap between them. The print-paths are additionally processed prior to transfer to the 3DCP manufacturer (Chapter 9).

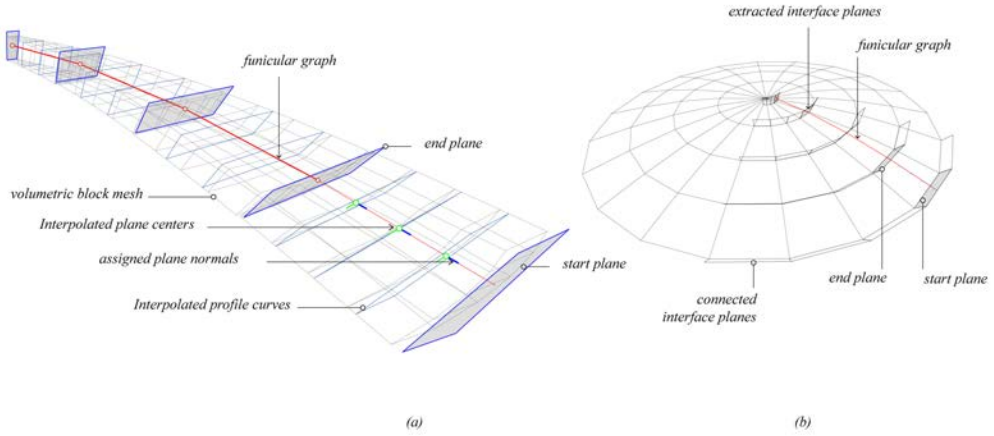

Figure 38 – Print-path synthesis. (a) Processing the funicular spine generated in the previously (b), to synthesise print profiles for each masonry block created by the stereotomy step.

The print-paths are synthesised by processing the volumetric cells produced by the stereotomy (Figure 38). The steps are:

(i) walking along the funicular graph from the start plane / mesh face of a block until the end face or plane is reached (Figure 38b);

(ii) the edges of the sub-graph constructed by the walk is subdivided equidistantly and a plane is placed at each subdivision point with its normal parallel with the edge of the graph. The normal placement is structurally beneficial because the printed material will be deposited on this plane and thus the compressive force flow will fully engage the compressive capacities of 3D printed concrete;

(iii) cross-sectional profiles are assigned to the starting and ending planes, and the cross-sectional profiles of the intermediate planes are a weighted interpolation between the starting and end profiles. The net result is print-paths that represent tubular topology, hollow blocks with a constantly varying, interpolated cross section. The intermediate profiles may also be created by intersecting the intermediate planes with the volumetric mesh, since the volumetric mesh is a so-called linear, piecewise simplex or in other words a linear interpolation between the start face and end face (Figure 38a). The implementation details and exploration of cross-sectional possibilities is detailed in Chapter 5 and 8; and,

(iv) The zero-contour of the Function Representation (FRep) image for each plane represents the print-path for the layer. The stack of zero contours together represents print-path for the entire 3DCP block (Figure 38a).

It would be useful to recall the capabilities of FRep images to easily Boolean the constituent layers (Section 3.5). Thus, many pairs of cross-sectional profiles can be interpolated and combined via Boolean operations to yield a compound profile. Each constituent signed distance field (SDF) independently serves a function such as the boundary profile, stiffening infill, removal of material, etc. The CF uses simple-to-implement foundational operations to create these constituent SDFs which are summarised next. Sections 7.4 and 9.3 describe practical applications of these.

4.4.1 Function Representation - Primitive field functions & operations

There are wide varieties of field functions that have been developed to adapt the use of Function Representation (FRep) within various application domains. The CF uses two simple-to-implement, two-dimensional SDF functions, their Booleans, blends, and evolution along a normal direction to generate the print-paths. The first field function is the so-called soft-objects field function (Wyvill et al., 1986), which is specified in relation to distance of field points from the nodes of an input graph (Figure 39a). The other field function uses the same function, albeit in relation to the shortest distance from the field point to each of the edges of a 2D input graph (Figure 39b). These simple functions may be replaced by more involved convolution field functions which improve the shortcomings of these simple functions (Sherstyuk, 1999b; Wyvill and Wyvill, 1989).

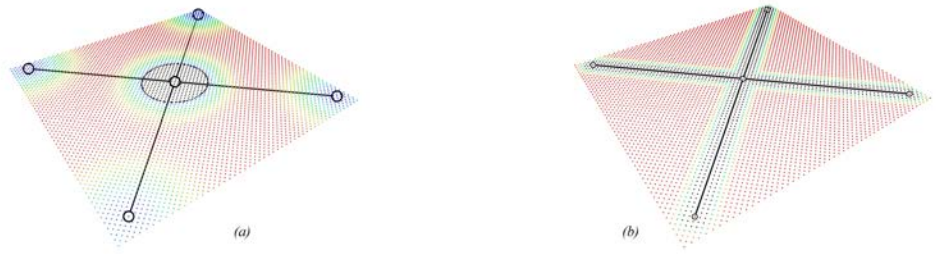

Figure 39 –Signed distance fields (SDF). (a) SDF in relation to the nodes a skeletal graph. (b) SDF in relation to the edges of a skeletal graph.

4.4.2 Booleans

The CF uses standard set-theoretic definitions to specify the Union, Difference, and Intersection between two scalar fields (Bloomenthal and Bajaj, 1997) (Figure 40a-e).

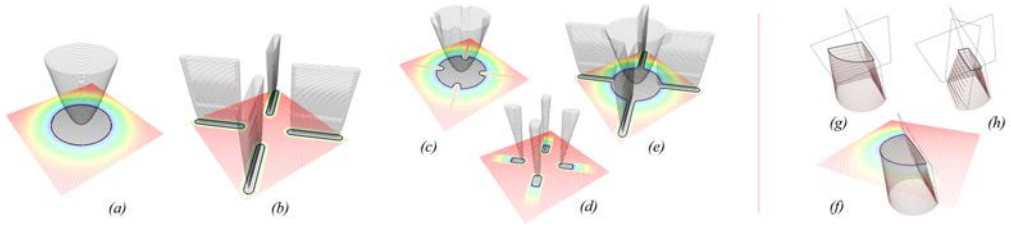

Figure 40 – Boolean operations. (a) and (b) Primitive fields. (c) Difference, (d) Intersection and (e) Union operations on (a) and (b). (f) Consequence of trim operation on the scalar field. (g) (h) trim operations applied successively.

4.4.3 Trim with plane

To specify a trim operation using an input plane, the field values of all field points that are on the negative side of the plane (w.r.t its normal) are replaced with a value of 1(Figure 40f-h). In other words, all points on the negative side of the plane are considered to be outside the object. This operation is primarily used to aid the assembly of printed parts or interface between parts that are consecutively printed (while the first part is still wet). See Section 7.3 where this is used.

4.4.4 Linear interpolation

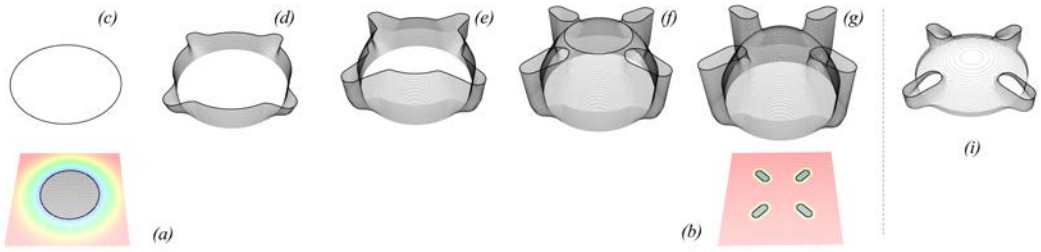

Figure 41 – Linear blend operation. (a,b) Two signed distance fields (SDF). (c-g) Blend sequence of the zero contour as SDF (a) blends to SDF (b). The effect of a faster blend rate on the shape of the geometry described by the stack of zero-contours is shown in (i).

The naïve, linear interpolation between two SDFs is the weighted average between the corresponding scalar values for each pixel of the field (Figure 41). Thus, this is fast to execute. However, it is prone to cross-fading artefacts and loss of spatial coherence in the corresponding print-paths. Consequently, this method of interpolation is rarely used, other than for cross profiles of tubular topology.

4.5 Print viability and guiding heuristic

3D printing in concrete has two important material and process aspects to be considered: i) the stability of the printed layers during printing, and ii) failure of the material upon non-axial loading after the print is hardened. The latter is a concern for the form finding step whilst the former is a function of the spatial coherence between the print layers, which is affected by the interpolated planes. Currently, there are no available tools to compute the buckling stability of the print layers, with the exception of recent work (Concre3DLab Ghent, 2019; Wu, 2020). The CF uses the corbelled-masonry analogy to provide a simple, geometric heuristic as guidance (S. Bhooshan et al., 2018b): the extent of overlap between print-paths lying on consecutive print planes (i.e., consecutive print layers). It is assumed that each path has a fixed in-plane width (the so-called print width) relating to the size of the printing nozzle. If a minimum overlap is not met – usually half the print width - it implies that a portion of the print-path is unsupported and thus likely to fall through. A minimum (but not sufficient) criterion for successful completion is that a minimum overlap is consistently met everywhere across each pair of consecutive layers (Figure 42). This heuristic is aligned with visual inspection practices of experienced 3D-printing professionals and like the well-known corbelled-brick heuristic in the masonry trade where one-third of the width of the upper brick can overhang the lower brick – in other words, one third of the upper brick can be cantilevered.

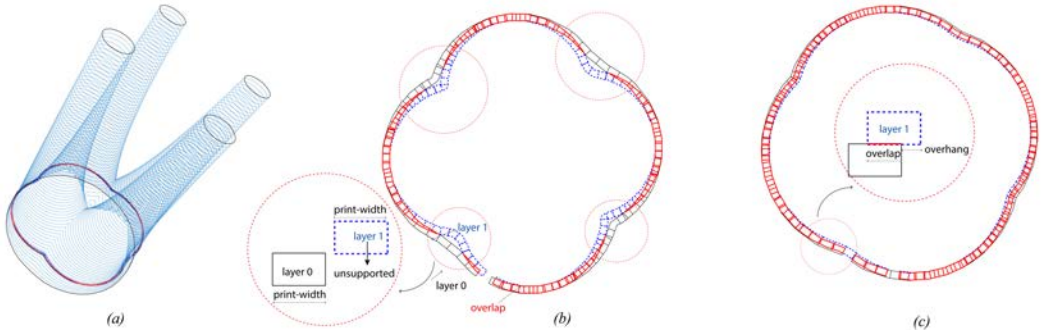

Figure 42 – Guiding heuristic. Typical check for spatial coherence between two consecutive print layers; (b) zoom-in of (a) and an example of two consecutive layers exhibiting partial lack of spatial coherence between them (dashed red circles). Layer 1(blue) is to be printed on top of layer 0 (black) and thus needs sufficient overlap interface (red) to be adequately supported. When curves are not fully coherent, layer 1 can become partially or entirely unsupported (inset); (c) zoom-in of (a) and an example of two consecutive layers exhibiting good spatial coherence between themselves and thus adequate overlap (red line in inset) and overhang within bounds.

The heuristic is easy to compute and thus computationally tractable to be used within an optimisation routine. Importantly, it is also intuitive from a design perspective. Thus, the heuristic can help users to manipulate the shape parameters to improve printability. It attempts to geometrically capture the many material and mechanical parameters that influence the stability of the layers during printing (Suiker, 2018; Wangler et al., 2016). Therefore, the simple heuristic, whilst not guaranteeing successful printing, does provide significant visual feedback to designers and an easy check for minimum (not sufficient) criterion for a successful print. This is particularly useful in the current context where computer simulation of the stability of the layers during printing is rapidly evolving, still experimental in nature and computationally expensive.

4.5.1 Extending the print viability heuristic

To evaluate the task graphs or print-paths for their printing viability, the heuristic previously mentioned could be extended with a geometrical approach that adopts its reasoning from the so-called Rigid Body Dynamics / Equilibrium methods (Section 3.4.1). In this approach, the print-paths can be populated with micro-scale blocks, and the linear and particularly rotational motion of the blocks predicted as a function of the configuration of blocks (Figure 43). If the motion is non-trivial, the print-paths are not stable and will likely lead to collapse of the block during printing. Some additional details of this approach are articulated in Appendix I. The approach was not developed further in the research herein and is suggested as potential future avenues of investigation.

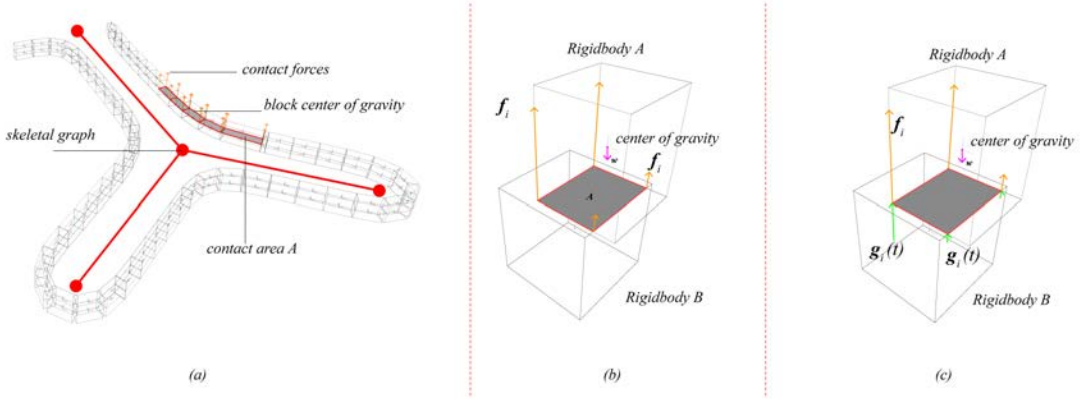

Figure 43 – Evaluating stability of the task graph. (a) A skeletal graph (red) and a micro-block model attached to the resulting print-path. (b) Contact interface and forces when two rigid-bodies are in resting contact. (c) Similar forces when two soft-rigid bodies are in contact See Appendix I for more.

4.6 Handling spatial skeletons

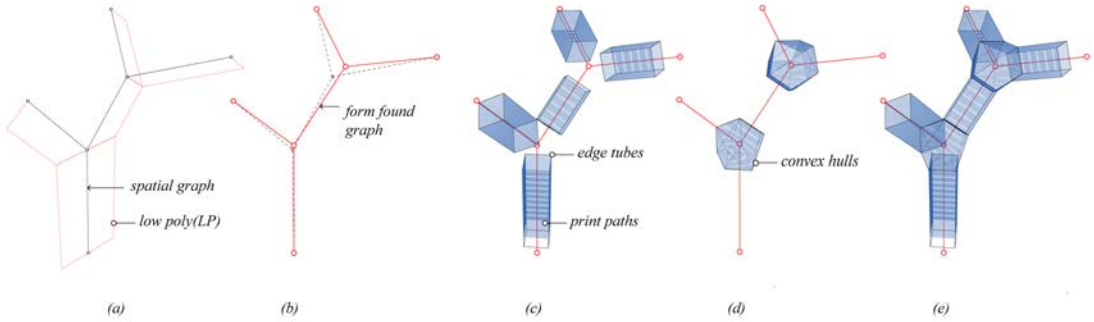

Figure 44 – Spatial funicular skeleton and its stereotomy. (a) Initial state of graph on host low-poly. (b) Form-found graph. (c) n-sided tubes around the edges of the graph. (d) Convex hulls computed around the nodes of the graph. (e) Combined mesh of (c) and (d). (e) Indicative print-paths computed on combined mesh.

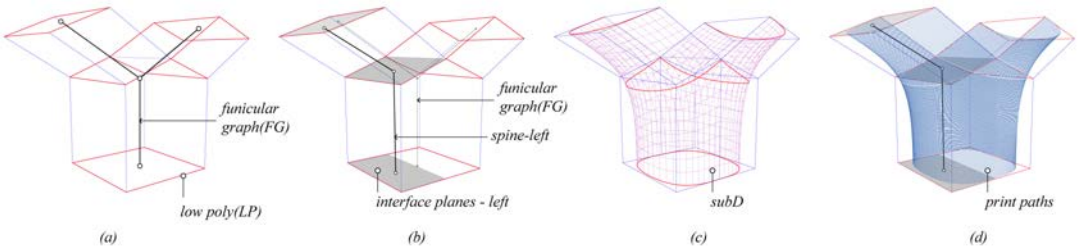

Figure 45 – Extending CF and MME to spatial funicular graphs. (a) Graph to tubular mesh. (b) Splitting the tube into left and right parts and using the bisector plane as the interface plane for blocks. (c) Subdivision meshes. (d) Using (c) and (b) to interpolate print-paths.

The MME based shape design procedure can be extended to fully spatial funicular graphs as seen in the work of Antonio Gaudi, particularly in the Sagrada Familia (Figure 44) (Hernandez, 2006; Monreal, 2012).

The vertices and edges of the funicular graph are processed to produce the volumetric mesh that represents the discrete masonry blocks (Figure 44a-e), using a modified version of the solidifying - wireframe algorithm (Srinivasan et al., 2005). Similar to their algorithm, tubular blocks that encase the edges of the funicular graph are produced simply by drawing a n-sided tube with the graph as the axis. For the blocks that are centred at the so-called nodes of the skeleton, i.e., vertices that have a valency of 3 or more, are created using the following alternative steps:

- The edges emanating from the vertex are processed pairwise. Planes are placed at a specified distance along the edge and a bisector plane is also computed. The three planes are then used to create a tubular, tray-like, coarse surface mesh (Figure 45a)
- Next, the coarse mesh is converted into a sub-division surface mesh (Figure 45c), and the corresponding print-paths are produced by processing the higher resolution mesh and the three planes. This is similar to the method used to process a surface mesh as previously described (Section 4.3 - 4.4). It can be noted that the processing of the nodes using this method is more computationally expensive. As such, for quick visualisation to alert users to the visual presence of the print layers, the CF fully implements the solidify algorithm to provide indicative feedback regarding likely print-path alignments (Figure 44e). More details about further processing of the node to physically realise it via 3DCP can be found in Section 7.4.

4.7 Interactive and informed design procedure

In summary, the interaction of the user-specified and edited graph with a form finding algorithm, coupled with visual feedback related to the alignment of the print-paths supports an informed design procedure. The didactic nature of the proposed work flow can be seen in results produced by students and designers after only summary instructions and the tools were provided (Figure 46-Figure 49) (Chapter 6). Furthermore, the serial design thread induces designers to consider both structural action such as block stereotomy and downstream fabrication implications like the spatial coherence of print-paths. Together, they provide valuable didactic information. In turn, this could help designers discover expressive design features or ‘making engineering logics visible’ (Schumacher, 2014b). The case-study project described in Chapter 8 hints at the potential that is on offer - a novel, striated language for concrete, with visible expression of 3DCP processes and lines of structural action.

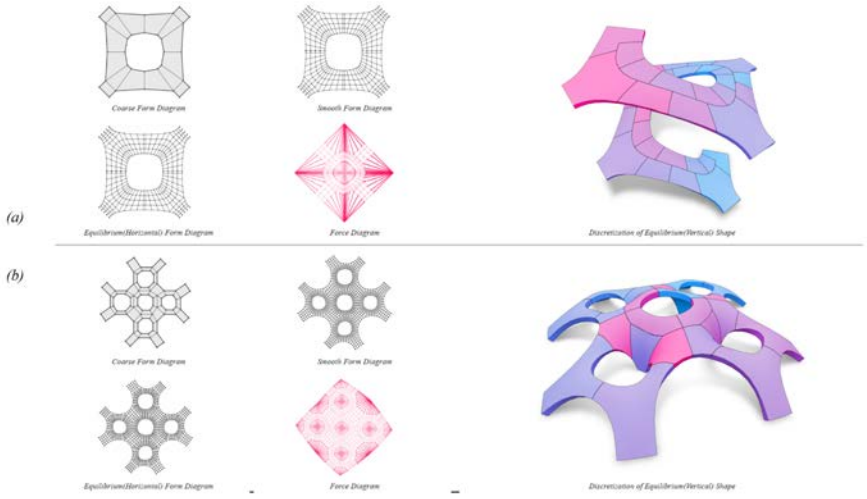

Figure 46 – Design of globally funicular shapes and their discretization, using Thrust Network Analysis and a mesh modelling environment. The results are from a 5-day workshop (“digitalFutures ,” 2017).

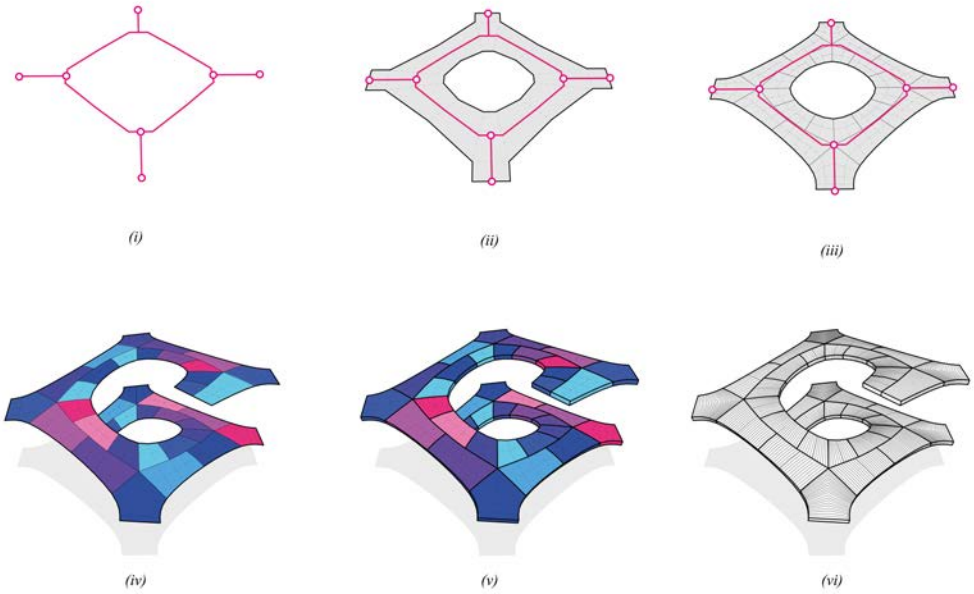

Figure 47 – Graph-to-print-paths workflow to recreate the funicular ramp example from Figure 46 . The study was explored and executed by professional designers at Zaha Hadid Architects in a few hours, after only summary instructions and the tools were provided (Chapter 6).

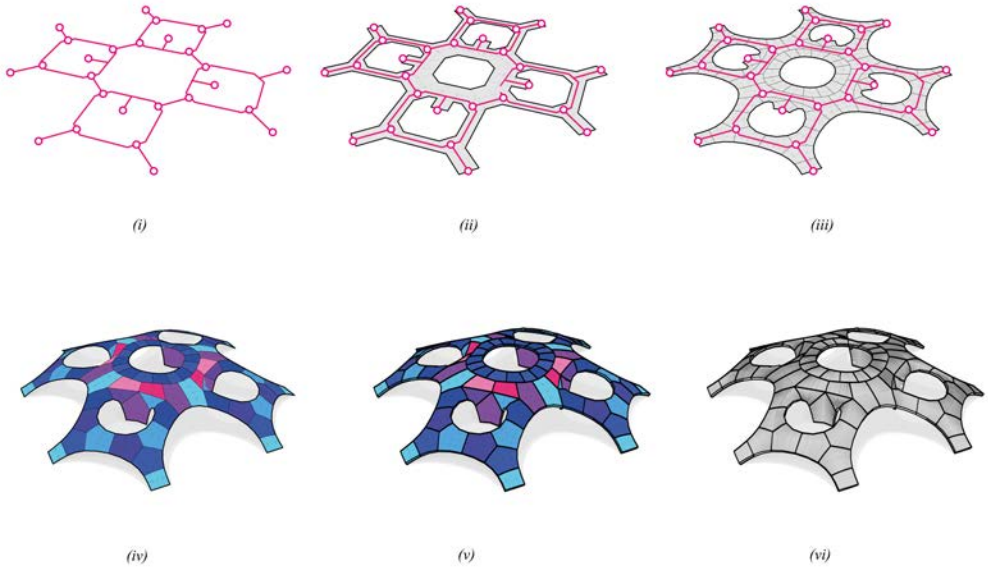

Figure 48 – Graph-to-Print-paths workflow to recreate the funicular shell example from Figure 46 . The study was explored and executed by professional designers at Zaha Hadid Architects in a few hours, after only summary instructions and the tools were provided (Chapter 6).

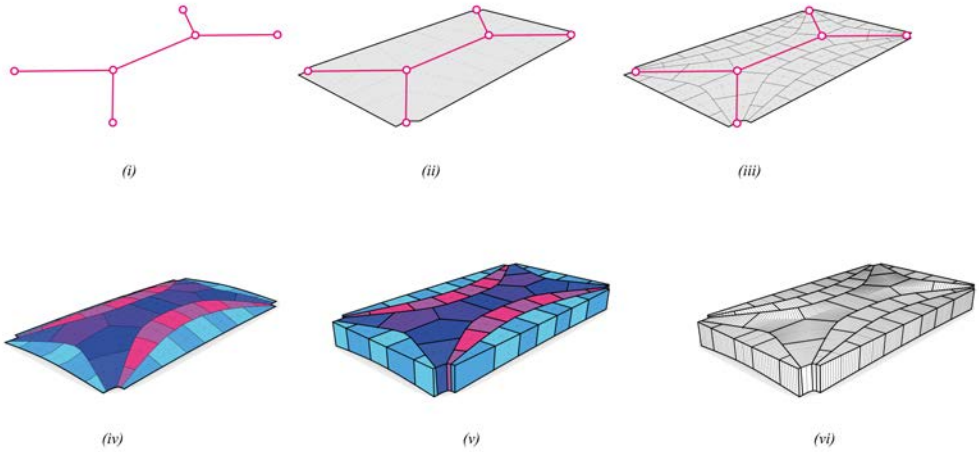

Figure 49 Graph-to-print-paths workflow for a funicular floor slab, explored and executed by professional designers at Zaha Hadid Architects within a few hours after only summary instructions and the tools were provided (Chapter 6).

5 PRINT PLANE AND PRINT-PATH INTERPOLATION

Synthesis of shapes that are guaranteed to be physically produced by Robotic 3D printing of concrete is the focus of the research herein. This is necessitated by the rapid development of the hardware, commercial availability of and interest in concrete printing. Further the need is amplified by the lack of easy-to-implement-and-use shape design tools. Together, they provide the context of the methods described in this chapter. Put simply, the methods described can, on the one hand, plug into to the interactive and informed design procedure to design unreinforced 3DCP masonry structures described previously, where they can be used to develop the print-paths for the 3DCP blocks (Chapter 4, and Section 4.5); On the other hand, they can also be easily adapted for independent use to design simple but viable, 3DCP structural components such as walls, nodes, and arches or large-format landscape furniture such as pots, barricades etc. (Chapter 7 for physically realised examples).

A necessary feature for geometries to be 'printable' is that each consecutive layer onto which material is deposited should change gradually such that it has sufficient overlap with the preceding layer (spatial coherence of print-paths). The computational handling of these aspects has been introduced previously (Section 3.6 and 4.4) including the use of a time evolving scalar-field to represent the shape to be designed – the so-called Function Representation (FRep). This chapter extends the previous descriptions by (a) fully parameterizing the shape description for 3DCP by decomposing the shape as a combination of shape interpolation (Morph) and affine interpolation (Slerp), and (b) replacing the linear, cross-fading interpolation scheme resulting in physically problematic artefacts (Section 4.4.4) with a scheme that produces smooth, spatially coherent outcomes.

The shape description, coupled with a guiding heuristic (Section 4.5) can be used to design topologically complex, physically plausible shapes with relative ease. The coupling significantly reduces the effort and expertise needed to produce shapes that are printable whilst also providing intuitive, visual feedback to designers. This is particularly useful in the current context where computer simulation of the stability of the layers during printing is actively being developed, experimental in nature and still computationally expensive. The presented approach does not, however, automatically guarantee printable outputs. The shape description and outputs may, nonetheless, be readily used as good candidates for further optimisation to guarantee print readiness (Section 5.6). The methods were also prototyped in a stand-alone software application to test ease-of-implementation (Section 5.6).

5.1 Benefits

The key consequence of the data structures and methods used is a fully parameterized shape description for 3DCP. The shape description decomposes the shape as a combination of shape interpolations between start and end cross sections (Morph) and affine interpolation between corresponding start and end planes (Slerp). The principal component of the shape description is a task-appropriate, shape-interpolation scheme adapted from the Displacement Interpolation and Optimal Mass Transport (Bonneel et al., 2011a; Papadakis, 2015).

The proposed shape description has the following benefits:

- It is intuitive, compatible with visual inspection and reasoning.
- It provides users with control handles to generate a variety of topologically complex shapes features with simple input.
- It is lightweight in terms of computational storage, with two RBF-based scalar-fields and two quaternions being sufficient to describe all the print-paths of a generated shape, often with complex topology.
- It is fully parametric; Thus, compatible to collate and compactly organize a large shape library, similar to image libraries.

The last two features may be useful for machine-learning applications that need compact and easy-to-process representations. Shape-to-vector type shape classification applications and applications that optimise process parameters of 3DCP.

Taken together, the proposed Morph & Slerp shape description provides the necessary foundation to build interactive and didactic applications to promote design for both the rapidly evolving robotic 3D printing of concrete and other historic layered construction techniques such as masonry vaulting.

5.2 Morph and slerp

The FRep-based, shape description for 3DCP consists of two parts: (i) start and end scalar-fields and their respective orientation planes and ii) interpolated in-between scalar-fields (Morph) and their respective interpolated planes (Slerp).

5.3 Morph: Shape Interpolation

Bonneel et al., (2011) developed a Lagrangian formulation to compute the interpolation between two Bidirectional Reflectance Distribution Functions (BRDF) – in other words, an interpolation between two continuous functions. Their pipeline consists of i) decomposing the two continuous functions into their respective radial basis functions (RBFs) by adequately sampling the functions, ii) computing the Optimal Transport between all paired RBFs represented as mass points with a radius of influence (Figure 50 a,d), iii) advecting the mass points along the geodesic paths between paired mass points (red dots in Figure 50 b,c), and, finally, iv) reconstructing the interpolated function (the interpolated BRDF image) from the advected RBFs. The interpolated functions are the scalar fields are corresponding to the transported mass points (red dots) in Figure 50a-d.

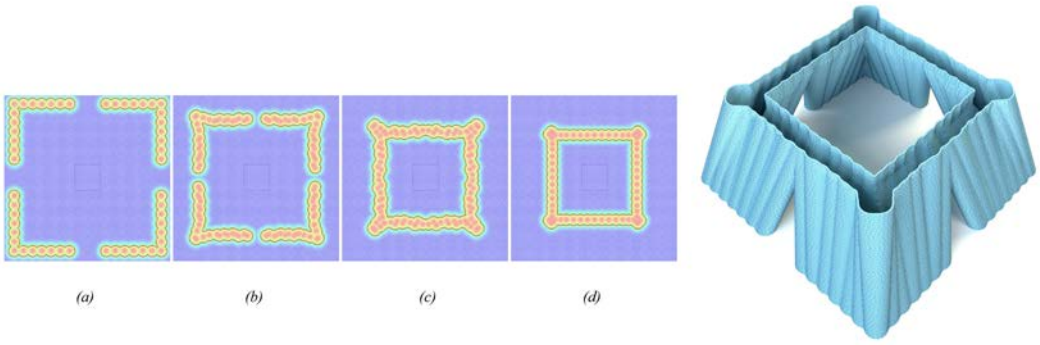

Figure 50 – Radial Basis Function (RBF) based, Lagragian optimal transport. (a,d) Source and target RBF-based scalar-field. (b,c) Intermediate, interpolated RBF and scalar-field state. The Displacement Interpolation algorithm and corresponding C++ code was adapted to produce this interpolation sequence (Bonneel, 2018) (Bonneel et al., 2011b; "Network Simplex," 2009). (e) Resultant 3D shape achieved by stacking the consecutive zero contours.

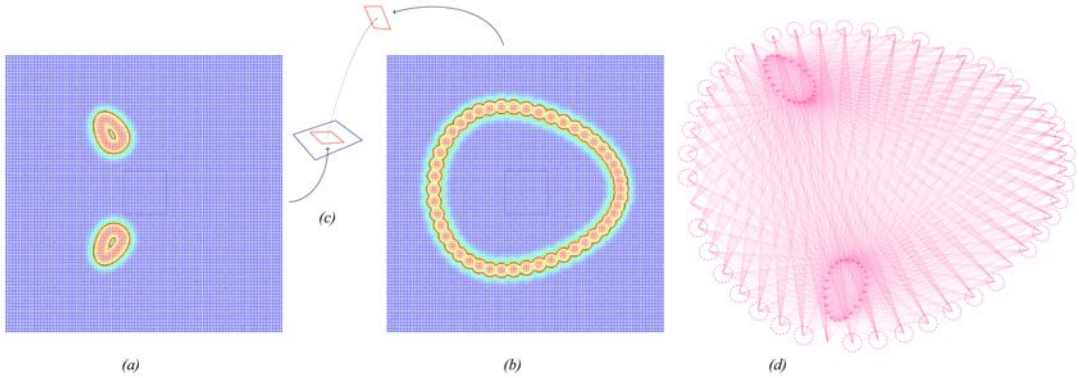

Figure 51 – Planar Inputs. (a,b) Starting and End scalar-fields and corresponding zero-contours (red) produced by respective Radial Basis Functions (RBFs) (dashed). (c) User-provided start and end print planes (red) and optionally a curve connecting them. (d) In-plane Euclidean paths between centres of all pairs of RBFs of starting and end scalar-fields. Alternatively, segmented paths may be generated from a graph connecting the centres (Figure 53).

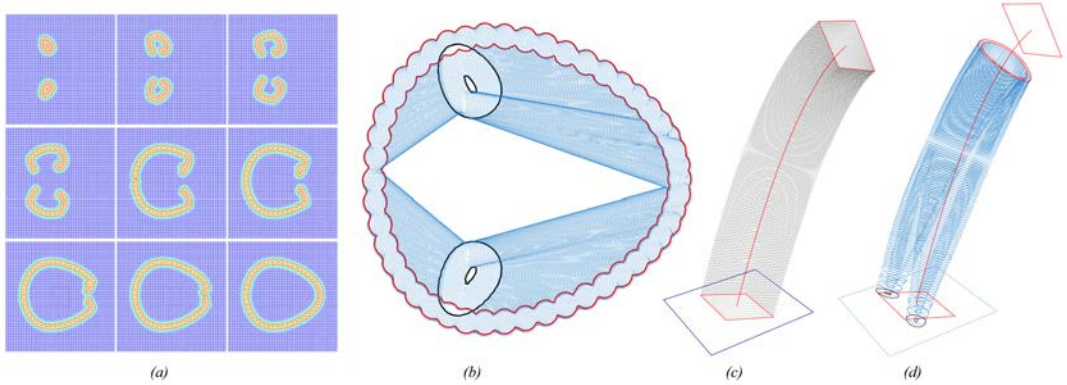

Figure 52 – Morph & Slerp. (a,b) Morph operation: blending two topological circles in the starting scalar-field to one circle in the end. (c,d) Slerp operation. (a) Displacement interpolation between start and end scalar-fields. (b) Zero-contours extracted in-plane and in-place, from various intermediate states of the evolving scalar-field shown in (a). (c) Moving frames (black) extracted from a curve connecting the start and end planes (red). (d) Resulting 3D shape achieved by transforming each in-plane curve in (b) unto respective planes in (c).

In order to design shapes for 3DCP using FRep, the RBF-based Lagrangian optimal-transport framework is adapted as follows:

a) Start with two user-defined RBFs thus omitting the first and last step (Figure 51a,b). The RBFs are represented as mass points with a radius of influence. The length of straight-line or curved paths between each pair of mass points represents the cost of moving a unit mass between the centres. In terms of shape design, they represent the paths along which the shape will evolve (Figure 51d, Figure 53(a,b), Figure 57c).

b) Retain the mass-transport and advection steps to compute the interpolated RBFs. We use the zero contours of the interpolated, time-evolving RBFs to represent consecutive print layers. Thus, the stack of *n* zero-contours represents the overall shape of the 3D object (Figure 52b). The number n provides intuitive user control over the 'resolution' or thickness of the print layers. These curves are transformed to their respective interpolated planes (Figure 52c). The resulting 3D shape (Figure 52d) is thus a combination of shape and plane interpolation between given end states.

c) Add parameters to control the rate of displacement of the individual mass points of the source RBF, as they move from source locations to computed target locations. This allows the calibration of rate of interpolation such that two consecutive zero contours have sufficient overlap i.e., have spatial coherence (see Section 5.5).

d) Add control curve handles to define the paths from sources to sinks. This allows for more user control of the resulting 3D shape (Figure 53). In particular, they allow for control over how the generated shape looks in the top-view or cross-sectional view (Figure 53b,c). We use procedurally generate these control curves by 'walking' between source and target mass points of a user-provided graph (Figure 52 a) and computing the so-called Dijkstra shortest paths (Figure 53b).

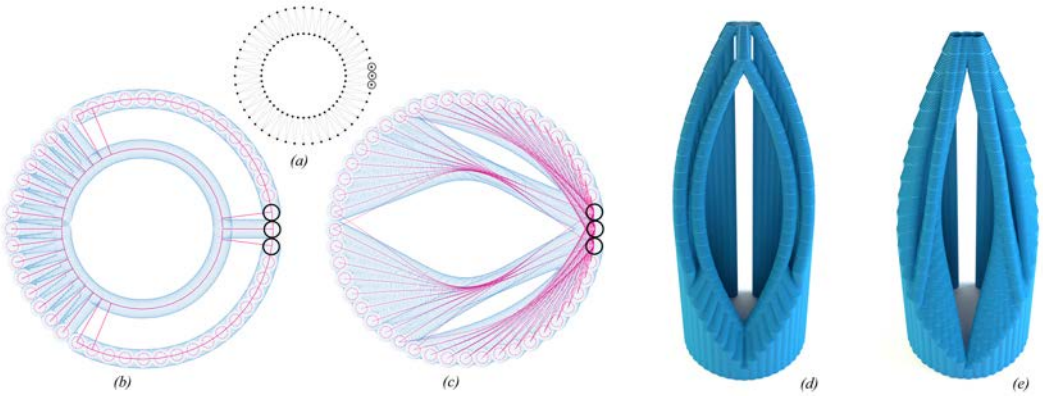

Figure 53 – Displacement trajectories. (a) User-provided graph connecting centres of source RBF (black circles) and sink RBF (black dots). (b) A family of segmented curve handles generated by walking between source (black circles) and target mass points (pink dashed circles) marked on graph in (a) and computing the so-called Dijkstra paths. (c) Smoothed version of the family of curves shown in (b). It can be noted that the zero-contours of the shape (blue) evolve along the control curves in both (b) and (c). (d,e) Resulting 3D shapes corresponding to (b) and (c) respectively, with the smooth family (c) producing more gentle curvature and inclination in the print layers, hence more amenable to printing with wet concrete. Thus, control handles like (c) is recommended.

5.4 Slerp: Plane Interpolation

The second part of the shape description for 3DCP consists of interpolating the start and end orientation planes. The zero-contour curves of the interpolated scalar-fields from the previous step are transformed to these interpolated planes. In effect, these interpolated planes represent the planes of the print-paths and material deposition. This is analogous to the titled planes of brick courses in pitched-brick masonry. Any affine interpolation scheme could be used for this purpose, and two well-established schemes used in computer animation are described next: curved motion paths and the associated Frenet-Serret moving frames (Figure 54b-left) and Spherical Interpolation (Figure 54b-right)

5.4.1 Motion paths and Frenet-Serret frames

A user-friendly method to generate the interpolated planes between user-provided start and end planes would be to extract in-between planes from a user-provided Bezier curve connecting the centres of the two planes. The Bezier curve can be drawn such that the start and end tangents of the curve are aligned with the normal of the start and end planes. In practice, the start and end planes are extracted from the drawn curve. The so-called Frenet-Serret moving frame consisting of the tangent, normal and binormal at each point along the curve can provide the in-between orientation planes.

We can use a curve based on the path of the resultant of the flow of forces in the final structure, which will improve the structural alignment of the print-paths normal to the expected force transmission across the layers (Figure 54c). This is structurally beneficial once the 3D print hardens. See section 4.3 for details of computing such a curve, and the structural benefits of aligning the planes orthogonal to such a funicular curve.

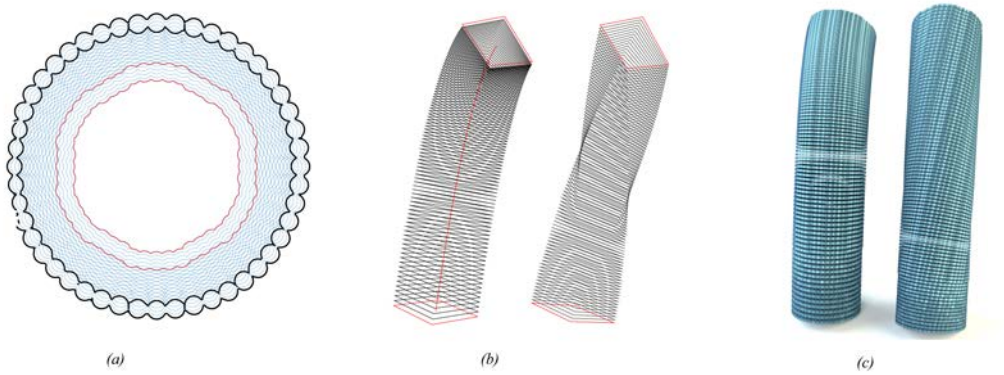

Figure 54 – Plane interpolation. (a) Intermediate profile curves (blue) obtained by interpolating between start (red) and end (black) profiles using the Morph operation (Section 3.1). (b-left) Frenet-Serret moving frames extracted from a curve (red) and (b-right) spherical linear interpolation of frames between start and end frames (red). (c) Resulting 3D shapes obtained by transforming (a) unto each family of planes (b-left and b-right) and subsequently thickening the curves.

5.4.2 Spherical Linear Interpolation

A robust, numerically stable, compact, and well-established way to represent orientation in 3D space is using quaternions. A natural interpolation that extends from this choice, is the so-called Spherical

Linear Interpolation scheme (Shoemake, 1985). This single-parameter interpolation is useful to produce an initial set of interpolated planes for user manipulation and also for procedural optimisation.

5.4.3 Affine transformation and spatial coherence

One of the consequences and an easy visual check of the spatial coherence of the zero-contours obtained from the Morph operation (Section 5.3) is the smooth gradation of the size of the bounding boxes of each of the contours (Figure 55a). Given such smoothness, the contours can individually be scaled to fit a unit square without loss of spatial coherence (Figure 55). This feature is useful when designing tubular shapes and to constrain the external boundary of the shape within a unit square (Figure 55d,e and Figure 57).

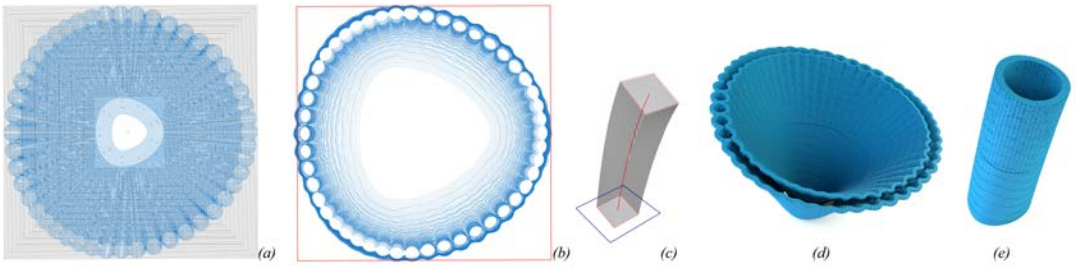

Figure 55 – Affine Transformation. (a) Zero-contours of interpolated scalar-field (blue) obtained from the Morph operation (Section 5.3). The smooth gradation of bounding boxes of each consecutive zero contour (black squares) is a consequence of the spatial coherence of the zero-contours. (b) Each of the zero-contours of (a) individually scaled to fit a unit square. (c) Interpolated planes using the Slerp operation (Section 5.4); (d) Resulting 3D shape obtained by affine transformation of each (a) unto (c). (e) Resulting 3D shape obtained by affine transformation of each (b) unto (c). This shows the use-case of scaling all zero-contours to fit within a unit square and generating tubular shapes.

5.5 Parameter choice

Given the two-part Morph & Slerp shape description, the intrinsic parameters that control the overall shape are:

a) RBFs defining start and end scalar-fields and corresponding centres / mass points.
b) individual rates of displacement of centres of source RBF towards target RBFs; and
c) orientation quaternions of each individual plane – if these quaternions come from Slerp, every interpolated plane will produce a control parameter; If a Bezier curve controls them, the location of the control points of the curve become the parameters.

In a typical example, there can be 50 centres and thus 50 displacement rates, and if the stack is of 100 layers say, we can have a 100-segment curve. Thus, finding a printable shape is the equivalent of finding 150 parameters. These parameters can be found either by heuristically guided user-manipulation or through procedural optimisation. In this work, we focus on the former.

5.6 Design-to-production

The highly sensitive combination of material and process parameters means that in practice, for all but the simplest extrusions, it is simpler and more reliable to physically validate the shape. This

requires that the design-to-production pipeline is as streamlined as possible. The proposed shape description is well aligned with the downstream requirements of print-paths and print-plane normals for end-effector orientation (Figure 56-right). As such, there is nominal downstream processing to turn the generated shape into a physical artefact. Further, two fully encapsulated software applications are sufficient to complete the design-to-production pipeline (Figure 56). The proposed, lightweight shape description enables the two applications to communicate via text-based file formats.

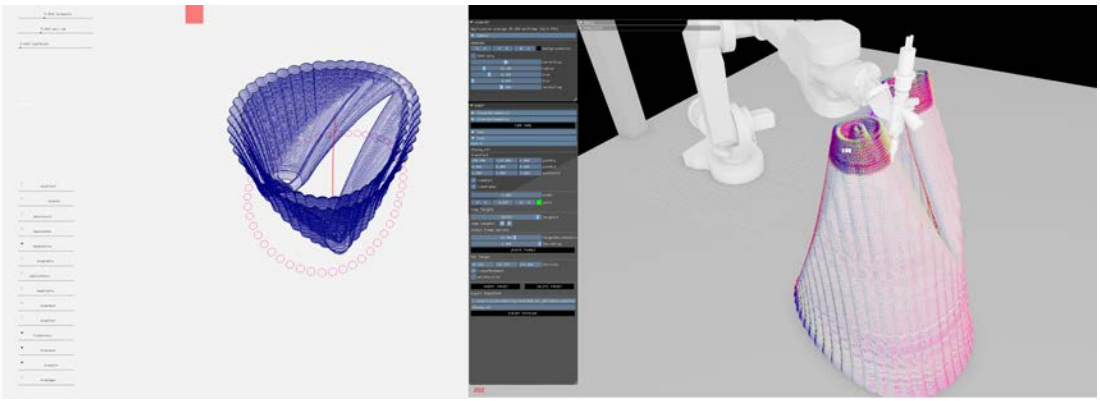

Figure 56 – Stand-alone applications. (left) Proof-of-concept, stand-alone computer application to synthesise shapes for robotic 3D printing using the proposed method. (right) application for downstream processing of geometry for manufacturing used (courtesy of Incremental 3D GmbH).

5.6.1 Complex topologies

The creation of topologically complex shapes and intricate shape features requires significant domain expertise and experience in the current 'slicing' paradigm (Section 2.5). This requirement is significantly reduced with the proposed paradigm (Figure 57 and Figure 58). Lastly, the bulbous curvature of the cross-sectional curves (undulating profile) (Figure 58), are a feature of the RBF-based formulation of mass transport used in the research (Section 3.6.2). Smooth curves are possible with the fluid-dynamics formulation mentioned previously (Figure 59). It can be noted again that the specific optimal transport formulation to be used (Fluid/Eulerian or RBF/Lagragian) does not change the Morph & Slerp shape description or the functioning of the tool.

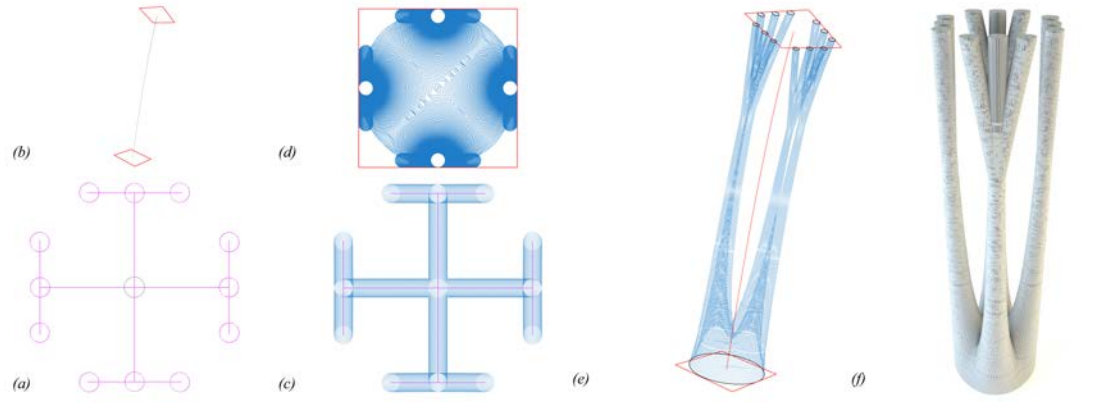

Figure 57 – Branching topology and inclined print-paths example. The proposed shape description only requires (a) graph with the location of start and end mass-points (pink and black dashed circles respectively), start and end planes (b) to automatically produce spatially coherent, gradually inclined print-paths of a topologically complex shape (e). (c,d) Intermediate zero-contours created from

inputs (a,b). It would require considerable expertise in both BRep based shape modelling and ‘slicing’ to produce (e) using currently ubiquitous methods. (f) 3D shape obtained by thickening the (blue) curves in (e).

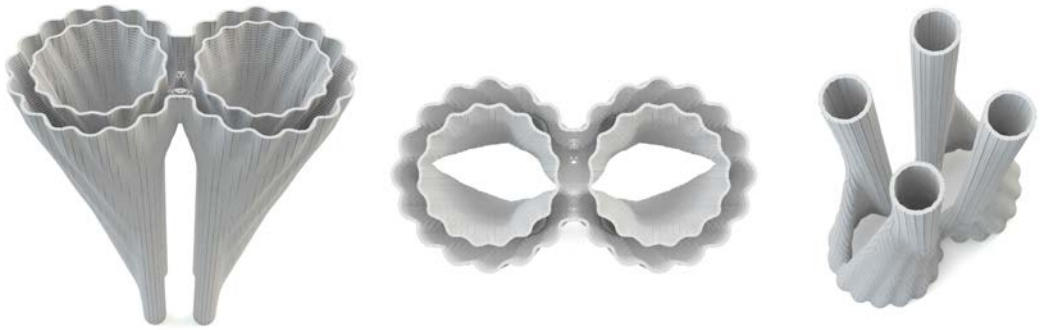

Figure 58 – Lagrangian Optimal mass transport example. (L-R) Top-down, top and bottom-up offline rendered views of an example geometry produced using the Morph & Slerp shape description. The displacement interpolation scheme used in this paper makes it easy to create spatially coherent blends between cross sectional curves with different topology such as in this example – four circles of the bottom profile are morphed into two touching circles on the top cross section. The bulbous curves are a feature of the RBF-based formulation.

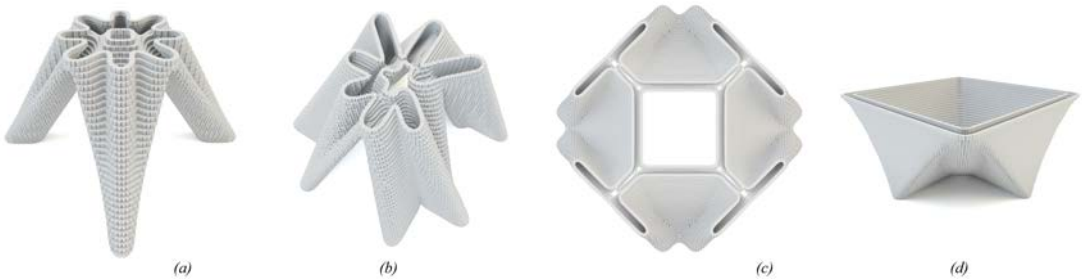

Figure 59 – Eulerian Optimal mass transport examples. (a-d) Offline rendered images of example geometries with spatially-coherent blends between pairs of profiles curves, produced with relative ease using the Morph & Slerp shape description; These examples highlight the possibility of having smooth curve profiles if we use the fluid-dynamics-based formulation of optimal transport instead of the bulbous curves that are a feature of the RBF-based formulation used in Figure 58. The M&S shape description can admit either of the two formulations of optimal transport.

6 SOFTWARE IMPLEMENTATION

The shape design to print-path visualisation workflow described in Chapter 4 may be readily executed using freely available software of rhino Vault 2 and COMPAS. This design procedure would aid in sufficiently informing the design of global shapes, their local discretisation into masonry blocks and visualise the print-paths. The physical realisation of the print-paths as a 3D concrete printed artefact could need bespoke extensions in close coordination with a 3DCP supplier.

6.1 Form finding of global shape

The goal of this step is to find a global compressive shape, given a input, typically flat or 2D mesh (Figure 59 right). For quick studies, a particle-spring simulation that is commonly found in a so-called mesh modelling environment (MME), such as Autodesk Maya, McNeel Rhino or Blender, maybe used to do the form finding. However, it is recommended to use RhinoVault (current version V 2.0), particularly for shapes that need fine control of the force flow, layout of edges in plan view etc. (Figure 60).

It is also recommended to use predominantly quad-faced meshes and preferably the input mesh for the form finding process is a Catmull-Clark subdivision mesh of a corresponding coarse mesh (Figure 61– right and middle). The combination of the coarse mesh, the subdivision mesh and a mesh modelling environment eases the user-specifications needed in the stereotomy step (Figure 61 middle and left).

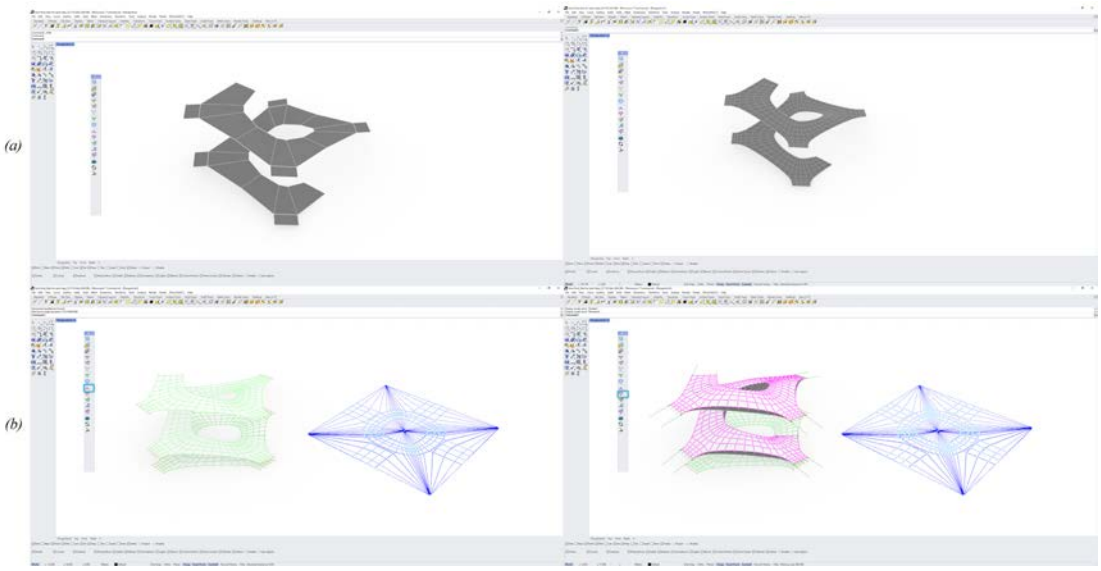

Figure 60 – Using Rhino Vault for form finding. (a) Coarse mesh (left) and Catmull Clark subdivision mesh (right). (b) Two important form finding steps - Horizontal equilibrium (left) and vertical equilibrium (right).

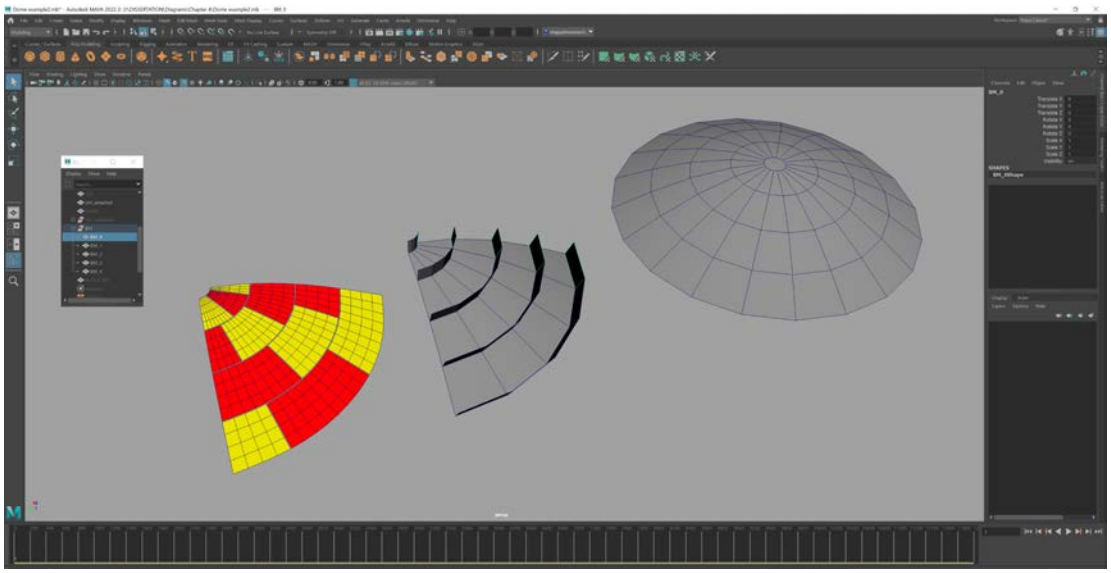

Figure 61 – Using a Mesh modelling environment (MME). Autodesk Maya (shown here) used to derive user specifications needed for stereotomy (left and middle) (Sections 4.3.2 and 6.2) from a form found mesh (right) (Sections 4.3 and 6.1)

6.2 Stereotomy

The final, structurally validated stereotomy of the global form-found shape requires detailed engineering, discrete element modelling etc, as briefly outlined in Chapter 8. Furthermore, there are no automatic tools to discretise a form-found surface into masonry blocks and the procedure requires iteration and collaboration with structural designers and 3DCP fabricators, as also outlined in Chapter 8 and 9.

However, at early design stage, for an informed stereotomy and to visualise the alignment of print-paths the following heuristic maybe followed:

- The primary ‘flow’, i.e., the spine of the slicing planes should be along the direction of compressive force flow.
- As a corollary, all blocks must have a start plane and end plane, which are as perpendicular to the spine as possible.
- The weight of a block is a function of its surface area, prior to thickening. This can be used to approximately size each of the blocks.

Using, the heuristics above, and the mesh face selection tools in a MME, the faces of the form-found or its higher resolution, subdivision mesh, maybe ‘coloured’ such that no two adjacent blocks that share a complete interface have the same colour. In practice it amounts to generating a staggered pattern (Figure 61 left).

6.2.1 Data export

The form found mesh, or its higher resolution subdivision mesh can then be separated into so-called ‘meshlets’ or sub-meshes, based on the face colouring. Subsequently, the meshlets and the original, coloured mesh can be processed to create information set needed in the next step:

- **Block plane interfaces**: the edges of the low-poly mesh may be extruded to produces a connected mesh. These mesh faces should ideally be planarized (Section 4.3.3). The mesh faces corresponding to a row of blocks can exported together (Figure 61 middle, highlighted in green)
- **Block meshes**: all the separated 'meshlets' (Figure 61 left) maybe given thickness and exported to the slicer to generate and visualize the print-path.

6.3 Print-path generation

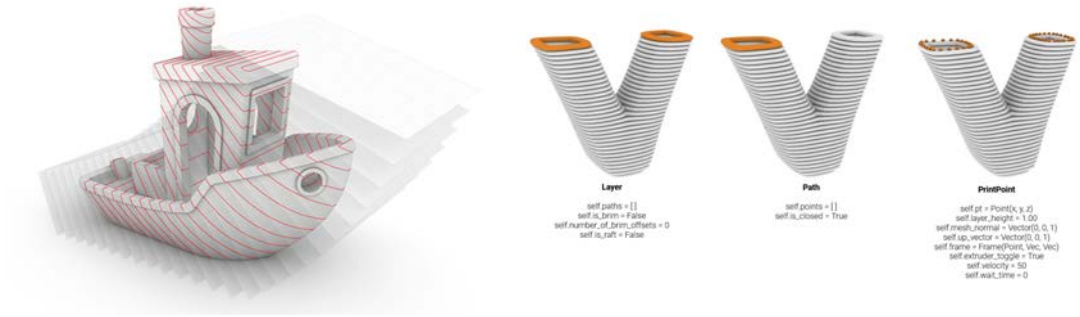

Figure 62 – Slicing example from COMPAS_Slicer object (Van Mele, 2020b). (Left) Set of slicing planes and the corresponding sliced contours on the mesh. (Right) Various constituent parts of a synthesized print-path that are useful to generate corresponding machine instructions or so-called G-Code.

For this step, COMPAS_SLICER or similar tool that can slice a mesh along a given plane or set or planes, maybe used. Thus, this step, requires two inputs – the object to be sliced and a set of slicing planes (Figure 62) (Van Mele, 2020b).

For each pair of start and end planes corresponding to each of the masonry blocks produced by the step above, new sets of planes maybe interpolated as a weighted average of the normals of start and end plane. The centres of the interpolated planes maybe placed equidistantly on the line connecting the centre of the start and end plane. The centres typically don't need to lie on a curve as the plane centres are derived form a form-found mesh. The process can be repeated for all the rows or strips of blocks (Figure 63).

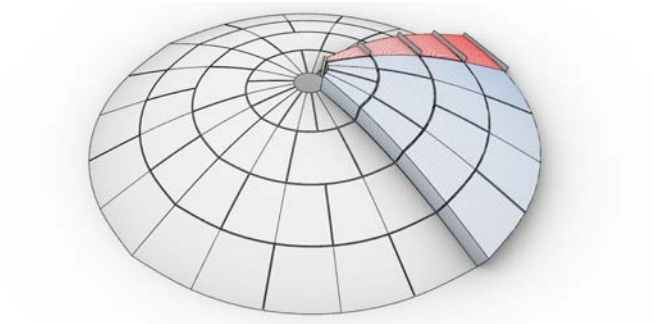

Figure 63 – Stereotomy of the form found surface mesh and print-paths visualised on the masonry blocks.

6.4 Expert users

Expert users are able to implement the full workflow within COMPAS:

- Form finding using COMPAS_TNA and COMPAS_Skeleton (Van Mele, 2021, 2020a).
- Stereotomy using the subdivision data structure in COMPAS and
- Print-path generation using COMPAS_Slicer (Van Mele, 2020b) ;

PART III - PROTOTYPES AND DEMONSTRATORS

7 PHYSICAL PROTOTYPES

It is worth remembering that, with regard to print-path synthesis, the motivations of the research presented in this dissertation are (i) integration of print-path synthesis within the interactive and iterative design cycles; (ii) synthesis of print-paths aligned orthogonal to expected, compressive force flow; and (iii) demonstration of practical application and encoding generalizable aspects from the practical exercise (Section 1.7.4, 1.7.5).

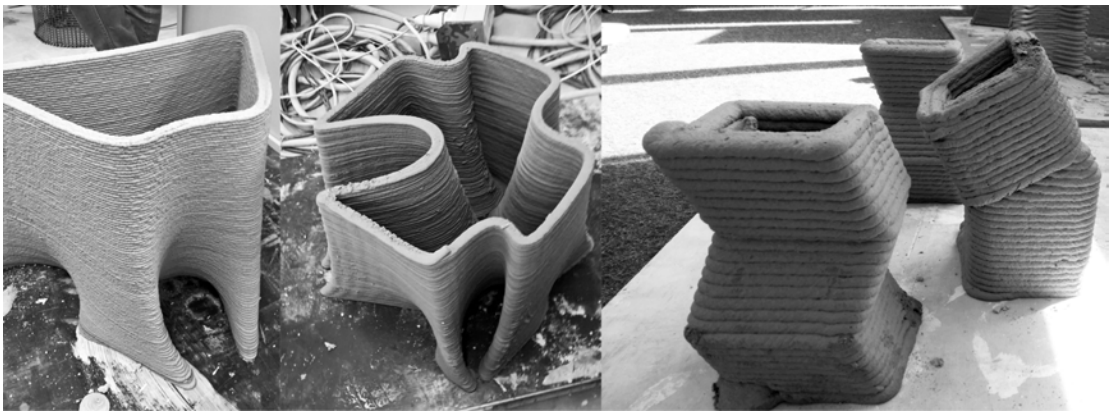

Figure 64 – Early tests of physically realising print-paths generated using the Interactive Design Explorer. (Left and Middle) Results from the 2.5D extrusion. (Right) Inclined-plane printing. Photographs from Johannes Megens (c).

7.1 Generalizing from early prototypes

The methods summarily generalized in Chapter 4 and 5, are based on the discoveries and refinements made during both experimentation with design procedures and the physical realisation of prototypes, including a 53 block, unreinforced masonry arch bridge structure called Striatus (Chapter 8). Described in this chapter are those salient discoveries.

7.1.1 Inclined-plane printing

Early printing tests indicated the viability of inclined plane printing (Figure 64-right). These early results had a significant influence on the development of the computational framework (chapter 4), the Morph and Slerp data structure (Chapter 5) and ultimately in the evolution of the insight of compatibility of unreinforced masonry and 3DCP into an operative design-to-production workflow (Chapter 8,9).

7.2 Simple, tubular topologies

For simple tubular topologies with printing planes parallel to the horizontal, we can omit specifying the start and end planes from the shape description (Section 5.4). Instead, simply the combination of implicit scalar field representation and resulting level curves would suffice as the data structure to represent the geometries to be printed. Additionally, the scalar field or level curve can be evolved as it is extruded in the z-direction, resulting in a so-called 2.5D extrusion of a tubular topology (Figure 65 and Figure 66 left).

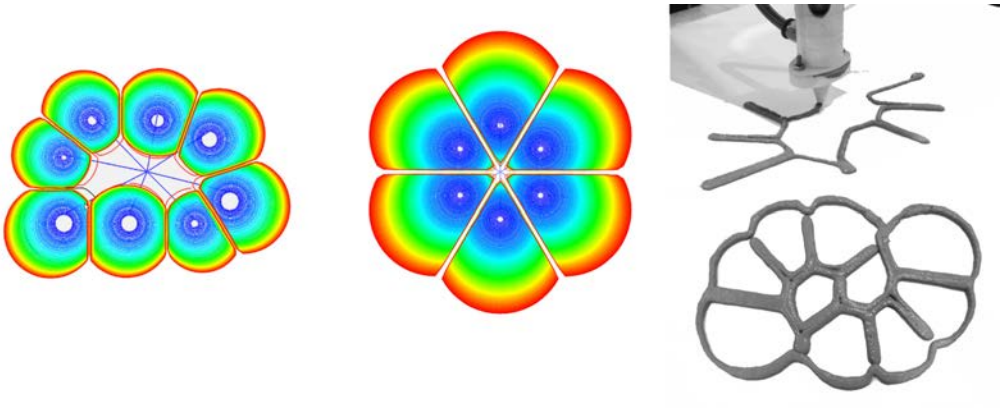

Figure 65 – Tests of using signed distance fields to generate print-paths and machine instructions to deposit clay. (Left and Middle): Outward radiating task graph because of a radial distance function. (Right) 3D printing of one of the layers in clay

The synthesised task graphs were evaluated for print viability in terms of overhangs using the heuristic as described previously (Section 4.5); Subsequently they were processed for printer related parameters such as accessibility of the print-head, speed etc., (Figure 66 right). The exported print-file is subsequently processed by the manufacturer for additional parameters before being printed (Figure 67). The 3D printed outcomes demonstrate areas of local overhang and under-cuts (Figure 67 right, Figure 64 left and middle). The overall stability of the prints and their feasibility were able to be reasoned geometrically as exemplified by the inverted printing direction of the shape shown in Figure 67-left.

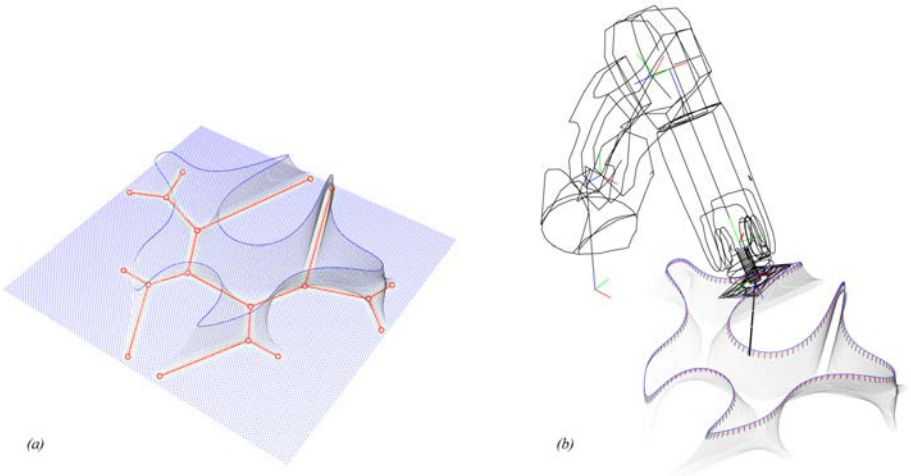

Figure 66 – Prototype for the Integrated Design Environment (IDE). (Left) Synthesis of print-paths, and their post-processing for printed related parameters (right).

Figure 67 – Post-processing of print paths by 3D concrete Printing (3DCP) manufacturer ("Incremental3d," 2017). (Left) Processing of an outcome produced by proposed IDE by the manufacturer. (Right) Prototype demonstrating the application of the proposed method.

The results also demonstrate the ease of the 2.5D extrusion method to generate simple tubular shapes, which can be used for the design of wall-like structural components, where the compressive force flow is vertical (Figure 68).

Figure 68 – Using the IDE to synthesize tubular topology objects. 2.5D wall-like structural components, produced user specified input graphs (Red).

7.3 Bifurcating tube topology

A bifurcating tube topology, whereby the cross section of the tube changes from a circular topology with a single hole to one with multiple holes, requires significant designerly expertise to achieve using a NURBS-based BRep representation. It is easier to achieve using mesh modeling tools in a so-called Mesh Modelling Environment (Chapter 6). However, as described previously, it much more intuitive and easier to achieve the same using implicit scalar field representation by simply specifying the desired 2D cross-sectional profiles as signed distance fields (Section 4.4.4, Section 5.6.1). Subsequently, the intermediate cross-sections can be generated by interpolating user-provided start and end SDFs (Figure 69). Furthermore, the intuition extends both to seeing the cross-section change as represented by the extracted zero-contours, and their direct use as print-paths (Section 2.5) (Figure 70). The work of students produced during a short 5-day workshop is testament to this ease of implementation and use (Figure 69 - Figure 71). Students did not have prior knowledge of 3D printing or the associated shape design. Furthermore, the design-to-production

tools, including the Frep interpolation, were produced using commercially available software platform (McNeel Rhinoceros and Grasshopper, visual programming platform). The students were able produce a variety of complex-topology 3D printed objects.

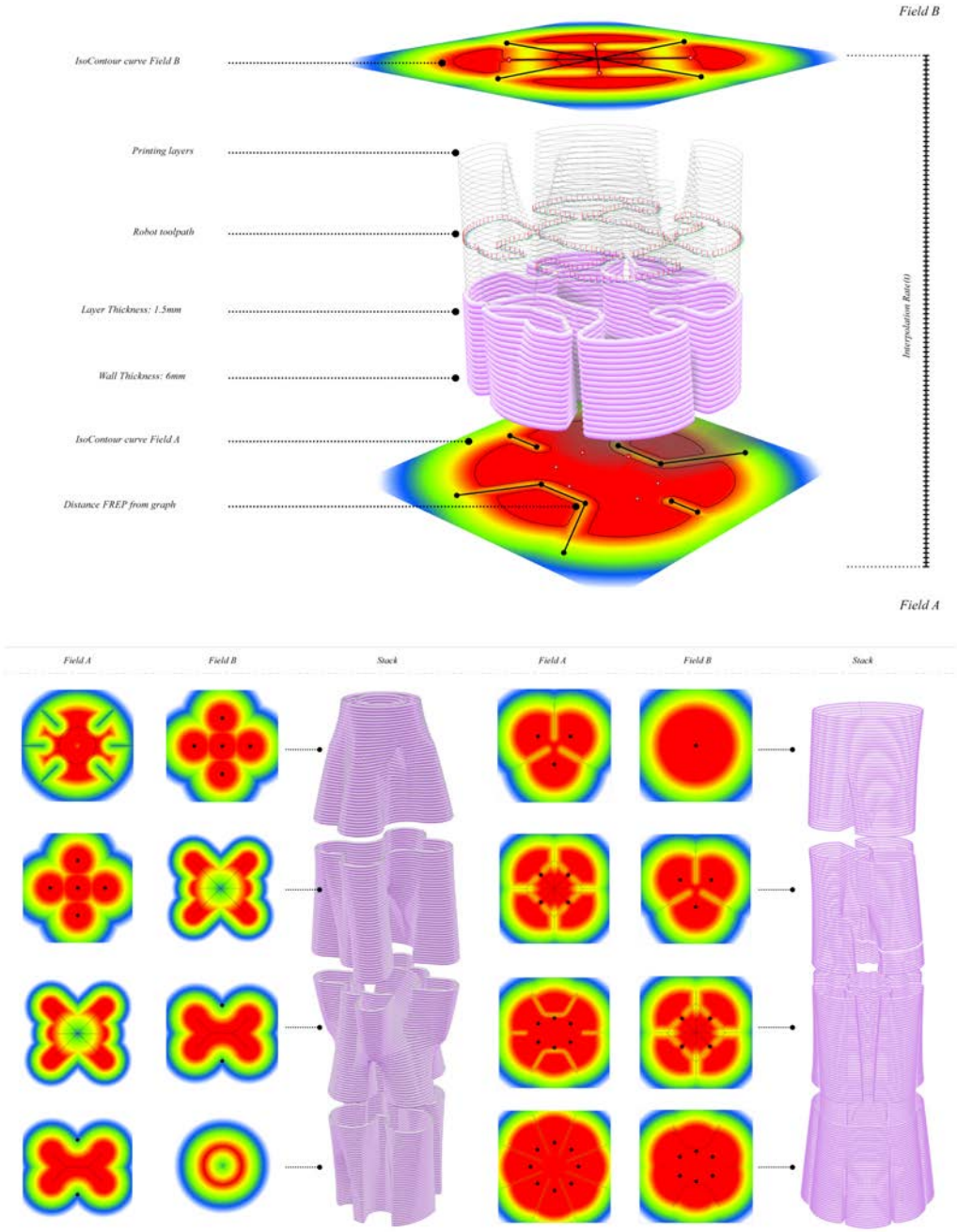

Figure 69 – Bifurcating tubular topology shape design results. Results produced by first-time user, architectural students during a 5-day design-to-production workshop ("digitalFutures," 2018).

Figure 70 – Bifurcating tubular topology shape design results. Results produced by first-time user, architectural students during a 5-day design-to-production workshop (“digitalFutures,” 2018).

Figure 71 – Bifurcating tubular topology shape design results. Results produced by first-time user, architectural students during a 5-day design-to-production workshop (“digitalFutures,” 2018).

7.4 Intersecting, multi-tube topology

Similar to the bifurcating tube topology, it would be possible to use a (mesh) BRep-based approach to process a multi-valent node of a funicular network for 3DCP. This can be achieved via the procedural thickening of the skeletal graph and subsequent contouring of the meshes that represent nodes (and bars) of the network (Section 4.6) (Figure 72a-d). However, such geometric processing of nodes increases in complexity when processing nodes requiring overhang support and/or with increased topological complexity. This approach holds further complications regarding assignment of ideal print directions to the node in addition to resolving complex interfaces between the print layers of the nodes and bars (Figure 72d). Furthermore, local processing of print layers does not guarantee good alignment with the funicular force flow over the node.

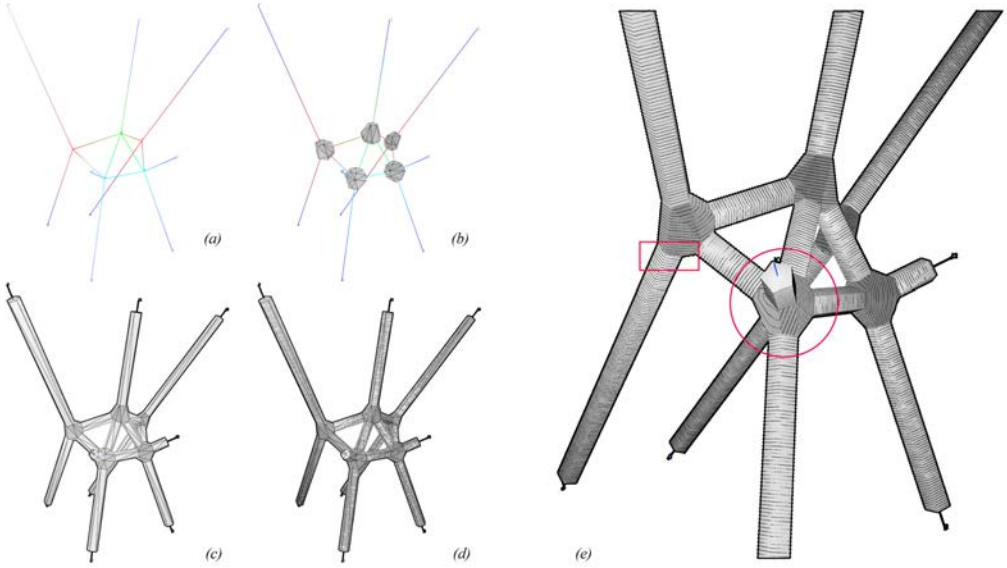

Figure 72 – Typical geometric processing of spatial graphs for 3D printing. (a-c) Generating convex hulls around nodes and bars of a graph, (c) contouring the combined mesh. (e) Alignment and interface problems with task graphs.

Alternatively, the rich and easy-to-implement operation set of FRep can be used to alleviate this complexity, and easily handle topological changes from one print layer to another (Section 3.6 and Section 4.4.1);

7.4.1 Geometry processing

The simplest procedure to produce the print-paths is by translating a circular cross-profile along the edge, and simultaneously trimming against the bisector planes defined between pairs of edges (Section 4.4.3) (Figure 73a). In other words, in this simple method, the cross-section or so-called 'front' does not really evolve.

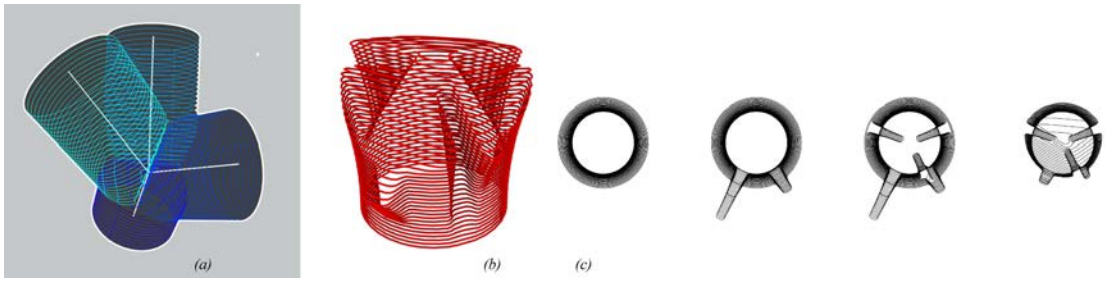

Figure 73 – A procedure of translate and trim to synthesise task graphs for each node segment. (b) Task graphs of one of the four parts meeting at node show in (a). (c) Stages of evolution of the print layers of print-path shown in (b).

In most practical cases on the other hand, the moving front needs to evolve features to ease steep overhangs and to provide internal support (Figure 73 b,c). In such cases, the evolving front utilises the full range of FRep operations: Booleans, blends and trims (Figure 74a). The input primitive fields for these operations are generated by first extracting an oriented sub-graph from edges that meet at a node. This sub-graph is projected onto the ground-plane to get a 2D skeletal graph, which is subsequently used to generate the primitive fields (Figure 74 b,c).

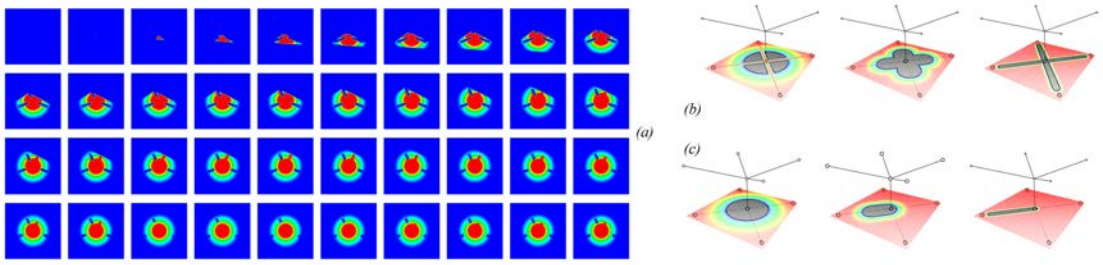

Figure 74 – FRep based processing of spatial graphs. (a) Secondary composite primitives formed by Boolean operations on primary primitives (b,c). (b,c) Primary primitive scalar fields generated as Signed Distance Fields (SDFs) in relation to the vertices and edges of the spatial graph.

The parts of a node are printed consecutively whilst the previous part is still wet, enabling a material bond across the node (Figure 75). In terms of the processing of the node, this does not pose any additional difficulty, except nominal post-processing of joining the individual print-paths into a singular sequence of robot-instructions.

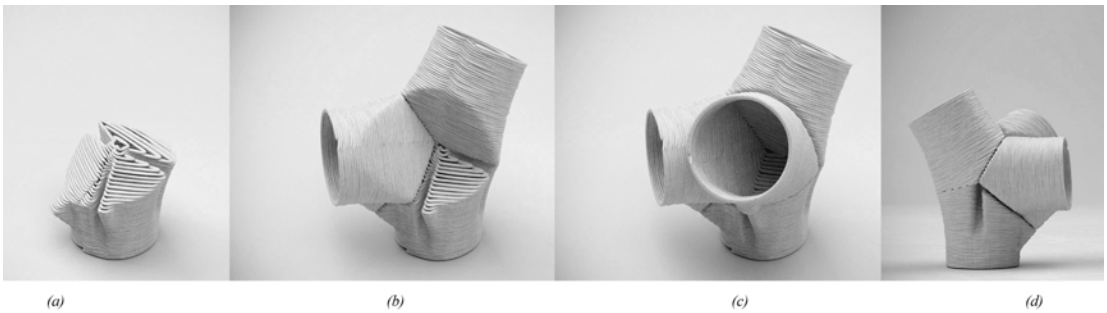

Figure 75 – Printing sequence of a compound, spatial print-path. Computer generated images showing (a - c) printing sequence of the constituent parts of a node and (b) result highlighting the groove feature that adds internal support to the print.

7.4.2 Robotic 3D printing

The conversion of the print-paths into motion instructions for the robot uses industry-standard procedures. The only significant geometric detail worth mentioning is that consecutive layers of task graphs need to be assembled into a single tool path. This involves first ensuring that the end of one layer and the start of the next are in proximity and subsequently adding a segment that will carry the print head smoothly across layers.

7.4.3 Path planning

The bounding volumes of the each of the nodes should be within the operating sphere of the robot used. Further, the dimensions of the print head and apparatus in relation to the size of the print should also be such that the need for extensive collision avoiding path planning is not necessary. However, the entire print trajectory of the robot along with the print head, is simulated and visually inspected to ensure there are no collisions, particularly of the print head with the ground (Figure 76).

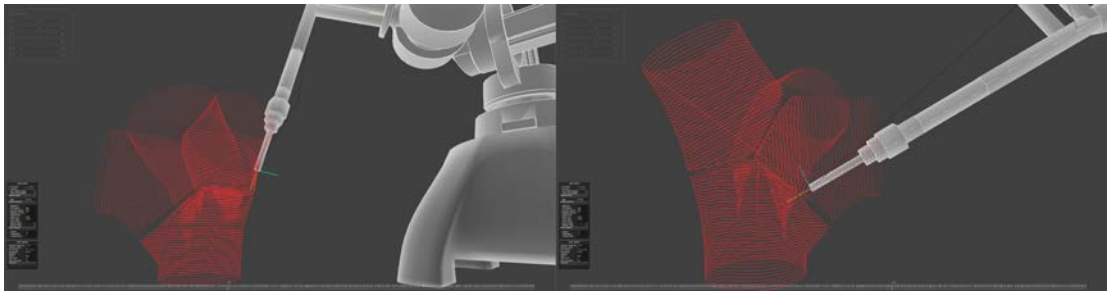

Figure 76 – Visual inspection of print trajectories, for potential collision of print head with the already printed parts and/or the ground

7.4.4 Results

All results use C25 concrete (Figure 77). The print duration for each of the prints is approximately 30 minutes and each segment of the nodes typically consists of 90-100 layers of 4mm each. The diameter of each of the node segments is approximately 15 cm. One of the nodes was also printed at twice the scale with the diameter of 30 cm (Figure 78), using the same print-path synthesis procedure.

Figure 77 – Materially bonded, compound 3DCP objects. Photographs showing various types of nodes that vary in valence and angles between incident edges.

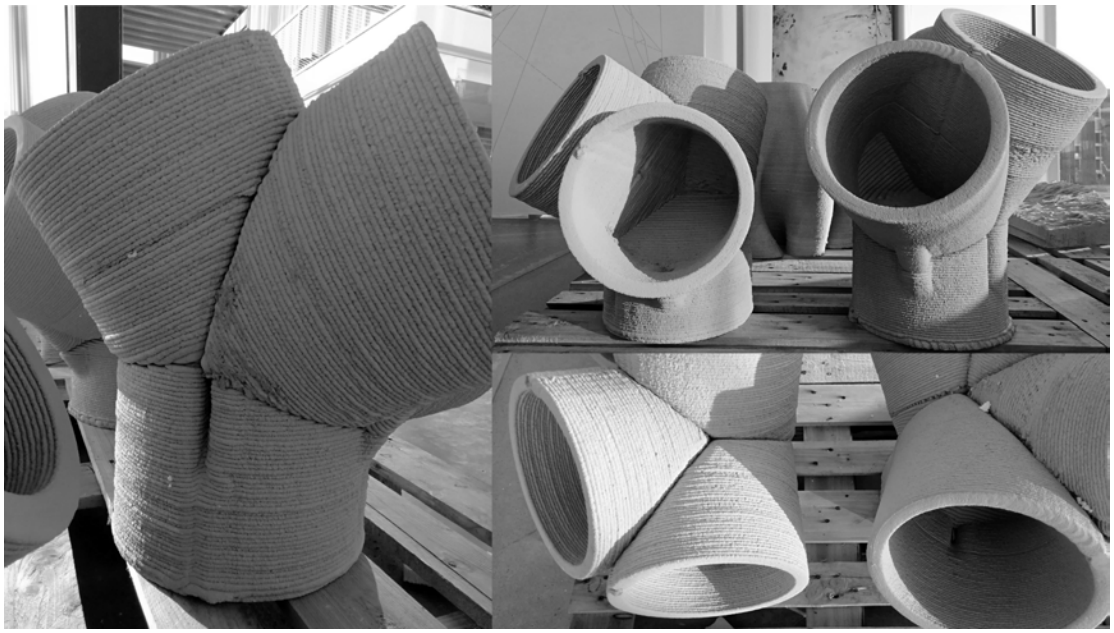

Figure 78 – Force-aligned, inclined-plane 3DCP of a node in a funicular skeleton.

8 STRIATUS – A FULL SCALE, TECHNOLOGY DEMONSTRATOR

Striatus is a 3D-concrete-printed, mortar-free, unreinforced masonry arched footbridge, designed for disassembly and reuse (Figure 79 and Figure 80). It is a full-scale, prototype demonstrating the relevance of the computational masonry paradigm to both delivering the ecological promises of 3DCP and to the development of a 3DCP-specific, design-to-production (DTP) toolkit. This chapter details the practical application and extension of the computational framework described previously (Chapters 4 and 5) and the resulting DTP workflow. The manufacturing and assembly processes used for the project, is also outlined.

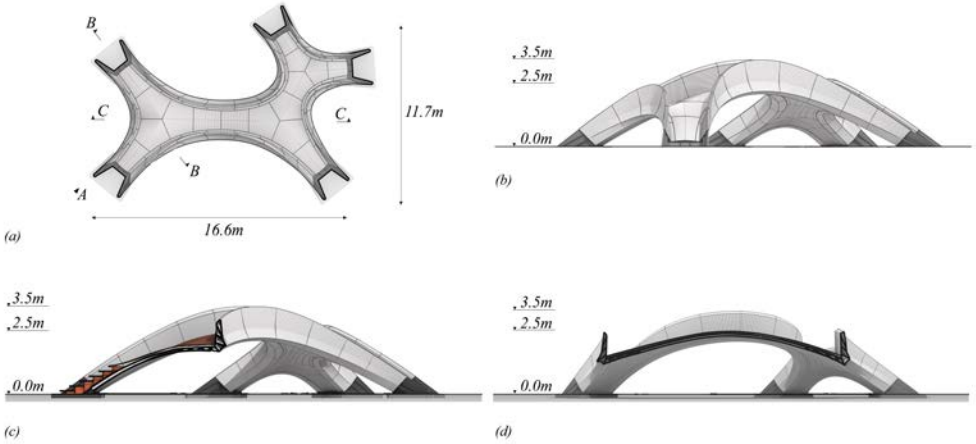

Figure 79 – Schematic drawings of Striatus. (a) plan, (b) elevation A, (c) section BB, and (d) section CC

Figure 80 – Photograph of Striatus, Venice 2021(naaro (c)).

8.1 Design-to-production toolchain

The collaborative, multi-author, design-to-production (DTP) process that we developed to practically realise the demonstrator bridge, can be unrolled into a serial thread (Figure 81a-c) and three structural guidance, verification and analysis threads (Figure 81i-iii) that insert information into the serial thread via strategic data interfaces.

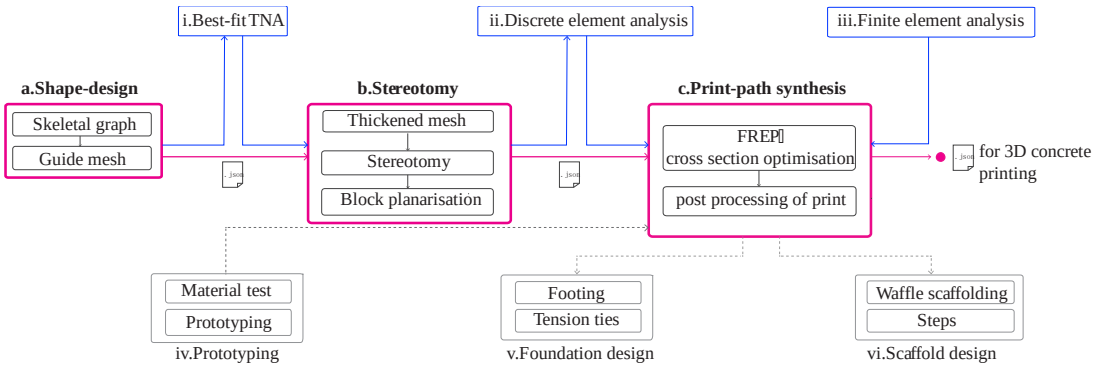

Figure 81 – DTP Tool chain unrolled into threads. (a,b,c) serial thread, (i, ii, iii) parallel structural threads, (iv) material testing and prototyping thread, (v) foundation design thread & (vi) scaffold design thread

The serial thread includes the three major process steps as generally described previously (Section 4) and outputs the print-paths, per 3DCP stone block:

- **Shape design:** designer-guided shape design of a medial surface (Figure 81a).
- **Stereotomy**: decomposition of the medial surface into patches, thickening of the patches by offset, and synthesis of block geometries, including inter-block, planar interfaces (Figure 81b).
- **Print-path synthesis**: Generation of the print-paths per block based on expected force flow and block interface planes as defined by the stereotomy (Figure 81c).

Interleaved with each of the three process steps of the serial thread, are three corresponding parallel, structural verification processes:

- **Best-fit TNA**: A best-fitting TNA algorithm is used to take the user-provided, medial surface as a target and fits a nearest compression-only surface to it (Lachauer and Block, 2014) (Figure 81i). This step modifies the shape of the user-provided medial surface.
- **Discrete-element modelling** is used to evaluate the structural stability of the discrete, rigid blocks produced as an outcome of the stereotomy. Through an iterative procedure, this step modifies the interface planes between blocks based on structural requirements (Figure 81ii).
- **Finite-element modelling** is performed to verify the local bending stresses in the blocks, which inform the print-path synthesis (Figure 81iii)

In addition to the design and structural threads above, there are three other threads- scaffold design, tension-tie and foundation design and material testing and printing prototyping (Figure 81 iv - vi). The first two output fabrication information to produce the timber falsework and the steel footings, tension ties and foundation information. These threads only receive information from the serial

threads and output information. The third thread informs the cross-section design of the blocks and imposes angular limits on the inclinations of structural interfaces-planes between the blocks. Subsequently, the 3DCP blocks, timber falsework and steel supports are digitally manufactured using the information produced by the DTP toolchain. The parts are then transported independently and assembled on site (See Section 8.11 for more).

It can be noted that each of the process steps described above are performed in stand-alone applications, are user-guided, and should not be viewed as single-step automation processes. However, the serial thread by itself can be used as a self-contained, parametric, or user-guided design explorer if the structural and fabrication bounds, as established, are not violated. In other words, the three structural threads, and the foundation and material testing threads may not participate in every iteration of the serial thread, depending on the extent of change in the medial mesh surface. Thus, the serial thread can rapidly iterate whilst remaining within bounds of structural and printing feasibility.

8.2 Structural principles and constraints

The integrated design-to-production toolchain, as described, is informed by a global understanding of the structural mechanics of the bridge and the specific geometric constraints imposed by non-parallel, inclined-plane 3D concrete printing.

Striatus follows masonry structural logic on two levels. The bridge behaves as a series of leaning unreinforced voussoir arches, with discretization orthogonal to the dominant flow of compressive forces, following the same structural principles as arched Roman bridges in stone. Locally, on the level of the voussoir, the 3DCP layers behave as traditional brick masonry evident in the inclined rows of bricks within Nubian or Mexican vaulting (Figure 82).

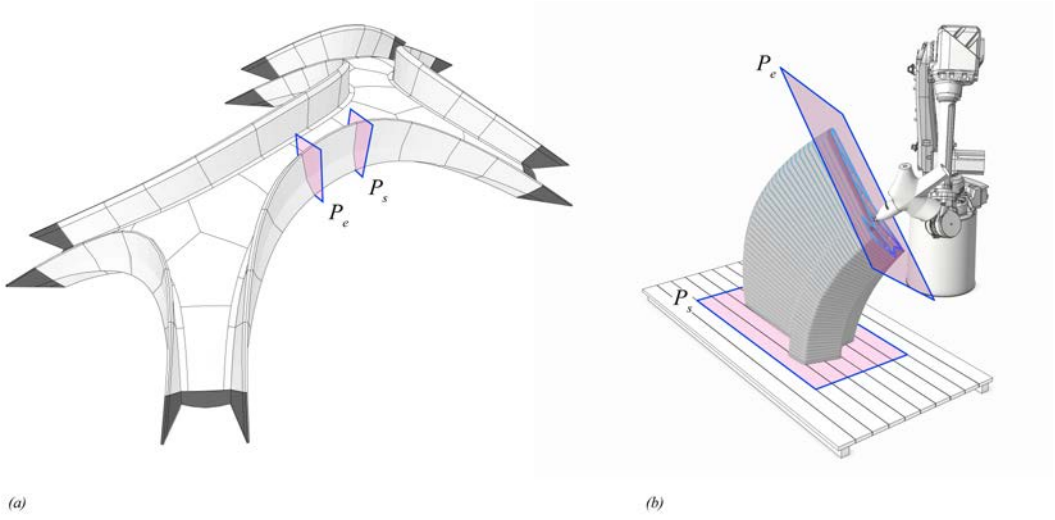

Figure 82 – Masonry logic at two scales. (a) Arched balustrade and deck voussoirs, (b) start and end plane of a print block - P_s, P_e

Viewed from the top, the balustrade arches are leaning inward towards each other and are prevented from falling over by the deck. Because of the chosen stereotomy, they additionally provide a

stabilizing surcharge onto the thin deck, reducing the effect of live loads versus this increased dead load. The deck arches are also composed of voussoirs with discretization orthogonal to compressive forces, which run along the spine (i.e., the skeleton) of the deck (Figure 83).

Geometrically, the masonry structural logic at two levels means that it is critical to coordinate the interfaces planes between voussoirs, in both the balustrades and the deck arches, as the dominant compressive forces flow across these planes (Fig. 6). In terms of printing, each pairwise group of the interface planes determines the start and end plane of the printing (Fig. 4a). This means that the angular differences between start and end planes of all 53 printed blocks must be globally coordinated to meet multiple criteria such as an appropriate structural contact, angle between adjacent blocks, and maximum print inclination.

As such, the main data interface between the serial thread and structural and prototyping threads are the interface planes. These planes are represented and manipulated as a non-manifold mesh (Figure 84) (Section 8.5).

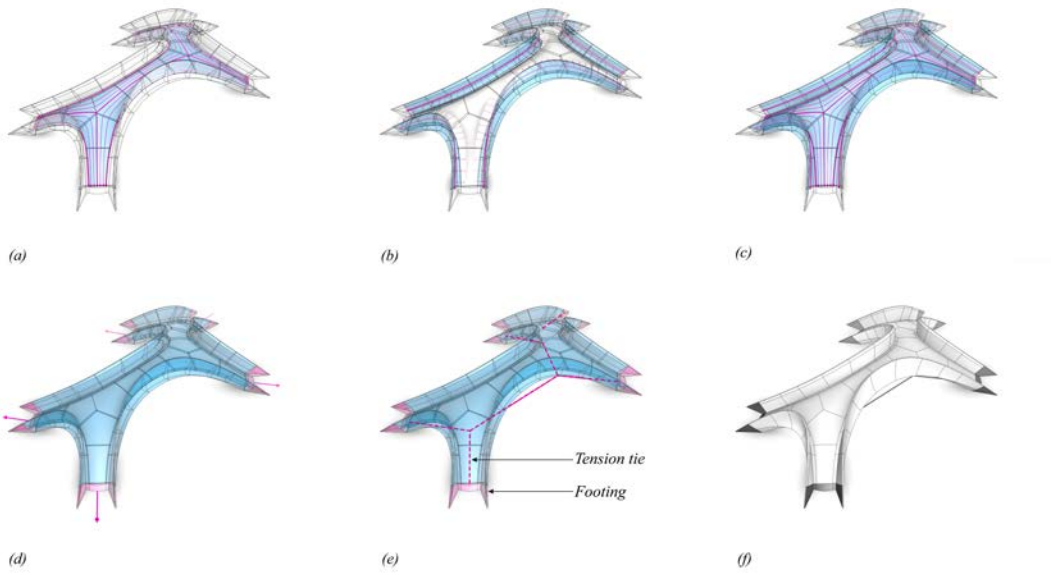

Figure 83 – Structural principles. (a) Stable, bifurcating deck arches. (b) Inward leaning balustrade arches. (c) Balustrade arches prevented from falling over by stable deck (d) Outward thrust resultants of masonry structure. (e) Tension ties to counter outward thrust resultants. (f) The final geometry.

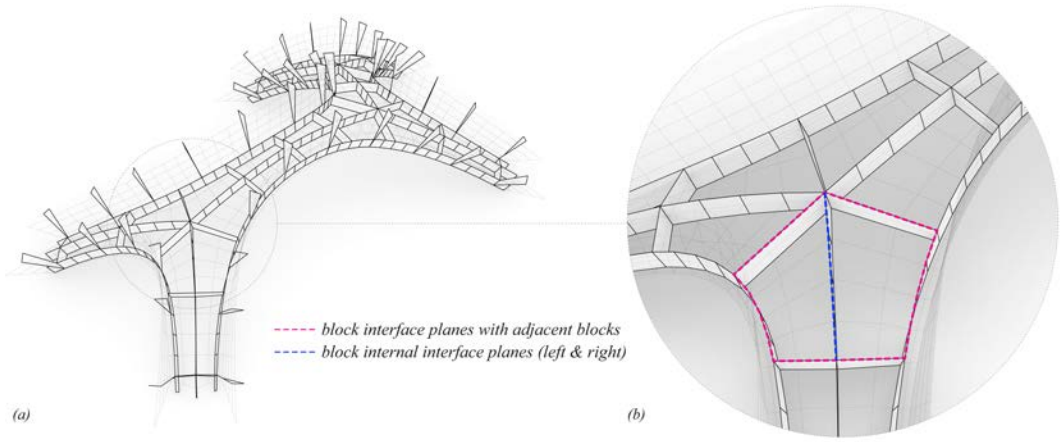

Figure 84 – Block interface planes. (a) Block interface planes represented as a non-manifold mesh. (b) Detail inset showing interface planes for one block - with adjacent blocks & internal left - right interface

8.3 File format and data structure

The collaborative design-to-production (DTP) toolchain described above is based on a mesh-based, geometry-processing paradigm. This allows for lightweight transmission and reconstruction of information by various participating tools in DTP. The DTP toolchain is supported by a custom file format that is loosely based on the GL Transmission Format (glTF), an increasingly widely used 3D file format. Similar to glTF, our file format uses JavaScript Object Notation (JSON) to store the 3D model information. The use of JSON enables the efficient transmission and loading of 3D scenes and models by applications, by minimizing the size of 3D assets and the runtime processing needed to use those assets (Khronos, 2021).

The main data structure that supports all the algorithmic operations in the DTP is a half-edge mesh. This data structure allows the run-time computing and storing of information per vertex, edge or face of the medial surface mesh that is created in the first step of the DTP process (Figure 81a and Figure 87). The data that is computed on the mesh using the half-edge data structure (Figure 85), is then stored in the JSON file with the attributes and schema noted in Figure 86 and transmitted throughout the serial and structural verification threads. At each consequent step of the DTP process, authors can parse relevant information and compute derivative information within their individual process threads. Any critical information that is relevant to the serial thread is added, as attributes, to the mesh vertices, edges or faces of the medial mesh surface. This information is mirrored in the JSON transmission file (see Figure 90 and Figure 111 for additional attributes added in the relevant serial thread).

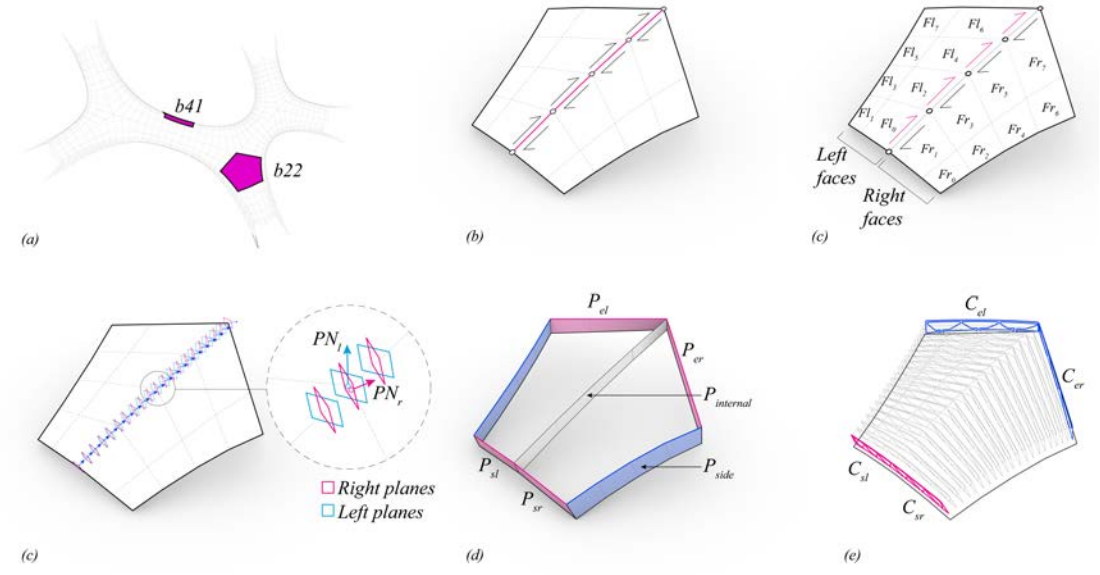

Figure 85 – Stereotomy. (a) Key plan highlighting mesh patches of block b22 & b41. (b) Medial Spine. (c) List for left & right faces of the block (F_l,F_r). (c) Interpolated left & right print plane normals (PN_l,PN_r). (d) Block interface planes - start (P_{sl}, P_{sr}), end (P_{el}, P_{er}), sides (P_{side}) & internal ($P_{internal}$). (e) Print contours left & right from start to end planes (C_{sl}, C_{sr},C_{el}, C_{er})

8.4 Implementation

The serial thread of the DTP toolchain was encapsulated in a lightweight, standalone C++ application of 800 Kilobytes. Similarly, on the structural thread, the best-fit TNA process was performed in a lightweight, standalone application produced using the COMPAS framework. The same lightweight application performed the translation of the JSON transmission file into DEM and FEM analysis friendly data. The application also controlled the batch processing of multiple analyses, subsequent parsing of the results and insertion of design-critical results into the JSON transmission file. The computationally expensive, well-established DEM and FEM analyses themselves were performed by commercially available software of 3DEC and SOFiSTiK, respectively.

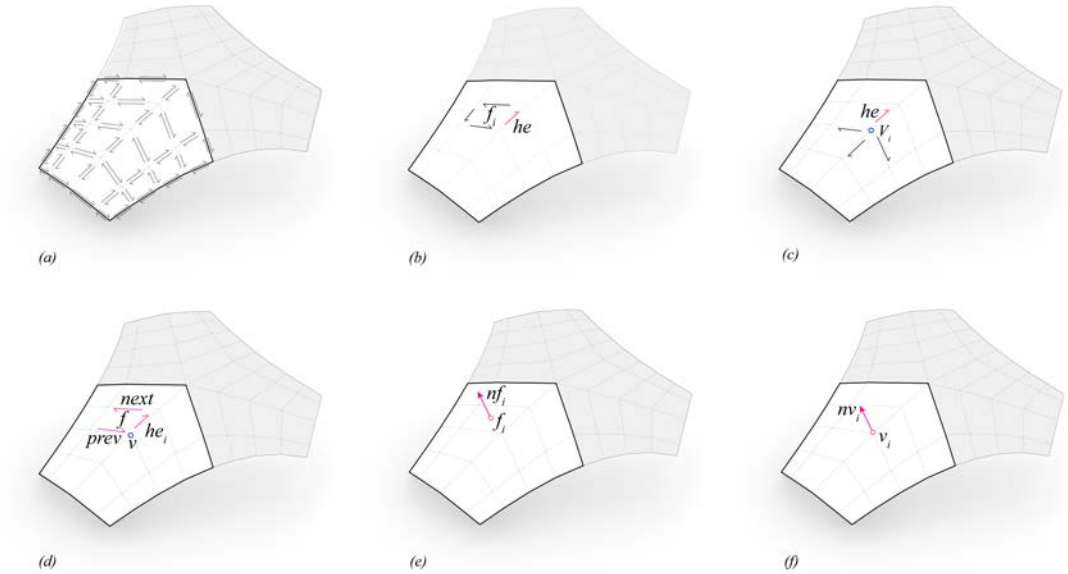

Figure 86 – Half-edge data structure. (a) JSON attributes & schema stored on a half edge mesh. (b) List storing per face f_i one of its half-edge index *he*, (c) List storing per vertex v_i, one of its outgoing half-edge index *he*. (d) List storing per half-edge he_i indices for next half-edge (next), previous half-edge (prev), associated face *f* & associate start vertex index *v*. (e) Attribute list storing face normal $\boldsymbol{nf}_i$ per face f_i. (f) Attribute list storing vertex position $\boldsymbol{vpos}_i$, vertex normal $\boldsymbol{nv}_i$ per vertex v_i.

8.5 Serial thread of DTP

The serial thread of the DTP toolchain takes a user-provided, 2D graph that represents the spine of the bridge, and outputs the printing information needed to 3DCP each of the discrete masonry blocks of the bridge. It comprises three major process steps: Shape design, stereotomy and print-path synthesis. It can be noted that, whilst the steps can proceed in an automated fashion, designer inspection and adjustment is currently required.

8.5.1 Shape design

The global shape design of the bridge begins with a user-specified, 2D graph representing the spine of the bridge (Figure 87a). By default, all 1-valence vertices of the graph are assumed to represent the footings of the bridge. Subsequently, the graph is converted into a corresponding coarse mesh (Figure 87b). This is done by processing the vertices and half-edges of the graph to compute the vertex positions and face connectivity of coarse mesh (Van Mele, 2020a).

The coarse mesh is subsequently subdivided using the Catmull-Clark subdivision algorithm (Catmull, 1974) (Figure 87c). The subdivided mesh is interactively shaped into a global, compressive surface by manipulating the parameters of the so-called force-density method (Schek, 1974) (Figure 87d). Alternatively, the coarse mesh and the corresponding smooth, subdivided mesh can be interactively manipulated by the designer to be approximately arched 3D shapes. (Figure 87e & f). Subsequently, the mesh faces representing the balustrade arches are added by extruding the boundary edges (Figure 87g)

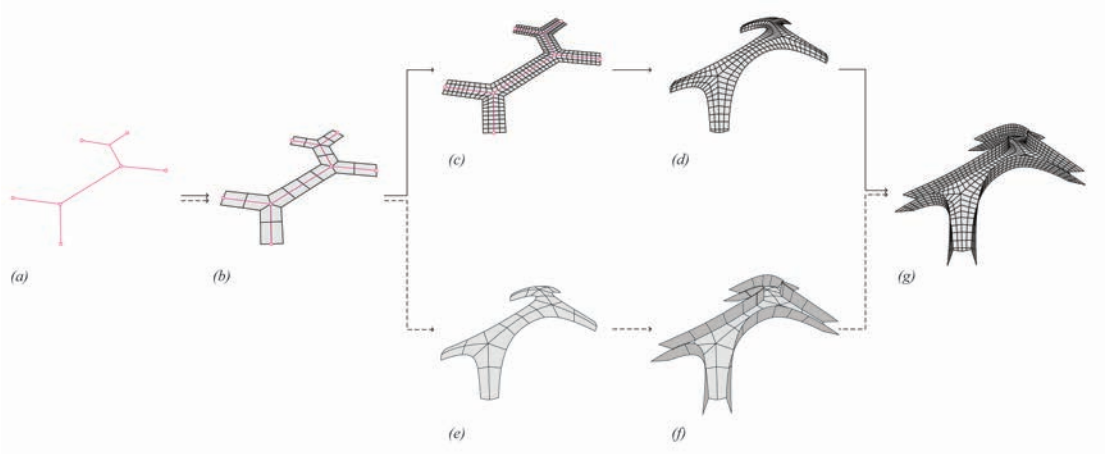

Figure 87 –Shape design. (a) 2D spine graph. (b) Coarse mesh. (c) Subdivision mesh. (d) Form found mesh. (e) Manipulated coarse mesh. (f) Subdivision mesh using the Catmull-Clark subdivision algorithm. (g) Guide mesh with balustrade for transmission via JSON format exchange file.

Both the 2D graph and the mesh are transmitted in the JSON-format exchange file. It can be noted that the procedural process of converting the graph into a coarse mesh and subsequently subdividing it, ensures that all the mesh vertices, half-edges and faces can be traced back to either a parent vertex

or half-edge of the input graph. This enables both interactive, associative editing of the 3D shape using the graph vertices as control handles and computing derivative information such as the stereotomy, as described next.

8.6 Stereotomy

First, the mesh is decomposed into patches of faces (Figure 88a-d). The half-edge data structure allows the original 2D graph to be traced on the 3D mesh as the spine of the bridge. The boundary edges of the balustrade faces can similarly be tracked as the spine of the balustrade faces (Figure 88a). Subsequently, we start at the 1-valence vertices of the spine, ’walk’ along the edges of each spine, and collect the faces attached to each edge (Figure 89a). The faces collected by this action, are grouped together for every four edges traversed on the spine (Figure 88b). The number of edges of the spine traversed per group of faces, four in this case, is called the stride of the ’walk’. The action is repeated for the balustrade arches, except the stride is offset by two at the beginning (Figure 88c). This creates a staggered set of patches along the deck and balustrade faces (Figure 88d). This procedure is closely related to the algorithm of two coloring of meshes. For more, see (Oval et al., 2018).

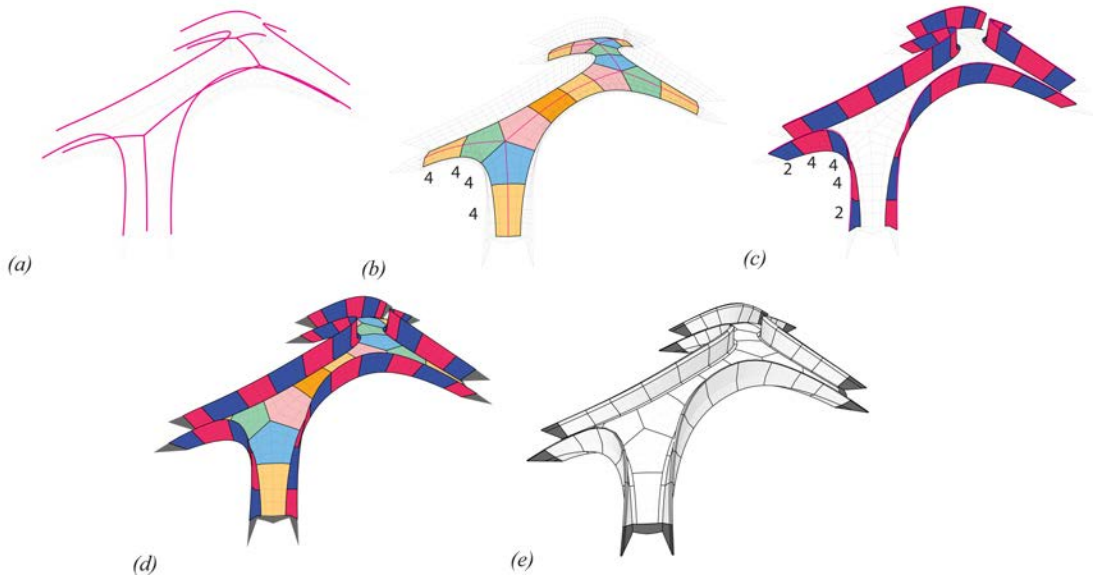

Figure 88 – Mesh two-colouring and stereotomy. (a) Spine edges for deck and balustrade. (b) Spine walk stride for deck. (c) Spine walk stride for balustrade. (d) Face coloured mesh. (e) Thickened mesh

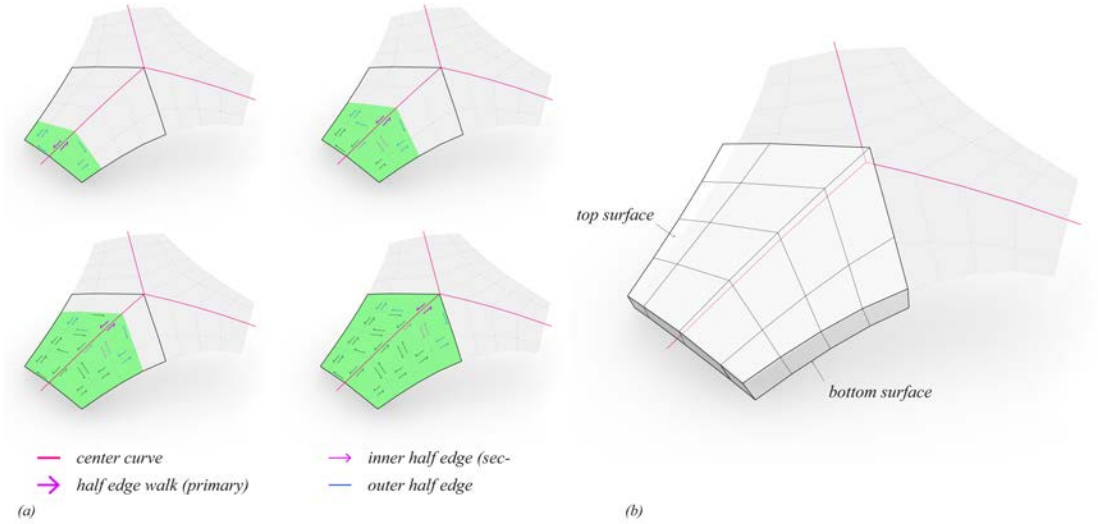

Figure 89 –Mesh walking. (a) Mesh walks on spine and block face collections using the half edge data structure. (b) Boundary representation of the solid voussoirs.

The user-specified graph and the mesh derived from it serve as the inputs to compute the stereotomy or the discretisation of the mesh surface of the bridge into 3D blocks. The boundary edges of each patch of faces are extruded on both sides of the mesh surface to create the boundary representation of the solid voussoirs (Figure 88e and Figure 89b). The normal associated with each of constituent vertices is used for this operation. These additional stereotomy related information of each block is inserted into the JSON transmission file using the schema in Figure 90.

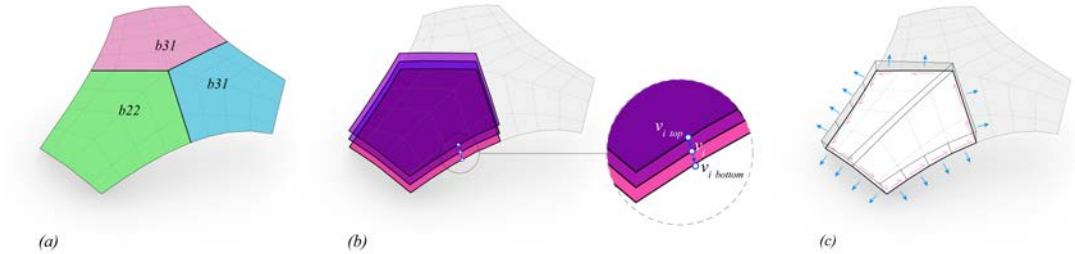

Figure 90 – JSON attributes & schema added in the stereotomy step. (a) block attribute stored as face colour, (b) thickness attribute storing corresponding vertex position of top $\boldsymbol{v}_{itop}$ and bottom $\boldsymbol{v}_{ibottom}$ per vertex v_i, (c) interface plane attribute storing plane origin $\mathbf{o}_i$ and normal $\mathbf{pn}_i$ per half-edge he_i

8.6.1 Block interface planarization

The faces that represent the interface between the blocks are not planar after the block creation process described above (Figure 91a). These are planarized (Figure 91b) using a so-called perturbation procedure (Bhooshan et al., 2015; Poranne et al., 2013)(Figure 92). The DEM step of the structural thread (Section 8.9.2) updates the normal of the block interfaces and the thickness of each block, as deemed necessary by structural analysis. The information of each block is inserted into the JSON transmission file using the schema in Figure 90. This completes the stereotomy of the bridge.

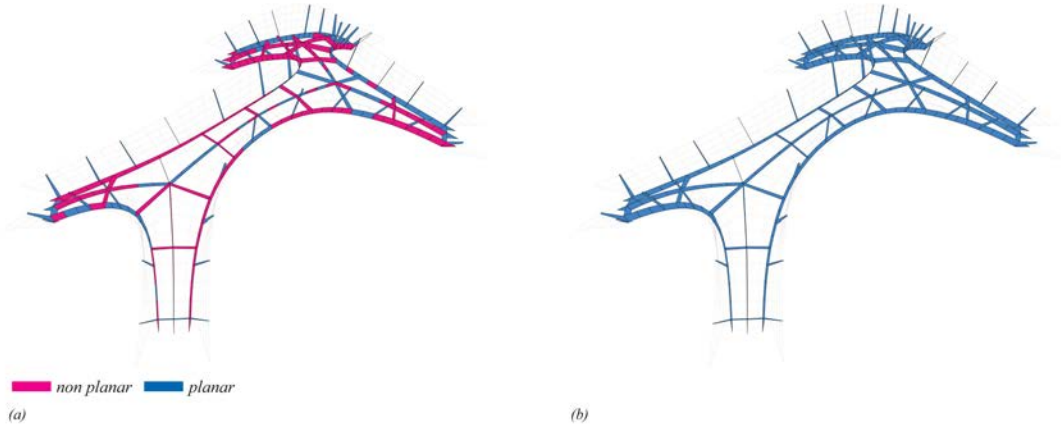

Figure 91 – Block interface planarization. (a) Block interface planes before and (b) after the perturbation procedure for planarization

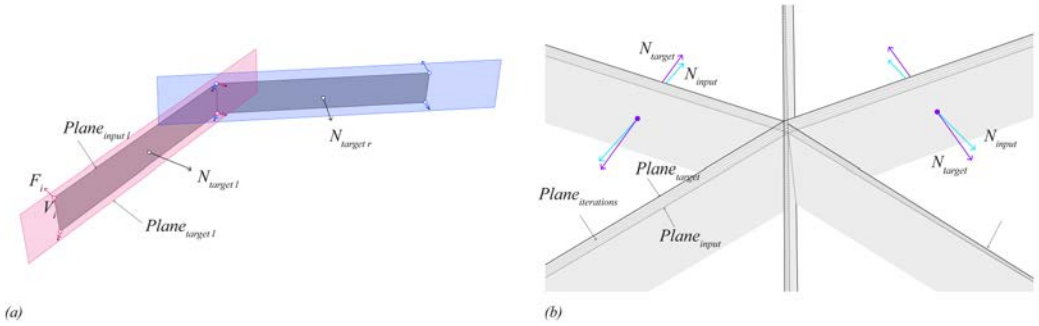

Figure 92 – Details of planarization of block interface faces. (a) Computing of the projection-based perturbation force $\boldsymbol{F}_i$ per vertex v_i of the interface planes -$Plane_{input}$, N_{input} - to make them planar using the best-fit target planes - $Plane_{target}$, N_{target}. (b) Showing the iterative steps ($Plane_{iterations}$) of the solver for 6 interface planes.

8.7 Print-path synthesis

The planarized block interface planes (Figure 91b) structurally verified 3D blocks (Figure 88e), the spines of the deck and balustrade arches (Figure 88a) are the input information needed to create the print-paths per block. Each block has a start and an end plane determined and assigned by the direction of the spine. First, the start and end planes are smoothly interpolated to create new planes (Figure 93) and subsequently a print-path is generated on each of the interpolated planes using signed distance functions and the interpolation schema described in Chapter 5.

8.7.1 Plane interpolation

The spine of edges associated with each block is subdivided at equal distances. New planes, centred at each of the subdivided points, are then generated (Figure 93). The normals of the planes are computed by interpolating between the start and end planes. A weighted non-linear interpolation scheme was implemented to optimise and ensure that the print height between subsequent plane lies within the domain specified by the robotic printing constraint (see Chapter 9 for more).

It can be noted that all the deck blocks have two sets of start and end planes – a left (Figure 94a) and right set (Figure 94b). Consequently, there are two sets of interpolated planes. All the print-paths on the left and right set of planes are first computed separately and merged in a post-processing step (Figure 109). The balustrade blocks are simple, consisting of only one set.

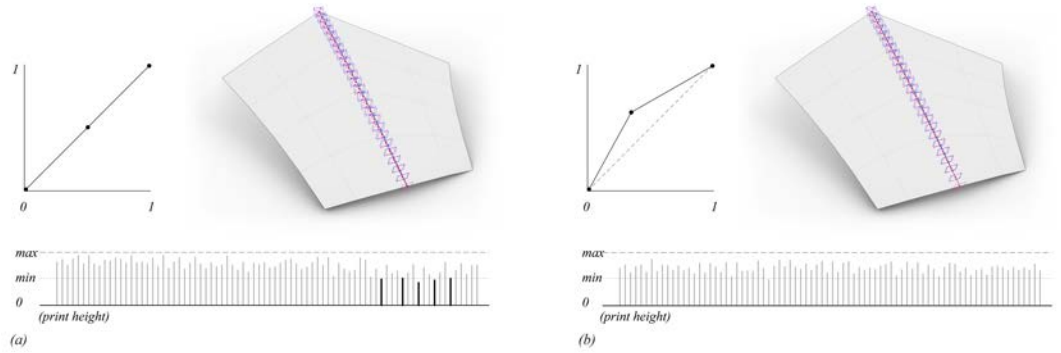

Figure 93 – Interpolation schemes to compute new planes between the start and end planes. (a) Linear interpolation scheme highlighting some print height is below the minimum printing height. (b) Optimised weighted non-linear interpolation scheme to ensure all print heights lie in the specified printing height domain.

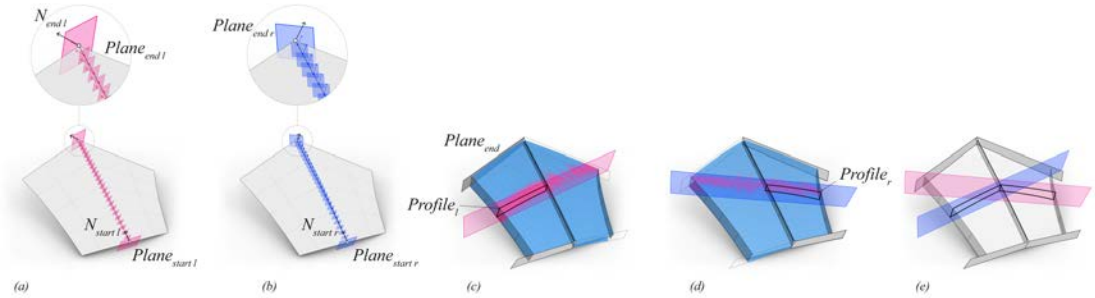

Figure 94 – Print plane interpolation. (a) Left Planes interpolated between start & end planes - P_{sl}, P_{el}. (b) Right planes interpolated between start & end planes - P_{sr}, P_{er}. (c) Example left plane profile generation. (d) Corresponding right plane profile generation. (e) Combined left and right profiles.

8.7.2 Cross section interpolation

Next, a base cross-sectional profile is computed for the start, end, and newly generated interpolated planes (Figure 94c-e). The base cross-sectional profile curve for each of the planes is computed as the intersection of the plane and block mesh (Figure 94e). After this, using the base profile curve as a discrete, contiguous graph, five other SDFs are created on each of the interpolated planes to generate a compound cross-sectional profile (Figure 95a-e). The resultant SDF (Figure 95f) is constituted as the Boolean of five individual SDFs. Together, this step creates two sets of profile curves for the left and right planes, respectively for the masonry blocks that are to be 3D concrete printed. Specific details are expanded in Chapter 9.

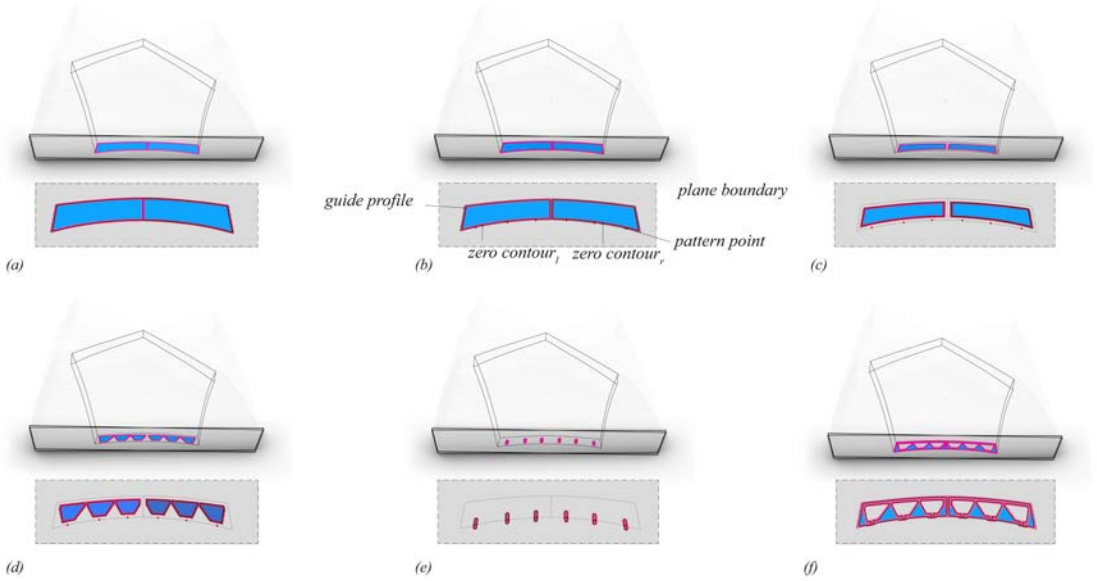

Figure 95 – SDFs for deck blocks. (a) Base cross-sectional profile, polygonal SDF. (b) Offset polygonal SDF. (c) Offset polygonal SDF. (d) Infill SDF. (e) Trim SDF. (f) Resultant SDF

8.8 Post processing

Lastly, the left and right sets of cross-sectional curves are post-processed and prepared for printing (Figure 96b). The artefacts created without appropriate post-processing can be noticed in Figure 96c and its fixes with appropriate post processing in Figure 96d.

8.9 Structural thread of DTP toolchain

Interleaved between each of the three main processing steps of the serial thread of the DTP are three parallel, corresponding, structural analysis and verification threads.

8.9.1 Best-fit TNA

This structural evaluation thread takes the mesh surface as output from the shape design step of the serial thread (Figure 81c) and computes the nearest compression-only surface using the so-called best-fit Thrust Network Analysis (TNA) algorithm (Lachauer and Block, 2014) (Figure 97). This thread then updates the positions of the vertices of the user-designed mesh surface and retains all the topological information. This thread may be skipped if the shape design includes a compression form finding step or already has a reference, compression-only surface to inform the shape manipulation.

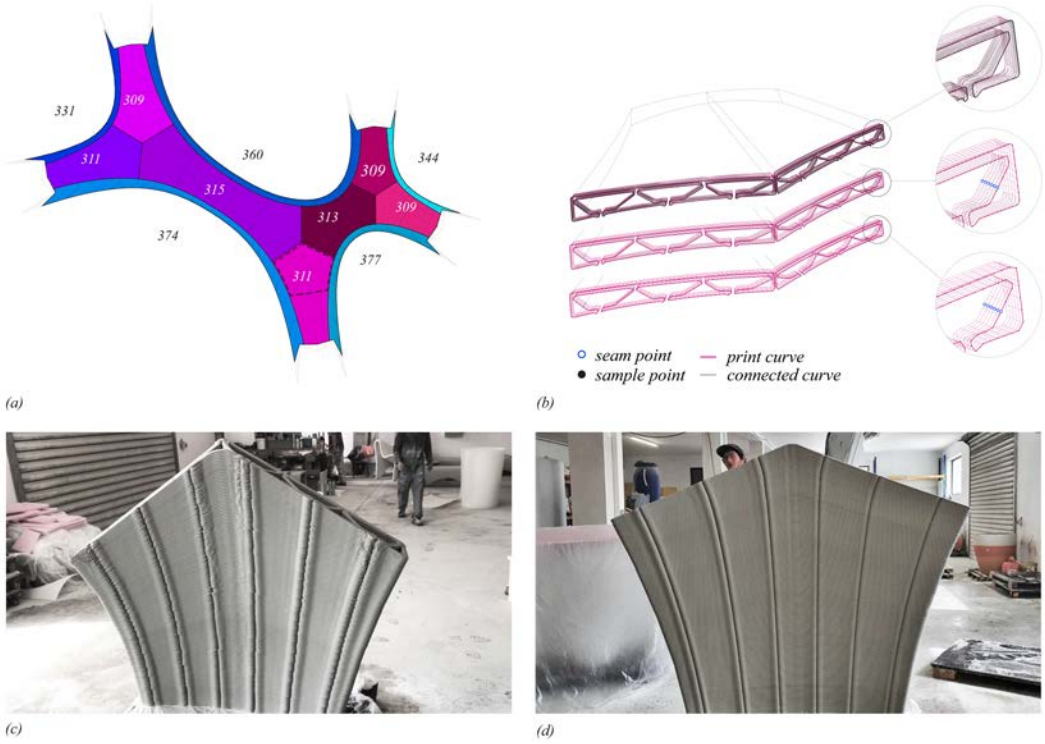

Figure 96 – Post processing of print-paths. Re-sampling of cross section profiles of the previous step (Figure 95) to make it amenable to robotic print constraints such as spacing and maximum number of points. (a) Key map showing the number of re-sampling points per block sequence. (b) Various re-sampling strategies tested on the contours: un-resampled print profile (top), distance-based resampling (middle) and adaptive feature-based resampling (bottom). (c,d) 3DCP result from uniform and adaptive feature-based resampling respectively.

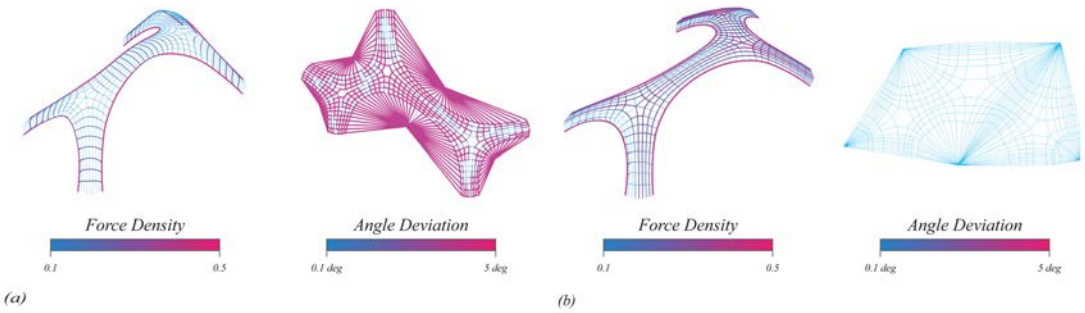

Figure 97 – Iterative solver for best-fit thrust network analysis (TNA), showing the form and force diagram. (a) Iteration 1. (b) Final iteration

8.9.2 DEM analysis

This thread receives the stereotomy or the discretised 3D blocks from the serial thread, and performs various analyses to determine structural stability, mechanics etc., (Figure 98). Discrete-element modelling (DEM) is the primary tool used to perform these analyses to evaluate structural performance such as response to loading, differential settlements of the footings, etc. This thread then updates both the normals of the interface planes between blocks (Figure 91 and Figure 92), and the thickness of each block to define the so-called intrados and extrados, which are the bottom and

top surfaces, respectively, of each voussoir (Figure 88e). This thread also informs the foundation and tension-tie design threads (Section 8.1).

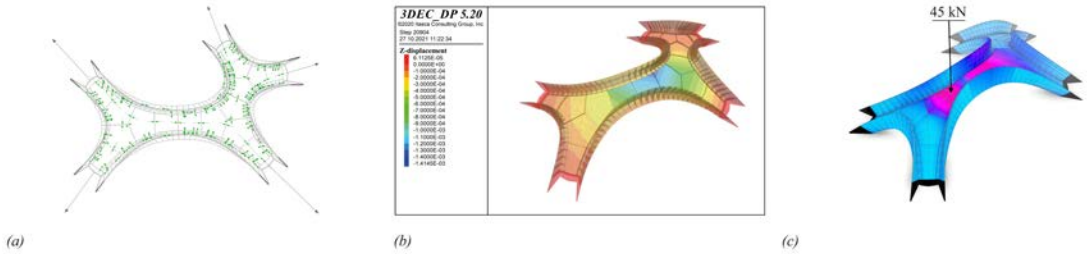

Figure 98 – Discrete element modelling. (a) Resultant force vectors at interface planes. (b) 3Dec Analysis. (c) example of a point-load test.

8.9.3 FEM analysis

This thread performs local structural evaluation on the various cross-sectional profiles generated by the print-synthesis step of the serial thread. These analyses are performed using Finite-element modelling (FEM) and inform cross-sectional design parameters such as width of the print, maximum spacing between stiffeners, overall cross-sectional depth, etc (Figure 99 and Figure 100). It can be noted that these analyses are performed only on representative cross sections in the deck and balustrade arches.

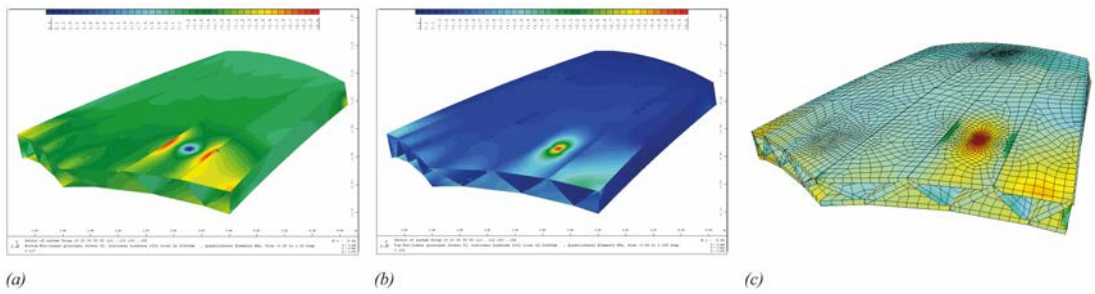

Figure 99 – Finite element modelling and analysis.

8.10 Material and prototyping thread of DTP toolchain

Inclined-plane printing is a new capacity in 3D concrete printing. The so-called two-component (2K) mortar formulation and printing setup needed for enable such inclined-plane, variable thickness printing is in rapid development. As such, this thread of the DTP was necessary for the physical realisation of the bridge. In the future, as the concrete characterization and the geometrical limits of the technology are better established, this thread may not be necessary.

Tector 3D Build cement was used for the 3D concrete printing (Holcim, 2021). However, several novel, proprietary formulations were developed and tried specifically for the project. Through several printing tests (Figure 100), geometrical limits such as the maximum inclination of a print plane, maximum and minimum thickness of a print layer (i.e., the layer height), minimum and maximum width of printed filament (i.e., the layer width) etc. were established (Figure 101a,b). The first two parameters of inclination and layer height impose angular limitations on the block

planarization step (Section 8.6.1) and the distance between planes in the plane-interpolation step of the serial thread, respectively (Section 8.7.1). The layer-width parameter, as empirically established, informs the cross-section design (Section 8.7.2).

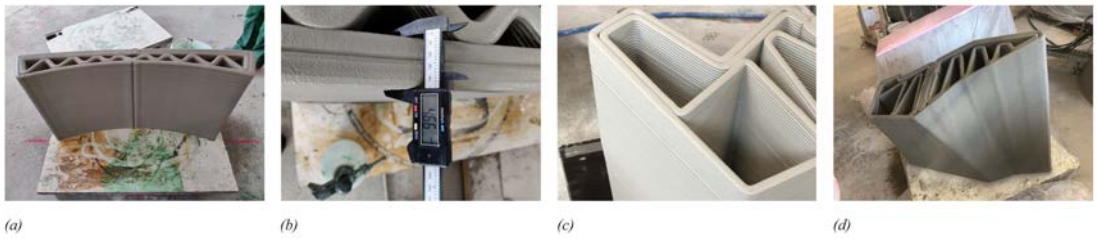

Figure 100 – Material testing and prototyping. (a,b) establishing Minimum and maximum for layer-height and print wdiths respectively. (c,d) Close-up views of the cross-sectional infill on a inclined-plane-printed block.

8.11 Printing, construction, and assembly

The print-path synthesis step of the DTP outputs a print file per block. The file contains information about the position of every vertex of the print-path curve and the normal of the plane it sits on. This information dictates the path that the print head will traverse to deposit material filaments. The positional and orientation information was converted into ABB-robot specific instructions. Proprietary printing-specific information such as pump rate, velocity control etc. were additionally included at this stage. See Chapter 9 for more.

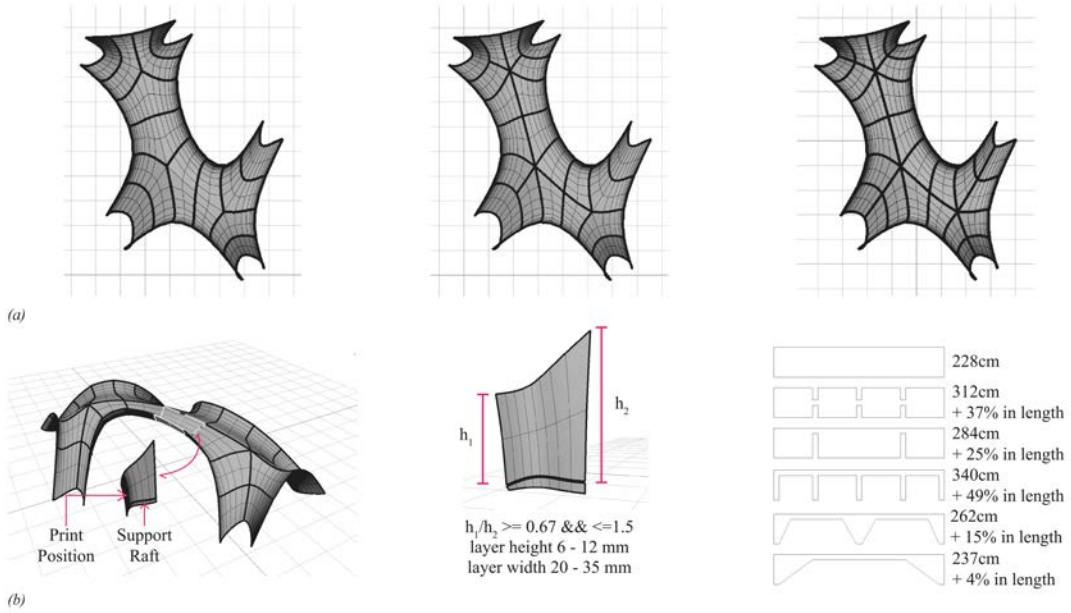

Figure 101 – Translation of material and prototyping tests to geometric constraints. (a) Initial sketches for a stereotomy strategy based on print constraints. (b) Print recommendations for block orientation, layer height and width, and material calculation with various infill patterns.

The structural design of the contact interfaces between the blocks assumed good contact and transfer of force across the interface. In the physically realised bridge, this was achieved by:

- placing at the bottom plane of each block a smooth plastic foil that separates the interface plane and the sacrificial raft that is printed to level out any imperfections in the print bed (Figure 103a).
- slightly sanding off the top plane of each plane; and,
- insertion of neoprene pads between blocks. The neoprene material has a much lower Young's modulus than the concrete offering a distribution of stress concentrations caused by interface irregularities. This strategy is similar to the traditional use of e.g., lead sheets in hard stone setting. Additionally, the friction properties of the neoprene-to-concrete interface could be quantified, and thus used in the engineering.

All constituent blocks of the bridge were produced using this DTP workflow and the resultant output files. In total, 53 blocks consisting of 7883 print planes and 58 kilometres of print-path were 3D-concrete-printed in approximately 84 hours by one 6-DOF robot. The blocks weighed between 200 and 800 Kilograms each, and the total weight of all 3DCP blocks was approximately 24.5 tonnes (Figure 102). In addition to the robotically 3DCP blocks, timber falsework and steel supports were produced by Computer Numerically Controlled (CNC) machines. The manufacturing information and construction drawings for the timber falsework, steel footings, tension ties and for the foundation were produced by the ancillary threads of the DTP toolchain (Section 8.1).

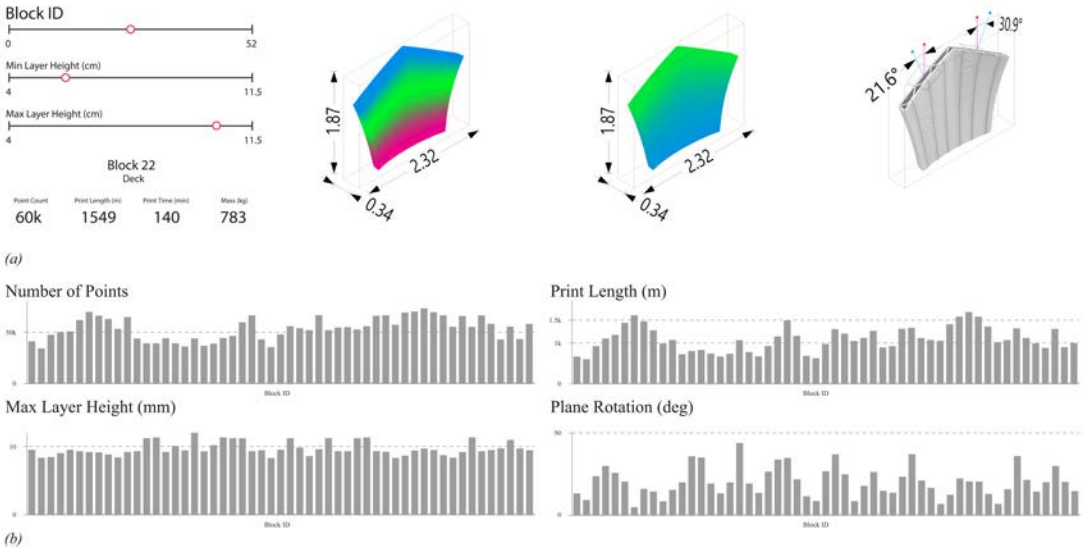

Figure 102 – data visualisations of (a) individual block metrics showing variation of print layer heights through the blocks, the print bounds, angle deviation between start and end plane, total number of points etc & (b) metrics for all 53 blocks.

The three main components of the bridge were then transported to site. The foundations, the steel footings and tension ties were first poured and installed. The timber falsework was then assembled. The printed blocks were subsequently assembled on top of the falsework – first, the deck blocks and then balustrade arches. In each case, the sequence of assembly was to start at the bottom of each of the deck or balustrade arch and proceed towards the keystones. Once all the blocks were assembled, the falsework was sequentially lowered until the blocks were fully structurally engaged (Figure 103). The construction and assembly processes used is similar to the one used for the precedent Armadillo

project (Block et al., 2018). The on-site manoeuvring and assembly of the 53 blocks required only one lightweight spider crane and a five-person construction team. The on-site construction and assembly spanned 35 days, including force-majeure logistical delays and full stoppage for approximately two weeks. The resulting, unreinforced masonry, 3D-concrete-printed bridge structure had a span of 16 meters.

Figure 103 – Printing, construction, and assembly. (a) 3D printing of block. (b) Preparation for transportation. (c,d,e) Transportation and storage on site. (f) Erection of scaffold. (g) Placement of deck blocks. (h) Placement of key stone balustrade block.

9 PRINT-PATH DESIGN FOR INCLINED-PLANE 3D CONCRETE PRINTING

The application and extension of the computational framework described in Chapter 4, into a design-to-production workflow for the execution of the Striatus footbridge technology demonstrator project was described in Chapter 8. In a similar vein, this chapter describes the full implementation of the print plane and print-path interpolation schema described in Chapter 5, for the large-batch production of 3DCP masonry blocks of Striatus (Figure 104). Additionally, specific extensions to visualize the toolpaths at design-time, achieve expressive textures in the printed blocks, and generate the infill print-paths and post- processing routines to alleviate print-time issues are also described.

Figure 104 – Print-path synthesis-to-manufacturing. (a) Print-path generation using function representation (FRep). (b) Post processing of print-paths. (c) Evaluation of printability & generation of machine code. (d) Robotic 3d Concrete Printing (3DCP) of blocks. (e) Assembly process. (f) Finished bridge.

9.1 Path synthesis-to-manufacture workflow

The printed concrete filaments of each block of Striatus, were placed in layers that are orthogonal to the expected, compressive force flow, resulting in the need for non-parallel, inclined print-path planes, thus also resulting in non-uniform print-layer heights. In addition, the bridge's global structural logic of stereotomic masonry necessitated the precise coordination of the interface planes between blocks. Approximately 58 kilometers of print-path, distributed over 7800 inclined layers, were generated, and coordinated with the resulting print-paths meet printing-related criteria such as good spatial coherence, minimum and maximum layer thickness, infill patterns etc. The print files generated were used to robotically print the 53 blocks in 85 hours.

The custom workflow and tools that were developed to synthesise printing paths and to batch manufacture the blocks, enabled:

- integration of print-path synthesis within the interactive and iterative design cycles.
- synthesis of print-paths aligned orthogonal to expected, compressive force flow; and

- coordinated, large-batch production of 53 blocks with negligible tolerance errors at the interface planes, which meant that the blocks were easily assembled on site into the global form.

9.2 Print-path synthesis to production

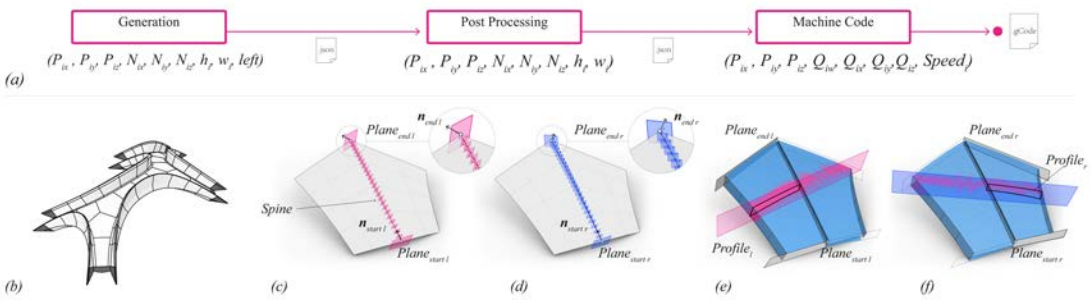

Figure 105 – Print-path synthesis. (a) Workflow diagram for print-path synthesis to production. (b) Global shape with stereotomy. (c,d) left & right planes interpolated between start (P_{sl}, P_{sr}) & end planes (P_{el}, P_{er}). (e,f) Base cross section profile.

Given a global compressive shape and the associated stereotomy (Figure 105b), three main steps follow: generation of the print-paths, their preparation for print readiness (post-processing) and the generation of robotic instructions or so-called GCode (machine code generation) (Figure 105a & Figure 104a-c). Information is passed from one encapsulated step into the next using a simple text-based file format that encodes information using the JavaScript Object Notation (JSON).

9.3 Print-path generation

The interface planes and spines of the 3D masonry blocks of deck and balustrade of the footbridge (Figure 105c,d) are the input information needed to create the print-paths per block. Each block has a start and an end plane.

9.3.1 Print plane interpolation

The spine of edges associated with each block is subdivided at equal input distances set as the mean of the minimum and maximum print layer height permissible. New planes, going through each of the subdivided points, are then generated (Figure 105c,d). The normals of the planes ($\boldsymbol{n}_i$) are computed by interpolating between the start ($\boldsymbol{n}_{start}$) and end ($\boldsymbol{n}_{end}$) planes, using a weighting factor (w_i).

$$\boldsymbol{n}_i = (1 - w_i) * \boldsymbol{n}_{start} + w_i * \boldsymbol{n}_{end}; \text{ where } w_i = (0.0, 1.0)$$

A weighted nonlinear interpolation scheme was implemented to ensure that the print height between subsequent planes lies within the domain specified by the robotic printing constraint (see section 9.6). It can be noted that, because of the bifurcating topology of the bridge, all the deck blocks have two sets of start and end planes – a left and right set. Consequently, there are two sets of interpolated planes (Figure 105e,f). The balustrade blocks consist of only one set.

9.3.2 Print profile generation

Next, for each of the interpolated planes, a cross-sectional profile was computed as the intersection of the plane with the block geometry. This profile curve is represented as a discrete polygonal graph. It is then used to generate a signed distance field (SDF) in relation to the edges of profile curve/graph (Figure 106e,f). The base profile graph is also used to create additional graph based SDFs on the interpolated planes to generate compound cross-sectional profile. All SDFs are created using the primitive operations described in 4.4.1.

For both the deck & balustrade blocks, there are 5 constituent SDFs (Figure 106 and Figure 107), each serving a specific purpose:

- base profile SDF f_0 to capture the intrados and extrados of the block (Figure 106b and Figure 107b).
- two boundary SDFs (f_1, f_2) to control the cross-sectional thicknesses based on specified print width & f_0 (Figure 106 c,d and Figure 107c,d)
- infill SDF (f_3) to provide local stiffeners in each cross section (Figure 106e and Figure 107e); and
- trim SDF (f4), at pattern points, aiding in the creation of one continuous print profile (Figure 106f and Figure 107f)

The resulting compound cross-section is defined as the set-theoretic Boolean of the 5 SDFS

$$f_{result} = (f_1 - (f_2 - f_3)) - f_4.$$

The combination of individual SDFs to compose the final print-path allowed the accommodation and fine control of discoveries made during the material and prototyping phase (Section 9.7). For example, the visible ribs in the blocks (Figure 108 d,e) were developed as a separate SDF after it was discovered that the turning of the robot-head necessitates a reduction of angular velocity which in turn produces a naturally occurring grove (Figure 114 c,d)

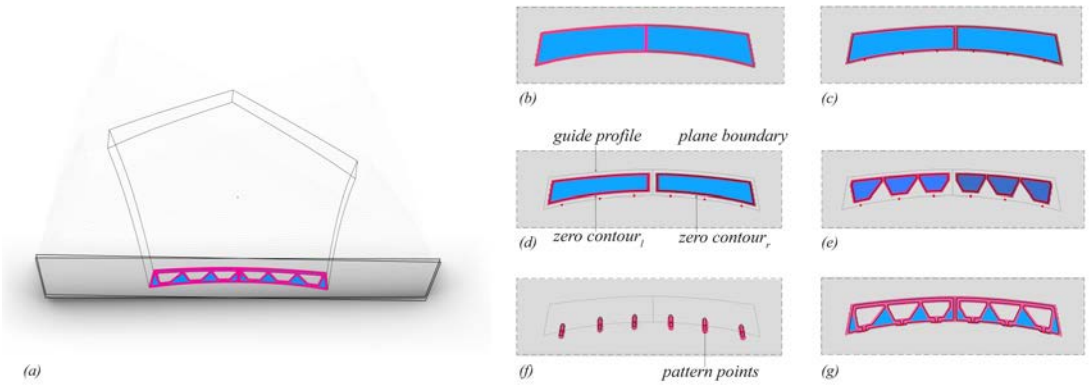

Figure 106 – Print profile generation. (a,g) The resultant SDF (f_{result}) representing the compound cross-sectional print-path. f_{result} is constituted as the Boolean of five individual SDFs (b-f).

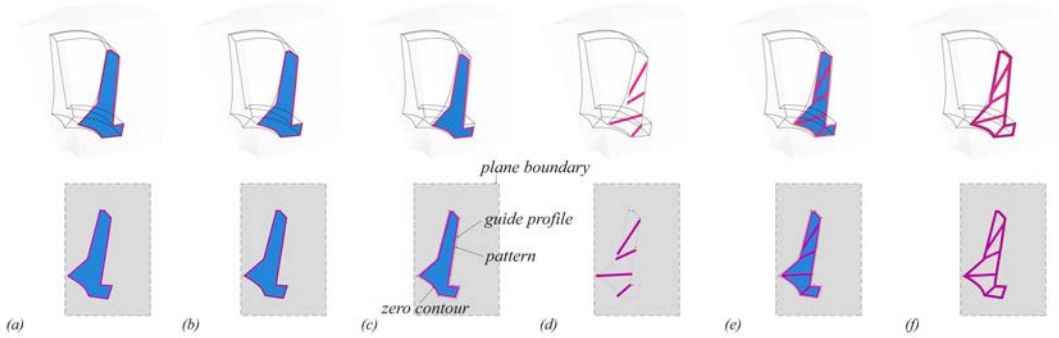

Figure 107 – SDFs for balustrade blocks. (a) Base profile polygonal SDF f_0. (b) Offset polygonal SDF f_1. (c) Offset polygonal SDF f_2. (d) Infill SDF f_3. (e) Trim SDF f_4. (f) Resultant SDF f_5.

Together, this step creates two sets of profile curves for the left and right planes respectively for the deck blocks and a single set for the balustrade blocks. All the print-paths on the left and right set of planes of the deck blocks are combined in the next post-processing step.

9.4 Post Processing

The resulting SDF contours generated from the previous step are polylines. The number of points and segments in each of the curves (sampling) depends on the cell size used in computing the SDF (Figure 108a). The sampling of the curve is a critical parameter in 3D printing, as it affects the speed and interpolated trajectory of the robot head and thus the deposition of concrete. As such, the contour curves need to be resampled.

Two resampling methods were tested: uniform resampling and feature-based adaptive resampling (Figure 108b and Figure 108c). Uniform resampling rebuilds the input curve with even spacing of the points (Figure 108b). Whilst this method successfully reduces the number of control points to be lower than the robot constraint (60,000 target points), it can cause misalignment of the points of the paths in consecutive layers, and thus artefacts to appear in the printed blocks (Figure 108d). Feature-based adaptive resampling splits the input curves into a set of individual segments based on feature points (Figure 108c and Figure 109). The segments are then uniformly resampled. The position of the feature point is spatially coherent across consecutive printing layers (Figure 109a). Consequently, the occurrence of artefacts in the printed blocks is significantly reduced (Figure 108f). Additionally, this method allows adaptive sampling - the sampling can be lower in the areas that do not necessitate high-quality finish, such as internal infills, and higher in areas which need a higher finish, such as visible faces of the blocks.

Resampled sets of contours are further processed to generate a single continuous printing path for each of the blocks.

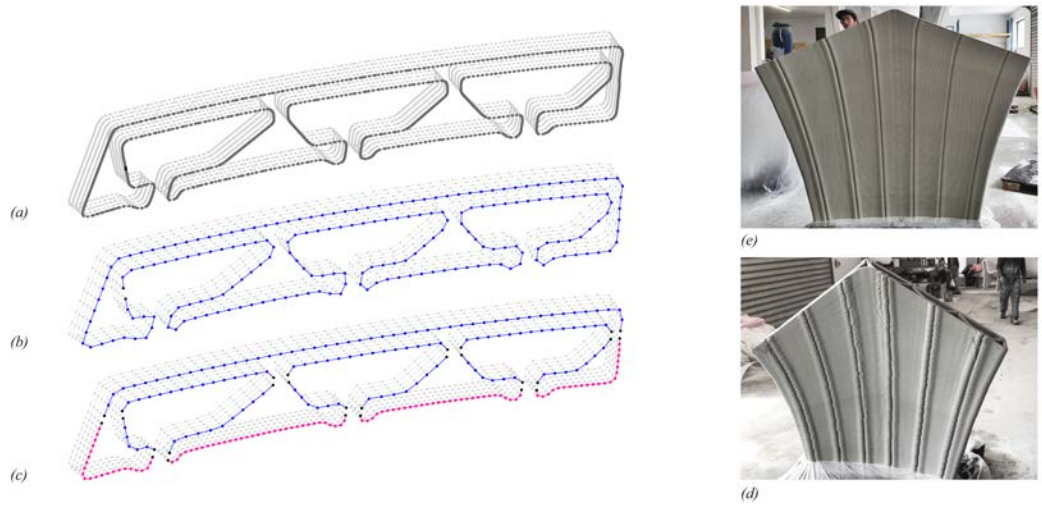

Figure 108 – Printing paths sampling. (a) Print-path synthesis from SDFs. (b) Uniform resampling. (c) Adaptive feature-based resampling. (d,e) Result of the printing uniform and adaptive feature-based resampling print-paths, respectively.

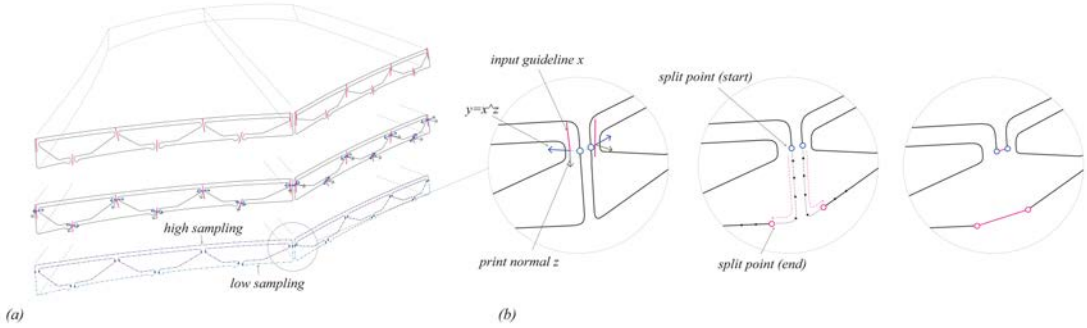

Figure 109 – Adaptive resampling. (a) Adaptive sampling of cross section profiles based on feature points. The feature point is computed as the nearest intersection of vector $\boldsymbol{y_i}$ with the cross-section profile, where $\boldsymbol{y}$ is the cross product of input guide vector $\boldsymbol{x_i}$ and the plane normal $\boldsymbol{z}$. The cross-section profiles are split at these feature point to maintain alignment with the planes below and the individual segments are sampled using adaptive distances - low sampling distance for segments on the outside and higher sampling distance for the internal parts of the block. (b) Procedure to connect the left and right cross section profiles to create one continuous print-path

9.5 Contiguous Print-paths

Resampled sets of contours are further processed to generate a single continuous printing path for each of the blocks (Figure 110). This is achieved in two steps: First, the left and right curves of each layer are connected by splitting the curves based on an input guideline curve (*gL* and *gR* for left and right path respectively) and then reconnecting the left and right paths with two straight segments (pt_1-pt_2 and pt_3-pt_4). The guideline curves are generated for every layer to have a consistent reference position at the inner upper corner of each path (L_1 and R_1). Next, consecutive layers are connected into a continuous spiralling path connecting the end of each layer path to the start of the next (Figure 110c).

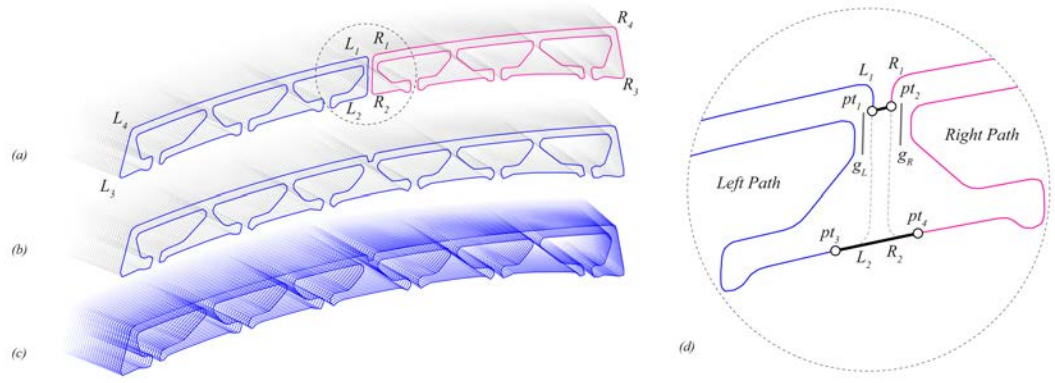

Figure 110 – Generation of continuous printing path. (a) Left and right contours. (b) Connected layer. (c) Spiralling path. (d) Sequence for the connection of the left and right paths.

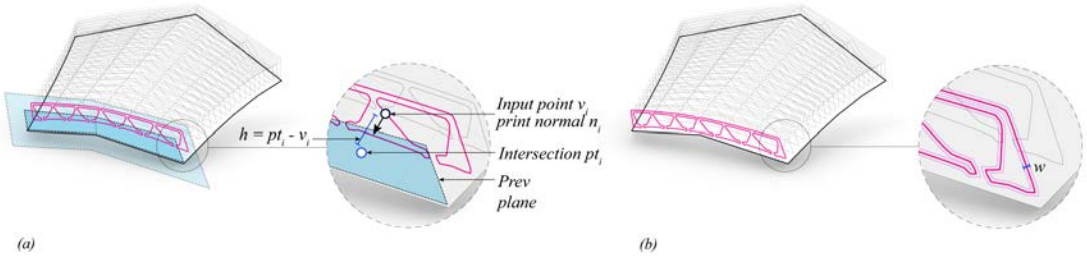

Figure 111 – JSON attributes & schema added in the print-path synthesis step. (a) List storing per vertex of the print contour, the position $\boldsymbol{v}_i$, print normal $\boldsymbol{n}_i$, print height h_i. print height is computed as distance between $\boldsymbol{v}_i$ and the intersection point $\boldsymbol{pt}_i$ of ray $\boldsymbol{n}_i$ with the previous print plane. (b) Specified print width w_i.

The information required to 3D print each block is inserted into the JSON transmission file using the schema in Figure 111 and is subsequently parsed to generate the machine code.

9.6 Machine Code Generation

Each block to be 3D printed is represented by one contiguous, spiralling curve as generated by the previous step (input path file). This file is further processed to generate the robotic instructions or so-called GCode, to print the block. As a quality check, a validation was performed by simulating and tracing the robot path as produced by the GCode (output path file). Both the input path file and output path file were meshed to visualise the tubular print layers. The two meshes were aligned and visually checked for deviation.

9.6.1 Raft generation

The print sequence of a single block consists of two steps: establishing a planar basis and printing the block. Thus, the final path includes base layers that are not part of the block called the Raft. The Raft levels out any unevenness in the print bed and ensures precise interfaces between blocks. A plastic sheet was inserted mid-print, to separate the raft from the actual block. The raft is additionally used to establish stable print orientations for all the blocks. In other words, the raft layers are used to print a plinth that aligns the blocks in an appropriate orientation to improves printability (Figure 112a).In particular, thin deck blocks and balustrade keystones would collapse during the print

without this correction, as the centre of gravity of the blocks would fall outside the block geometry in the original orientation.

Two approaches were tested for the orientation correction of the block (Figure 112b) – so-called geometric and centre-of-gravity transformations. In the former, the block is realigned such that the axis passing through the centre of the print-curves in the first layer and the last layer, coincides with the vertical axis. In the latter, the axis passing through the centre of print-curves in the first layer and the centre of gravity of the entire block, is used as the reference axis to perform the reorientation. The latter solution proved to be a good compromise between vertical alignment of the block and the inclination of the plinth itself.

9.6.2 Assigning robot speed

Next, a speed variable (*robot target speed*) was computed per point in the print-path, using the parameters l_w and l_h which represent the width and height of the printed extrusion (Figure 113). The speed variable in effect controls the volume of the tubular print layers, as it affects volume of material deposition at every local segment of the path, centred around target points on the print-path. The depth of the print layer is determined automatically since the width and height are already defined in the input path file. Together, the points on the print-path, the normal of the print plane, and speed variable are compiled into GCode, which is then used to print the block. This software solution significantly reduces hardware complexity.

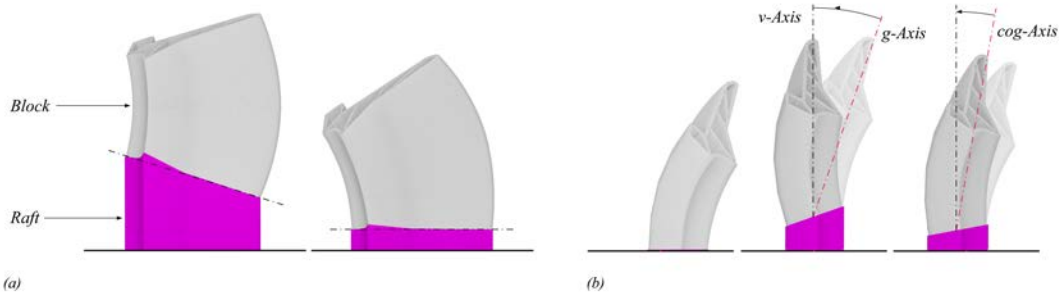

Figure 112 – Block reorientation for printing. (a) Horizontally aligned unstable axis of base layer (right), to correct reorientation axis and to minimise raft (magenta). (b) Rotation around unstable axis: alignment along centre of gravity axis avoids slipping between block and raft as well as providing a stable print position.

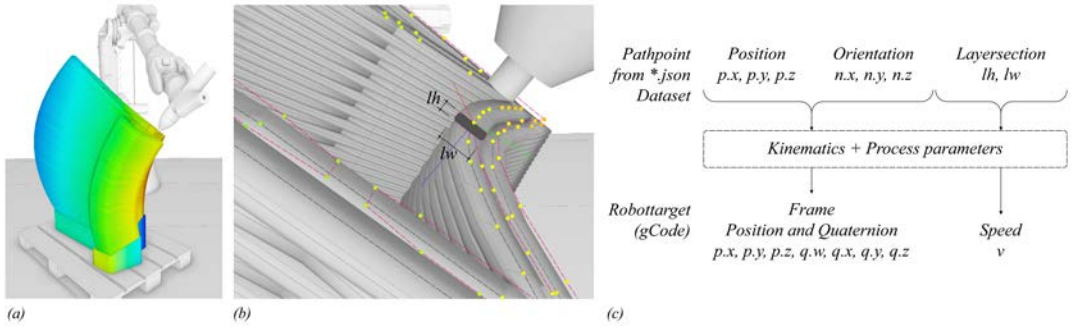

Figure 113 – Kinematic simulation with colour indication of print speeds. (a) via mesh color and (b) via so-called Robot Targets. (c) Per print point layer, dimensions *lw* and *lh* are transformed into speed settings for each robot target, along with common kinematic parameters.

9.7 Material Tests and Prototyping

Preliminary print tests addressed material processing, quality, curing time and the definition of minimum and maximum limits for the layer heights, which is critical for the print-path generation as described previously (Section 9.2) (Figure 114). These parameters affect the actual print speed in relation to the material flow rate. These details were defined by multiple print-tests that mostly consisted of block prototypes, which allowed developing an efficient workflow between the collaborating parties. As a result, two basic settings for deck and balustrade blocks were defined: a lower pump rate for the balustrade blocks to address the reduced wall thickness and delicate details, and a higher flow rate to allow an efficient production of the deck blocks.

Figure 114 – Material tests and prototyping. (a) Path and infill tests. (b) Defining material and processing parameters for consistency. (c,d) Learnings had been reintroduced for the final design, most relevant being the seam details for the deck blocks.

Figure 115 – Photo of the finished project on site, Giardini della Marinaressa, Venice, Italy. Photographs by naaro ©

9.8 Generalization

In summary, the custom toolchain that was developed enables print-path synthesis, verification, and generation of robotic instructions or so-called GCode. The toolchain and the constituent, standalone applets were designed to be easy to implement, fast to execute, and enable rapid iteration and refinement, whilst being free of external dependencies. Together, the toolkit provides a blueprint for real-time, printing-aware, interactive shape design. Furthermore, the print-path design detailed in this chapter had a significant role in the realisation of Striatus, an unreinforced masonry arched footbridge (Figure 115). Striatus articulates the relevance of unreinforced masonry design to both achieve a sustainable use of concrete and realise the benefits of 3D concrete printing (3DCP). Striatus thus demonstrates a practical pathway to design and construct bridge structures that are repair, reuse and recycling friendly.

PART IV - CONCLUSIONS

10 DISCUSSION

The research in this dissertation, as exemplified by the physically realised technology demonstrator – Striatus (Figure 116), benefits from the rapid evolution and simultaneous maturation of three contributing streams:

(i) **Computational masonry** (Section 3.3), rejuvenated by the advent of Thrust Network Analysis (Block, 2009), the development of rhinoVault (Rippmann, 2012), the extensive PhD thesis of Mattias Rippman(Rippmann, 2016), Armadillo technology demonstrator project (Block et al., 2018), the assimilation of the field-tested state-of-the-art into *Shell structures for Architecture* (Adriaenssens et al., 2014), and further unto COMPAS framework(van Mele et al., 2017).

(ii) **Architectural Geometry and Tectonism** (Section 1.2), bringing a keen focus on the edit-observe paradigm of shape design, mesh modelling environments, and an increased appetite for the greater degrees of problem-solving, expressive freedom and the didactic tools, that is associated with this common language of geometry (Pottmann, 2010, 2007; Schumacher, 2018, 2017). The unifying effect engenders a congenial and positive feedback loop between computational design and research (Bhooshan, 2017, 2016a, 2016c).

(iii) **3D Concrete Printing** (3DCP) technologies including fabrication workflows compatible with the geometric approach to design, sophistication in the material engineering of the ink, the prior experience and evolving expertise of logistics, assembly, and construction teams (Section 8.10, 8.11, 9.6, Chapter 11) etc.

Figure 116 – Striatus, an arched unreinforced masonry footbridge. Photograph by Shajay Bhooshan ©

10.1 Summaries

The intellectual and technical maturation across the three domains mentioned above, provided resources for the research herein to summarily extend into insightful and practice-relevant contributions (Section 1.7). These contributions structure the three parts of the dissertation:

(i) **Part I - Framing and context.** Chapters 1, 2, and 3 contextualize the novel insight on the synergies between 3DCP and unreinforced masonry. The insight is further unfolded into an argument for Sustainable Digital Concrete (SDC). SDC proposes the geometric, didactic and collaboration friendly tools of masonry design as a strong contender for the digitalization of concrete (digital design and realisation of high-performance shapes in concrete) and its subsequent sustainable use.

(ii) **Part II - Computational framework.** Chapters 4, 5, 6 describe the so-called Integrated design Explorer (IDE) to enable design-manipulation friendly, shape design procedures. Chapter 4 concludes with the early experiments in masonry design using mesh modelling environments (MME) and their adaption into workflows suitable for masonry and 3DCP-aware shape design. (V. Bhooshan et al., 2018; Computation and Design group and Block Research Group, 2017; Oval et al., 2018))

(iii) **Part III - Prototypes and demonstrators**. Chapters 7,8,9 describe the early experiments in printing and their influence on the CF and IDE above, the full-scale technology demonstrator project called Striatus, and the design-to-production workflows therein. The DTP workflows were generalized into the CF and IDE above.

10.2 Outlook

Immediate future work and extensions of the research described in this dissertation relate to improving the interactive shape design as enabled by the CF, the refinement of the Function Representation based scheme to synthesise and visualize the print-paths and extending the learnings from the Striatus project for permanent structures.

10.2.1 Computational Framework

The research set out to address the following, previously ear-marked to be addressed by hitherto ignored, design-related aspects of 3DCP (Khoshnevis et al., 2006a):

(i) abstraction of feasibility analysis into geometric reasoning,

(ii) developing of an atlas of feasible and novel geometries,

(iii) the applicability of historic techniques of masonry to 3DCP

(iv) data structures amenable to interactive design exploration and

(v) unifying the equilibrium of printed geometries with the print feasibility of the parts.

It is safe to that say that these goals have been addressed by the Computational Framework (CF) and the Interactive Design Environment (IDE) for a masonry informed and 3DCP-aware shape design as outlined in Part II. Furthermore, the proposed shape description method takes a foundational step towards addressing the current lack of shape design tools that are designer friendly in the edit-and-

observe, didactic sense. Thus, the outlook for the CF stems from the ultimate motivation for the CF and IDE – to impact design practice, and support practical innovations that promote SDC:

(i) **incorporation into an MME**, to take advantage of the increased popularity and availability of mesh geometry processing tools in popular CAD platforms such as McNeel Rhino, Blender etc. The discrete data structures, the minimal dependency form finding and stereotomy algorithms, along with easy-to-implement FRep operations should aid the effort. Together, the MME and the geometry tools should foster design innovations (Figure 117. The compatibility with MMEs could also be beneficial in the easy production of virtual and mixed reality experiences and other game-technology based promotional assets (Figure 118).

(ii) **deep integration into the COMPAS framework**, to take advantage of the ecosystem of relevant libraries for Discrete Element Modelling, Rigid Block Equilibrium analysis, Robotic control etc. Furthermore, the ever-expanding, state-of-the-art research in optimal transport is becomes available as Python libraries. This can support the refinement and acceleration of the print-path synthesis to support real time interactive design (Section 5.3).

(iii) **development of DTP workflows** specifically for building products, such as concrete podiums, floor slabs, stairs, footbridges etc. (Figure 117). Furthermore, the packaged availability of DTP workflows as easy-to-use tools with a simple interface, preferably running natively on a browser, can aid the mainstream adoption of 3DCP building products as envisioned in Section 2.4.

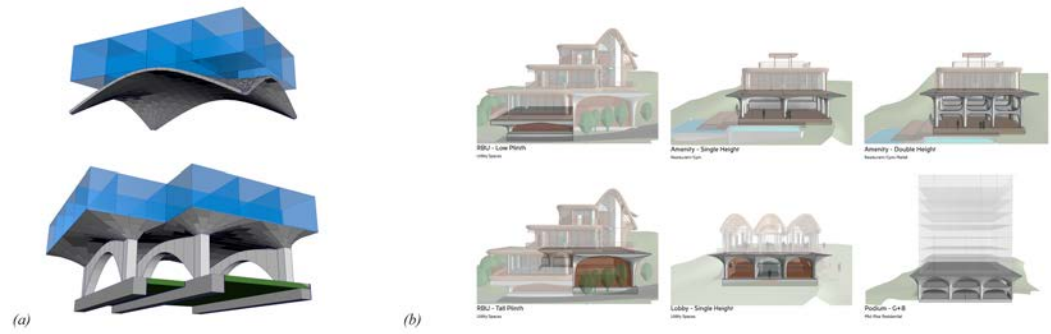

Figure 117 – Reinterpreting the so-called 5-over-1 housing typology with 3DCP podium. Early sketches for a 3DCP podium (a) to support stacked modular timber houses (b), considered after nominal instructions regarding a workflow for 3DCP informed design was suggested (Chapter 6). Courtesy: Zaha Hadid Architects, London ©

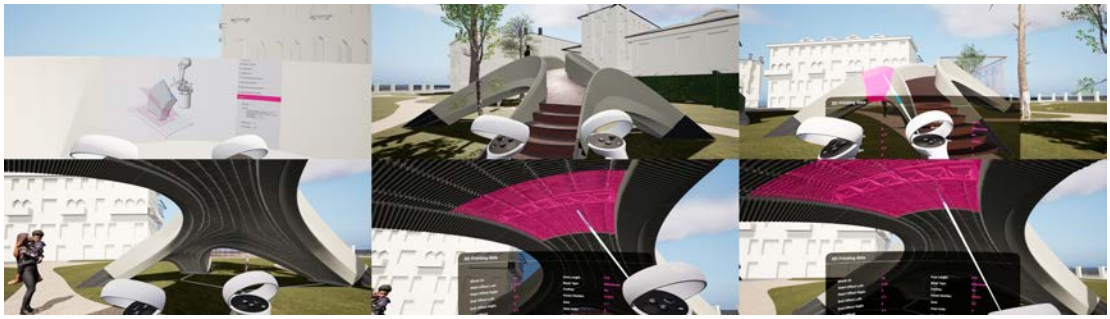

Figure 118 – Benefits of MME compatibility. The design procedures being compatible with a MME lends well to the quick production of virtual reality, mixed reality experiences and other game-technology based promotional assets. Courtesy : Zaha Hadid Architects, London ©.

10.2.2 Function representation and print-path synthesis

The use of Function Representation (FRep) to synthesise and specify geometries for 3D printing is finding renewed interest (Keeter, 2013; Ntopology, 2021; Schmidt and Singh, 2010). Thus, the immediate outlook for the print-path synthesis component (Chapter 5 and 9) of the research relates both to the limitations of current work and to the yet-to-be explored branches leading from the main thrust of the work so far:

(i) Currently, the input scalar-fields and the interpolated fields are restricted to Radial Basis Fields. However, the recovery of a continuous function from interpolated RBFs using convolution methods is possible, as noted previously. In addition, we can note that if the final step of recovering a continuous function from point samples were required, quick convolution methods can be used(Fuchs, 2020).

(ii) Currently, print-paths are restricted to be planar paths. Physically, non-planar print-paths are physically feasible to a limited extent. As such, an immediate extension of the proposed data structure, could be to describe such print-paths within the local coordinate frame of the orientation planes.

(iii) Exploring the use of Optimal Mass Transport with relaxed optimality criteria as they will still yield spatially coherent print-paths whilst improving the computational speed of the interpolation scheme.

(iv) An interesting future avenue of exploration would be to calibrate the shape description for other layered constructions, particularly pitched-brick vaulting.

10.2.3 Striatus, technology demonstrator

The proof of concept, the physically realised bridge, and the associated design-to-production toolchain, together demonstrate the viability of applying unreinforced masonry paradigm and methods to the design of 3DCP bridges (Chapter 8). The following areas of work could be improved to help its mainstream adoption:

(i) **Stereotomy and DEM for 3DCP blocks**: Stereotomy or discretization of the form-found, medial surface mesh into 3D solid blocks and the discrete element modelling (DEM) of the those blocks to structural verify their stability, are inter-related. Currently DEM evaluation happens entirely in the structural thread, at non-interactive rates. Developing a fast-approximation of the DEM evaluations within the serial thread will improve the interactive editing and didactic aspects of the design-to-production toolchain.

(ii) **Print-path synthesis**: The interpolation of the printing planes results in non-parallel planes. In some cases, this causes the limits of inter-plane distance and the corresponding maximum or minimum layer-height to be exceeded. A fast, constrained optimisation routine to guarantee that interpolation will meet the layer-height limits will alleviate the need for manual intervention.

(iii) **Block Interface design**: Development of male-female interface details to provide resistance against local sliding and resulting misalignment. The design of the interface can also consider reference and registration points that will aid the assembly process, including potentially unique and automatic registration.

(iv) **Transport of unreinforced 3DCP blocks**, starting from removal off the print bed, is an important consideration. Since the blocks use an unreinforced cement fix, handling and transportation induced loads needs to be carefully considered and can be incorporated in the design process.

(v) **False-work design**: The design of the false work can be optimised to minimize the amount of timber used, for repeated reuse of the timber parts, easy decentring etc.

(vi) **Low-emissions concrete:** The compressive stresses developed in the structure is very low given the unreinforced masonry structural principles. This opens a pathway for low-strength and thus low-carbon emissions concrete formulations that can be 3D printed along inclined planes. Currently, the printing-compatible mortar has high compressive strength.

(vii) **Automated calibration** procedure to check and minimize the deviation between as-printed and as-designed blocks would improve construction tolerance and production time. In the current project, we relied on spot-checking and experience.

The continued design development of the prototype of the footbridge itself may build upon disruptive improvements on sustainability and circularity that are offered by considering the use of 3DCP concrete as an artificial stone and the unreinforced masonry paradigm of design and construction. This is relevant to other structures such as floor slabs (Block et al., 2019). The structural design principles and structural behaviour features from unreinforced masonry, combined with the benefits of 3DCP could potentially pave the way for improvements in the so-called concrete 'ink', such as reducing the requirement for high-strength concrete, reducing the amount of virgin materials used, alternative binders in the concrete etc.

10.3 Conclusions

The thesis articulated the relevance of unreinforced masonry design to provide an operative pathway to achieve a Sustainable Digital Concrete (SDC) and expressive, collaborative computational design. The following concluding remarks stem from this central thrust of the thesis.

10.3.1 Benefits of the masonry paradigm & incline-plane 3D Concrete Printing

The unreinforced masonry design paradigm and techniques are highly compatible with the compression-dominant, orthotropic material properties of layered 3D Concrete Printing (3DCP) (Part I). The compatibility is at two scales: the overall funicular form of the structure and the force flow through each 3DCP block. Globally, the structure's funicular form engages the compression-dominant properties of 3DCP, offers a clear discretization strategy orthogonal to the designed force flow, enables the separation of compressive and tensile structural elements, makes dry assembly of the prefabricated components, results in significant lower stresses overall in comparison with bending solutions, etc. Locally, the alignment of the printed layers orthogonal to expected compressive force flows engages the compressive strength of 3DCP whilst eliminating the need for tensile reinforcement or post-tensioning to prevent shear failure along the print planes in the 3DCP blocks (Chapter 5). Furthermore, the wider benefits of structural geometry and the masonry paradigm to improve recyclability, maintenance and repair and reuse of material due to dry-assembly and clean separation of tensile and compressive materials has also been highlighted.

10.3.2 Integrated computational design, robotic 3DCP and construction

Procedures to design structurally informed, printing-feasible, and expressive 3DCP structures that reduce the amount concrete and steel used in addition to being repair, reuse and recycling friendly, was detailed (Part II). Furthermore design-to-production toolchains to physically realise the structures was also described (Part III). Both the shape design procedures and the design-to-production (DTP) toolchain was critical for the collaborative, multi-author, and integrated computational design, robotic 3DCP and construction of the Striatus footbridge project. The key contributions as described and practically demonstrated, suggest a clear pathway to incorporate the DTP toolchain into

- an equilibrium and 3DCP aware, didactic, and expressive computational design pipeline for architectural design.
- an end-to-end, industrial, integrated design-to-production solution for 3DCP bridges, and potential extension to other building components such as stairs, and floor slabs.

Furthermore, the paradigm, file format and data structure of this proof-of-concept DTP, based on COMPAS, makes it suitable for open-source publication and thus improve chances of its extension. These aspects are critical to fully realizing the ecological, labor-saving and worker-safety benefits promised by 3DCP.

10.3.3 New language for concrete

The proposed geometric, didactic and collaborative-authorship friendly design paradigm, its deep compatibility with designer friendly mesh modelling environments (MMEs), and alignment procedures in robotic 3DCP, could

- promote collaborative problem solving needed to create sustainable and engaging design
- address economical design (material, energy, carbon emissions, waste, labour) and durable construction including reuse and repair.
- build on historic knowledge
- re-inject intelligence and vocational pride in the construction industry
- afford new expressive possibilities for design teams

Physical prototypes and demonstrators described in Part III, including the Striatus footbridge project, highlights the congeniality between masonry structures, 3D Concrete Printing and contemporary design. It strives for a new language for concrete, and seeks an alternative to ‘beton brut’, the raw concrete that dominated 20th-century architecture. Instead, Striatus is a ‘beton nouveau’, a structurally informed, fabrication-aware, ecologically responsible, precisely placed, and articulate alternative to the ubiquitous ways of building with concrete. More importantly, it is hoped that the new language is reflective of a structural change in the way buildings are designed and built. Together, the work points to a new structural and architectural language of force-aligned, precision 3DCP emerging from the historic paradigm of unreinforced masonry.

11 STRIATUS PROJECT CREDITS

Striatus - an arched 3D-concrete-printed masonry bridge.

A project by the Block Research Group (BRG) at ETH Zurich and Zaha Hadid Architects Computation and Design Group (ZHACODE), in collaboration with incremental3D (in3D), made possible by Holcim.

11.1 Full credits

11.1.1 Design

- ZHACODE: Jianfei Chu, Vishu Bhooshan, Henry David Louth, Shajay Bhooshan, Patrik Schumacher
- ETH BRG: Tom Van Mele, Alessandro Dell'Endice, Philippe Block

11.1.2 Structural engineering

- ETH BRG: Tom Van Mele, Alessandro Dell'Endice, Sam Bouten, Philippe Block

11.1.3 Fabrication design

- ETH BRG: Shajay Bhooshan, Alessandro Dell'Endice, Sam Bouten, Chaoyu Du, Tom Van Mele
- ZHACODE: Vishu Bhooshan, Philip Singer, Tommaso Casucci

11.1.4 3D concrete printing

- In3D: Johannes Megens, Georg Grasser, Sandro Sanin, Nikolas Janitsch, Janos Mohacsi

11.1.5 Concrete material development

- Holcim: Christian Blachier, Marjorie Chantin-Coquard, Helene Lombois-Burger, Francis Steiner
- LafargeHolcim Spain: Benito Carrion, Jose Manuel Arnau

11.1.6 Assembly & Construction

- Bürgin Creations: Theo Bürgin, Semir Mächler, Calvin Graf
- ETH BRG: Alessandro Dell'Endice, Tom Van Mele

11.1.7 Logistics

- ETH BRG: Alessandro Dell'Endice, Tom Van Mele
- Holcim Switzerland & Italy: Michele Alverdi
- LafargeHolcim Spain: Ricardo de Pablos, José Luis Romero

11.1.8 Additional partners

- Ackermann GmbH [CNC timber formwork]
- L2F Architettura [site measurements]
- Pletscher [steel supports]

- ZB Laser [lasercutting neoprene]

11.1.9 Documentation

- ZHACODE: Jianfei Chu, Cesar Fragachan, Vishu Bhooshan, Philip Singer, Edward Meyers, Shajay Bhooshan
- ETH BRG: Tom Van Mele, Alessandro Dell'Endice, Philippe Block
- In3D: Alexander Gugitscher, Sandro Sanin, Nikolas Janitsch
- naaro
- LBS Fotografia

12 APPENDIX I

The proposed Computational Framework (CF), attempts to extend the Rigid Block Equilibrium (RBE) method to accommodate the soft-rigid aspects of 3D printing of concrete, and thus provide feedback regarding the stability of the print-layers during the printing process (Section 4.5.1). The approach was not developed further in the research herein and only the central ideas are presented here to aid potential future investigation.

12.1 Rigid-Block Equilibrium

Popular implementations of RBE and Rigid Body Dynamics (RBD), share a common mathematical formulation: computations at a single time instance of RBD calculates the linear and angular accelerations of each block, whilst RBE inverse computes the forces and torques on each block by setting their accelerations to zero. Further, the two algorithms converge to be exactly the same when RBD computes the so-called resting contact forces – forces needed to keep two static rigid bodies from inter-penetrating (Baraff, 1997). In this case, both algorithms find the necessary equilibrating forces (shown in orange in Figure 119) that satisfy linear constraints using quadratic programming.

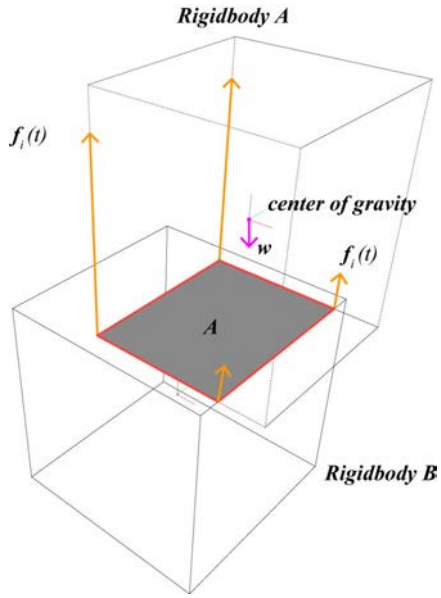

Figure 119 – Contact interface and forces when two rigid-bodies are in resting contact

12.1.1 Equilibrium formulation

The formulation for resting contact forces in RBD (Baraff, 1997) (Figure 119) is

$$\boldsymbol{A}_{eq}\boldsymbol{f} + \boldsymbol{b} = \boldsymbol{a} \qquad (1)$$

Where $\boldsymbol{a}$ is a column vector that encodes accelerations of the blocks, $\boldsymbol{A_{eq}}$ is the so-called *n* x *n* equilibrium matrix, $\boldsymbol{b}$ is a column of constants, $\boldsymbol{f}$ a column vector of unknown force magnitudes, and *n* is the number of vertices in the contact interface.

When computing *resting contact* forces, $\boldsymbol{b}$ is a column vector of weights of the rigid blocks, $\boldsymbol{a}$ is $\mathbf{0}$. Thus (1) becomes,

$$\boldsymbol{A_{eq}f} + \boldsymbol{w} = \mathbf{0} \qquad (2)$$

This is the equilibrium formulation used in RBE to solve for $\boldsymbol{f}$ in a least-squares sense

$$min\, g(\boldsymbol{f}) = \boldsymbol{f}^T \boldsymbol{H}\, \boldsymbol{f} + \boldsymbol{b}^T \qquad (3)$$

$$s.t \;\; A_{eq}\boldsymbol{f} + \boldsymbol{w} = \mathbf{0}$$

For derivation, detailed explanation, and pseudo code, see (Baraff, 1997; Frick et al., 2015; Livesley, 1978)

12.2 Soft-Rigid Body Equilibrium (sRBE)

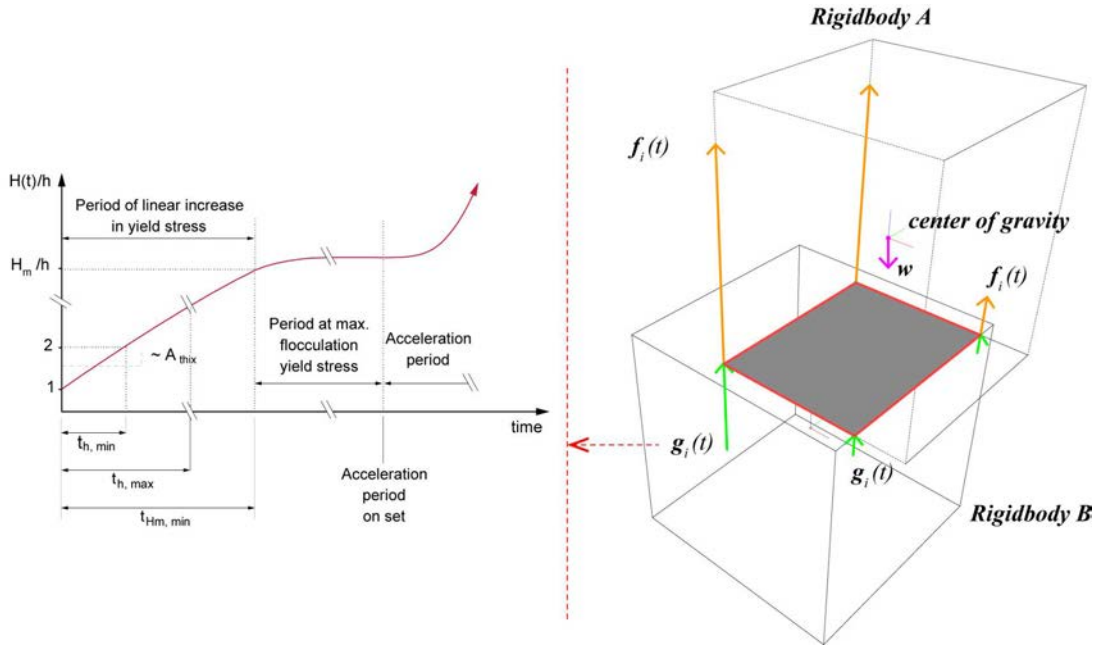

Figure 120 – Soft-rigid body equilibrium forces (right) and (Left) time-dependent evolution of the bearing capacity of the material. Graph from (Wangler et al., 2016).

The proposed CF extends the RBE method above, to semi-rigid and rigidifying materials such as fresh concrete and clay. The insight here is that the necessary forces at the contact interface, $\boldsymbol{f}_i(t)$

and highlighted orange in Figure 120, that ensure static equilibrium of the rigidified blocks is a function of the configuration of the blocks. On the other hand, the capacity of the rigidifying material to be able to offer the necessary reaction forces $\boldsymbol{g}_i(t)$ (highlighted green in Figure 120), are a function of time. In other words, the time-dependent reaction forces (Le et al., 2012a; Wangler et al., 2016) can be added as an additional constraint to the quadratic program (3) that computes the equilibrating forces.

12.3 Implementation

The current implementation of the Computational Framework (Section 4.5), utilises extensions to the RBE method as stated in (Frick et al. 2015), and resting contact formulations and quadratic programming (QP) as stated in (Baraff, 1997). The ALGLIB library is used to numerically solve the QP.

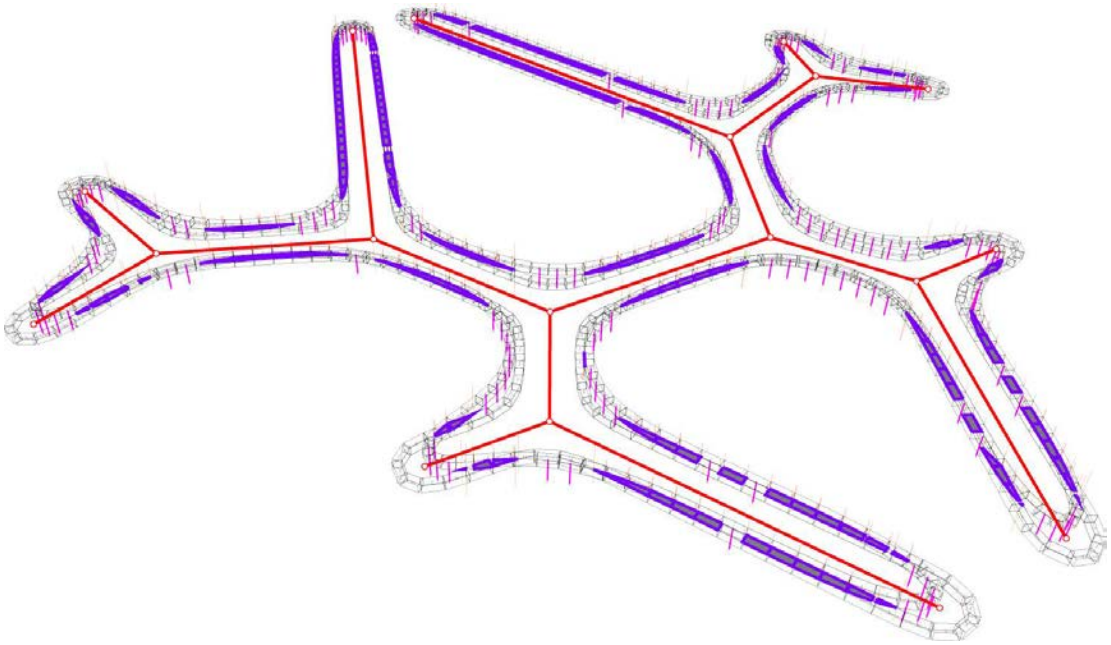

Figure 121 – Application of method to test print feasibility. In the current implementation, areas where a non-trivial contact (blue) interface exists, the sRBE method is executed to evaluate feasibility. If such contact is not found, the infeasibility is indicated by pink arrows. The skeletal graph (red) is manipulated based on this visual feedback.

12.3.1 Contact interfaces and collisions

In order to compute the forces or accelerations, both RBD and RBE methods require efficient routines to calculate the so-called contact interface between two colliding or touching rigid bodies (Cundall, 1988; Frick et al., 2016). This research implemented only the *face-to-face* contact interface as described in (Frick et al. 2016), since it was found to be sufficient to provide interactive feedback to designers. The other interfaces including *face-edge*, are likely to be a result of un-printable geometry.

Acciona, 2016. acciona-introduces-large-scale-3d-printing-technology-feria-in3dustry-needs-solutions-barcelona [WWW Document]. acciona.com. URL http://www.acciona-engineering.com/press-room/news/noticias_externas.aspx?id=36644&page= (accessed 6.29.16).

Adriaenssens, S., Block, P., Veenendaal, D., Williams, C., 2014. Shell structures for architecture: form finding and optimization. Routledge.

Akbarzadeh, M., van Mele, T., Block, P., 2015. On the equilibrium of funicular polyhedral frames and convex polyhedral force diagrams. Computer-Aided Design 63, 118–128.

Andres, J., Bock, T., Gebhart, F., Steck, W., 1994. First results of the development of the masonry robot system ROCCO: a fault tolerant assembly tool. Autom Rob Constr XI 11, 87–93.

Anton, A., Reiter, L., Wangler, T., Frangez, V., Flatt, R.J., Dillenburger, B., 2021. A 3D concrete printing prefabrication platform for bespoke columns. Autom Constr 122, 103467.

Anton, A., Yoo, A., Bedarf, P., Reiter, L., Wangler, T., Dillenburger, B., 2019. Vertical Modulations.

Bächer, M., Whiting, E., Bickel, B., Sorkine-Hornung, O., 2014. Spin-it: optimizing moment of inertia for spinnable objects. ACM Transactions on Graphics (TOG) 33, 96.

Bærentzen, J.A., Abdrashitov, R., Singh, K., 2014. Interactive shape modeling using a skeleton-mesh co-representation. ACM Transactions on Graphics (TOG) 33, 132.

Baker, W.F., Beghini, L.L., Mazurek, A., Carrion, J., Beghini, A., 2013. Maxwell's reciprocal diagrams and discrete Michell frames. Structural and multidisciplinary optimization 48, 267–277.

Baraff, D., 1997. An introduction to physically based modeling: Rigid body simulation II—Nonpenetration constraints. SIGGRAPH course notes D31–D68.

Beaman, J.J., Barlow, J.W., Bourell, D.L., Crawford, R.H., Marcus, H.L., McAlea, K.P., 1997. Solid freeform fabrication: a new direction in manufacturing. Kluwer Academic Publishers, Norwell, MA 2061, 25–49.

Beghini, L.L., Carrion, J., Beghini, A., Mazurek, A., Baker, W.F., 2014. Structural optimization using graphic statics. Structural and Multidisciplinary optimization 49, 351–366.

Bezier, P.E., 1971. Example of an existing system in the motor industry: the Unisurf system. In: Proceedings of the Royal Society of London A: Mathematical, Physical and Engineering Sciences. The Royal Society, pp. 207–218.

Bhooshan, S., 2016a. Collaborative Design - A case for combining CA(G)D and BIM. Architectural Design.

Bhooshan, S., 2016b. Interactive Design of Curved Crease Folding.

Bhooshan, S., 2016c. Upgrading Computational Design. Architectural Design 86, 44–53.

Bhooshan, S., 2017. Parametric design thinking: A case-study of practice-embedded architectural research. Des Stud.

Bhooshan, S., Bhooshan, V., Shah, A., Louth, H., Reeves, D., Shah, A., Bhooshan, V., Reeves, D., Bhooshan, S., 2015. Curve-folded form-work for cast, compressive skeletons,. In: Proceedings of the SIMAUD 2015 Conference, Alexandria, USA.

Bhooshan, S., el Sayed, M., 2011. Use of sub-division surfaces in architectural form-finding and procedural modelling. In: Proceedings of the 2011 Symposium on Simulation for Architecture and Urban Design. Society for Computer Simulation International, pp. 60–67.

Bhooshan, S., Ladinig, J., van Mele, T., Block, P., 2018a. Function Representation for Robotic 3D Printed Concrete. In: Robotic Fabrication in Architecture, Art and Design. Springer, pp. 98–109.

Bhooshan, S., Van Mele, T., Block, P., 2018b. Equilibrium-Aware Shape Design for Concrete Printing. In: Et al., K.D.R. (Ed.), Humanizing Digital Reality. Springer Singapore, Paris, pp. 493–508.

Bhooshan, S., Van Mele, T., Block, P., 2020. Morph & Slerp: Shape description for 3D printing of concrete. In: Symposium on Computational Fabrication. pp. 1–10.

Bhooshan, V., Reeves, D., Bhooshan, S., Block, P., 2018. MayaVault—a Mesh Modelling Environment for Discrete Funicular Structures. Nexus Netw J 20, 567–582.

Blanther, J.E., 1892. Manufacture of contour relief-maps.

Bletzinger, K.-U., Ramm, E., 2001. Structural optimization and form finding of light weight structures. Comput Struct 79, 2053–2062.

Block, P., 2009. Thrust network analysis: exploring three-dimensional equilibrium.

Block, P., 2016. Parametricism's Structural Congeniality. Architectural Design 86, 68–75.

Block, P., Calvo Barentin, C., Ranaudo, F., Paulson, N., 2019. Imposing challenges, disruptive changes: rethinking the floor slab. The materials book: inspired by the 6th lafargeholcim foundation.

Block, P., Lachauer, L., Rippmann, M., 2014. Thrust Network Analysis - Design of a cut-stone masonry vault. In: Shell Structures for Architecture: Form Finding and Optimization. Routledge, p. 71.

Block, P., Ochsendorf, J., 2007. Thrust network analysis: A new methodology for three-dimensional equilibrium. In: Journal of the International Association for Shell and Spatial Structures.

Block, P., van Mele, T., Liew, A., DeJong, M., Escobedo, D., Ochsendorf, J.A., 2018. Structural design, fabrication and construction of the Armadillo vault. The Structural Engineer: journal of the Institution of Structural Engineer 96, 10–20.

Block, P., Van Mele, T., Rippmann, M., Ranaudo, F., Calvo Barentin, C.J., Paulson, N., 2020. Redefining structural art: strategies, necessities and opportunities. The Structural Engineer 98, 66–72.

Bloomenthal, J., Bajaj, C., 1997. Introduction to implicit surfaces. Morgan Kaufmann.

Bloomenthal, J., Shoemake, K., 1991. Convolution surfaces. In: ACM SIGGRAPH Computer Graphics. ACM, pp. 251–256.

Bonneel, N., 2013. Optimal Transport with Proximal Splitting.

Bonneel, N., 2018. Fast Network Simplex for Optimal Transport.

Bonneel, N., van de Panne, M., Paris, S., Heidrich, W., 2011a. Displacement interpolation using Lagrangian mass transport. In: Proceedings of the 2011 SIGGRAPH Asia Conference. pp. 1–12.

Bonneel, N., Van De Panne, M., Paris, S., Heidrich, W., 2011b. Displacement interpolation using Lagrangian mass transport. In: Proceedings of the 2011 SIGGRAPH Asia Conference. pp. 1–12.

Bos, F., Wolfs, R., Ahmed, Z., Salet, T., 2016. Additive manufacturing of concrete in construction: potentials and challenges of 3D concrete printing. Virtual Phys Prototyp 11.

Bos, F.P., Lucas, S.S., Wolfs, R.J.M., Salet, T.A.M., 2020. Second RILEM International Conference on Concrete and Digital Fabrication: Digital Concrete 2020. Springer Nature.

Botsch, M., Kobbelt, L., Pauly, M., Alliez, P., Lévy, B., 2010. Polygon mesh processing. CRC press.

Bouaziz, S., Deuss, M., Schwartzburg, Y., Weise, T., Pauly, M., 2012. Shape-up: Shaping discrete geometry with projections. Computer Graphics Forum 31, 1657–1667.

Breseghello, L., Sanin, S., Naboni, R., 2021. Toolpath simulation, design and manipulation in robotic 3D concrete printing.

Buswell, R.A., Soar, R.C., Gibb, A.G.F., Thorpe, A., 2007. Freeform construction: mega-scale rapid manufacturing for construction. Autom Constr 16, 224–231.

Buswell, R.A., Thorpe, A., Soar, R.C., Gibb, A.G.F., 2008. Design, data and process issues for mega-scale rapid manufacturing machines used for construction. Autom Constr 17, 923–929.

Cacace, S., Cristiani, E., Rocchi, L., 2017. A level set based method for fixing overhangs in 3D printing. Appl Math Model 44, 446–455.

Catmull, E., 1974. A subdivision algorithm for computer display of curved surfaces. DTIC Document.

Charnes, A., Lemke, C.E., Zienkiewicz, O.C., 1959. Virtual work, linear programming and plastic limit analysis. In: Proceedings of the Royal Society of London A: Mathematical, Physical and Engineering Sciences. The Royal Society, pp. 110–116.

Chien, S., Choo, S., Schnabel, M.A., Nakapan, W., Kim, M.J., Roudavski, S., 2016. Parametric customisation of a 3d concrete printed pavilion. In: Proceedings of the 21st International Conference of the Association for Computer-Aided Architectural Design Research in Asia CAADRIA 2016,. The Association for Computer-Aided Architectural Design Research in Asia (CAADRIA), Hong Kong, pp. 549–558.

Cima, M.J., Lauder, A., Khanuja, S., Sachs, E., 1992. Microstructural elements of components derived from 3D printing. In: Solid Freeform Fabrication Symposium. pp. 220–227.

Cohen, L.D., 1991. On active contour models and balloons. CVGIP: Image understanding 53, 211–218.

Computation and Design group, Z.H.A., Block Research Group, E.Z., 2017. digital futures 2017 [WWW Document]. https://block.arch.ethz.ch/brg/files/2017_Digital%20FUTURE-Shanghai_RhinoVault_1499601025.pdf.

Concre3DLab Ghent, 2019. Numerical Simulation of 3D Concrete Printing [WWW Document]. URL https://www.food4rhino.com/en/app/concre3dlab (accessed 10.5.22).

Culmann, K., 1875. Die graphische statik. Meyer & Zeller (A. Reimann).

Cundall, P.A., 1988. Formulation of a three-dimensional distinct element model—Part I. A scheme to detect and represent contacts in a system composed of many polyhedral blocks. In: International Journal of Rock Mechanics and Mining Sciences & Geomechanics Abstracts. Elsevier, pp. 107–116.

Cundall, P.A., Strack, O.D.L., 1979. A discrete numerical model for granular assemblies. Geotechnique 29, 47–65.

CyBe-Construction, 2016. CyBe Construction - Redefining Construction [WWW Document].

De Casteljau, P. de F., 1986. Shape mathematics and CAD. Kogan Page.

De Goes, F., Alliez, P., Owhadi, H., Desbrun, M., 2013. On the equilibrium of simplicial masonry structures. ACM Transactions on Graphics (TOG) 32, 93.

De Kestelier, X., Buswell, R.A., 2009. A digital design environment for large-scale rapid manufacturing. In: Proceedings of the 29th Annual Conference of the Association for Computer Aided Design in Architecture. pp. 201–208.

DeJong, M.J., 2009. Seismic assessment strategies for masonry structures.

Dell'Endice, A., Iannuzzo, A., DeJong, M.J., van Mele, T., Block, P., 2021. Modelling imperfections in unreinforced masonry structures: Discrete Element simulations and scale model experiments of a pavilion vault. Eng Struct 228, 111499.

Desbrun, M., Gascuel, M.-P., 1995. Animating soft substances with implicit surfaces. In: Proceedings of the 22nd Annual Conference on Computer Graphics and Interactive Techniques. ACM, pp. 287–290.

Deuss, M., Panozzo, D., Whiting, E., Liu, Y., Block, P., Sorkine-Hornung, O., Pauly, M., 2014. Assembling Self-supporting Structures. ACM Trans. Graph. 33, 214:1--214:10.

Dickens, P.M., Pridham, M.S., Cobb, R.C., Gibson, I., Dixon, G., 1992. Rapid prototyping using 3-D welding. In: Proc. Solid Freeform Fabrication Symp. DTIC Document, pp. 280–290.

digitalFutures [WWW Document], 2017. URL https://block.arch.ethz.ch/brg/files/2017_Digital%20FUTURE-Shanghai_RhinoVault_1499601025.pdf (accessed 5.10.23).

digitalFutures [WWW Document], 2018. URL https://digitalfutures.international/workshops-2011-2019/ (accessed 5.13.23).

Dillenburger, B., Hansmeyer, M., 2013. The resolution of architecture in the digital age. In: International Conference on Computer-Aided Architectural Design Futures. Springer, pp. 347–357.

Dini, E., 2009. D-shape. Monolite UK Ltd. http://www. d-shape. com/cose. htm.

Donea, J., Huerta, A., Ponthot, J.-P., Rodriguez-Ferran, A., 2004. Encyclopedia of Computational Mechanics Vol. 1: Fundamentals., Chapter 14: Arbitrary Lagrangian-Eulerian Methods. John Wiley & Sons, Ltd.

Dörfler, K., Sandy, T., Giftthaler, M., Gramazio, F., Kohler, M., Buchli, J., 2016. Mobile Robotic Brickwork-Automation of a Discrete Robotic Fabrication Process Using an Autonomous Mobile Robot. Robotic Fabrication in Architecture, Art and Design.

DUSArchitects, 2014. 3D Print Canal House [WWW Document]. 3dprintcanalhouse. URL http://3dprintcanalhouse.com/ (accessed 8.12.14).

Emerging-Objects, 2016. Emerging Objects [WWW Document].

engineering, S., 2019. 3DCP bridge modelling.

Evans, R., 2000. The projective cast: architecture and its three geometries. MIT press.

FastBrickRobotics, 2015. FastBrick Robotics [WWW Document]. FastBrick Robotics. URL http://www.fbr.com.au/ (accessed 4.3.16).

Fivet, C., Zastavni, D., 2012. Robert Maillart's key methods from the Salginatobel Bridge design process (1928). JOURNAL OF THE INTERNATIONAL ASSOCIATION FOR SHELL AND SPATIAL STRUCTURES: J. IASS 53, 39–47.

Flatt, R.J., Wangler, T., 2022. On sustainability and digital fabrication with concrete. Cem Concr Res 106837.

Frick, U., Van Mele, T., Block, P., 2015. Decomposing Three-Dimensional Shapes into Self-supporting, Discrete-Element Assemblies. In: Modelling Behaviour. Springer, pp. 187–201.

Frick, U., Van Mele, T., Block, P., 2016. Data management and modelling of complex interfaces in imperfect discrete-element assemblies.

Fuchs, M., 2020. quick convolution [WWW Document]. URL https://github.com/Mathias-Fuchs/quickconvolution

Gardiner, J.B., Janssen, S.R., 2014. FreeFab. In: Robotic Fabrication in Architecture, Art and Design 2014. Springer, pp. 131–146.

Giannakopoulos, S., Markopoulou, A., 2015. pylos [WWW Document]. IAAC.com. URL https://iaac.net/research-projects/large-scale-3d-printing/pylos/ (accessed 5.5.15).

Gilbert, M., Melbourne, C., 1994. Rigid-block analysis of masonry structures. Structural engineer 72.

Gosselin, C., Duballet, R., Roux, P., Gaudillière, N., Dirrenberger, J., Morel, P., 2016. Large-scale 3D printing of ultra-high performance concrete–a new processing route for architects and builders. Mater Des 100, 102–109.

Gramazio, F., Kohler, M., Flatt, R., Kristensen, E.L., 2015. Apparatus and method for vertical slip forming of concrete structures.

Hack, N., Lauer, W.V., 2014. Mesh-Mould: Robotically Fabricated Spatial Meshes as Reinforced Concrete Formwork. Architectural Design 84, 44–53.

Hahn, J.K., 1988. Realistic animation of rigid bodies. In: ACM SIGGRAPH Computer Graphics. ACM, pp. 299–308.

Harada, T., 2007. Real-time rigid body simulation on GPUs. GPU gems 3, 123–148.

Hart, G., 1998. Conway Notation for Polyhedra.

Hart, R., Cundall, P.A., Lemos, J., 1988. Formulation of a three-dimensional distinct element model—Part II. Mechanical calculations for motion and interaction of a system composed of many polyhedral blocks. In: International Journal of Rock Mechanics and Mining Sciences & Geomechanics Abstracts. Elsevier, pp. 117–125.

Hernandez, C.R.B., 2006. Thinking parametric design: introducing parametric Gaudi. Des Stud 27, 309–324.

Heyman, J., 1966. The stone skeleton. Int J Solids Struct 2, 249–279.

Holcim, 2021. Tector 3D Build [WWW Document]. URL https://www.holcim.com/lafargeholcim-spain-introduces-our-first-dry-mortar-range-3d-printing

Hopkinson, N., Dicknes, P., 2003. Analysis of rapid manufacturing—using layer manufacturing processes for production. Proc Inst Mech Eng C J Mech Eng Sci 217, 31–39.

Hu, D., Mei, H., Kovacevic, R., 2002. Improving solid freeform fabrication by laser-based additive manufacturing. Proc Inst Mech Eng B J Eng Manuf 216, 1253–1264.

Hubert, E., Cani, M.-P., 2012. Convolution surfaces based on polygonal curve skeletons. J Symb Comput 47, 680–699.

Huerta, S., 2006. Structural design in the work of Gaudi. Archit Sci Rev 49, 324–339.

Hull, C.W., 1986. Apparatus for production of three-dimensional objects by stereolithography.

IAAC, 2016. IAAC 3DCP bridge. iaac.net.

IAAC, Acciona, 2017. IAAC and ACCIONA.

Incremental3d [WWW Document], 2017. . https://www.incremental3d.eu/. URL https://www.incremental3d.eu/ (accessed 5.9.23).

Ji, Z., Liu, L., Wang, Y., 2010a. B-Mesh: A Modeling System for Base Meshes of 3D Articulated Shapes. In: Computer Graphics Forum. Wiley Online Library, pp. 2169–2177.

Ji, Z., Liu, L., Wang, Y., 2010b. B-Mesh: A Modeling System for Base Meshes of 3D Articulated Shapes. In: Computer Graphics Forum. Wiley Online Library, pp. 2169–2177.

Jiang, C., Tang, C., Tomičí, M., Wallner, J., Pottmann, H., 2015. Interactive Modeling of Architectural Freeform Structures: Combining Geometry with Fabrication and Statics. In: Advances in Architectural Geometry 2014. Springer, pp. 95–108.

Json.org, 1999. JSON.

Kass, M., Witkin, A., Terzopoulos, D., 1988a. Snakes: Active contour models. Int J Comput Vis 1, 321–331.

Keeter, matthew, 2013. Hierarchical volumetric object representations for digital fabrication workflows. Massachusetts Institute of Technology.

Khoshnevis, B., 2004. Automated construction by contour crafting—related robotics and information technologies. Autom Constr 13, 5–19.

Khoshnevis, B., Hwang, D., Yao, K.-T., Yeh, Z., 2006a. Mega-scale fabrication by contour crafting. International Journal of Industrial and Systems Engineering 1, 301–320.

Khoshnevis, B., Yuan, X., Zahiri, B., Xia, B., 2017. Construction by Contour Crafting using Sulfur Concrete with Planetary Applications. Rapid Prototyp J.

Khronos, 2021. glTF.

Kilian, A., 2006. Design exploration through bidirectional modeling of constraints.

Klahn, C., Leutenecker, B., Meboldt, M., 2015. Design strategies for the process of additive manufacturing. Procedia CIRP 36, 230–235.

Klein, J., Stern, M., Franchin, G., Kayser, M., Inamura, C., Dave, S., Weaver, J.C., Houk, P., Colombo, P., Yang, M., 2015. Additive manufacturing of optically transparent glass. 3D Print Addit Manuf 2, 92–105.

Kley, M. van der, TU Eindhoven, Witteveen+Bos, 2018. The Bridge Project.

Kooij, D., 2016. dirk vander kooij [WWW Document]. dirkvanderkooij.com. URL http://www.dirkvanderkooij.com/pages/about (accessed 2.16.16).

Kwon, H., 2002. Experimentation and analysis of contour crafting (CC) process using uncured ceramic materials.

Lachauer, L., 2015. Interactive Equilibrium Modelling - A new approach to the computer-aided exploration of structures in architecture. ETH Zurich, Department of Architecture, Zurich.

Lachauer, L., Block, P., 2014. Interactive Equilibrium Modelling. Journal of the International Association for Shell and Spatial Structures 29.

Le, T.T., Austin, S.A., Lim, S., Buswell, R.A., Gibb, A.G.F., Thorpe, T., 2012a. Mix design and fresh properties for high-performance printing concrete. Mater Struct 45, 1221–1232.

Le, T.T., Austin, S.A., Lim, S., Buswell, R.A., Law, R., Gibb, A.G.F., Thorpe, T., 2012b. Hardened properties of high-performance printing concrete. Cem Concr Res 42, 558–566.

Lim, S., Buswell, R.A., Le, T.T., Austin, S.A., Gibb, A.G.F., Thorpe, T., 2012. Developments in construction-scale additive manufacturing processes. Autom Constr 21, 262–268.

Lim, S., Buswell, R.A., Valentine, P.J., Piker, D., Austin, S.A., De Kestelier, X., 2016. Modelling curved-layered printing paths for fabricating large-scale construction components. Addit Manuf 12, 216–230.

Liu, Y., Pan, H., Snyder, J., Wang, W., Guo, B., 2013. Computing self-supporting surfaces by regular triangulation. ACM Transactions on Graphics (TOG) 32, 92.

Livesley, R.K., 1978. Limit analysis of structures formed from rigid blocks. Int J Numer Methods Eng 12, 1853–1871.

Livesley, R.K., 1992. A computational model for the limit analysis of three-dimensional masonry structures. Meccanica 27, 161–172.

Lloret, E., Shahab, A.R., Linus, M., Flatt, R.J., Gramazio, F., Kohler, M., Langenberg, S., 2015. Complex concrete structures: Merging existing casting techniques with digital fabrication. Computer-Aided Design 60, 40–49.

Loughborough University, 2014. Partnership aims to develop 3D concrete printing in construction [WWW Document]. Loughborough University. URL http://www.lboro.ac.uk/news-events/news/2014/november/204-skanska.html (accessed 5.1.16).

Lowke, D., Dini, E., Perrot, A., Weger, D., Gehlen, C., Dillenburger, B., 2018. Particle-bed 3D printing in concrete construction–possibilities and challenges. Cem Concr Res 112, 50–65.

Ma, G., Buswell, R., da Silva, W.R.L., Wang, L., Xu, J., Jones, S.Z., 2022. Technology readiness: a global snapshot of 3D concrete printing and the frontiers for development. Cem Concr Res 156, 106774.

Maxwell, J.C., 1870. I.—On Reciprocal Figures, Frames, and Diagrams of Forces. Transactions of the Royal Society of Edinburgh 26, 1–40.

Mechtcherine, V., Gram, A., Krenzer, K., Schwabe, J.-H., Shyshko, S., Roussel, N., 2014. Simulation of fresh concrete flow using Discrete Element Method (DEM): theory and applications. Mater Struct 47, 615–630.

Michalatos, P., Payne, A., 2016. Monolith: the biomedical paradigm and the inner complexity of hierarchical material design.

Michell, A.G.M., 1904. LVIII. The limits of economy of material in frame-structures. The London, Edinburgh, and Dublin Philosophical Magazine and Journal of Science 8, 589–597.

Monreal, A., 2012. T-Norms, T-Conorms, Aggregation Operators and Gaudí's Columns. In: Soft Computing in Humanities and Social Sciences. Springer, pp. 497–515.

Motamedi, M., Oval, R., Carneau, P., Baverel, O., 2019. Supportless 3D Printing of Shells: Adaptation of Ancient Vaulting Techniques to Digital Fabrication. In: Design Modelling Symposium Berlin. Springer, pp. 714–726.

Mozaffari, S., Akbarzadeh, M., Vogel, T., 2020. Graphic statics in a continuum: Strut-and-tie models for reinforced concrete. Comput Struct 240, 106335.

MX3D, 2015. MX3D Bridge [WWW Document]. mx3d.com. URL http://mx3d.com/projects/bridge/

Network Simplex, 2009.

Ntopology, 2021. Ntopology [WWW Document]. https://ntopology.com/webinars/webinar/implicit-modeling-for-mechanical-design/.

Opalach, A., Maddock, S.C., 1995. An overview of implicit surfaces. Introduction to modelling and animation using implicit surfaces 1.

Oval, R., Rippmann, M., Mesnil, R., van Mele, T., Baverel, O., Block, P., 2018. Topology finding of structural patterns.

Oxman, R., 2017. Parametric design thinking. Des Stud.

Panozzo, D., Block, P., Sorkine-Hornung, O., 2013. Designing unreinforced masonry models. ACM Transactions on Graphics (TOG) 32, 91.

Papadakis, N., 2015. Optimal transport for image processing.

Papadakis, N., Peyré, G., Oudet, E., 2014. Optimal transport with proximal splitting. SIAM J Imaging Sci 7, 212–238.

Pasko, A., Adzhiev, V., 2002. Function-based shape modeling: mathematical framework and specialized language. In: International Workshop on Automated Deduction in Geometry. Springer, pp. 132–160.

Paull, G., 2015. Fastbrick Robotics [WWW Document]. youtube.com. URL https://www.youtube.com/watch?v=7Zw7qHxMtrY (accessed 7.22.16).

Pegna, J., 1997. Exploratory investigation of solid freeform construction. Autom Constr 5, 427–437.

Pérez, F., Suárez, J. a., 2007. Quasi-developable B-spline surfaces in ship hull design. CAD Computer Aided Design 39, 853–862.

Perrot, A., Rangeard, D., Pierre, A., 2016. Structural built-up of cement-based materials used for 3D-printing extrusion techniques. Mater Struct 49, 1213–1220.

Peyré, G., Cuturi, M., 2019. Computational optimal transport. Foundations and Trends® in Machine Learning 11, 355–607.

Photosculpture, 2016. . Threedscans.com.

Picon, A., 1988. Navier and the introduction of suspension bridges in France. Construction History 4, 21–34.

Pivac, M.J., Wood, M.B., 2012. Automated brick laying system for constructing a building from a plurality of bricks.

Poranne, R., Ovreiu, E., Gotsman, C., 2013. Interactive planarization and optimization of 3D meshes. Computer Graphics Forum 32, 152–163.

Pottmann, H., 2007. Architectural geometry. Bentley Institute Press.

Pottmann, H., 2010. Architectural geometry as design knowledge. Architectural Design 80, 72–77.

Pottmann, H., Wallner, J., 1999. Approximation algorithms for developable surfaces. Comput Aided Geom Des 16, 539–556.

Prévost, R., Whiting, E., Lefebvre, S., Sorkine-Hornung, O., 2013. Make it stand: balancing shapes for 3D fabrication. ACM Transactions on Graphics (TOG) 32, 81.

Rankine, W.J.M., 1864. XVII. Principle of the equilibrium of polyhedral frames. The London, Edinburgh, and Dublin Philosophical Magazine and Journal of Science 27, 92.

Rippmann, M., 2012. Lachauer., L., and Block, P., RhinoVAULT-Designing funicular form with Rhino, computer software,.

Rippmann, M., 2016. Funicular Shell Design: Geometric Approaches to Form Finding and Fabrication of Discrete Funicular Structures. ETH Zurich, Department of Architecture, Zurich.

Rippmann, M., Block, P., 2013. Rethinking Structural Masonry: Unreinforced, Stone-cut Shells. In: Proceedings of the ICE - Construction Materials. pp. 378–389.

Rippmann, M., Lachauer, L., Block, P., 2012. Interactive vault design. International Journal of Space Structures 27, 219–230.

Rippmann, M., Van Mele, T., Popescu, M., Augustynowicz, E., M&#xfffd;ndez Echenagucia, T., Calvo Barentin, C., Frick, U., Block, P., 2016. The Armadillo Vault: Computational design and digital fabrication of a freeform stone shell. In: Advances in Architectural Geometry. pp. 64–83.

Rock, S.J., Wozny, M.J., 1991. A flexible file format for solid freeform fabrication. In: Solid Freeform Fabrication Symposium Proceedings. Citeseer, pp. 1–12.

Rock, S.J., Wozny, M.J., 1992. Generating topological information from a bucket of facets. In: Proceedings of Solid Freeform Fabrication Symposium, Austin, TX, Aug. Citeseer, pp. 3–5.

Rossignac, J., 1985. Blending and offsetting solid models.

Sabin, M.A., 1971. An existing system in the aircraft industry. The British Aircraft Corporation numerical master geometry system. Proc R Soc Lond A Math Phys Sci 321, 197–205.

Saint, A., 2007. Architect and engineer: a study in sibling rivalry. Yale Univ Pr.

Sakarovitch, J., 2003. Stereotomy, a multifaceted technique. In: Proceedings of the 1st International Congress on Construction History, S. Huerta Ed., Madrid. pp. 69–79.

Salet, T.A.M., Ahmed, Z.Y., Bos, F.P., Laagland, H.L.M., 2018. Design of a 3D printed concrete bridge by testing. Virtual Phys Prototyp 13, 222–236.

Salonitis, K., Al Zarban, S., 2015. Redesign optimization for manufacturing using additive layer techniques. Procedia CIRP 36, 193–198.

Saravanan, U., 2013. Advanced Solid Mechanics. Department of Civil Engineering, Indian Institute of Technology Madras.

Schek, H.-J., 1974. The force density method for form finding and computation of general networks. Comput Methods Appl Mech Eng 3, 115–134.

Schlaich, J., Schlaich, M., 2000. LIGHTWEIGHT STRUCTURES. In: Widespan Roof Structures. Thomas Telford Publishing, pp. 177–188.

Schmidt, R., Singh, K., 2010. Meshmixer: an interface for rapid mesh composition. In: ACM SIGGRAPH 2010 Talks. p. 1.

Schumacher, P., 2014a. The congeniality of architecture and engineering. Shell structures for architecture: Form finding and optimization 271.

Schumacher, P., 2014b. Tectonic Articulation: Making Engineering Logics Speak. Architectural Design 84, 44–51.

Schumacher, P., 2017. Tectonism in Architecture, Design and Fashion: Innovations in Digital Fabrication as Stylistic Drivers. Architectural Design 87, 106–113.

Schumacher, P., 2018. The Progress of Geometry as Design Resource. Log.

Schwartzburg, Y., Pauly, M., 2013. Fabrication-aware Design with Intersecting Planar Pieces. In: Computer Graphics Forum. Wiley Online Library, pp. 317–326.

Scott, D., 2021. The Importance of DfAM Education [WWW Document]. https://www.designforam.com/p/dfam-education-in-2022. URL https://www.designforam.com/p/dfam-education-in-2022 (accessed 9.13.22).

Sethian, J., 1998. Fast marching methods and level set methods for propagating interfaces. Computational Fluid Dynamics, Annual Lecture Series, 29 th, Rhode-Saint-Genese, Belgium.

Sherstyuk, A., 1999a. Interactive shape design with convolution surfaces. In: Shape Modeling and Applications, 1999. Proceedings. Shape Modeling International'99. International Conference On. IEEE, pp. 56–65.

Sherstyuk, A., 1999b. Kernel functions in convolution surfaces: a comparative analysis. Vis Comput 15, 171–182.

Shoemake, K., 1985. Animating rotation with quaternion curves. In: Proceedings of the 12th Annual Conference on Computer Graphics and Interactive Techniques. pp. 245–254.

Shyshko, S., Mechtcherine, V., 2008. Simulating the workability of fresh concrete. In: Proceedings of the International RILEM Symposium of Concrete Modelling—CONMOD. pp. 173–181.

SlicerXL, 2021. SLicerXL.

Sobieszek, R.A., 1980. Sculpture as the Sum of Its Profiles: Francois Willeme and Photosculpture in France, 1859-1868. Art Bull 62, 617–630.

Solomon, J., de Goes, F., Peyré, G., Cuturi, M., Butscher, A., Nguyen, A., Du, T., Guibas, L., 2015. Convolutional wasserstein distances: Efficient optimal transportation on geometric domains. ACM Transactions on Graphics (TOG) 34, 1–11.

Song, P., Fu, C.-W., Cohen-Or, D., 2012. Recursive interlocking puzzles. ACM Transactions on Graphics (TOG) 31, 128.

Srinivasan, V., Mandal, E., Akleman, E., 2005. Solidifying wireframes. In: Proceedings of the 2004 Bridges Conference on Mathematical Connections in Art, Music, and Science.

Stomakhin, A., Schroeder, C., Chai, L., Teran, J., Selle, A., 2013. A material point method for snow simulation. ACM Transactions on Graphics (TOG) 32, 102.

Stratasys, 2016. Stratasys Partners with Adobe [WWW Document]. URL http://investors.stratasys.com/releasedetail.cfm?ReleaseID=952717 (accessed 7.25.16).

Suiker, A.S.J., 2018. Mechanical performance of wall structures in 3D printing processes: Theory, design tools and experiments. Int J Mech Sci 137, 145–170.

Sulsky, D., Zhou, S.-J., Schreyer, H.L., 1995. Application of a particle-in-cell method to solid mechanics. Comput Phys Commun 87, 236–252.

Swainson, W.K., 1977. Method, medium and apparatus for producing three-dimensional figure product.

Tang, C., Sun, X., Gomes, A., Wallner, J., 2012. Form-finding with Polyhedral Meshes Made Simple.

Tang, Y., Fuh, J.Y.H., Loh, H.T., Wong, Y.S., Lu, L., 2003. Direct laser sintering of a silica sand. Mater Des 24, 623–629.

Tang, Y., Zhao, Y.F., 2016. A survey of the design methods for additive manufacturing to improve functional performance. Rapid Prototyp J.

Tanigawa, Y., Mori, H., 1989. Analytical study on deformation of fresh concrete. J Eng Mech 115, 493–508.

Tessmann, O., 2008. Collaborative Design Procedures for Architects and Engineers. University of Kassel.

Van Mele, T., 2020a. compas_skeleton [WWW Document]. URL https://blockresearchgroup.github.io/compas_skeleton/latest/index.html

Van Mele, T., 2020b. COMPAS_SLICER [WWW Document]. https://compas.dev/compas_slicer/latest/.

Van Mele, T., 2021. COMPAS_TNA [WWW Document]. https://blockresearchgroup.github.io/compas_tna/latest/.

van Mele, T., Liew, A., Mendez, T., Rippmann, M., 2017. COMPAS: A framework for computational research in architecture and structures.

Van Mele, T., Panozzo, D., Sorkine-Hornung, O., Block, P., 2014. Best-fit thrust network analysis. Shell structures for architecture-form finding and optimization, Routledge 157–170.

Vertico [WWW Document], 2017. . https://www.vertico.xyz/. URL https://www.vertico.xyz/ (accessed 5.9.23).

Vouga, E., Mathias, H., Wallner, J., Pottmann, H., 2012. Design of Self-supporting Surfaces. ACM Trans Graph 31.

Wangler, T., Lloret, E., Reiter, L., Hack, N., Gramazio, F., Kohler, M., Bernhard, M., Dillenburger, B., Buchli, J., Roussel, N., 2016. Digital Concrete: Opportunities and Challenges. RILEM Technical Letters 1, 67–75.

Wangler, T., Roussel, N., Bos, F.P., Salet, T.A.M., Flatt, R.J., 2019. Digital concrete: a review. Cem Concr Res 123, 105780.

Warton, J., Dwivedi, R., Kovacevic, R., 2014. Additive Manufacturing of Metallic Alloys. In: Robotic Fabrication in Architecture, Art and Design 2014. Springer, pp. 147–161.

Wendland, D., 2007. Traditional vault construction without formwork: Masonry pattern and vault shape in the historical technical literature and in experimental studies. International Journal of Architectural Heritage 1, 311–365.

Westerlind, H., Hernández, J., 2020. Knitting Concrete. In: RILEM International Conference on Concrete and Digital Fabrication. Springer, pp. 988–997.

Whiting, E., Shin, H., Wang, R., Ochsendorf, J., Durand, F., 2012a. Structural optimization of 3D masonry buildings. ACM Trans Graph 31, 1.

Whiting, E., Shin, H., Wang, R., Ochsendorf, J., Durand, F., 2012b. Structural optimization of 3D masonry buildings. ACM Trans Graph 31, 1.

Whiting, E.J.W., 2012. Design of structurally-sound masonry buildings using 3d static analysis.

Witt, A.J., 2010. A Machine Epistemology in Architecture. Encapsulated Knowledge and the Instrumentation of Design. Candide. Journal for architectural knowledge 3, 37–88.

Wolfe, W.S., 1921. Graphical Analysis: A text book on graphic statics. McGraw-Hill book Company, Incorporated.

Wolfs, R., Salet, T.A.M., 2015. An optimization strategy for 3D concrete printing.

Wozny, M.J., 1992. Systems issues in solid freeform fabrication. In: Solid Freeform Fabrication Symposium 1992. University of Texas, Austin, pp. 1–15.

Wu, S., 2020. Buckling simulation in Karamba3D.

Wyvill, B., Wyvill, G., 1989. Field functions for implicit surfaces. Vis Comput 5, 75–82.

Wyvill, G., McPheeters, C., Wyvill, B., 1986. Soft objects. In: Advanced Computer Graphics. Springer, pp. 113–128.

XtreeE, 2016. XtreeE | The large-scale 3d [WWW Document].

Yingchuang, 2015. 3D Printing construction [WWW Document]. yhbm.com. URL http://www.yhbm.com/index.php?a=lists&c=index&catid=67&m=content (accessed 5.1.16).

Zastavni, D., 2008. The structural design of Maillart's Chiasso Shed (1924): a graphic procedure. Structural Engineering International 18, 247–252.

Zhao, H., Gu, F., Huang, Q.-X., Garcia, J., Chen, Y., Tu, C., Benes, B., Zhang, H., Cohen-Or, D., Chen, B., 2016. Connected fermat spirals for layered fabrication. ACM Transactions on Graphics (TOG) 35, 1–10.

RELEVANT PUBLICATIONS BY AUTHOR

Bhooshan, Shajay Bhooshan, V., Dell'endice, A., Megens, J., Chu, J., Singer, P., VanMele, T., Block, P., 2022. The Striatus arched bridge Computational design and robotic fabrication of an unreinforced, 3D-concrete-printed, masonry bridge. Archit. Struct. Constr.

Bhooshan, S., Bhooshan, V., Megens, J., Casucci, T., VanMele, T., Block, P., 2022. Print-path design for inclined-plane robotic 3D printing of unreinforced concrete. In: 3rd RILEM International Conference on Concrete and Digital Fabrication (Digital Concrete).

Bhooshan, S., Ladinig, J., Van Mele, T., Block, P., 2018a. Function Representation for Robotic 3D Printed Concrete. In: Robotic Fabrication in Architecture, Art and Design. Springer, pp. 98–109.

Bhooshan, S., Van Mele, T., Block, P., 2018b. Equilibrium-Aware Shape Design for Concrete Printing. In: et al., K.D.R. (Ed.), Humanizing Digital Reality. Springer Singapore, Paris, pp. 493–508.

Bhooshan, S., Van Mele, T., Block, P., 2020. Morph & Slerp: Shape description for 3D printing of concrete. In: Symposium on Computational Fabrication. pp. 1–10.

Bhooshan, V., Reeves, D., Bhooshan, S., Block, P., 2018. MayaVault—a Mesh Modelling Environment for Discrete Funicular Structures. Nexus Netw. J. 20, 567–582.

CURRICULUM VITAE

Education

2018 – 2023	Doctoral Candidate: Block Research Group, Institute of Technology in Architecture, of ETH Zurich, Thesis: “Shape Design of 3D-Concrete-Printed Masonry Structures”, Prof.Dr.Philippe Block, Dr.Tom Van Mele and Dr.Patrik Schumacher.
2014 – 2016	Master of Philosophy: Digital Architectonics at the University of Bath, UK. Thesis: “Interactive Design of Curved-Crease Folding”, Dr. Paul Shepherd, Prof. Paul Richens.
2004 – 2006	Master of Architecture and Urbanism: Design Research Laboratory at the Architectural Association London, Open University, UK. Thesis: “Manifold: Swarm Mobility“, Dr.Theodore Spyropolous, Vasilis Stroumpakos.
1997 – 2002	Bachelor of Architecture: TVB School of Habitat Studies at the Guru Gobind Indraprasta University, New Delhi, India Thesis: “Method to architectural design in historic precincts”, Dr. AGK Menon.

Professional

since 2007	Head of Computation and Design group, and Associate Director, Zaha Hadid Architects, Zaha Hadid Computation and Design Group, London, UK
2018-2022	Thesis advisor, Architectural Computation Programme, Bartlett School of Architecture University College London, London, UK.
since 2012	Studio master, Architectural Association Design Research Laboratory (ADDRL), London, UK.
2008-2012	Course tutor, Architectural Association Design Research Laboratory (ADDRL), London, UK.
2015	Guest studio professor, University of Innsbruck, Innsbruck, Austria.